Geomorphic and Thermochronologic Signatures of Active Tectonics in the Central Nepalese Himalaya

by

Cameron W. Wobus

A.B. Bowdoin College, 1995
M.S. Dartmouth College, 1997

SUBMITTED TO THE DEPARTMENT OF EARTH, ATMOSPHERIC, AND PLANETARY SCIENCES IN PARTIAL FULFILLMENT OF THE REQUIREMENTS FOR THE DEGREE OF

DOCTOR OF PHILOSOPHY
AT THE
MASSACHUSETTS INSTITUTE OF TECHNOLOGY

SEPTEMBER 2005

Signature of Author: _____
Department of Earth, Atmospheric and Planetary Sciences
July 29, 2005

Certified by: _____
Kip V. Hodges, PhD.
Professor of Geology
Thesis supervisor

Certified by: _____
Kelin X. Whipple, PhD.
Professor of Geology
Thesis supervisor

Accepted by: _____
Maria T. Zuber, PhD.
E.A. Griswold Professor of Geophysics and Planetary Science
Department Head

Geomorphic and Thermochronologic Signatures of Active Tectonics in the Central Nepalese Himalaya

by

Cameron W. Wobus

Submitted to the Department of Earth, Atmospheric, and Planetary Sciences
on July 15, 2005 in Partial Fulfillment of the
Requirements for the Degree of Doctor of Philosophy

ABSTRACT

The central Nepalese Himalaya are characterized by a sharp transition in physiography that does not correlate with previously mapped faults. Rates of rock uplift, erosion, and exhumation for rocks surrounding this physiographic transition are investigated using digital topographic data, $^{40}Ar/^{39}Ar$ thermochronology, cosmogenic radionuclides, and thermal modeling, to determine whether this break in landscape morphology reflects active tectonic displacements at the foot of the Himalaya. The goals of the thesis are 1) to understand the degree to which landscape morphology can be used to delineate breaks in rock uplift in active orogens; 2) to characterize the neotectonics of central Nepal using data representing varied temporal and spatial scales of inquiry; and 3) to move closer to understanding the dynamic interactions among climate, erosion and tectonics in a field setting.

Analysis of digital topographic data from Nepal and other tectonically active settings demonstrates how breaks in the simple scaling characterizing river systems can be used to identify tectonic boundaries. Limitations to these methods are illustrated by way of an example from the Eastern Central Range of Taiwan, but changes in landscape morphology become the foundation upon which further investigations are built for central Nepal. These investigations include data from detrital $^{40}Ar/^{39}Ar$ thermochronology to characterize changes in exhumation rates at million-year timescales; cosmogenic ^{10}Be to characterize changes in erosion rates at millennial timescales; and simple thermal modeling to evaluate a range of alternative tectonic geometries for central Nepal. The data point to the existence of a tectonically significant, thrust-sense shear zone at the base of the high Himalaya in central Nepal, nearly 100 km north of the active thrust front. The existence of this fault zone in a location where the Indian summer monsoon is concentrated is consistent with the predictions of numerical and analytical models of orogenic growth, which suggest a direct feedback between focused erosion and tectonic displacements in active orogens. Future work is warranted to evaluate the persistence of climatic and tectonic signals over a variety of time and space scales in central Nepal, and to determine whether correlations between climate and tectonics exist in other field settings.

Thesis Supervisors: Kip V. Hodges, Professor of Geology
Kelin X. Whipple, Professor of Geology

ACKNOWLEDGEMENTS

First, I wish to thank my advisors, Kelin Whipple and Kip Hodges, for their willingness to experiment with me as their first co-advised student. Throughout my time at MIT, I was continually amazed by their ability to come up with new and exciting research ideas, their multidisciplinary approaches to problems, and their accessibility despite their ridiculously hectic schedules. I cannot imagine a better team of advisors to help me build my own way of thinking, and to help me build a broad background to start coming up with my own research ideas.

I am also grateful to Arjun Heimsath, who has become both a collaborator and friend during this process. Laboratory analyses conducted in Arjun's lab formed the backbone of Chapter 5 of this thesis, which may become the most visible aspect of this work. I would also like to thank my other committee members, Wiki Royden and David Mohrig, for their suggestions and guidance on various components of this thesis and for their willingness to spend a sunny July morning in the Ida Green Lounge for my thesis defense.

None of this work would have been possible without my wife Nicole, who has been a constant source of support, love, and guidance throughout my time at MIT. Our time in Boston has been marked by major milestones for both of us, most notably the arrival of our son Ethan in August of 2004, and I express my love and thanks to her for being a wonderful wife, mother, and companion through all of it. I am excited to begin the next chapter of our lives in Colorado and to continue the wild ride of parenthood together.

I would like to thank my dad for sending me down the path of becoming a geologist, despite early resistance on my part when I thought I might do something more lucrative. My curiosity and love for the outdoors began with his inspiration, and I would undoubtably be somewhere less exciting today were it not for him. I would also like to thank my mom and my brother Erik, who have always supported me in every aspect of my life.

All of the thermochronologic data in this thesis represent the hard work of those who keep the lab running: Bill Olszewski, Xifan Zhang, and Malcolm Pringle not only amazed me with their technical abilities, but were always available to help with analyses, turn things on and off at extremely odd hours, and help to process the data that were generated from the spectrometer at widely variable rates.

Finally, I would like to thank all of the Geology and Geochemistry graduate students that I have been fortunate to interact with during my time at MIT. In particular, I'd like to thank the members of the Whipple and Hodges teams that I've overlapped with, including Eric Kirby, Noah Snyder, Simon Brocklehurst, Ben Crosby, Joel Johnson, Taylor Schildgen, Will Ouimet, Arthur White, Jose Hurtado, Karen Viskupic, Jeremy Boyce, Kate Ruhl, and Ryan Clark. In addition, I was lucky to have a big group of G&G recruits coming in with me, including some of those listed above, as well as Blair Schoene, Chris Studnicki-Gizbert, Becky Flowers, and Maureen Long. Last, and hopefully leaving no one out, thanks to Sinan Akciz, Julie Baldwin, Marin Clark, Alison Cohen, Kristen Cook, Amy Draut, David Fike, Nicole Gasparini, Doug Jerolmack, Bill Lyons, Daniel MacPhee, Jenny Matzel, Brendan Meade, Mark Schmitz, Lindsay Schoenbohm, Frederik Simons, Steve Singletary, Kyle Straub, John Thurmond, Jessica Warren, Wes Watters, and Rhea Workman.

TABLE OF CONTENTS

Chapter 1: Introduction

1.1 Motivation

The central Nepalese Himalaya are home to almost all of the world's highest peaks, and summer monsoon rains bring some of the most intense sustained precipitation on the planet. These topographic and climatic extremes create a setting in which erosion rates may be among the highest in the world (Vance et al., 2003). At the base of this erosion machine, a suite of major strike-parallel fault systems accommodates between 15-20 mm yr^{-1} of tectonic convergence between India and Eurasia (Chen et al., 2004; Hodges, 2000; Wang et al., 2001). This combination of strong forcing from both surface processes and tectonics suggests that central Nepal may be one of the best places on earth to test the hypothesis that surface erosion can exert first-order control on the tectonics of active orogens (Beaumont et al., 2001; Koons et al., 1998; Molnar, 2003; Willett, 1999).

The primary objectives of this thesis are to characterize the present-day tectonics of the central Nepalese Himalaya, and to test the degree to which landscape morphology can be used as a tool for tectonic analysis. The approach is to combine geomorphic observations, thermochronology, cosmogenic isotope data, and thermal modeling to construct as complete a picture as possible of erosion, exhumation, and thermal history in central Nepal. This integrative approach allows the characterization of relative displacements of rock packages at a range of spatial and temporal scales, which can then place constraints on the distribution of active faulting at the base of the high Himalaya. As a tectonic picture of the Himalaya emerges, there is then some room to consider the degree to which this tectonic configuration might reflect a link between climate and tectonics at the orogen scale.

1.2 Background

In a 1983 paper, Seeber and Gornitz noted that most of the major knickpoints on the trans-Himalayan trunk streams were found at or near the surface trace of the Main Central Thrust, between 50 and 100 km north of the toe of the Himalayan orogenic wedge (Seeber and Gornitz, 1983). These knickpoints generally correspond with broader transitions in landscape morphology that define a prominent physiographic transition along the length of the Himalaya. This physiographic transition is referred to in this thesis as Physiographic Transition 2, or PT_2, after Hodges et al. (Hodges et al., 2001). In central Nepal, this physiographic transition diverges from the Main Central Thrust at the position of the Burhi Gandaki and Trisuli Rivers, which were the focus of much of the fieldwork for this thesis.

The abrupt change in landscape morphology noted by Seeber and Gornitz (1983) and Hodges et al. (2001) creates a challenge for tectonic models which presume that all tectonic convergence in Nepal is accommodated by the Main Frontal Thrust, the southernmost fault in the Himalayan system (Cattin and Avouac, 2000; Lave and Avouac, 2001): why is the physiographic transition so abrupt in central Nepal if active tectonic displacements are concentrated nearly 100 km to the south? To the degree that surface displacements are implied by the data from central Nepal, a more important underlying question also arises: why would surface faulting remain active near the foot of the high Himalaya if the thrust systems farther south can account for nearly all of the presumed tectonic convergence at the southern margin of the Himalayan system (Chen et al., 2004; Lave and Avouac, 2000; Wang et al., 2001)?

Both of these questions are revisited throughout this thesis. The first question is inherently answerable, and motivates an integrative study of a variety of data to characterize the

distribution of rock uplift, exhumation and erosion rates along the rangefront. In Chapters 2, 4, 5, and 6, a broad suite of data and tools are described and implemented, including quantitative metrics of landscape morphology; detrital $^{40}Ar/^{39}Ar$ thermochronology; cosmogenic radionuclides; and simple 2-D thermal modeling. The second question may be inherently unanswerable, but motivates a deeper understanding of orogenic growth as a dynamic earth system in which climate, tectonics and surface processes may be inextricably linked (Burbank, 2005; Molnar, 2003). This idea is revisited in Chapters 4, 5, and 6 as a framework for understanding our observations in central Nepal.

1.3 Summary of Chapters 2-7

Our digital topographic data and our models for correlating channel gradients with rock uplift rates have greatly improved since the Seeber and Gornitz paper was published (Fielding et al., 1994; Howard et al., 1994; Kirby and Whipple, 2001; Snyder et al., 2000; Whipple and Tucker, 1999; Whipple and Tucker, 2002). Chapter 2 lays the groundwork for an analysis of landscape morphology in central Nepal by summarizing the methods, applications and limitations of stream profile analysis for extracting tectonic information from digital topographic data. The chapter begins with a theoretical backdrop, describing empirical descriptions of fluvial profile form and the range of bedrock erosion models that are consistent with these empirical observations (Hack, 1973; Howard, 1994; Howard and Kerby, 1983; Whipple and Tucker, 1999). The chapter then discusses the methods employed for characterizing stream profiles, and summarizes a number of studies in which well-constrained tectonic settings have been used to establish a correlation between channel gradient and rock uplift rate (Kirby and Whipple, 2001; Snyder et al., 2000). It then describes two field sites – the San Gabriel Mountains of California

and the central Nepalese Himalaya – where the underlying tectonics are not well constrained, and the distribution of channel gradients can be used to make inferences about the distribution of rock uplift rates. The methods described and refined in Chapter 2 summarize the tools used in later chapters to evaluate the neotectonics of central Nepal.

Chapter 2 provides the framework for extracting tectonic information from digital topographic data, but this chapter also underscores many of the gaps in our understanding of fluvial incision that undermine our ability to link channel morphology directly to tectonic forcing (Whipple, 2004). Chapter 3 explores some of these shortcomings, and describes how a simple modification to our rules for fluvial erosion might lead to substantial changes in the expected morphology of river systems. The chapter focuses on the Eastern Central Range of Taiwan, where the presence of hanging valleys at tributary mouths suggests a decoupling of the local channel gradient from the rate of rock uplift. This decoupling between morphology and tectonics in an actively uplifting landscape suggests that extracting tectonic information directly from channel morphology may not always be a straightforward task. However, in the context of understanding the response of a fluvial network to tectonic forcing, the study from eastern Taiwan helps us to build our intuition about how tectonic signals can be reflected in landscape morphology.

In Chapters 4-6, the methods described in the previous two chapters are applied to central Nepal, as reconnaissance tools for describing variations in rock uplift rates along the Himalayan front. In each of these chapters, the inferences drawn from landscape morphology are supplemented with new data, including $^{40}Ar/^{39}Ar$ thermochronology (Chapters 4-6), cosmogenic radionuclides (Chapter 5), and the results of a simple thermal and kinematic model (Chapter 6). These independent techniques for estimating rock uplift, exhumation, and erosion rates provide a

verification of the stream profile analysis tools described in Chapter 2. In addition, the synopsis of data from a variety of spatial and temporal scales allows us to evaluate the persistence and tectonic significance of changes in rock uplift rates inferred from landscape morphology in central Nepal.

Chapter 4 describes a spatial coincidence between changes in the steepness of rivers along the Himalayan front and a break in cooling ages from detrital $^{40}Ar/^{39}Ar$ thermochronology. Samples for thermochronology are derived from seven small, strike-parallel tributary drainages, and from one trunk stream sediment sample within the Burhi Gandaki catchment. The cooling ages in these modern sediment samples change from Miocene and younger in the region defined by steep river gradients, to Paleozoic and older in the region defined by more gentle topography. These thermochronologic data indicate that a break in rock uplift rates has persisted at the physiographic transition at least long enough to juxtapose rocks with very different cooling histories integrated over million-year timescales. This finding suggests that the prominent physiographic transition in central Nepal represents a significant tectonic boundary.

Chapter 5 utilizes cosmogenic isotopes (^{10}Be) from modern river sediments to estimate millennial timescale, basin-averaged surface erosion rates from many of the same basins analyzed in Chapter 4. One of the questions addressed in Chapter 5 is whether the observed break in exhumation rates over million-year timescales is also reflected in erosion rates over much shorter timescales. The ^{10}Be data indicate a fourfold increase in millennial timescale erosion rates, co-located with the transition in physiography and the break in $^{40}Ar/^{39}Ar$ cooling ages described in Chapter 4. This co-location of breaks in $^{40}Ar/^{39}Ar$ and ^{10}Be data demonstrates a persistence of tectonic displacements at the physiographic transition over multiple timescales. Furthermore, the millennial timescale erosion rates reported in Chapter 5 come closer to the

timescale of our modern precipitation records in the same region (Putkonen, 2004) drawing us one step closer to demonstrating a direct relationship between intense monsoon precipitation, rapid erosion, and tectonic uplift in central Nepal.

Chapter 6 provides a synthesis of data from throughout central Nepal, extending the analyses from the Burhi Gandaki drainage along strike to the east and west. More comprehensive geomorphic analyses are used in this chapter to evaluate along-strike variations in physiography that might reflect along-strike changes in tectonic architecture. Two additional transects of detrital $^{40}Ar/^{39}Ar$ thermochronologic data are included from the Trisuli and Bhote Kosi rivers to evaluate the along-strike persistence of the cooling-age break described in Chapter 4. Finally, a simple thermal and kinematic model is used to evaluate the viability of an alternative to a surface thrusting geometry. In this alternative geometry, the distribution of cooling ages at the surface is explained by continuous accretion of material from the hanging wall to the footwall of the main décollement separating India from Eurasia (Bollinger et al., 2004). Incorporating all of the available data and the findings of our thermal and kinematic model, this chapter suggests that there might be substantial along-strike variations in the structural geometry of the central Nepalese Himalaya, which may reflect varying stages of tectonic development in an evolving orogenic system.

Finally, chapter 7 summarizes the major conclusions of the thesis, and explores some of the broader implications of the work. Implications specific to the neotectonics Himalaya are discussed, as well as the broader context of understanding the way active orogens evolve when subject to extreme forcing from topography, tectonics and climate.

Chapters 2-6 were prepared as manuscripts to be submitted for publication as stand-alone journal articles. As such, there is some unavoidable overlap in the content of these chapters.

Chapter 2 is in press in the *GSA Special Penrose Publication on Tectonics, Climate and Landscape evolution*, due for publication later in 2005. Chapter 3 was prepared for submittal to *GSA Bulletin*. Chapter 4 was published in the October, 2003 issue of *Geology*. Chapter 5 was published in the April 21, 2005 issue of *Nature*. Chapter 6 was prepared for submittal to *Tectonics*. Some formatting of the previously published papers was changed in order to maintain a consistent look to the thesis; however, the contents of Chapters 4 and 5 are identical to those found in the published versions.

References

Beaumont, C., Jamieson, R. A., Nguyen, M. H., and Lee, B., 2001, Himalayan tectonics explained by extrusion of a low-viscosity crustal channel coupled to focused surface denudation: Nature, v. 414, p. 738-742.

Bollinger, L., Avouac, J. P., Beyssac, O., Catlos, E. J., Harrison, T. M., Grove, M., Goffe, B., and Sapkota, S., 2004, Thermal structure and exhumation history of the Lesser Himalaya in central Nepal: Tectonics, v. 23, no. doi: 10.1029/2003TC001564.

Burbank, D., 2005, Cracking the Himalaya: nature, v. 434, p. 963-964.

Cattin, R., and Avouac, J. P., 2000, Modeling mountain building and the seismic cycle in the Himalaya of Nepal: Journal of Geophysical Research, v. 105, p. 13389-13407.

Chen, Q., Freymuller, J. T., Yang, Z., Xu, C., Jiang, W., Wang, Q., and Liu, J., 2004, Spatially variable extension in southern Tibet based on GPS measurements: Journal of Geophysical Research, v. 109, no. B09401, p. doi:10.1029/2002JB002350.

Fielding, E., Isacks, B., Barazangi, M., and Duncan, C., 1994, How flat is Tibet? Geology, v. 22, p. 163-167.

Hack, J. T., 1973, Stream profile analysis and stream-gradient index: J. Res. U.S. Geol. Surv., v. 1, no. 4, p. 421-429.

Hodges, K. V., 2000, Tectonics of the Himalaya and southern Tibet from two perspectives: GSA Bulletin, v. 112, no. 3, p. 324-350.

Hodges, K. V., Hurtado, J. M., and Whipple, K. X., 2001, Southward Extrusion of Tibetan Crust and its Effect on Himalayan Tectonics: Tectonics, v. 20, no. 6, p. 799-809.

Howard, A. D., 1994, A detachment-limited model of drainage basin evolution: Water Resources Research, v. 30, p. 2261-2285.

Howard, A. D., and Kerby, G., 1983, Channel changes in badlands: Geological Society of America Bulletin, v. 94, p. 739-752.

Howard, A. D., Seidl, M. A., and Dietrich, W. E., 1994, Modeling fluvial erosion on regional to continental scales: Journal of Geophysical Research, v. 99, p. 13,971-13,986.

Kirby, E., and Whipple, K. X., 2001, Quantifying differential rock-uplift rates via stream profile analysis: Geology, v. 29, no. 5, p. 415-418.

Koons, P. O., Craw, D., Cox, S. C., Upton, P., Templeton, A. S., and Chamberlain, C. P., 1998, Fluid flow during active oblique convergence: a Southern Alps model from mechanical and geochemical observations: Geology, v. 26, no. 2, p. 159-162.

Lave, J., and Avouac, J. P., 2000, Active folding of fluvial terraces across the Siwaliks Hills, Himalayas of central Nepal: Journal of Geophysical Research, v. 105, no. B3, p. 5735-5770.

-, 2001, Fluvial incision and tectonic uplift across the Himalayas of central Nepal: Journal of Geophysical Research, v. 106, no. B11, p. 26561-26591.

Molnar, P., 2003, Nature, nurture, and landscape: Nature, v. 426, p. 612-614.

Putkonen, J., 2004, Continuous snow and rain data at 500 to 4400 m altitude near Annapurna, Nepal, 1999-2001: Arctic, Antarctic and Alpine Research, v. 36, no. 2, p. 244-248.

Seeber, L., and Gornitz, V., 1983, River profiles along the Himalayan arc as indicators of active tectonics: Tectonophysics, v. 92, p. 335-367.

Snyder, N., Whipple, K., Tucker, G., and Merritts, D., 2000, Landscape response to tectonic forcing: DEM analysis of stream profiles in the Mendocino triple junction region, northern California: Geological Society of America, Bulletin, v. 112, no. 8, p. 1250-1263.

Vance, D., Bickle, M., Ivy-Ochs, S., and Kubik, P. W., 2003, Erosion and exhumation in the Himalaya from cosmogenic isotope inventories in river sediments: Earth and Planetary Science Letters, v. 206, p. 273-288.

Wang, Q., Zhang, P.-Z., Freymuller, J. T., Bilham, R., Larson, K. M., Lai, X., You, X., Niu, Z., Wu, J., Li, Y., Liu, J., Yang, Z., and Chen, Q., 2001, Present-day crustal deformation in China constrained by Global Positioning System measurements: Science, v. 294, p. 574-577.

Whipple, K., 2004, Bedrock rivers and the geomorphology of active orogens: Annual Reviews of Earth and Planetary Science, v. 32, p. 151-185.

Whipple, K. X., and Tucker, G. E., 1999, Dynamics of the stream-power river incision model: Implications for height limits of mountain ranges, landscape response timescales, and research needs: Journal of Geophysical Research, v. 104, p. 17661-17674.

-, 2002, Implications of sediment-flux-dependent river incision models for landscape evolution: JGR, v. 107, no. B2, p. doi:10.1029/2000JB000044.

Willett, S. D., 1999, Orogeny and orography: the effects of erosion on the structure of mountain belts: Journal of Geophysical Research, v. 104, p. 28957-28981.

Chapter 2: Tectonics from topography: Procedures, promise and pitfalls

Cameron Wobus[1]
Kelin Whipple[1]
Eric Kirby[2]
Noah Snyder[3]
Joel Johnson[1]
Katerina Spyropolou[1]
Benjamin Crosby[1]
Daniel Sheehan[4]

[1]Dept. of Earth Atmospheric and Planetary Sciences
Massachusetts Institute of Technology, Cambridge, MA 02139

[2]Department of Geosciences
The Pennsylvania State University, University Park, PA 16802

[3]Department of Geology and Geophysics
Boston College, Chestnut Hill, MA 02467

[4]Information Systems
Massachusetts Institute of Technology, Cambridge, MA 02139

In Press at *GSA Special Penrose publication on tectonics, climate and landscape evolution*

Abstract

Empirical observations from fluvial systems across the globe reveal a consistent power-law scaling between channel slope and contributing drainage area. Theoretical arguments for both detachment and transport limited erosion regimes suggest that rock uplift rate should exert first-order control on this scaling. Here we describe in detail a method for exploiting this relationship, in which topographic indices of longitudinal profile shape and character are derived from digital topographic data. The stream profile data can then be used to delineate breaks in scaling which may be associated with tectonic boundaries. The description of the method is followed by three case studies from varied tectonic settings. The case studies illustrate the power of stream profile analysis in delineating spatial patterns of, and in some cases, temporal changes in, rock uplift rate. Owing to an incomplete understanding of river response to rock uplift, the method remains primarily a qualitative tool for neotectonic investigations; we conclude with a discussion of research needs which must be met before we can extract quantitative information about tectonics directly from topography.

1. Introduction

Across the globe, with few notable exceptions, the steepest landscapes are associated with regions of rapid rock uplift. Given this empirical observation, one might expect that meaningful tectonic information could be extracted from some parameterization of landscape morphology, such as mean topographic gradient. Hillslopes, however, reach threshold slopes wherever erosion rates approach the surface soil production rate (Burbank et al., 1996; Heimsath et al., 1997; Montgomery and Brandon, 2002), limiting their utility as a "fingerprint" of tectonic forcing to relatively low uplift-rate environments. Only the fluvial network consistently maintains its connection to tectonic forcing, and therefore contains potentially useful information about variations in rock uplift rates across the landscape. A number of studies have laid the groundwork for extracting this information, by exploring the theoretical response of channels to variations in rock uplift rate, and by analyzing fluvial profiles in field settings where the tectonics have been independently determined (e.g., Whipple and Tucker, 1999, 2002; Snyder et al., 2000; Kirby and Whipple, 2001; Lague and Davy, 2003). Against this theoretical and empirical backdrop, however, there remains some uncertainty as to what can and cannot be learned from an analysis of river profiles, and there still exists no standard method for extracting tectonic information from these data.

In this contribution we attempt to bridge this gap, and discuss the "state of the art" in our ability to extract tectonic information directly from river profiles. The discussion focuses on the use of digital elevation models (DEMs), which are inexpensive, easily obtained, and can be used to extract much of this information quickly and easily prior to embarking on field campaigns. We discuss the methods employed in delineating tectonic information from DEMs, including

data sources, data handling, and interpretation. Case studies from diverse settings are then used to illustrate the utility of DEM analyses in extracting tectonic information from the landscape. We conclude with a discussion of research needs which must be met before we can have a reliable quantitative tool for neotectonics. Throughout the paper, we purposefully restrict our focus to empirical data analysis, discussing theory only as a rudimentary backdrop, and in the context of unresolved issues that limit our ability to extract quantitative tectonic information from stream profiles.

2. Background

In a variety of natural settings, topographic data from fluvial channels exhibit a scaling in which local channel slope can be expressed as a power law function of contributing drainage area (e.g., Hack, 1973; Flint, 1974; Howard and Kerby, 1983):

$$S = k_s A^{-\theta} \tag{1}$$

where S represents local channel slope, A is the upstream drainage area, and k_s and θ are referred to as the steepness and concavity indices, respectively. Equation (1) holds only for drainage areas above a critical threshold, A_{cr}, variably interpreted as the transition from divergent to convergent topography or from debris flow to fluvial processes (Tarboton, 1989; Montgomery and Foufoula-Georgiou, 1993). While many stream profiles will exhibit a single slope-area scaling for their entire length downstream of A_{cr}, segments of an individual profile are often characterized by different values of k_s, θ, or both. These aberrations may appear to be exceptions to the empirical result in (1); however, it is actually these variations we wish to exploit to extract tectonic information from the landscape. Much of the remainder of this paper outlines the methodologies employed to extract this information.

As has often been reported, simple models for both detachment- and transport-limited river systems predict power-law relations between channel gradient and drainage area in the form of equation (1) (e.g., Howard, 1994; Willgoose et al., 1991; Whipple and Tucker, 1999). In these models the concavity index, θ, is independent of rock uplift rate, U, assuming U is spatially uniform (Whipple and Tucker, 1999). These models further predict direct power-law relations between the steepness index, k_s, and rock uplift rate (e.g., Howard, 1994; Willgoose et al., 1991). However, although there is strong empirical support for a positive correlation between k_s and U, many factors not incorporated into these simple models can be expected to influence the quantitative relation between k_s and U. Known complexities include: 1) non-linearities in the incision process (e.g., Whipple et al., 2000; Whipple and Tucker, 1999), including the presence of thresholds (e.g., Tucker and Bras, 2000; Snyder et al., 2003b; Tucker, 2004) and possible changes in dominant incision processes with increasing incision rate (Whipple et al., 2000); 2) adjustments in channel width or sinuosity, herein referred to as "channel morphology" (e.g., Harbor, 1998; Lavé and Avouac 2000, 2001; Snyder et al., 2000; 2003a); 3) adjustments in the extent alluvial cover, bed material grainsize, bed morphology, and hydraulic roughness, herein referred to as "bed state" (e.g., Sklar and Dietrich, 1998; 2001; Hancock and Anderson, 2002; Whipple and Tucker, 2002; Sklar 2003); 4) changes in the frequency of erosive debris flows (Stock and Dietrich, 2003); and 5) orographic enhancement of precipitation (e.g., Roe et al., 2002, 2003; Snyder et al., 2000; 2003a). Due to the possible influence of each of these complexities, the functional relationship between k_s and U can be expected to vary depending on the geologic setting. While many of these complexities will be important over large length scales over which rock uplift rates are likely to be nonuniform, we must nonetheless consider these varied feedbacks and nonlinearities if we hope to quantitatively map steepness to rock

uplift rates. Additional climatic factors and substrate rock properties also strongly influence k_s, and are difficult to deconvolve from uplift rate signals. Thus at present we do not know how to quantitatively map channel steepness to incision rate (or rock uplift rate at steady state) except, to some extent, through local calibration of incision model parameters, as discussed in the Siwalik Hills example in Section 4.2.

Most models predict that profile concavity will be independent of rock uplift rate (if spatially uniform); however, any river response that differs at small and large drainage areas could theoretically induce a change in concavity. For instance, at greater drainage area one might expect the channel to have more freedom to adjust channel width and sinuosity. Similarly at smaller drainage area one might expect more variability in the fraction of exposed bedrock, hydraulic roughness, and the relative influence of debris flows. Despite these theoretical considerations, available data suggest little change in the concavity index, θ, of adjusted river profiles as a function of rock uplift rate (e.g., Tucker and Whipple, 2002). Because k_s is a function of U, however (see below and Snyder et al., 2000; Kirby and Whipple, 2001; Kirby et al., 2003), a downstream change in rock uplift rate may be manifested as a change in profile concavity (e.g., Kirby and Whipple, 2001). Thus, changes in profile concavity can also be exploited in evaluating regional tectonics from topography.

While the qualitative relationships among steepness, concavity and rock uplift rates can be readily predicted for "adjusted" longitudinal profiles, we note that temporal changes in the climatic and/or tectonic state can complicate these relationships. For example, fluvial systems in a transient state may contain knickpoints caught sweeping through the system in response to baselevel fall. If such discontinuities in channel profiles and slope-area scaling are always assumed to reflect spatial variations in rock uplift rate, these profiles may be subject to misinterpretation. However,

planview maps illustrating the spatial distribution of these knickpoints, along with an examination of long profiles and slope-area data, will typically allow these situations to be readily identified, as discussed in Section 3.3. Furthermore, such transient profiles, if properly identified, can provide extremely useful information for neotectonic analysis, as described in the San Gabriels example in Section 4.1.2

Because the steepness and concavity indices each reflect spatial variations in rock uplift rate, stream profile parameters derived from regressions on natural slope-area data allow us to extract information about regional tectonics. We proceed by discussing the methodologies for extracting these data and delineating breaks in slope-area scaling. We then discuss applications of these methods to deriving tectonic information from longitudinal profile form. We stress that our approach is empirical, and is therefore not tied to any particular river incision model.

3. Methods

3.1 Data Handling

Digital topographic data suitable for long profile analysis are widely available for sites within the United States, and can be obtained for download directly from the USGS or its affiliated data repositories (http://seamless.usgs.gov/ or http://www.gisdatadepot.com/dem/). For field areas outside of the United States, DEMs can be obtained from local sources or from NASA's shuttle radar topography mission (SRTM) (http://www.jpl.nasa.gov/srtm/). DEMs can also be created from stereo pairs of spaceborne satellite imagery (e.g. ASTER http://asterweb.jpl.nasa.gov/, or SPOT http://www.spot.com), or from digitized aerial photographs, where available. Note that any DEMs created from remotely sensed data may contain data holes or anomalies due to extreme relief or cloud cover. Depending on the data

source, DEMs may also require a projection from geographic coordinates to a format with rectangular, equidimensional pixels throughout the region of interest (c.f., Finalyson and Montgomery, 2003).

Once digital data have been obtained, a variety of methods is appropriate for extracting the requisite stream profile parameters. In practice, any suite of computer scripts which can follow a path of pixels downstream while recording elevation, cumulative streamwise distance, and contributing drainage area data is sufficient for collecting long profile data from a DEM. The methods developed by Snyder et al. (2000) and Kirby et al. (2003) utilize a group of built-in functions in ARC/INFO to create flow accumulation arrays and delineate drainage basins, a suite of MATLAB scripts to extract and analyze stream profile data from these basins, and an Arcview interface for color-coding stream profiles by their steepness and concavity indices in a GIS. While pits and data holes in a DEM usually need to be filled to create flow direction and flow accumulation arrays for basin delineation, profile data should be extracted from the raw DEM matrix to ensure that no data are lost or created at this early stage in the processing.

Once the elevation, distance, and drainage area data are compiled, the next step is to calculate local channel slopes to be used in slope-area plots. If using built-in ARC/INFO functions, slope values should not be extracted from a slope grid computed from a 3x3 moving window across the entire DEM: high slopes on channel walls will cause significant upward bias in channel slopes in this case, particularly at large drainage area in narrow bedrock canyons. There are also several problems with using raw pixel-to-pixel slopes from the channel itself (rise/run): 1) many DEMs are created by interpolation of digitized topographic contour maps, grossly oversampling the available data at large drainage area and low channel gradient and leading to bias toward the data at large drainage area in regressions of logS on logA; 2) the

algorithms used to convert topographic maps to a raster format often give rise to interpolation errors, which characteristically produce artificial stair-steps associated with each contour crossing of the stream line and tremendous artificial scatter in pixel-to-pixel slope data (Figures 1 and 2); 3) these stair-steps and the integer format of many DEMs produce multiple flats with zero slope, which cannot be handled in a log-log plot of slope and area (see Figure 1a); and 4) DEMs with low resolution will often short-circuit meander bends in a river profile, resulting in an overestimate of local channel slope, typically in floodplains at large drainage area.

In order to circumvent many of the problems with raw pixel-to-pixel slopes, raw elevation data can be resampled at equal vertical intervals (Δz), using the contour interval from the original data source as Δz (if known). This step has several benefits: 1) it remains true to the original contour data from which many DEMs are derived; 2) it yields a data set much more evenly distributed in logS-logA space, reducing bias in regression analysis; and 3) it results in considerable smoothing of raw DEM profiles (see Figures 2a and 2b). As the last two benefits apply even to DEM data not derived from contour maps, we favor the implementation of this resampling in all cases. For high-quality data sources such as the USGS 10m-pixel DEMs, contour-interval subsampling can be shown to recover faithfully the original contour crossings (Figure 1b). Profiles extracted from lower resolution data sources, however, will often exhibit considerable scatter on slope-area plots even after this subsampling (e.g., Figure 2b); in these cases, additional smoothing can significantly aid interpretation.

As noted by many researchers, slope-area data often exhibit a pronounced break in scaling at $A_{cr} \leq 10^6$ m^2, which in unglaciated environments may represent the transition from debris-flow-dominated colluvial channels to stream-flow-dominated fluvial channels (e.g., Montgomery and Foufoula-Geogiou, 1993) (see Figures 3a and 3b). This scaling break may be

less pronounced in some settings, as a gradual transition from debris-flow-dominated to stream-flow-dominated conditions is reasonably expected (Stock and Dietrich, 2003); Figure 2c between a drainage area of 10^4 and 10^6 m^2 may be an example of this behavior. Regardless of the details at low drainage area, plots of slope-area data at this stage in the processing may reveal a smooth, linear trend below this scaling break, or multiple segments with easily identifiable values of k_s and θ, as illustrated in Figures 3a and 3b. More often, however, slope-area data will exhibit considerable scatter, which may be obscuring natural breaks in scaling along the profile. Further smoothing of the slope data greatly aids identification of scaling breaks without influencing their position, and with predictable effects on the values of k_s and θ (see below). Smoothing methods include using a moving-window average to smooth elevation data prior to calculating channel slopes over a specified vertical interval; regressing on elevation data over a fixed number of elevation points to derive local slope estimates; or averaging the logarithm of raw slopes over log-bins in drainage area (termed log-bin averaging).

While the position of scaling breaks tends to be insensitive to the choice of smoothing window style and size, steepness indices can be expected to decrease subtly but systematically as the smoothing window grows and spikes in the data are reduced in magnitude (Figure 2d). The effects of smoothing on concavity values will also be predictable, but will depend on the relative position of outliers in a particular profile: if the data contain spikes high in the profile, we expect the concavities to decrease with increased smoothing as the regression pivots counterclockwise (flattens); the opposite will be true for data containing spikes near the toe of the channel. Despite these systematic and predictable biases, note that steepness and concavity values will typically fall within ~10% of one another for a wide range of smoothing windows (Figures 2c-2e). The

data in Figure (2) also demonstrate that with appropriate smoothing, data from different sources with greatly varying resolution and quality in fact yield comparable results at long wavelength.

Each smoothing method has its strengths and weaknesses. Log-bin averaging has the advantage that the smoothing window both grows in size with distance downstream and does not produce any averaging of disparate slope values across tributary junctions with a large change in drainage area – the two primary weaknesses of the moving-window averaging approach. However, log-bin averaging alone is susceptible to outliers in particularly rough or low-resolution DEM profiles. Smoothing elevation data with a moving window that grows in size proportional to drainage area may be preferable in some cases.

We stress that investigators must be circumspect about the appropriate scale of observation for DEM analysis. For example, while our algorithms can be shown to recover contour crossings from 10 meter DEMs and therefore reproduce the information provided by the original contour map, there may be considerable information missed *between* these contour crossings. Montgomery et al. (1998) note up to a four-fold difference in reach-scale channel slopes measured in the field versus those derived from contour maps; Massong and Montgomery (2000) find that slopes derived from field surveys and high resolution DEMs can be different by up to 100%. In general, we expect the tectonic signals we are interested in to manifest themselves at a scale significantly greater than the contour interval of a topographic map; indeed, Finlayson and colleagues have had success extracting useful information from 30 arc second (~1km) GTOPO30 data (Finlayson et al., 2002; Finlayson and Montgomery, 2003). However, without extremely high resolution digital topographic data (e.g. laser altimetry) it is clearly inappropriate to extend DEM analysis to geomorphic questions addressed below the reach scale.

3.2 Model fits

Following data smoothing, we can begin to examine the slope-area data and make decisions about the number of distinct channel segments and the appropriate regression limits for each segment. Many channels can be adequately modeled below A_{cr} with only a single segment, using unique values of k_s and θ (e.g., Figure 2c). Others may contain multiple segments, reflecting spatial or temporal variations in rock uplift rate, climatic factors, or the mass strength of rock exposed along the profile (e.g., Figure 3b). In either case, linear regressions on slope-area data are typically conducted in two ways for each segment to allow intercomparison among different profiles in the basin.

In the first of the two regressions, segments of slope-area data with distinct steepness and/or concavity indices are identified, and are fit with k_s and θ as free parameters using equation (1) as the regression model. In the second regression, individual segments of slope-area data are fit using a "reference" concavity, θ_{ref}, to determine normalized steepness indices, k_{sn}. A reference concavity is required for interpretation of steepness values because k_s and θ as determined by regression analysis are, of course, strongly correlated (see Equation 1). In practice, θ_{ref} is usually taken as the regional mean of observed θ values in "undisturbed" channel segments (i.e., those exhibiting no known knickpoints, uplift rate gradients, or changes in rock strength along stream), and can be estimated from a plot superimposing all of the data from a catchment. Reference concavities typically fall in the range of 0.35-0.65 (Snyder et al., 2000; Kirby and Whipple, 2001; Brocklehurst and Whipple, 2002; Kirby et al., 2003; Wobus et al., 2003).

If raw data from a previously completed analysis are not readily available, one can approximately determine the normalized steepness index, k_{sn}, for a reference concavity, θ_{ref}, as follows:

$$k_{sn} = k_s A_{cent}^{(\theta_{ref} - \theta)} \quad (2)$$

$$A_{cent} = 10^{(\log A_{max} + \log A_{min})/2} \quad (3)$$

where k_s and θ are determined by regression and A_{min} and A_{max} bound the segment of the profile analyzed. In practice, equation (2) is found to match k_{sn} found by regression analysis to within ~10%. Where the difference between θ and θ_{ref} is large, however, (> 0.2), the k_{sn} value is meaningful only over a short range of drainage area near A_{cent}.

The normalized steepness index is analogous to the S_r index proposed by Sklar and Dietrich (1998). Where a regional concavity index is apparent, normalized steepness indices can be shown to correspond closely to S_r indices (see Kirby et al., 2003, Figure 5b). The advantage of the normalized steepness index k_{sn} is that the reference area (A_{cent} here) need not be the same for all channels, or channel segments, analyzed. However, where no typical regional concavity index is apparent, the S_r index may be preferable. Other measures of channel gradient have also been used in tectonic analyses, including the Hack gradient index (e.g. Hack, 1973). Where basin shapes are similar throughout a region, comparison of Hack gradient indices among different channels may be appropriate. However, if we assume that incision rate is related to fluvial discharge, normalized steepness indices may be a more appropriate metric, since contributing drainage area is explicitly incorporated into the analysis as a proxy for fluvial discharge.

3.3 Tectonic Analysis

In the context of extracting tectonic information from longitudinal profiles, the data obtained for steepness and concavity will often yield similar information: a downstream transition between disparate steepness values will typically be bridged by a zone of very high or low concavity (see Figure 3 and below). This "transition zone" may be a result of spatially or temporally varying rock uplift rates, temporally varying climatic conditions, or spatially varying rock mass strength. Even abrupt spatial changes in either rock uplift rate or rock properties (across a fault, for instance) may be manifested as a gradual transition in channel gradient (i.e., a high concavity zone) due to gradual downstream changes in sediment size, transport of resistant boulders downstream, or other blurring agents which may diffuse knickpoints in space and time (see Whipple and Tucker, 2002). Moreover, some data-smoothing algorithms have the disadvantage of blurring abrupt changes in channel gradient or elevation (knickpoints). In practice, normalized steepness data are often more useful than concavity data for evaluating regional tectonics, especially for short channel segments given the sensitivity of θ to scatter in slope data, both real and artificial. However, concavity data are often useful for gross delineation of zones where uplift rates may be systematically changing along a profile (e.g., Kirby and Whipple, 2001; Kirby et al., 2003).

It should be emphasized here that slope-area data are plotted in log-log space, and it is important to be mindful of the compression of data at large drainage area. In particular, when selecting the downstream regression limit for channel segments, small changes in log drainage area are typically associated with large changes in distance along the profile. Large errors may therefore be inherent in any estimates of the distribution of rock uplift rates based on the width of high concavity zones. In addition, one needs to be wary of possible downstream changes in river

characteristics not necessarily associated with the underlying tectonics, such as a transition to increasingly alluviated, or even depositional, conditions that may be associated with a rapid decrease in slope and therefore locally high concavity. In other cases, concavity may actually decrease where channels transition to increasingly transport-limited, but incisional, conditions with distance downstream (e.g., Whipple and Tucker, 2002; Sklar, 2003). In other words, some apparent downstream changes in channel steepness or concavity indices may simply be associated with an increase in drainage area. Comparing slope-area data on smaller tributaries that enter orthogonal to the mainstem throughout the zone of interest has proven an effective tool in this regard (see Kirby et al., 2003, Section 6.2; Wobus et al., 2003), as will be illustrated in the Nepal case study below.

Once slope-area data have been extracted and smoothed from each tributary in a basin, it is often useful to superimpose all of the profile data from a catchment on a single plot (e.g. Figures 4d and 5d). This tool aids in determination of the upper and lower bounds on steepness values in the catchment, segregation of populations with distinct steepness values, and determination of an appropriate reference concavity, as discussed above. With these composite plots, the analysis can be extended from individual tributaries to the regional scale.

The planview distribution of normalized steepness indices for all the tributaries in a catchment can be an extremely useful tool for delineating tectonic boundaries (e.g., Kirby et al., 2003; Wobus et al., 2003). In tectonic settings containing a discrete break in rock uplift rates, we expect channels with high steepness indices to characterize the high uplift zone, while those with lower steepness indices should characterize the low uplift zone (e.g., Snyder et al., 2000). Channels crossing spatial gradients in rock uplift rate may exhibit readily identifiable knickpoints on longitudinal profile (z vs x) and slope-area plots. In planview, the boundary

between zones of high and low steepness will also help us to evaluate whether we are seeing a temporally stable break in rock uplift rates (i.e., a fault or shear zone) or a transient condition: the rate of knickpoint migration, and therefore the position of knickpoints in a catchment through time, can be predicted (e.g., Whipple and Tucker, 1999; Niemann et al., 2001), and suggests a spatial distribution of knickpoints very different from that expected in regions of spatially varying uplift rates (Figure 3c and 3d). In particular, if erodibility is spatially uniform we expect the vertical rate of knickpoint migration to be constant, suggesting that knickpoints recording a transient condition (due to baselevel fall, for example) should lie near a constant elevation (e.g., Niemann et al., 2001). This condition is demonstrated in the San Gabriel mountains example discussed in Section 4.1.2.

If regional geologic maps or field observations are available, a superposition of important lithologic contacts is also useful to determine whether regional trends in channel steepness values might be correlative with lithologic boundaries, rather than with a tectonic signal (e.g. Hack, 1957; Kirby et al., 2003, Figure 9). In such efforts it is critical to recall that lithology is not synonymous with rock properties: a competent, well-cemented sandstone can be stronger than a fractured and weathered granite, and the strength of a single unit may vary markedly along strike. However, if depositional or intrusive lithologic boundaries can be demonstrated to correspond to changes in channel gradient, we can often rule out breaks in rock uplift rate as the cause of the channel steepening.

4. Case Studies

Utilizing the methodologies outlined above, we now discuss a series of case studies in which river profile data have been used to extract tectonic information from the landscape. In

the first two case studies, both from California, channel steepness values correlate with known variations in rock uplift and exhumation rates as determined from marine terraces, thermochronologic data, and cosmogenic data; however, there is insufficient data available at present to calibrate and uniquely test river incision models. In the third case study, steepness and concavity values derived from stream profiles correlate with the distribution of rock uplift rates above a fault-bend fold in the Siwalik hills of south-central Nepal, and allow a local calibration of the stream power river incision model. Comparison of two independent calibration methods and application of the calibrated model to predict incision rates across the rest of the landscape allows a semi-quantitative verification of the model in this field site. Finally, in the central Nepal Himalaya, breaks in steepness values across the landscape help us to delineate a recently active and previously unrecognized shear zone, the tectonic significance of which is corroborated by $^{40}Ar/^{39}Ar$ thermochronology and structural observations in the field.

4.1 California: King Range and San Gabriel Mountains

In the King Range and San Gabriel mountains of northern and southern California, respectively, strong spatial gradients in rock uplift and exhumation rates each provide excellent opportunities to test the stream profile method in a controlled environment. In the King Range, rock uplift rates near the Mendocino triple junction are quantified from flights of uplifted marine terraces, using radiocarbon dating and correlations with a eustatic sea level curve (Merritts and Bull, 1989; Merritts, 1996). Based on the record from marine terraces, the field area can be divided into high and low uplift zones, with rock uplift rates varying over approximately an order of magnitude between the two zones (3-4 mm/yr and 0.5 mm/yr, respectively). In the San Gabriels, a restraining bend on the San Andreas fault creates strong east-west gradients in long-

term exhumation rates, as determined from (U-Th)/He and apatite fission track (AFT) thermochronology. Based on the thermochronologic data, the eastern and western San Gabriels can be divided into blocks with distinct exhumation histories, with AFT ages ranging from 4 to 64 Ma and rock uplift rates from 0.5 mm/yr in the western block to 2-3 mm/yr in the eastern block (e.g., Blythe et al., 2000; Spotila et al., 2002).

4.1.1 King Range

Using a 30 meter USGS DEM of the King Range, Snyder et al (2000) extracted 21 mainstem river profiles and calculated model parameters for equation (1) from slope-area data. Most of the tributaries in the study area were found to have relatively smooth, concave profiles for much of their length, suggesting a condition in which the rivers have equilibrated with local rock uplift rates. Our data handling methods have been refined and improved over the years since our initial efforts in stream profile analysis (Snyder et al., 2000). That analysis also pre-dates the extensive field work in the region reported in Snyder et al. (2003a). In addition, since that time higher resolution and higher quality 10-meter-pixel USGS DEMs have become available for the entire King Range study area. We take the opportunity here to re-visit the King Range stream profile analysis using better data, refined methods, and in light of field observations. This re-analysis is at once a cautionary tale regarding the uncertainty in best-fit profile concavity indices, and an encouraging example of the robustness of measured channel steepness indices for a reference concavity (k_{sn}), especially within a study area. The two principal conclusions of Snyder et al. (2000) are upheld in this re-analysis: (1) channel steepness increases by a factor of ~1.8 between the low- and high-uplift rate zones, and (2) there is no

statistically significant difference in the concavity index between channels in the low- and high-uplift rate zones (Figure 4).

Here we re-analyze only a subset of the 21 drainages studied by Snyder et al. (2000): the largest of the drainages in the high-uplift zone (Gitchell, Shipman, Bigflat, and Big Creeks), and the most comparable low-uplift zone channels (Hardy, Juan, Howard, and Dehaven Creeks) using 10m USGS DEMs. We select regression bounds on a case-by-case basis, rather than simply adhering to the common set of regression limits (0.1 km^2 - 5 km^2) used by Snyder et al. (2000). The upstream regression limit is still typically near 0.1 km^2, as defined by a kink in the slope-area data, but varies somewhat from drainage to drainage (Figure 4). The downstream regression limit is set by the sudden reduction in channel gradient associated with the transition to alluviated conditions (typically at ~10^7 m^2, Figure 4). This transition was mapped in the field (Snyder et al., 2003a) and was likely driven by rapid Holocene sea level rise (Snyder et al., 2002). Between these regression limits, we find uncorrelated residuals to the model fits.

This revised analysis finds no statistically significant difference in concavity index between the channels sampled in the low- and high-uplift rate zones, and a regional best-fit mean value of 0.57 ± 0.1 (2σ), considerably higher than, and yet within error of, the 0.43 ± .22 (2σ) estimate reported by Snyder et al. (2000). Re-analysis of the 30m DEMs with our original data handling methods (contour extraction but no smoothing) on this subset of drainages confirms that the difference in best-fit concavity results mostly from the change in regression limits, rather than a difference in data quality or data handling methods. Using a reference concavity of 0.45 (for convenience of comparison to data from the other case studies presented here), we find mean k_{sn} values of 66 and 117 $m^{0.9}$ in the low- and high-uplift-rate zones, respectively, yielding a ratio of k_{sn}(high)/k_{sn}(low) of 1.8. Further, the ratio of high-uplift zone to low-uplift zone average k_{sn}

values varies by less than 5% when using all permutations of: smoothing, no smoothing, 30 meter data, 10 meter data, new regression limits, and old regression limits. Thus while the concavity index may be sensitive to the choice of regression limits, steepness indices appear to be robust across a broad range of data quality and user-chosen regression limits. In all cases we find no statistically significant difference in the concavity index of channels in the high- and low-uplift-rate zones.

The positive relationship between steepness index and rock uplift rate is expected, and is consistent with Merritts and Vincent's (1989) data. However, despite the re-analysis with higher quality data, a number of conditions limit our ability to quantitatively relate steepness indices to uplift rates in this field setting. First, steepness values in the high uplift zone show considerable variability. Although this may reflect the spatial variations seen in Holocene uplift rates of marine platforms (Merritts, 1996), it does suggest that other variables may influence channel steepness despite the lithologic homogeneity among these drainages. Second, although the uplift rates vary over approximately an order of magnitude, the most reliable estimates of rock uplift rates in the field area are confined to the low and high ends of this range (~0.5 mm/yr and ~3-4 mm/yr). We therefore have only two reliable points to define the functional relationship between steepness index and uplift rate, which does not strongly constrain the range of models which can be fit to the data (e.g., Snyder et al., 2000; 2003a; 2003b).

4.1.2 San Gabriel Mountains

In the San Gabriel mountains, stream profile data for over 100 streams were extracted from a 10 meter USGS DEM of the region, and a composite plot was created from the slope-area data. Most of the tributaries analyzed in the San Gabriel mountains exhibit smoothly concave

profiles, with uniform slope-area scaling below a threshold drainage area of 10^6 m^2 or less (Figure 5). Among these profiles, concavity indices again show no systematic relationship to rock uplift rates, and a reference concavity of 0.45 was chosen based on the composite slope-area data. Normalized steepness indices in the San Gabriels range from approximately 65 to 175 $m^{0.9}$; the highest k_{sn} values (~150-175) are coincident with the youngest cooling ages and highest long term erosion rates, while the lowest k_{sn} values (~65-80) are coincident with the oldest cooling ages and lowest long-term erosion rates (Figure 5).

In addition to the "adjusted" fluvial profiles from which the relationship between steepness and rock uplift rate can be evaluated, a number of rivers in the western San Gabriel Mountains contain abrupt knickpoints that separate upstream and downstream channel segments with distinct steepness indices. The best examples of this are in the Big Tujunga drainage basin, within the slowly uplifting western San Gabriels (e.g., Blythe et al., 2000; Spotila et al., 2002). In this basin, knickpoints in multiple rivers are found at different points in the basin but nearly constant elevation, suggesting a transient condition as the channels adjust to changing boundary conditions (Figure 6). Regressions on slope area data above this knickpoint find k_{sn} values indistinguishable from the regional lower bound (e.g., Figure 5d), while k_{sn} values below the knickpoint are slightly higher (Figure 6a). In some of the tributaries, the boundary between these zones is characterized by a significantly oversteepened reach, possibly reflecting a disequilibrium state related to changes in sediment flux during landscape adjustment (e.g., Sklar and Dietrich, 1998; Gasparini, 2003; Gasparini et al., this volume). A preliminary interpretation is that these profiles record a transient response to a recent increase in rock uplift rate—probably during the Quaternary given the plausible range of rock uplift rates and the height of the knickpoints. A total offset of ~300m during this period can be inferred from the height of

knickpoints and the downstream projection of the less-steep upper channel segments (Figure 6a), and may be important both for interpreting young fission-track cooling ages along the lower Big Tujunga (e.g., Blythe et al., 2000), and for understanding the long-term evolution of active fault systems in the Los Angeles region.

In neither the King Range nor the San Gabriels are we able to quantify the relationship between k_{sn} and U: in the King Range, we do not have enough data to differentiate among various threshold and nonlinear models of k_s vs U and the potential effects of changing bed state on erosional efficiency (e.g. Snyder et al., 2003a); in the San Gabriels, modern rock uplift rates are not as well constrained and an analysis of (approximately) steady-state channel segments would suffer from similar limitations. Despite these complexities, however, the qualitative results from both field areas are both robust and important: the highest steepness values consistently correspond to the regions with the highest rock uplift and exhumation rates, while the lowest steepness values correspond to the lowest rock uplift and exhumation rates. In both field areas, lithologic differences between the high and low uplift regions are minimal, suggesting that channel steepness is tracking rock uplift rate. If we were to approach either of these field areas without any *a priori* knowledge of the tectonic setting, a map of steepness indices across the range would provide a great deal of information about the underlying tectonics. A planview map of knickpoints in longitudinal profiles can also provide constraints on the location and magnitude of recent deformation in the region: in the San Gabriels, this analysis reveals an apparently recent (~1 Ma?) change in rock uplift rates in the Big Tujunga basin. Importantly, with high-resolution DEMs throughout the United States publicly available, these analyses could be conducted in a matter of hours.

4.2 Siwalik Hills, Nepal

The case study from the Siwalik Hills in central Nepal is similar to the previous examples, in that steepness indices can be compared from zones of different rock uplift rates in a region of spatially uniform lithology. However, the Siwaliks provide the additional opportunity to examine the topographic signature of rock uplift rate gradients *along* individual channel profiles, particularly as these gradients affect channel concavities (e.g., Kirby and Whipple, 2001). The Siwaliks record modern deformation above a fault-bend fold in the Himalayan foreland, along the Main Frontal Thrust system. Deformation rates inferred from the distribution of Holocene terraces vary from ~4 mm/yr north of the range, to ~17 mm/yr at the range crest, and back to near zero just south of the Main Frontal Thrust. Multiple flights of terraces suggest relatively constant incision rate with time, and data from transverse drainages suggest steady-state profiles in these catchments (Lavé and Avouac, 2000). The fault-bend fold is dissected by drainages oriented both parallel and perpendicular to the strike of the range, and all of the rivers traverse relatively uniform sandstones and siltstones of the Lower and Middle Siwaliks (Lavé and Avouac, 2000).

Kirby and Whipple (2001) analyzed 22 channels in the Siwalik hills, using a 90-meter DEM of the region in an effort to assess to what degree strong spatial gradients in rock uplift rate influenced channel concavity and steepness. They argued that systematic changes in concavity indices could be exploited to place bounds on the relationship between channel gradient and incision rate. Here we update those results with analysis of a higher-resolution (30 meter) DEM generated from ASTER stereo scenes. Channels parallel to the range crest, and therefore experiencing relatively uniform rock uplift rate, again yield concavity indices ranging from 0.45 – 0.55. Moreover, these strike-parallel drainages exhibit a predictable and quantifiable pattern of

k_{sn} values: channels in high uplift settings have the highest steepness indices, while those in low uplift zones have the lowest steepnesses. A plot of steepness coefficients vs uplift rate for these strike-parallel drainages reveals a linear relationship with an intercept statistically indistinguishable from zero (Figure 7a). This relationship is consistent with a simple detachment-limited stream power model with n = 1, where $k_s = \left(\frac{U}{K}\right)^{1/n}$ (e.g., Howard, 1994). Normalized steepness indices, k_{sn}, for $\theta_{ref} = 0.52$, range from approximately 85 in low uplift regions (~7 mm/yr) to approximately 200 in high uplift regions (~14 mm/yr).

Although most of the channels contained within uniform uplift regimes have moderate concavities near 0.5, channel segments crossing spatially varying rock uplift rates have anomalously high or low concavities depending on the direction of flow relative to the gradient in uplift rate. Channels entering the Siwalik anticline from the north have rapidly increasing slopes (negative concavities), as uplift rates increase downstream. Of note is the observation that changes in gradient on these channels span the entire range of increase in gradients on strike-parallel channels (Figure 7b), suggesting that both the strike-parallel and strike-perpendicular systems exhibit the same manner and degree of response to increasing rock uplift rates. This observation, coupled with the lack of abrupt knickpoints within these channels and the consistency between two independent estimates of the erosion coefficient K (see below), lends support to the hypothesis that these channels have reached a steady-state balance between channel incision and rock uplift.

Using the known range in uplift rates and observed channel geometries across these channel segments, Kirby and Whipple (2001) note that the concavity index provides an independent means of determining n and K. These authors argued that the change in gradient along two tributaries (Dhansar and Chadi Khola) was consistent with n ranging between 0.6 and

1. Re-analysis of the ASTER DEM gives estimated values for n of 0.72 and 0.88, close to the value of n=1 derived in Figure 7a from strike parallel drainages. The erosion coefficient (K) determined from the k_s vs. U relation (Figure 7a) is 7.41 x 10^{-5} $m^{.04}yr^{-1}$ while K derived independently from the strike-perpendicular channels ranges from 5.25 x 10^{-5} to 5.76 x 10^{-5} $m^{.04}yr^{-1}$. Note that k_{sn} and K are dimensional coefficients, whose dimensions depend on the ratio of m/n and the value of m, respectively: the estimates reported here assume that $m/n = \theta_{ref}$, and use $\theta_{ref} = 0.52$, and $n = 1$ (i.e. $m = 0.52$). The consistency between estimates derived using both strike-parallel and strike-perpendicular channels suggests that we may be well on our way to deriving quantitative estimates of uplift rates directly from topography in regions with relatively simple tectonics and uniform lithology. For example, a map of the distribution of predicted channel incision rates from calibrated model parameters displays good correspondence with an independent estimate of rock uplift rate in this landscape that has been argued to be in steady state (Hurtrez et al., 1999; Lave and Avouac, 2000) (Figure 8).

If this type of analysis can be extended to other field settings, it represents a promising avenue for neotectonic research: if calibration sites can be identified with known uplift rates and similar channel morphologies to a field site of interest, it may be possible to obtain quantitative estimates of uplift rates and their spatial variability at the catchment scale prior to ever setting foot in the field. In the absence of a calibration site, the spatial patterns of uplift rates can still be estimated from the patterns of steepness and concavity identified from stream profiles. The accuracy of our quantitative estimates may decrease with decreasing knowledge of the field site; in particular, downstream changes in channel width that differ from the typical scaling of $W \sim A^{0.4}$ (e.g., Whipple, 2004 and references therein) will not be captured on slope/area plots, and may substantially modify the relationships between uplift rates and steepness indices in ways that

must be explored through future work. At a minimum, however, the method provides a quick and easy way to evaluate patterns of rock uplift with a high degree of spatial resolution.

4.3 Central Nepalese Himalaya

The preceding case studies illustrate a consistent relationship between steepness and uplift rate in regions where rock uplift rates have been independently determined. The next logical step is to utilize stream profiles for tectonic analysis in regions where modern rock uplift rates are less well understood. The case study discussed here is from central Nepal, where stream profiles are used along with thermochronologic and structural analysis to evaluate two competing models for the tectonic architecture of the Himalaya.

The High Himalayan peaks in central Nepal are bounded to the south by a sharp topographic break, which can be delineated on a map of hillslope gradients as a WNW-ESE trending line separating the High Himalaya to the north from the Lesser Himalaya to the south (Wobus et al., 2003, Figure 1). This physiographic transition—herein referred to as PT_2 for consistency with Wobus et al. (2003) and Hodges et al. (2004)—may be consistent with one of two endmember models for Himalayan tectonics (Figure 9). In the first model, the topographic transition is sustained entirely by rock uplift gradients due to material transport over a ramp in the Himalayan Sole Thrust. This model predicts similar thermal and deformational histories for rocks on opposite sides of PT_2, and broadly distributed gradients in rock uplift rates from south to north (e.g., Cattin and Avouac, 2000; Lave and Avouac, 2001). In the second model, surface-breaking thrusts—perhaps including young strands of the Main Central Thrust System (MCT)—remain active at the foot of the High Himalaya. This model predicts disparate thermal and

structural histories on either side of PT_2, and more abrupt changes in rock uplift and exhumation rates across discrete structures (e.g., Hodges et al., 2001; Wobus et al., 2003).

As a first step in evaluating which of these models is most relevant to central Nepal, stream profiles were extracted from a 90-meter DEM of the region (see Fielding et al., 1994 for description of the dataset). Composite plots of slope-area data from all tributaries define regional upper and lower limits of steepness values of 650 and 95 $m^{0.9}$, respectively. In each case, the upper limit is defined by northern tributaries and trunk stream segments, and the lower limit is defined by southern tributaries and trunk stream segments (Figure 10). This trend is consistent with a decrease in rock uplift rate, rock strength, or both from north to south. Because rock mass quality is typically very similar across these transitions, and because both of the tectonic models considered for the Himalaya include a decrease in rock uplift rates from north to south, we assume that a change in rock uplift rate is the major driving force for the change in k_{sn}. Furthermore, monsoon precipitation appears to be focused just upstream of this major break in steepness indices (Hodges et al., 2004), suggesting that our estimate of the southward decrease in k_{sn} for central Nepal may be conservative as a proxy for rock uplift rate. We focus here on the nature and spatial extent of this steepness transition, to evaluate which of the competing tectonic models is most appropriate for this portion of the Himalaya.

The analysis is similar to that used in the Siwalik hills (e.g., Kirby and Whipple, 2001), in that tributaries both parallel and perpendicular to the inferred uplift rate gradient are utilized. For the trunk streams perpendicular to the uplift gradient, the width of the high concavity channel segments (the downstream transition from high to low steepness values) provides one estimate of the distance over which rock uplift rates are decreasing downstream (Figure 10). Note that this should be a maximum estimate of the distance over which uplift rates are changing: downstream

adjustments in sediment load across the tectonic boundary may diffuse any uplift rate signal (e.g., Whipple and Tucker, 2002), as will the smoothing algorithm applied in analysis of the data. The smaller tributary channels subparallel to the structural grain typically exhibit smooth profiles without abrupt knickpoints, normal concavities in the range of 0.4-0.6, and uniform steepness values down to the trunk stream junction; furthermore, either of the tectonic models for central Nepal predicts nearly constant uplift rate within these narrow, east-west trending basins. We therefore infer that these channels record equilibrium profile forms, and use the spatial distribution of high and low steepness tributaries as a second means of estimating the distance over which uplift rates are changing in the system.

Slope-area data from the Burhi Gandaki trunk stream allow us to delineate a high concavity zone along approximately 40 kilometers of streamwise distance, which spans the range in steepness values on a composite plot of slope-area data (Figure 10b). As discussed above, this represents a maximum estimate of the width of the assumed uplift gradient. Tributary profiles allow us to place more precise constraints on the width of the transition zone: steepness values in strike-parallel streams decrease from ~400 to ~100 over approximately 20 kilometers in map view (Figure 11). $^{40}Ar/^{39}Ar$ thermochronologic data from detrital muscovites in the Burhi Gandaki and Trisuli catchments suggest a profound change in time-averaged exhumation rates (or total depth of late Cenozoic exhumation) over an even narrower zone—8 to 10 kilometers—suggesting that stream profile analysis is capturing a profound tectonic boundary in this setting. Similar results from the Trisuli river suggest that this boundary may continue along strike (Figure 11; Wobus et al., 2003).

Similar methodologies can be used to delineate the width of the transition zone throughout central Nepal, and additional structural and thermochronologic data can be used to

corroborate the stream profile analyses in many cases (Figure 11). In the Marsyandi trunk stream, a high concavity zone across the topographic break spans a streamwise distance of approximately 40 kilometers, suggesting a decrease in rock uplift rates over this distance. Tributaries along this segment of the basin allow us to narrow this estimate to between 15 and 20 km (Figure 11). Detailed structural mapping along the Marsyandi trunk and its tributaries indicate a penetrative brittle shear zone crosscutting all previous fabrics along the upper part of this same river reach. Consistent top-to-the south kinematics on these north-dipping shear zones suggest that these structures may be accommodating differential motion in this zone, consistent with a model including recently active surface-breaking thrusts in this region (e.g., Hodges et al., 2004).

In the absence of a detailed stream profile analysis to guide structural and thermochronologic studies, sparse data coverage and model uncertainties render geophysical and geodetic data equivocal in discriminating between a surface breaking shear zone and a subsurface ramp in central Nepal. Stream profiles provide an additional piece of data that favors a narrowly distributed rock uplift gradient throughout the study area, and informs our sampling strategy for thermochronologic analyses. Although we are unable to provide an exact estimate of the distance over which rock uplift rates are increasing, stream profiles are a crucial tool in this setting for evaluating a range of tectonic models and identifying sites for future field and laboratory work.

5. Discussion

The correlation between steepness and uplift rate in established tectonic settings, and the ability to delineate temporal and spatial breaks in rock uplift rate in more poorly constrained

settings, demonstrate the power of stream profile analysis. However, a number of shortcomings must yet be overcome if stream profile analysis is to become a mainstream tool for neotectonic investigations. In particular, if we wish to derive quantitative estimates of rock uplift rates directly from topography, a great deal of work remains to be done (e.g., Whipple, 2004).

Foremost among our research needs is a continued, systematic dissection of the varied influences on river incision into rock. For example, how do the relative importance of mesoscale processes such as plucking and abrasion change with channel slope and incision rate, and how do the rates of these processes differ from simple shear-stress dependent incision at the bed (e.g., Whipple et al., 2000)? How do changes in bed roughness, sediment flux, and bed cover influence erosion rates (e.g., Sklar and Dietrich, 1998, 2001; Hancock and Anderson, 2002; Sklar, 2003)? What controls changes in bedrock channel width, and how do changes in width influence erosion rates (e.g., Hancock and Anderson, 2002; Montgomery and Gran, 2001; Snyder et al., 2003a; Lague and Davy, 2003)? How do we incorporate critical thresholds for river incision and a stochastic distribution of storms into our erosion models (e.g., Tucker and Bras, 2000; Snyder et al., 2003b; Tucker, 2004)? We have only begun to ask these questions, and more comprehensive field, experimental, and numerical studies must be undertaken before we can hope to have a reliable quantitative tool for neotectonics (e.g.,Whipple, 2004).

Although we cannot yet deconvolve the relative contributions of lithology, adjustments in channel morphology and bed state, climatic variables, and uplift rate on channel steepness, we must continue to incorporate as much of this information as we can into our analysis. Where available, lithologic and climatic information can already be used to qualitatively ascertain the importance of rock uplift rate variations on long profile form. For example, in some settings large breaks in channel steepness across lithologic boundaries may be entirely contained within a

single uplift regime; ignoring the effects of lithology would lead to dramatic misconceptions of tectonic signals. In other field areas, a decrease in rock uplift rate may be co-located with an increase in rock strength across major structures, such that the two effects moderate one another in the context of profile steepness. Ultimately, utilizing stream profile analysis to inform detailed structural, thermochronologic, and cosmogenic analyses will continue to be the best approach for neotectonic investigations (e.g., Kirby et al., 2003; Wobus et al., 2003; Hodges et al., 2004). Stream profile analyses cannot be conducted in a vacuum; informing our investigations with as much additional data as possible must remain a priority in any topographic analysis.

Numerical experiments incorporating an orographic forcing of precipitation predict systematic, if minor, changes in profile concavity due to an uneven distribution of precipitation at the range scale (e.g., Roe et al., 2002, 2003). Because precipitation effects are manifested in models of fluvial erosion only through their contribution to river discharge, we typically do not expect fluvial profiles to change abruptly due to spatial gradients in climate. However, the effects of temporal changes in climate may be more pronounced, particularly in settings where river systems take over previously glaciated valleys, or where glacial-interglacial cycling high in a basin creates profound changes in sediment flux within the fluvial part of the system (e.g., Brocklehurst and Whipple, 2002; Hancock and Anderson, 2002). Spatial and temporal changes in climate must both be more fully incorporated into our models if we hope to one day derive quantitative estimates of uplift rates from topography.

The stream profile method measures only changes in channel slope. However, a river's response to changes in uplift rate may include adjustments in a variety of other factors related to dominant incision processes, channel morphology, and bed state (e.g., Whipple and Tucker,

1999; 2002; Sklar and Dietrich, 1998; 2001; Sklar, 2003). Where channels cross boundaries between rocks with considerable differences in rock strength without any change in steepness index, adjustments in channel morphology or bed state may be fully compensating for the change in rock properties (see Montgomery and Gran, 2001; Sklar, 2001). Alternatively, transport- rather than detachment-limited conditions may be indicated (e.g., Whipple and Tucker, 2002). As discussed in Section 2, our ability to quantify many of these feedbacks and internal adjustments is limited. As our understanding of the mechanisms of fluvial response to differential rock uplift improves, these additional degrees of freedom should be incorporated into both modeling and empirical studies of the interrelations among climate, erosion, tectonics and topography. Until then, we must recognize that adjustments in channel slope are only part of a more complicated equation.

In order to make the connection between topography and tectonics, an assumption is often made that a steady state balance between uplift and erosion prevails. In many landscapes, this condition will not be met, leading to transient forms such as propagating knickpoints, knickzones, and other disequilibrium channel forms (e.g., Whipple and Tucker, 1999; Stock et al., 2004; Anderson et al., this volume). The severe limitations of the steady-state assumption are well known. However, it is incorrect to presume that model parameters can be constrained only through analysis of steady state forms. Where data quality is high, deviations from steady state are often readily discernable through analysis of stream profiles and planview maps (e.g., Figures 3 and 6). Recognition of such transient forms is important for at least two reasons. First, they can be useful indicators of tectonic history, such as a sudden baselevel fall or a change in differential rock uplift rate at the outlet of a drainage network, as illustrated for the San Gabriels (Figure 6). Second, under the right circumstances, profiles with such forms can provide

information about two steady-state conditions: above and below the knickpoint the channel is incising at different, often knowable, rates, such that an upper steady state profile is being "replaced" by a lower steady-state profile as the knickpoint advances (e.g., Whipple and Tucker, 1999; Niemann et al., 2001). Where sediment flux and channel bed state play important roles, transient response may be complex. For example, these disequilibrium channels may be characterized by transient oversteepened reaches downstream of knickpoints (Gasparini, 2003; Gasparini et al., this volume), which may be mistaken for equilibrium high concavity segments if data quality and resolution are low. It is potential complexities in the transient response of rivers such as this that afford the best opportunity to quantitatively test competing river incision models.

Finally, many DEMs, particularly those with low spatial resolution, contain "bad" data points along a channel due to topographic variability at a smaller spatial scale than the cell size, short-circuiting of sinuous channels in extraction of long profile data, or errors in the algorithm converting an original data source to a raster format. As a result, we often must make a decision as to whether unusual data represent noise or real geological complexity. One potential source of the latter is the influence of large landslides, which may temporarily block fluvial systems causing alternating flats and steps in long profiles. Often the distinction between data noise and geologic complexity is easily made; however, at present there are no quantitative criteria to evaluate whether or not anomalies in stream profiles are "real" without complementary field investigation. As data quality improves across the globe, part of this difficulty will gradually be overcome. Until then, determining the difference between bad data and geological complexity will typically require field observations to resolve satisfactorily.

6. Conclusions

Empirical observations and simple models of fluvial erosion suggest a positive correlation between channel gradient and rock uplift rate, which we exploit in the method of stream profile analysis outlined here. Despite our incomplete understanding of the varied processes contributing to fluvial erosion, the stream profile method is an invaluable qualitative tool for neotectonic investigations. In northern and southern California, we show that channel steepness is directly related to rock uplift rate. In the Siwalik hills, changes in steepness and concavity each correlate in a predictable way with rock uplift rate variations, and we can begin constructing a quantitative means of translating topography into tectonics through local calibration of a simple river incision model. Finally, in central Nepal, stream profile analysis provides a crucial discriminator between two models of Himalayan tectonics, and has led to identification of a previously unrecognized shear zone. Our next steps should be focused on refining this promising qualitative tool by incorporating recent advances in process geomorphology into models of stream profile evolution and form. While further numerical studies will be useful in this regard, we are ultimately limited by our lack of empirical data to characterize fluvial response. As such, we should focus on field and laboratory work geared toward understanding variations in fluvial erosion processes and rates with changes in incision rate, bed morphology and bed state, and climate. Only when we can confidently describe all of these feedbacks can we hope to have a reliable quantitative tool for neotectonic analysis.

Acknowledgements

This work was conducted with support from NSF grant EAR-008758 to K.X. Whipple and K.V. Hodges, and additional NSF grants supporting prior work by Kirby, Snyder, Johnson and Crosby. We thank Jerome Lavé for providing access to data and figures for the Siwaliks case study, and Bob Anderson and David Montgomery for thoughtful reviews of the original manuscript. We also thank all of the organizers and participants of the Penrose conference for a fantastic meeting.

References

Anderson, R. S., Riihimaki, C. A., Safran, E., and MacGregor, K., in review, Facing reality: Late Cenozoic evolution of smooth peaks, glacially ornamented valleys and deep river gorges of Colorado's Front Range, *in* Willett, S., Hovius, N., Fisher, D., and Brandon, M., eds., Penrose Special Paper: Tectonics, climate and landscape evolution: Boulder, Geological Society of America.

Blythe, A. E., Burbank, D. W., Farley, K. A., and Fielding, E. J., 2000, Structural and topographic evolution of the central Transverse Ranges, California, from apatite fission-track, (U-Th)/He and digital elevation model analyses: Basin Research, v. 12, p. 97-114.

Brocklehurst, S. H., and Whipple, K. X., 2002, Glacial erosion and relief production in the Eastern Sierra Nevada, California: Geomorphology, v. 42, p. 1-24.

Burbank, D. W., Leland, J., Fielding, E., Anderson, R. S., Brozovic, N., Reid, M. R., and Duncan, C., 1996, Bedrock incision, rock uplift and threshold hillslopes in the northwestern Himalayas: Nature (London), v. 379, no. 6565, p. 505-510.

Cattin, R., and Avouac, J. P., 2000, Modeling mountain building and the seismic cycle in the Himalaya of Nepal: Journal of Geophysical Research, v. 105, p. 13389-13407.

Fielding, E., Isacks, B., Barazangi, M., and Duncan, C., 1994, How flat is Tibet?: Geology, v. 22, p. 163-167.

Finlayson, D. P., and Montgomery, D. R., 2003, Modeling large-scale fluvial erosion in geographic information systems: Geomorphology, v. 53, p. 147-164.

Finlayson, D. P., Montgomery, D. R., and Hallet, B., 2002, Spatial coincidence of rapid inferred erosion with young metamorphic massifs in the Himalayas: Geology, v. 30, no. 3, p. 219-222.

Flint, J. J., 1974, Stream gradient as a function of order, magnitude, and discharge: Water Resources Research, v. 10, no. 5, p. 969-973.

Gasparini, N., 2003, Equilibrium and transient morphologies of river networks: discriminating among fluvial erosion models [PhD thesis]: Massachusetts Institute of Technology.

Gasparini, N.M., Bras, R.L. and Whipple, K.X., in review, The role of a sediment-flux-dependent erosion equation in transient bedrock river networks, *in* Willett, S., Hovius, N., Fisher, D., and Brandon, M., eds., Penrose Special Paper: Tectonics, climate and landscape evolution: Boulder, Geological Society of America.

Hack, J. T., 1957, Studies of longitudinal stream profiles in Virginia and Maryland: U.S. Geological Survey Professional Paper, v. 294-B, p. 97.

-, 1973, Stream profile analysis and stream-gradient index: J. Res. U.S. Geol. Surv., v. 1, no. 4, p. 421-429.

Hancock, G. S., and Anderson, R. S., 2002, Numerical modeling of fluvial strath-terrace formation in response to oscillating climate: GSA Bulletin, v. 114, no. 9, p. 1131-1142.

Harbor, D. J., 1998, Dynamic equilibrium between an active uplift and the Sevier River, Utah: Journal of Geology, v. 106, p. 181-198.

Heimsath, A. M., Dietrich, W. E., Nishiizumi, K., and Finkel, R. C., 1997, The soil production function and landscape equilibrium: Nature, v. 388, p. 358-361.

Hodges, K., Wobus, C., Ruhl, K., Schildgen, T., and Whipple, K., 2004, Quaternary deformation, river steepening and heavy precipitation at the front of the Higher Himalayan ranges: Earth and Planetary Science Letters, v. 220, no. 3-4, p. 379-389.

Howard, A. D., 1994, A detachment-limited model of drainage basin evolution: Water Resources Research, v. 30, no. 7, p. 2261-2285.

Howard, A. D., and Kerby, G., 1983, Channel changes in badlands: Geological Society of America Bulletin, v. 94, p. 739-752.

Hurtrez, J. E., Lucazeau, F., Lave, J., and Avouac, J. P., 1999, Investigation of the relationships between basin morphology, tectonic uplift, and denudation from the study of an active fold belt in the Siwalik Hills, central Nepal: Journal of Geophysical Research, v. 104, no. B6, p. 12,779-12,976.

Kirby, E., Whipple, K., Tang, W., and Chen, Z., 2003, Distribution of active rock uplift along the eastern margin of the Tibetan Plateau: inferences from bedrock channel longitudinal profiles: Journal of Geophysical Research, v. 108, no. B4, p. doi: 10.1029/2001JB000861.

Kirby, E., and Whipple, K. X., 2001, Quantifying differential rock-uplift rates via stream profile analysis: Geology, v. 29, no. 5, p. 415-418.

Lague, D., and Davy, P., 2003, Constraints on the long-term colluvial erosion law by analyzing slope-area relationships at various tectonic uplift rates in the Siwaliks Hills (Nepal): Journal of Geophysical Research, v. 108, no. B2, p. doi:10.1029/2002JB001893.

Lave, J., and Avouac, J. P., 2000, Active folding of fluvial terraces across the Siwaliks Hills, Himalayas of central Nepal: Journal of Geophysical Research, v. 105, no. B3, p. 5735-5770.

-, 2001, Fluvial incision and tectonic uplift across the Himalayas of central Nepal: Journal of Geophysical Research, v. 106, no. B11, p. 26561-26591.

Massong, T. M., and Montgomery, D. R., 2000, Influence of sediment supply, lithology, and wood debris on the distribution of bedrock and alluvial channels: Geological Society of America Bulletin, v. 112, no. 5, p. 591-599.

Merrits, D. J., 1996, The Mendocino triple junction: Active faults, episodic coastal emergence, and rapid uplift: Journal of Geophysical Research, v. 101, p. 6051-6070.

Merrits, D. J., and Bull, W. B., 1989, Interpreting Quaternary uplift rates at the Mendocino triple junction, northern California, from uplifted marine terraces: Geology, v. 17, p. 1020-1024.

Merritts, D., and Vincent, K. R., 1989, Geomorphic response of coastal streams to low, intermediate, and high rates of uplift, Mendocino junction region, northern California: Geological Society of America Bulletin, v. 101, p. 1373-1388.

Montgomery, D. R., and Brandon, M. T., 2002, Topographic controls on erosion rates in tectonically active mountain ranges: Earth and Planetary Science Letters, v. 201, p. 481-489.

Montgomery, D. R., Dietrich, W. E., and Sullivan, K., 1998, The role of GIS in watershed analysis, *in* Lane, S. N., Richards, K. S., and Chandler, J. H., eds., Landform monitoring, modelling and analysis: Chichester, England, John Wiley and Sons, p. 241-261.

Montgomery, D. R., and Foufoula-Georgiou, E., 1993, Channel network representation using digital elevation models: Water Resources Research, v. 29, p. 1178-1191.

Montgomery, D. R., and Gran, K. B., 2001, Downstream variations in the width of bedrock channels: Water Resources Research, v. 37, no. 6, p. 1841-1846.

Niemann, J. D., Gasparini, N. M., Tucker, G. E., and Bras, R. L., 2001, A quantitative evaluation of Playfair's law and its use in testing long-term stream erosion models: Earth Surface Processes and Landforms, v. 26, no. 12, p. 1317-1332.

Roe, G. H., Montgomery, D. R., and Hallet, B., 2002, Effects of orographic precipitation variations on the concavity of steady-state river profiles: Geology, v. 30, no. 2, p. 143-146.

Roe, G. H., Montgomery, D. R., and Hallet, B., 2003, Orographic precipitation and the relief of mountain ranges: Journal of Geophysical Research, v. 108, no. B6, p. 2315, doi:10.1029/2001JB001521.

Sklar, L., 2003, The influence of grain size, sediment supply, and rock strength on rates of river incision into bedrock. [PhD. thesis]: University of California, Berkeley, 343 p.

Sklar, L., and Dietrich, W. E., 1998, River longitudinal profiles and bedrock incision models: Stream power and the influence of sediment supply, *in* Tinkler, K. J., and Wohl, E. E., eds., Rivers Over Rock: Fluvial Processes in Bedrock Channels: Washington, D. C., AGU, p. 237-260.

Sklar, L. S., and Dietrich, W. E., 2001, Sediment and rock strength controls on river incision into bedrock: Geology, v. 29, no. 12, p. 1087-1090.

Snyder, N., Whipple, K., Tucker, G., and Merritts, D., 2000, Landscape response to tectonic forcing: DEM analysis of stream profiles in the Mendocino triple junction region, northern California: Geological Society of America, Bulletin, v. 112, no. 8, p. 1250-1263.

Snyder, N. P., Whipple, K. X., Tucker, G. E., and Merritts, D. M., 2002, Interactions between onshore bedrock-channel incision and nearshore wave-base erosion forced by eustacy and tectonics: Basin Research, v. 14, p. 105-127.

Snyder, N. P., Whipple, K. X., Tucker, G. E., and Merrits, D. J., 2003a, Channel response to tectonic forcing: field analysis of stream morphology and hydrology in the Mendocino triple junction region, northern California: Geomorphology, v. 53, p. 97-127.

-, 2003b, Importance of a stochastic distribution of floods and erosion thresholds in the bedrock river incision problem: Journal of Geophysical Research, v. 39, p. doi:10.1029/2001WR001057.

Spotila, J. A., House, M. A., Blythe, A., Niemi, N. A., and Bank, G. C., 2002, Controls on the erosion and geomorphic evolution of the San Bernadino and San Gabriel Mountains, Southern California, in Barth, A. P., ed., Contributions to crustal evolution of the Southwestern United States: Special Paper: Boulder, Geological Society of America, p. 205-230.

Stock, G. M., Anderson, R. S., and Finkel, R. C., 2004, Pace of landscape evolution in the Sierra Nevada, California, revealed by cosmogenic dating of cave sediments: Geology, v. 32, no. 3, p. 193-196.

Stock, J. D., and Dietrich, W. E., 2003, Valley incision by debris flows: evidence of a topographic signature: Water Resources Research, v. 39, no. 4, p. doi: 10.1029/2001WR001057.

Tarboten, D. G., Bras, R. L., and Rodriguez-Iturbe, I., 1989, Scaling and elevation in river networks: Water Resources Research, v. 25, p. 2037-2051.

Tucker, G. E., 2004, Drainage basin sensitivity to tectonic and climatic forcing: Implications of a stochastic model for the role of entrainment and erosion thresholds: Earth Surface Processes and Landforms, v. 29, p. 185-205.

Tucker, G. E., and Bras, R. L., 2000, A stochastic approach to modeling the role of rainfall variability in drainage basin evolution: Water Resources Research, v. 36, p. 1953-1964.

Tucker, G. E., and Whipple, K. X., 2002, Topographic outcomes predicted by stream erosion models: sensitivity analysis and intermodel comparison: Journal of Geophysical Research, v. 107, no. B9, p. doi:10.1029/2001JB000162.

Whipple, K., 2004, Bedrock rivers and the geomorphology of active orogens: Annual Reviews of Earth and Planetary Science, v. 32, p. 151-185.

Whipple, K. X., Hancock, G. S., and Anderson, R. S., 2000, River incision into bedrock: Mechanics and relative efficacy of plucking, abrasion, and cavitation: Geological Society of America Bulletin, v. 112, no. 3, p. 490-503.

Whipple, K. X., and Tucker, G. E., 1999, Dynamics of the stream-power river incision model: Implications for height limits of mountain ranges, landscape response timescales, and research needs: Journal of Geophysical Research, v. 104, p. 17661-17674.

-, 2002, Implications of sediment-flux-dependent river incision models for landscape evolution: JGR, v. 107, no. B2, p. doi:10.1029/2000JB000044.

Willgoose, G., Bras, R. L., and Rodriguez-Iturbe, I., 1991, A coupled channel network growth and hillslope evolution model, I Theory: Water Resources Research, v. 27, no. 7, p. 1671-1684.

Wobus, C. W., Hodges, K. V., and Whipple, K. X., 2003, Has focused denudation sustained active thrusting at the Himalayan topographic front?: Geology, v. 31, p. 861-864.

Figure Captions

1. Example of contour extraction method for high-quality USGS 10 meter DEM. A) Prior to contour extraction, DEM is characterized by abundant artificial data between contour crossings, resulting in a stepped pattern on the profile. Sub-sampling data at equal vertical intervals (grey dots) produces a smoother, more realistic profile consistent with the source data (see text for discussion). B) Contour extraction method faithfully reproduces stream profile crossings of contour lines on original USGS topographic map (grey dots). Dashed line = stream line extracted from DEM (compare to dash-dot stream line on the map).

2. Effects of smoothing on longitudinal profile data, from San Gabriel Mountains in southern California. A) Profile data extracted from USGS 10 meter DEM, showing raw profile (light grey crosses) and data extracted at equal vertical intervals of 12.192 m (40 ft) (black crosses). B) Profile data extracted from SRTM 90 meter DEM, showing raw profile data (light grey crosses) and data extracted at 12.192 m intervals (black crosses). Note the considerable reduction in scatter in both cases. C) Superposition of smoothed data from SRTM 90 meter DEM (720 m smoothing window, light grey crosses), log-bin averaged data for SRTM 90 meter DEM (light grey squares), smoothed data from USGS 10 meter DEM (180 m smoothing window, black crosses), and log-bin averaged data for USGS 10 meter DEM (black squares). Note general correspondence among all datasets despite variations in resolution. D) Plot of k_{sn}, normalized to average value of each group, vs. smoothing window. E) Plot of θ, normalized to average value of each group, vs smoothing window. Note that steepness and concavity indices for any dataset are consistent within ~10%, regardless of the choice of smoothing window size or style.

3. Schematic long profile and map view plots comparing transient and steady-state systems. A) Transient long profile showing short oversteepened reach separating old and new equilibrium states. B) Profile crossing from one uplift regime to another showing channel reaches with constant k_s values, separated by a high or low concavity transition zone in between. In this and all subsequent plots, long profile data (elevation vs.

distance) will be shown as solid lines with linear axes labeled on top and at right; slope-area data (log(S) vs log(A)) will be shown as crosses with logarithmic axes labeled at bottom and at left. A_{cr} marks transition to fluvial scaling (see text); slope of log(S) vs log(A) scaling is the concavity index θ; y-intercept is the steepness index k_s. C) Transient wave of incision propagates through system at a nearly constant vertical rate; knickpoints (white dots) should therefore closely follow lines of constant elevation (dashed line) in plan view. D) In contrast, knickpoints separating zones of high and low uplift rates (white dots) follow the trend of the accommodating shear zone in map view (dashed line). In many cases, the map pattern of knickpoints may be a better diagnostic of a transient state than long profile form.

4. Long profile and slope-area data from a 10-meter resolution DEM of the King Range in northern California. Top three plots show pairs of tributaries from high uplift zone (black) and low uplift zone (grey). In all plots, solid lines are fits to data with θ_{ref}= 0.57; dashed lines are fits to data with concavity as a free parameter. Squares are slope-area data using log-bin averaging method; crosses are data using 200 meter smoothing window to calculate channel slopes (see text). Arrows above long profiles show regression limits for slope-area fits. A) Gitchell Creek and Hardy Creek; B) Shipman Creek and Howard Creek; C) Big Creek and Juan Creek. D) Composite slope-area data from all six rivers. Note that in all cases the channels from the high uplift zone are consistently steeper than those in the low uplift zone. Dramatic drop in channel gradient in lowermost segments of the channels reflects a transition to increasingly alluviated conditions, reflecting a decrease in effective rock uplift rate due to Holocene rise in sealevel (Snyder et al., 2002), alluviation at channel mouth, or both.

5. Long profile and slope-area data from a 10-meter resolution DEM from the San Gabriel mountains east of Los Angeles, California. Top three plots show pairs of tributaries from high uplift zone (black) and low uplift zone (grey). In all plots, solid lines are fits to data with θ_{ref}=0.45; dashed lines are fits to data with concavity as a free parameter. Squares are slope-area data using log-bin averaging method; crosses are data using 400 meter smoothing window to calculate channel slopes (see text). Arrows above long profiles

show regression limits from slope-area data. Rivers shown are: A) Minegulch and Beartrap; B) Iron Fork and Little Tujunga; C) Coldwater and Pacoima. D) Composite slope-area data from all six rivers. Steps in profiles and spikes in slope-area data are dams and reservoirs in the lower reaches of the drainage basins.

6. A) Long profiles of four tributaries to the Big Tujunga river and slope-area data from Trail Canyon, showing apparent transient in long profiles and map pattern. Note that transient is easily seen in z vs x plots for Mill, Fox, and Clear Creek; but slope-area plot greatly aids interpretation for Trail Canyon. Dashed line extending from Mill Creek shows projection of upper profile to mountain front. B) Map pattern of knickpoints (white dots) in Big Tujunga basin. Close correspondence of knicks to 1000 meter contour (black line) and irregular pattern in map view again suggests a transient feature (see Figure 1).

7. A) Plot of normalized steepness index (k_{sn}) vs. uplift rate (U) for seven strike-parallel channels from the Siwalik hills in southern Nepal. Data suggest a linear correlation between k_{sn} and U with a zero intercept, consistent with a stream power scaling with n = 1. Uplift rates estimated by Hurtrez et al. (1999) from a fault-bend-fold kinematic model and bedding dips. B) Example of slope-area data from the Siwalik hills in southern Nepal. Grey crosses show data from a representative strike-parallel stream in the low-uplift-rate regime (U = 7 mm/yr). Black crosses show data from a representative strike-parallel stream in the high-uplift-rate regime (U = 13 mm/yr). Open dots show data from a strike-perpendicular stream crossing the entire anticline, from low rock uplift rate (U = 4 mm/yr) to high rock uplift rate (U = 13 mm/yr) and back. Negative concavity segment in strike-perpendicular stream can be explained by spatially varying rock uplift rate along the profile (e.g., Kirby and Whipple, 2001). C) Channel profiles shown in part B. Thick grey lines show approximate extent of slope-area fits in used in part B. Negative concavity in transitional profile manifests as a rollover just above junction with the high uplift channel.

8. Comparison of incision rate estimates derived from A) Stream profile method, assuming a stream-power incision rule with $n = 1$, and B) structural study of Hurtrez et al. (1999) and Lavé and Avouac (2000). Note general correspondence of location and magnitude of high incision rate zones from the two methods, suggesting that quantitative estimates of incision rates may be attainable in regions with relatively simple patterns of lithology and uplift. Figure B adapted from Hurtrez et al. (1999).

9. Schematic showing two competing models for Himalayan tectonic architecture and predicted patterns of rock uplift rates for each model. A) Ramp model predicts uplift gradient spread over 20-30 kilometers, with MCT carried passively over ramp in Himalayan sole thrust (HST). Uplift gradient should be broadly distributed (B), and thermal history for rocks on opposite sides of PT_2 should be similar. Surface breaking thrust model (C) predicts more abrupt break in rock uplift rates centered at PT_2 (D) and distinct thermal histories for rocks on opposite sides of the inferred surface-breaking shear zone. MFT—Main Frontal Thrust; MBT—Main Boundary Thrust; MCT—Main Central Thrust; MT—Mahabarat Thrust; STF—South Tibetan Fault system; HST—Himalayan Sole Thrust; KTM—Kathmandu; PT_2—Physiographic transition. (adapted from Wobus et al., 2003).

10. Slope-area plots and trunk stream longitudinal profiles from A) Trisuli river catchment, B) Burhi Gandaki catchment, and C) Marsyandi catchment, all in central Nepal. Smoothing method and contour interval for all cases are 10 km moving average and 30 m, respectively. In each plot, grey crosses show data from representative southern (low uplift zone) tributaries; black crosses show data from representative northern (high uplift zone) tributaries; and open circles show data from trunk streams carving through the range. Dashed lines show approximate regional upper and lower bounds on steepness indices of 650 and 95 $m^{0.9}$, respectively. Grey shading on slope area and long profile data shows extent of high concavity zone in trunk streams, representing a maximum estimate of the width of rock uplift gradients (see text). Open stars show position of abrupt physiographic transition (PT_2) in central Nepal, as identified from slope maps and

satellite photography (see text and Figure 9). Note that Marsyandi long profile begins on a valley sidewall due to a data gap at the western edge of the catchment.

11. Digital elevation map of central Nepal, showing transition zone between high and low uplift rates as determined from stream profile analyses. Diamonds along Trisuli and Burhi Gandaki rivers show locations of detrital $^{40}Ar/^{39}Ar$ thermochronologic analysis: grey diamonds represent Miocene and younger apparent ages; white diamonds represent Paleozoic and older apparent ages. Note general correspondence of break in cooling history with change in stream profiles, suggesting a long-lived structure accommodating differential exhumation in this region. Dashed white lines in Marsyandi basin show location of intense Quaternary deformation, possibly responsible for accommodating the inferred gradient in rock uplift rates (e.g., Hodges et al., 2004).

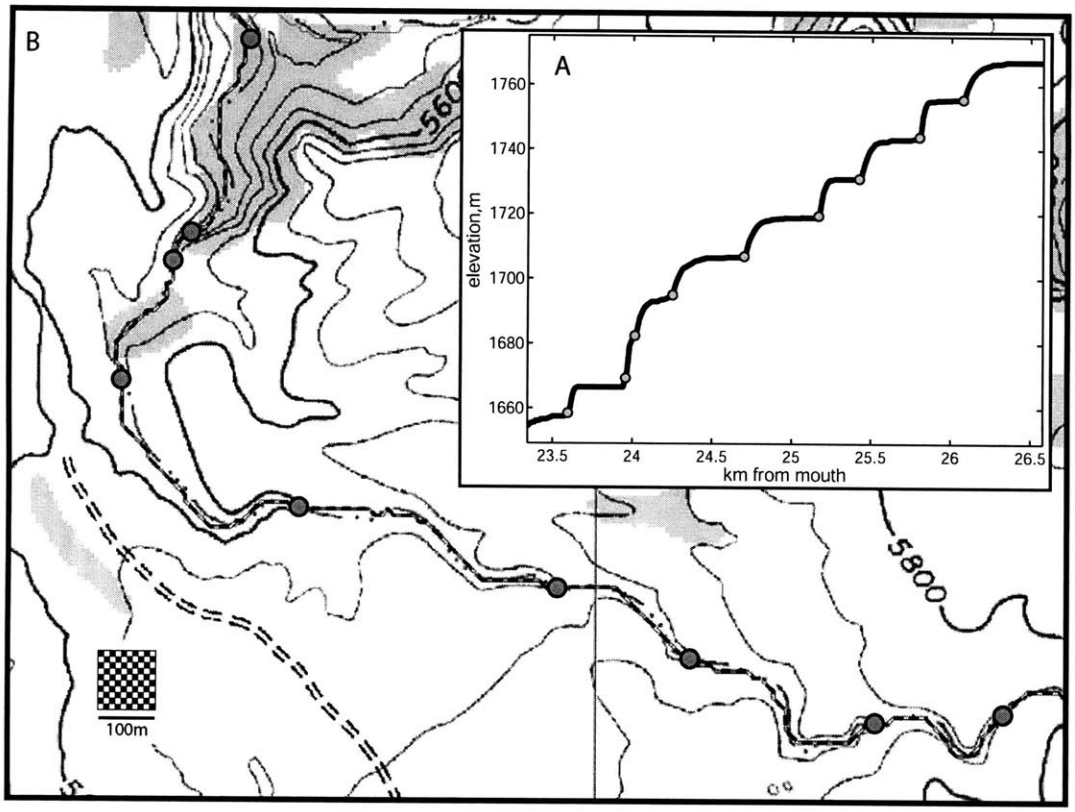

Wobus et al., Figure 1

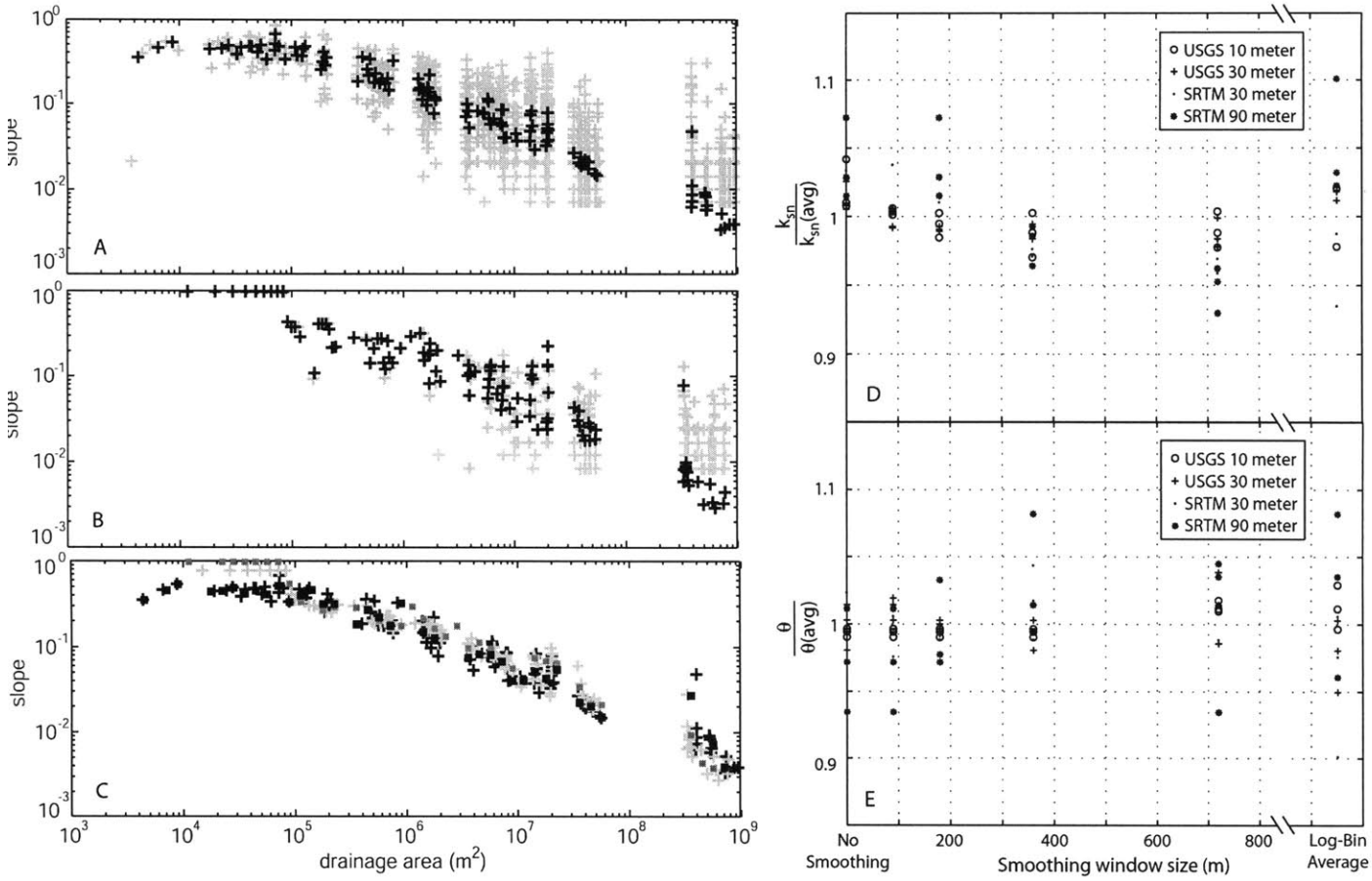

Wobus et al., Figure 2

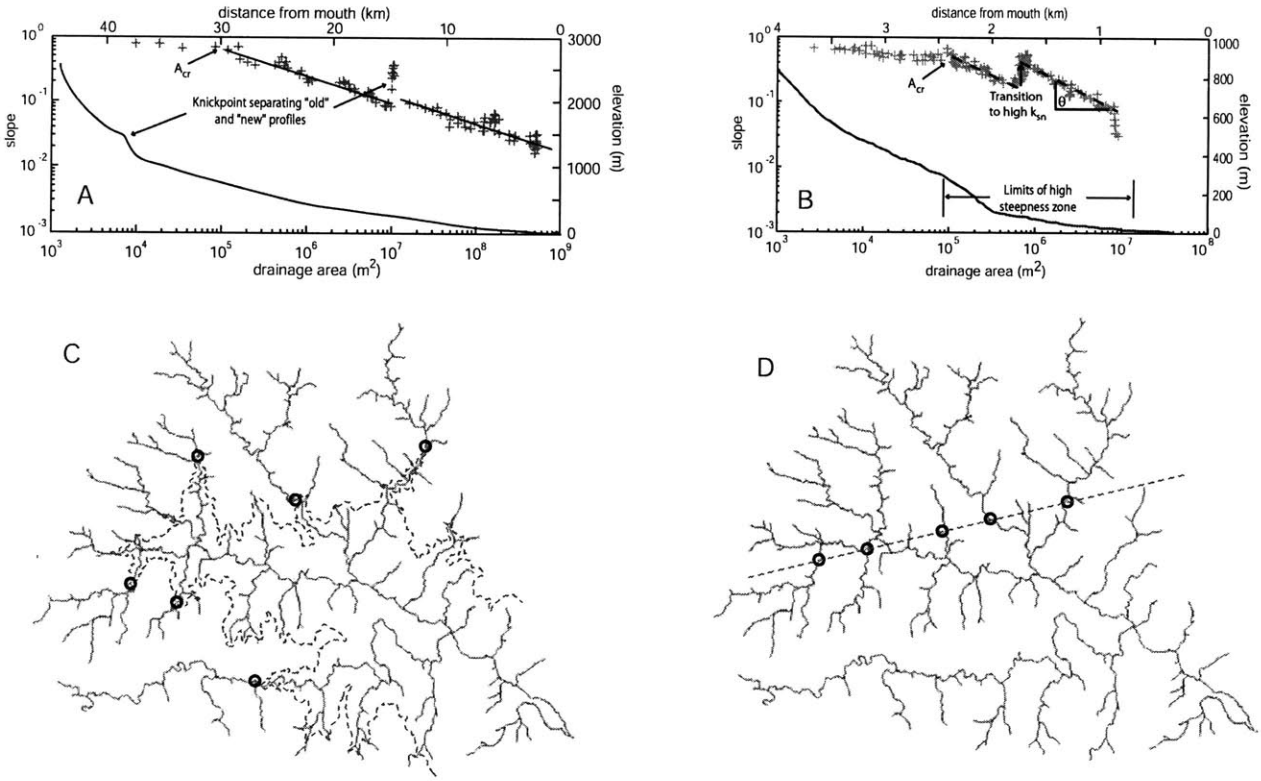

Wobus et al., Figure 3

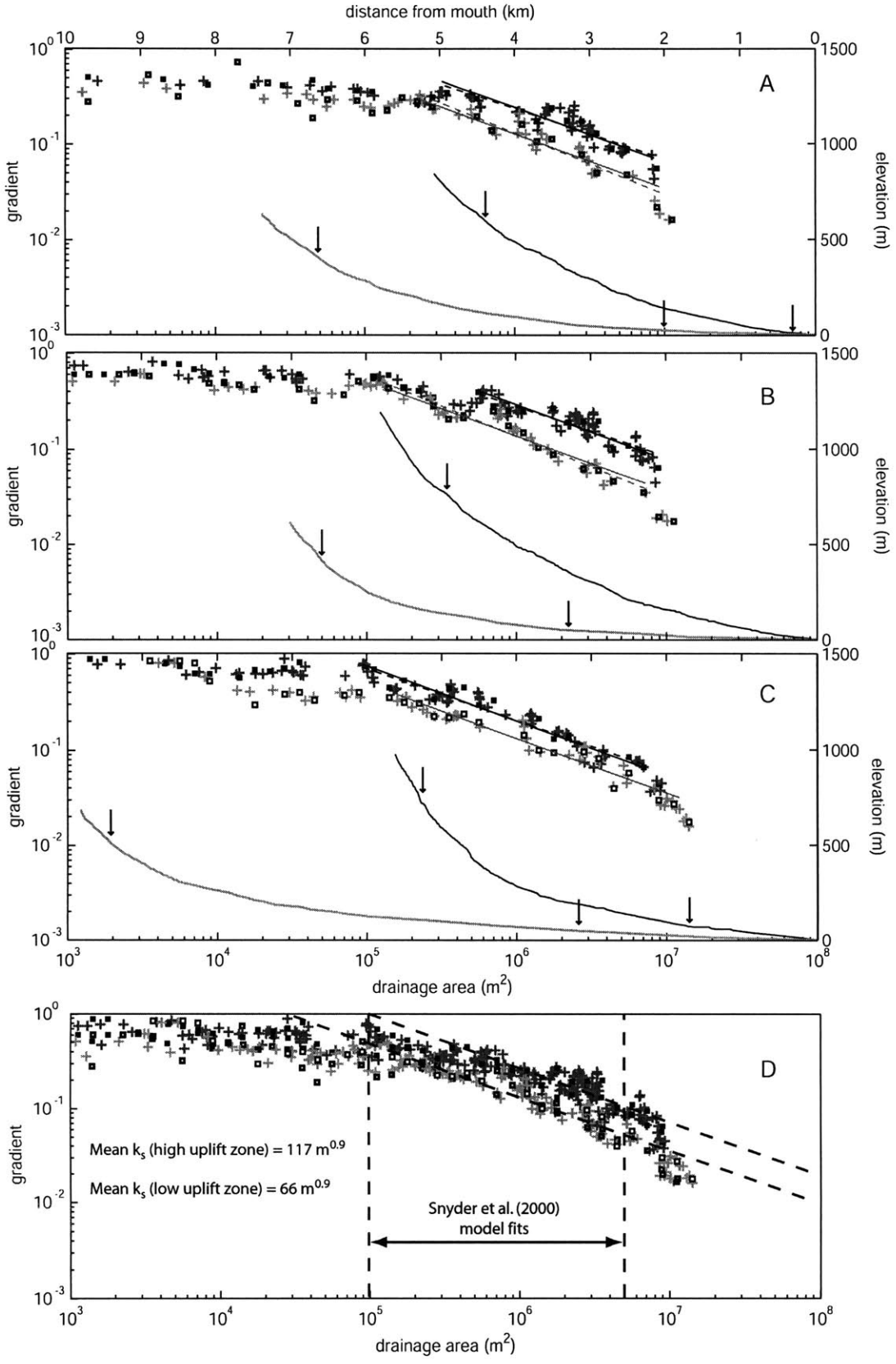

Wobus et al., Figure 4

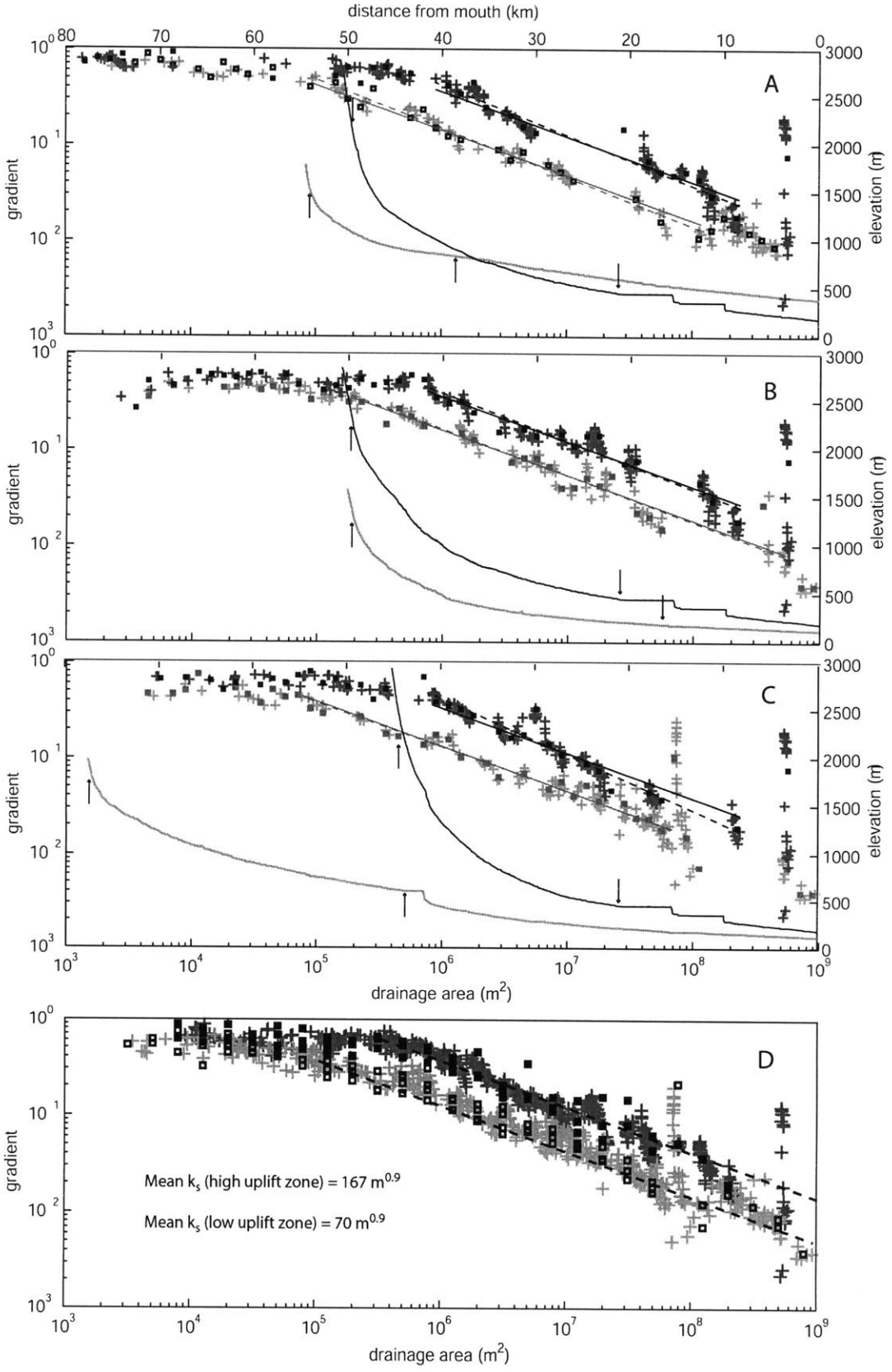

Wobus et al., Figure 5

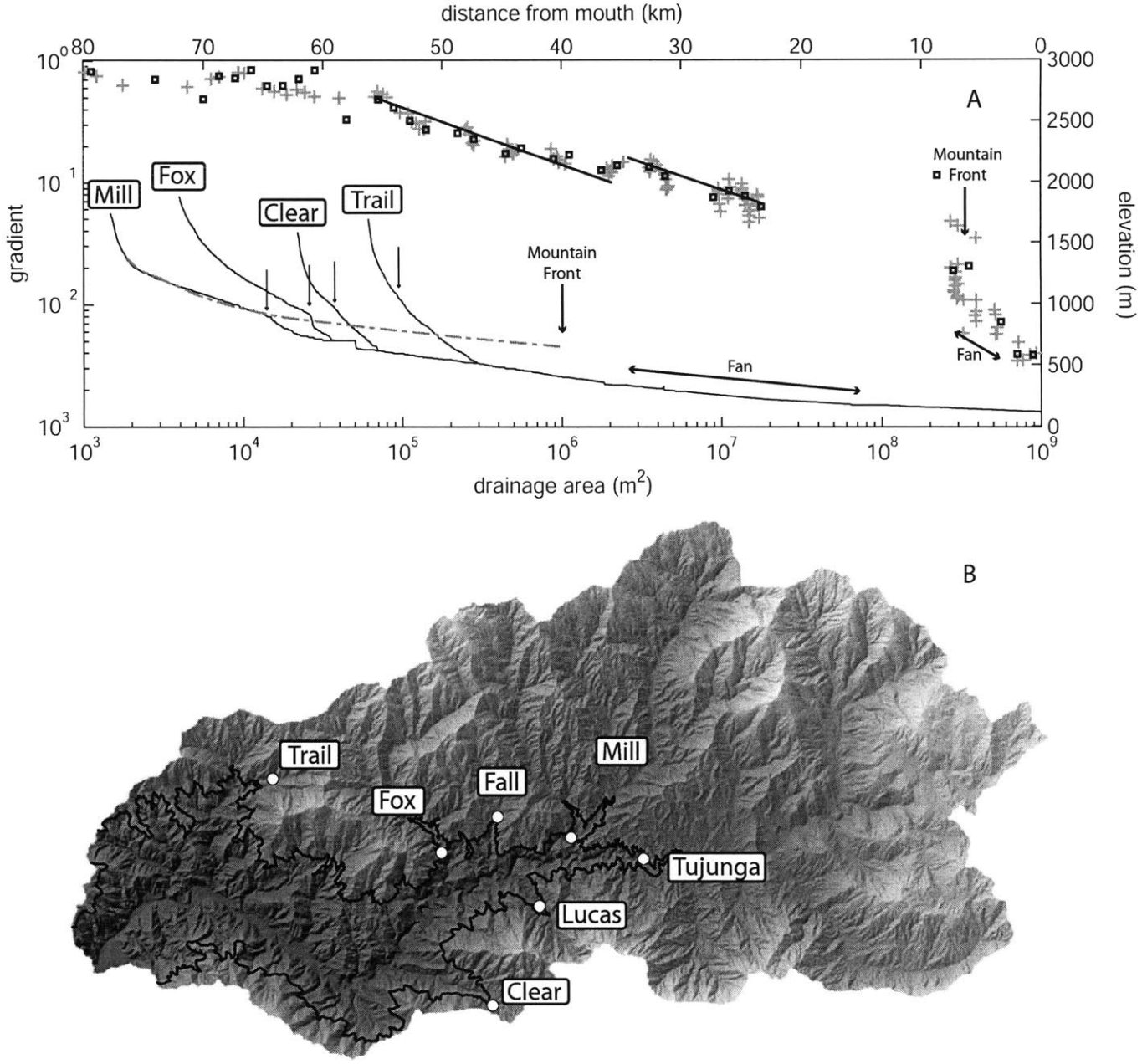

Wobus et al., Figure 6

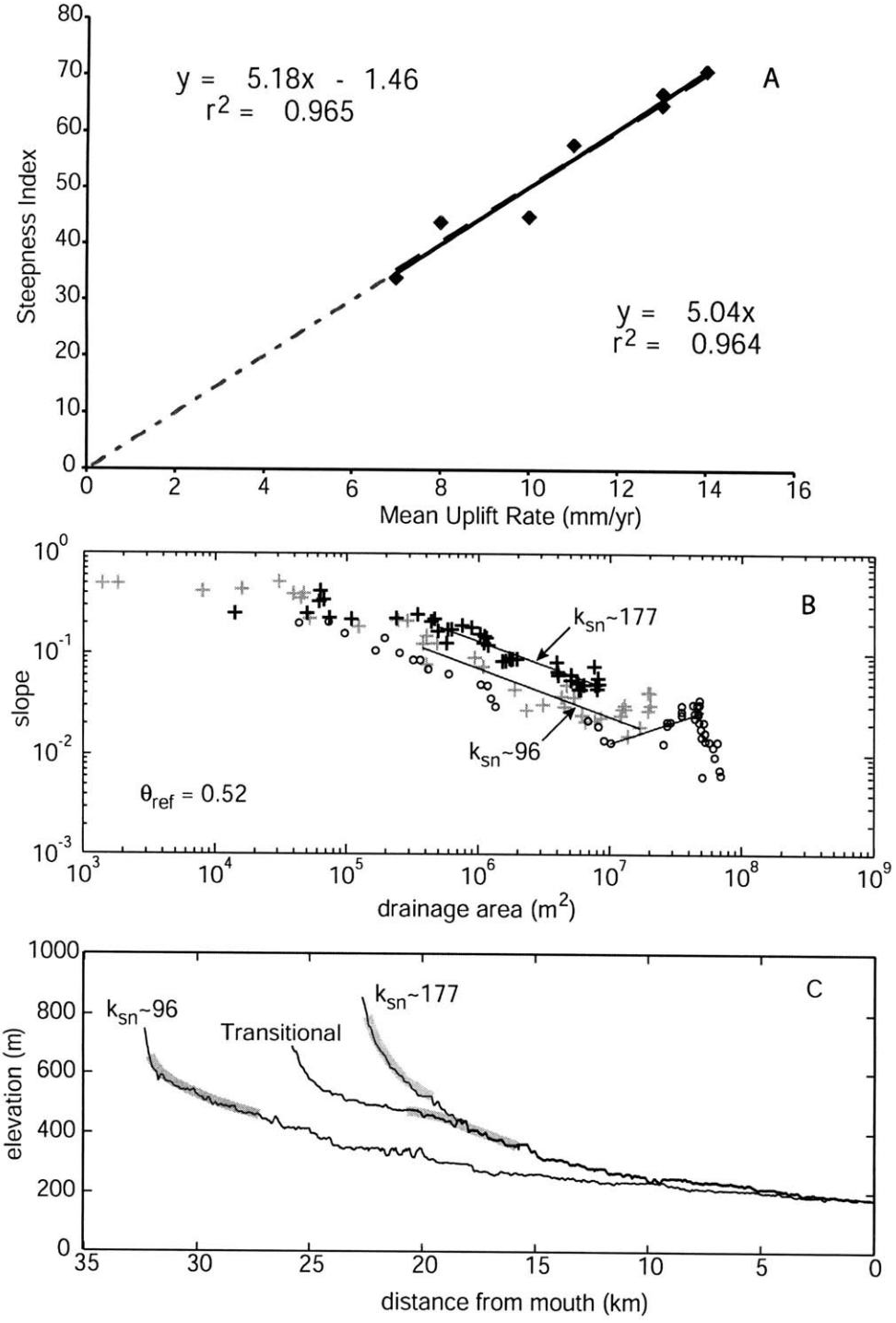

Wobus et al., figure 7

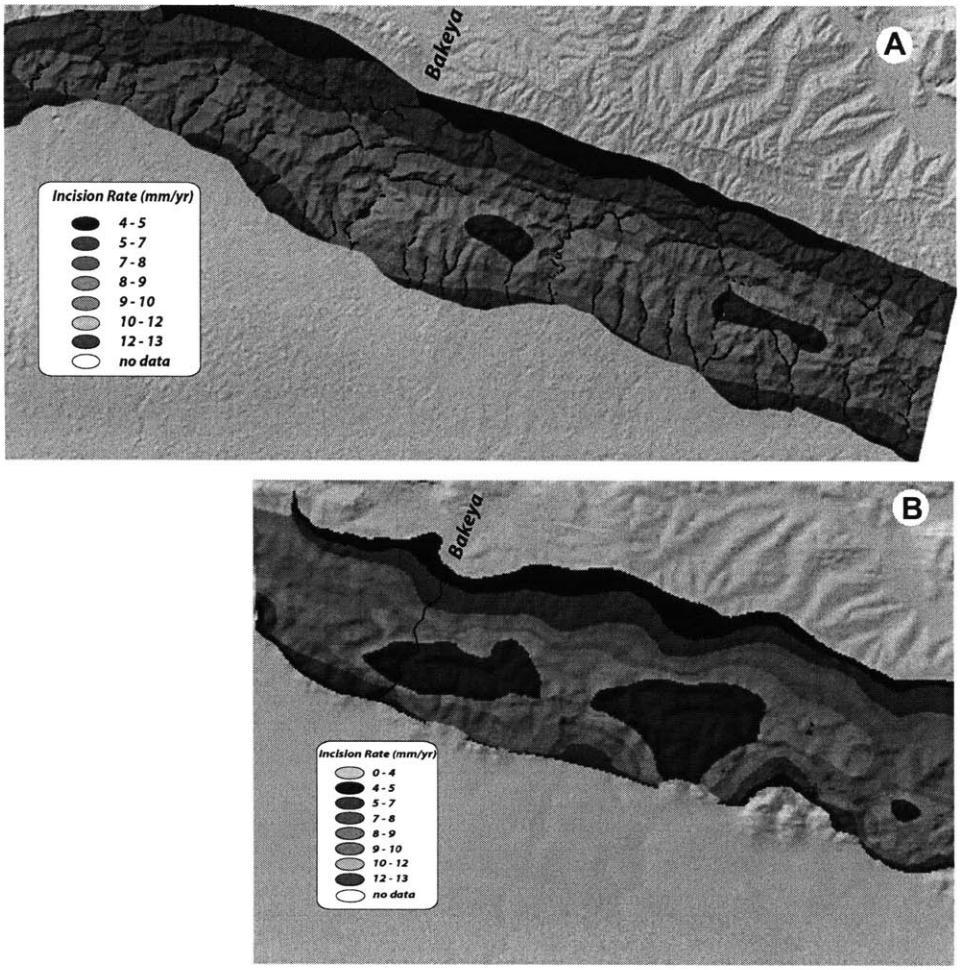

Wobus et al., figure 8

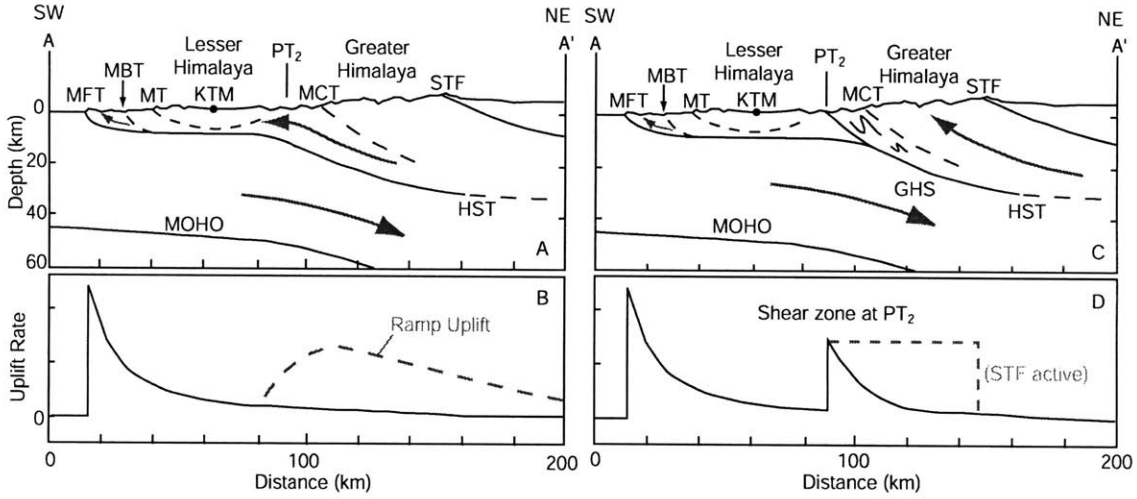

Wobus et al., Figure 9

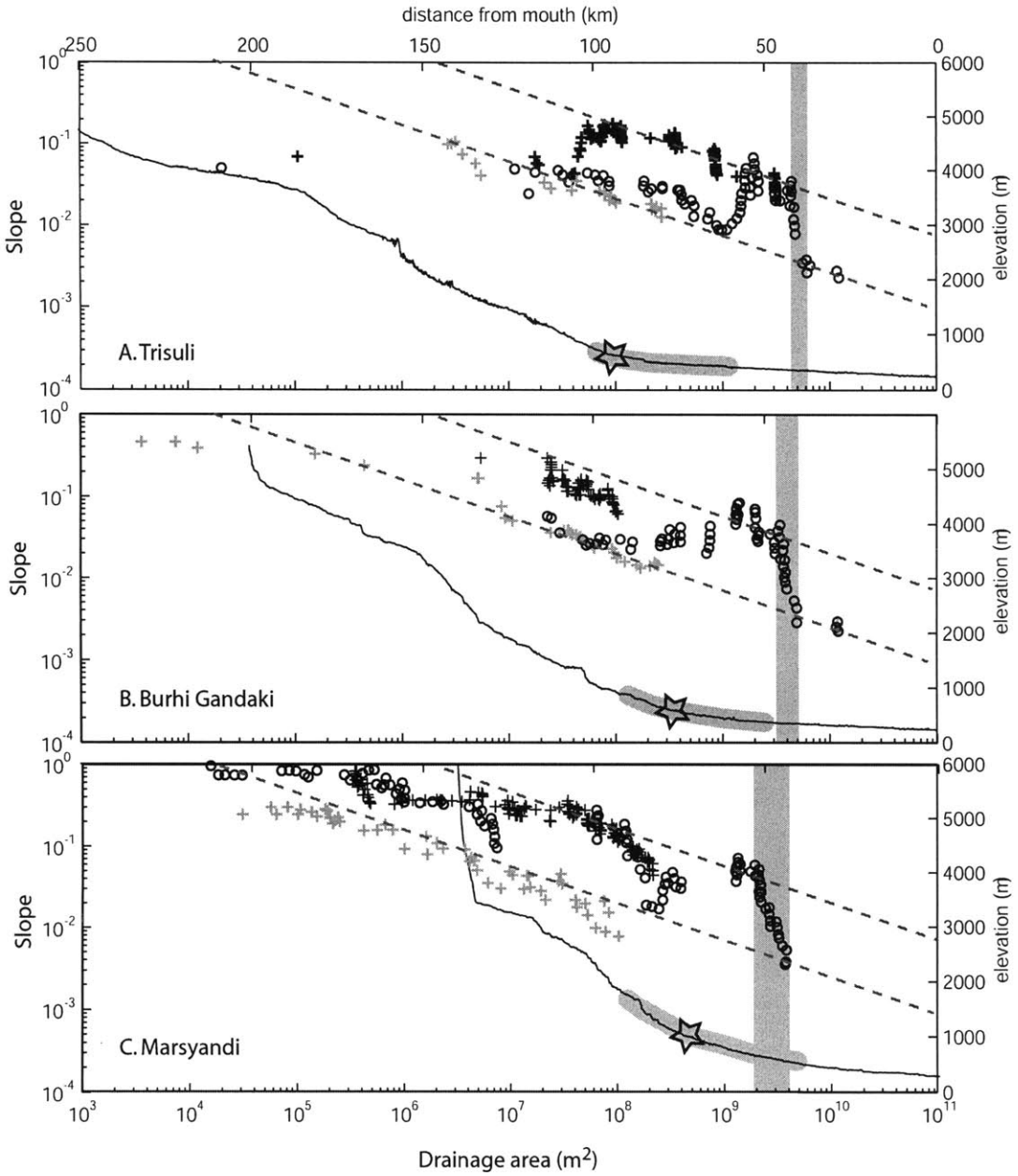

Wobus et al., Figure 10

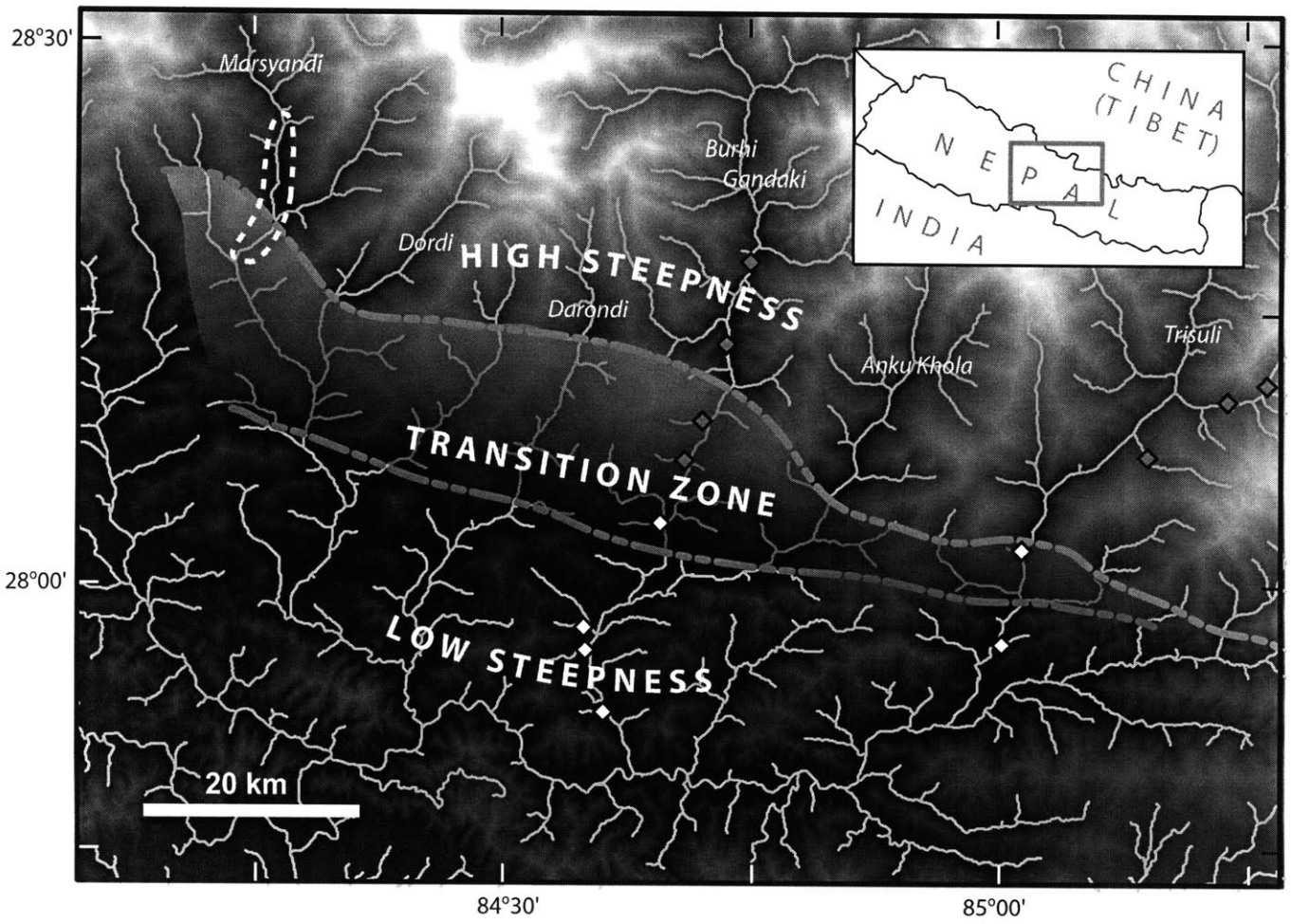

Wobus et al., Figure 11

Chapter 3: Hanging valleys in fluvial systems: a failure of stream power and implications for landscape evolution

Cameron W. Wobus
Benjamin T. Crosby
Kelin X. Whipple

Department of Earth, Atmospheric and Planetary Sciences
Massachusetts Institute of Technology
Cambridge, Massachusetts 02139

For submittal to *JGR – Earth Surface*

Abstract

We document and characterize hanging valleys in a fluvially sculpted landscape in the Eastern Central Range of Taiwan. Our conceptual model for the initiation of hanging valleys builds on a recently proposed model of bedrock incision, which suggest that the highest transport stage flows are actually less efficient at eroding bedrock than moderate stages. As tributary mouths steepen in response to an incisional pulse in the mainstem, channel gradients may therefore pass a threshold value beyond which erosional efficiency is hindered, giving rise to a mismatch between trunk and tributary erosion rates. This mismatch is naturally expected at tributary junctions, where a step-function in drainage area also leads to sharp contrasts in water and sediment flux between trunk and tributary basins. The presence of hanging valleys in fluvial landscapes suggests that our most simplified parameterizations of bedrock erosion – which typically assume a monotonic positive correlation between channel gradient and incision rate – may be applicable only to a range of moderate channel gradients. In addition, the presence of these features may have important implications for landscape response timescales, since catchments above these tributary mouths may be insulated for some time from incisional signals propagating through the channel network. The results of this study underscore the need for a more complete understanding of bedrock erosion processes, and the incorporation of process transitions into landscape evolution models.

1. Introduction

To quantify the feedbacks among climate, tectonics and surface processes, we require a set of testable, process-based rules to describe how fluvial networks respond to external forcing. In general, fluvial networks in a transient state or those containing spatially variable tectonic forcing provide the best opportunity to test these rules, since the concave-up form of steady-state river profiles is inherently nonunique in its reflection of dominant erosive process (Howard et al., 1994; Whipple and Tucker, 2002; Willgoose et al., 1991). Field sites experiencing transient responses and nonuniform forcing have been used to calibrate the parameters in fluvial erosion laws assuming a stream power or shear stress control on erosion rate (Bishop et al., 2005; Howard and Kerby, 1983; Kirby and Whipple, 2001; Rosenbloom and Anderson, 1994; Snyder et al., 2000). While these studies have had some success, the generality of such an approach requires simplified formulations of erosional process that clearly cannot capture all of the underlying physics (Whipple, 2004). This shortcoming of stream profile analysis, while unavoidable, provides fertile ground for additional research into the mechanisms of landscape response. In particular, the suggestion that thresholds and nonlinearities in shear stress, transport stage, or sediment supply are important in controlling the transient response of landscapes has only begun to be evaluated (Gasparini, 2003; Sklar and Dietrich, 1998; Sklar and Dietrich, 2004; Snyder et al., 2003; Tucker, 2004) and studies exploring these effects in field settings are even more rare (Crosby and Whipple, in review). Field settings in which simple models of landscape evolution fail may provide an important opportunity to improve our understanding of landscape response.

In this paper, we describe hanging valleys in the Eastern Central Range of Taiwan, and suggest that nonlinearities in the relationships among transport stage, drainage area and erosion

rate may lead naturally to the formation of these features. We begin with a review of fluvial scaling in natural systems, using the network geometry to predict the distribution of channel gradients if simple shear stress or unit stream power erosion rules are invoked. We then turn to a field example from the San Gabriel Mountains of southern California, where the scaling relationships predicted by such erosion rules provide a reasonable estimate of the transient channel geometry. Next, we examine the distribution of channel gradients in three basins in northeastern Taiwan, where the steepest portions of the fluvial network are almost always found at tributary mouths. At many of these tributary mouths, channel gradients are significantly oversteepened compared to expectations from simple river incision models. We classify these basins as hanging valleys, since the gradients at their mouths suggest a disequilibrium between rock uplift and river incision. Using this classification, we examine the distribution of hanging valleys in the fluvial network relative to tributary drainage area, trunk to tributary drainage area ratio, and proximity to lithologic boundaries. Based on the model of Sklar and Dietrich incorporating a non-monotonic relationship between transport stage and erosion rate (Sklar and Dietrich, 1998; Sklar and Dietrich, 2004), we suggest that a simple modification to our most simplified erosion laws may help to explain the formation of hanging valleys in fluvial systems. Finally, we discuss the implications of our observations for the evolution of the Central Range of Taiwan, and for landscape evolution models, response timescales, and the attainment of steady-state conditions.

2. Background

2.1 Scaling in fluvial systems

Longitudinal profiles from rivers around the globe commonly yield a scaling in which channel gradient is a power-law function of contributing drainage area:

$$S = k_s A^{-\theta} \quad (1)$$

Here, S is the local channel gradient, A is the upstream drainage area, θ is the concavity index, and k_s is the steepness index. The concavity index θ typically falls in a narrow range between 0.3 and 0.6, and appears to be independent of the rate of rock uplift based on empirical data (Kirby and Whipple, 2001; Tucker and Whipple, 2002; Whipple and Meade, 2004; Wobus et al., in press). At steady-state, the steepness index k_s has been shown to be a function of the rock uplift rate (Snyder et al., 2000; Wobus et al., in press), but other factors such as substrate erodibility, channel geometry, sediment properties, and climatic variables also influence k_s (Whipple, 2004). Note that "steepness" as defined here is the channel gradient normalized to the contributing drainage area, and should not be confused with the channel gradient.

The form of equation (1) predicts that zones with spatially uniform rock uplift should be manifested as linear arrays on logarithmic plots of slope vs. drainage area. Shifts in these linear arrays are expected where the rock uplift rate (or other influences on k_s, as listed above) is spatially variable (Kirby and Whipple, 2001; Wobus et al., in press). Shifts in these arrays also occur where transient incisional pulses are sweeping through the fluvial network (Snyder et al., 2002; Whipple and Tucker, 1999; Whipple and Tucker, 2002) (see Figure 1). In the case of a transient incisional pulse, the upstream-migrating boundary between adjusting and relict portions of the landscape is defined as a knickpoint, most commonly manifested as a convexity on the longitudinal profile (Crosby and Whipple, in review).

Based entirely on geometric considerations and the assumption that the concavity index is independent of rock uplift rate, the horizontal rate of knickpoint migration (celerity) during the adjustment of a fluvial profile to a change in uplift rate can be expressed as a simple function of the local channel gradient and the vertical incision rate (Niemann et al., 2001):

$$Ce_H = -\frac{1}{S_1\left(1 - S_2/S_1\right)}\frac{dz}{dt} \tag{2}$$

Where Ce_H represents the horizontal celerity, S is the local channel gradient, dz/dt is the local incision rate, and subscripts 1 and 2 represent the original and perturbed states, respectively. Substituting equation (1) into equation (2), we can then relate the horizontal celerity to drainage area as:

$$Ce_H = \frac{U_1 - U_2}{k_{s_1} - k_{s_2}} A^{\theta} \tag{3}$$

Equation (3) suggests that knickpoints should migrate upstream at an ever-decreasing rate proportional to the contributing drainage area (see also (Bishop et al., 2005; Rosenbloom and Anderson, 1994; Whipple and Tucker, 1999)).

Noting that the vertical celerity is simply the horizontal celerity multiplied by the local channel gradient, we can express the vertical rate of knickpoint migration following a change in uplift rate as follows:

$$Ce_V = \frac{U_1 - U_2}{k_{s_1} - k_{s_2}} k_{s_2} \tag{4}$$

Equation (4) can be derived without making any assumptions about the form of the erosion law: we have simply utilized the geometry of the system, and the empirical observation that channel gradient is a power function of contributing drainage area with a concavity index that does not vary with rock uplift rate (i.e., equation 1).

If we further assume that the local erosion rate scales with shear stress or stream power, the steady-state channel gradient in equation (1) can be written in terms of the rock uplift rate and drainage area as follows (Snyder et al., 2000; Whipple and Tucker, 1999):

$$S = \left(\frac{U}{K}\right)^{1/n} A^{-m/n} \tag{5}$$

where m and n represent the exponents on area and slope in the stream power or shear stress erosion rule, and K is a coefficient representing erodibility parameters such as rock type, channel geometry, sediment properties, climate, and vegetative cover. Noting the similarities in the form of equation (5) and equation (1) and substituting for k_s in equation (4), the vertical celerity can then be expressed as a function only of the rock uplift rate and the slope exponent n (Niemann et al., 2001):

$$Ce_V = \frac{U_1 - U_2}{U_1^{1/n} - U_2^{1/n}} U_2^{1/n} \tag{6}$$

where for $n = 1$, we find $Ce_V = U_2$.

In general, assuming a monotonic relationship between erosion rate and channel gradient (i.e. a constant value of n), equation (6) predicts that the rate of vertical translation of knickpoints is a constant, which is uniquely determined by the initial and perturbed rock uplift rates, U_1 and U_2. This result predicts that migrating knickpoints created by a change in the rock uplift rate should lie along a single contour line at any point in time. Discovery of natural systems in which a transient state adheres to this spatial pattern of knickpoint migration would suggest that our simple parameterization of the controls on channel gradient (i.e., equation 5) may be adequate for predicting landscape response at the catchment scale. Such behavior will be shown in the following section using an example from the Big Tujunga basin in the San Gabriel Mountains of California. Substantial deviations from this simplified pattern of landscape adjustment, on the

other hand, suggest that something is missing in our simplified parameterizations of scaling in natural systems. This is the focus of the remainder of the paper, where we examine complex patterns of landscape adjustment in the eastern Central Range of Taiwan.

2.2 Example – Big Tujunga river, CA

The San Gabriel Mountains of southern California result from a restraining bend in the San Andreas fault, and have been subject to spatially and temporally variable rock uplift rates through the late Cenozoic (Blythe et al., 2000; Lave and Burbank, 2004; Spotila et al., 2002). The Big Tujunga river drains the northwestern end of the San Gabriel Mountains, immediately to the north of Los Angeles, and contains a spatial pattern of knickpoints that appears to be consistent with the descriptions in equations (1) and (4) above. The basin is small enough that climatic conditions are relatively constant throughout the basin, and lithology is characterized by a combination of coarse grained anorthosite and granite intrusives. Landscape morphology is relatively uniform across the anorthosite-granite boundaries, and none of the knickpoints correspond to lithologic boundaries, suggesting that lithology is not a first-order control on knickpoint location.

We analyzed 31 stream profiles from the Big Tujunga basin, using a 10-meter USGS digital elevation model (DEM). Methods used in stream profile extraction and analysis followed those of (Snyder et al., 2000; Wobus et al., 2005). For each profile, data collected along the length of the stream included elevation, streamwise distance from the outlet, contributing drainage area, and local slope calculated over a 12.2 meter vertical interval (corresponding to USGS 40' contours). Following the extraction of these raw data, plots of log(S) vs. log(A) were created to evaluate the linearity of this relationship. Excepting abrupt changes in steepness

associated with knickpoints and dams, equation (1) explains the data well with a uniform concavity index between 0.4 and 0.5 (Wobus et al., 2005). Steepness indices normalized to a concavity of 0.45 (k_{sn}) were calculated along the length of each channel profile (Kirby and Whipple, 2001; Snyder et al., 2000; Wobus et al., 2005), by regressing on the slope-area data in short segments corresponding to a half-kilometer of channel length. Color-coded plots of these normalized steepness indices can then be used to objectively evaluate the distribution of channel gradients in the basin.

Normalized steepness indices in the Big Tujunga basin range from ~90 to ~240 for a reference concavity of 0.45. Slope-area data from channels spanning the entire range of elevations are well approximated by two parallel linear segments separated by a single step, with high steepness indices downstream and lower steepness indices upstream (Figure 1). This pattern of steepness values is consistent with a transient condition in which the lower reaches of the basin have adjusted to an increase in rock uplift rate and the upper reaches have not yet responded to this tectonic perturbation. Furthermore, the boundary between the "adjusted" (high k_{sn}) and "relict" (low k_{sn}) channel reaches lies very close to a single elevation of 1000 meters above sealevel (Figure 2), suggesting that the knickpoints separating these channel segments have migrated upstream at a constant vertical rate.

The Big Tujunga example illustrates the expected behavior of a drainage basin in a transient state if our simplified parameterizations of erosion and our method of data analysis are adequate: channels have responded to their new conditions in their lower reaches, but remain temporarily insulated from perturbation upstream of the knickpoints. With the exception of locally extreme gradients created by man-made dams, steepness indices calculated for knickpoints throughout the channel network fall within an envelope defined by the "adjusted"

and "relict" k_s values (Wobus et al., 2005). Furthermore, the relatively constant elevation of the knickpoints suggests a spatially and temporally constant vertical celerity, consistent with the geometic constraints of Equations 1 and 4 with an invariant concavity index. This is in turn consistent with a fluvial erosion rule based on shear stress or unit stream power (equations 5-6). With this background, we now turn to the central range of Taiwan, where a breakdown in the scaling predicted by equation (6) highlights a change in erosional process at tributary mouths, leading to a dramatically different pattern of channel gradients throughout the landscape.

3. Hanging valleys in Taiwan

3.1 Geologic setting

The Taiwan orogen is a result of oblique convergence between the Luzon arc, riding on the Philippine Sea plate, and the Eurasian continental margin (Teng, 1990). Subduction of the Eurasian plate has progressed southward through time, such that there is a rough space for time substitution from north to south (Willett et al., 2003): in the south, the collision has just begun and the orogen is correspondingly young, while in the north the orogen has already begun an extensional collapse due to extension behind the Ryukyu trench. Within the greenschist-grade metamorphic core of the orogen, corresponding to the physiographic Eastern Central Range, the landscape is characterized by rapid denudation and bedrock incision, driven by extremely steep topography and a humid, subtropical climate (Dadson et al., 2003; Hartshorn et al., 2002; Schaller et al., in press).

Erosion and exhumation rate data for Taiwan are available for a variety of timescales. Dadson et al. (2003) report exhumation rates of 3-6 mm/yr based on fission-track dating of apatites from the metamorphic core of the orogen, while Holocene bedrock incision rates derived

from ^{14}C dating of strath terraces approach 10 mm/yr along the eastern margin of the island, and a 30-year record of sediment yield data indicates basin-averaged rates locally exceeding 30 mm/yr (Dadson et al., 2003). Measurements of cosmogenic ^{21}Ne within the steep-walled canyons of the Liwu basin suggest incision rates as high as 26 mm/yr, although these rates may have been perturbed by temporary filling of the basins or lateral retreat of the canyon walls (Schaller et al., in press). Finally, repeat high precision measurements of bedrock ribs in active channels yield local incision rates between 2 and 6 mm/yr over annual timescales (Hartshorn et al., 2002). While erosion rates measured over different timescales yield different results, the very broad agreement among these rates and the geometric form of the orogen have been used to support the hypothesis that Taiwan may have achieved a topographic or exhumational steady state (Suppe, 1981; Willett and Brandon, 2002). Nonetheless, regional geomorphic studies document the presence of substantial convexities and knickpoints within the fluvial network, suggesting that the geomorphic response of this system may be considerably more complex than suggested by a model of a steady-state orogen (Slingerland and Willett, 1999).

We focus our analysis on three basins in northeastern Taiwan: the Hoping, Liwu and Mukua basins (Figure 3). The position of these three drainages lies within the zone of maximum exhumation rates defined by Dadson et al. (2003). Furthermore, the physiography of these basins suggests rapid denudation throughout the drainage network: trunk streams are steep and narrow, and hillslopes are nearly linear with steep (35°) gradients (Hovius et al., 2000). Bedrock in these basins comprises greenschist-facies metasedimentary rocks dominated by metapelites, with locally significant marbles and gneisses along the easternmost side of the study area. Foliations generally trend north-northeast, with major trunk streams approximately orthogonal to this dominant foliation.

3.2 Methods and Results

Longitudinal profile data for 182 rivers were extracted from the three drainage basins in northeastern Taiwan, using a 40 meter resolution DEM. As in the example from the Big Tujunga basin, we generated plots of channel longitudinal profiles and log(S) vs log(A) for each individual channel, and created a map of normalized steepness indices for each drainage basin by regressing on half-kilometer segments of the slope-area data with a reference concavity of 0.45. We also recorded the drainage areas in the trunk and tributary basins at each tributary junction. Using all of the data, we classified each tributary channel as adjusted, linear, transient (containing knickpoints) or hanging (Figure 4).

Tributary channels classified as adjusted are those in which the profiles are smooth, concave-up, and graded to the tributary mouth, with steepness values comparable to those in the trunk stream (Figure 4b). Channels classified as linear have concavity values near zero, possibly representing erosion by non-fluvial agents such as debris flows (Montgomery and Foufoula-Georgiou, 1993; Stock and Dietrich, 2003) (Figure 4c). Channels placed in the generalized "knickpoint" category are distinguished from those classified as "hanging" by the form of the slope-area relationship: the former have knickpoints whose steepness index is commensurate with k_s values in the adjusted portion of the profile (Figure 4d), while the latter contain reaches that are significantly oversteepened relative to the trunk stream. Note that these classifications are largely qualitative; however, the basins classified as hanging valleys were easily identified due to a characteristic spike in slope-area data (Figure 4e).

Planview maps of reach-averaged steepness indices in Taiwan reveal more complex patterns of landscape adjustment than those found in the Big Tujunga catchment. In the Liwu

basin, for example, all of the highest steepness indices are found at tributary mouths (Figure 5). The presence of these high-k_s zones suggests a transient landscape, but their spatial distribution indicates that landscape adjustment in this basin is not achieved simply by knickpoints sweeping through the channel network at a predictable rate (e.g., equation 6). Instead, knickpoints appear to be stalled at tributary mouths, which are found at a range of elevations (Figure 6). Channel gradients immediately downstream of the convexities in these tributary profiles are commonly much higher than those typical for mountain streams (up to 85%, or 40°), and steepness indices are substantially higher than those in the trunk streams they enter. All of these observations suggest that the relationship between steepness index and rock uplift rate can be more complicated during transient adjustment than implied by simple parameterizations such as equation 5 (Gasparini et al., in review).

Our field observations are limited to those collected during a reconnaissance trip along the Liwu basin in 2001. However, the field observations we do have suggest a transition from simple bedrock abrasion and plucking in streams with abundant gravel cover to waterfall plunge-pool erosion, boulder jams, and extensive bedrock exposure at many tributary mouths (Figure 7). This transition in the erosive regime suggests that the mechanisms responsible for transmitting transient conditions upstream are no longer described by our simplified rules for bedrock erosion.

The clustering of steep channel gradients near tributary mouths and the field observation that many of these channels have become waterfalls suggests that local bedrock incision rates are much slower at the tributary mouths than in the trunk streams. Such a disconnect between erosion rates in the tributary and trunk streams indicates that these oversteepened tributary mouths temporarily insulate the basins upstream from incisional pulses in the mainstem, and can

therefore be classified as hanging valleys. We suggest that a highly nonlinear and non-monotonic relationship between transport stage and erosion rate as described by Sklar and Dietrich (Sklar and Dietrich, 1998; Sklar and Dietrich, 2004) can generate a negative feedback that will lead to the formation of hanging valleys in natural systems. If this model is correct, it may have significant implications for landscape response timescales in natural systems.

3.3 Conceptual Model for hanging valley formation

Recent work by Sklar and Dietrich (Sklar and Dietrich, 1998; Sklar and Dietrich, 2004) suggests that for erosion by bedload abrasion, the highest transport stages – defined as the ratio of shear stress to the critical shear stress required to mobilize bedload – may actually be less erosive than more moderate transport stages. The decreasing erosion rate with increasing transport stage in their model results from a decrease in the frequency of bedload impacts on the bed. At low transport stages, for example, fluid velocities are low and bedload may be just above the threshold of motion. These transport conditions lead to low erosion rates since there is very little excess energy available to erode the bed. As slopes increase, both the mean and the deviatoric fluid velocities increase, mobilizing more bedload by the increased shear stress and turbulence at the bed. At these moderate slopes, saltation hop lengths are short, and the high frequency of impacts from saltating bedload results in high erosion rates (Sklar and Dietrich, 1998; Wiberg and Smith, 1985). Beyond some threshold value, however, further increases in channel slope result in longer saltation hop lengths and less frequent bedload impacts, thereby outpacing the increase in kinetic energy of individual bedload impacts and leading to a net negative feedback. Erosion rates therefore begin to decrease with increasing transport stage above some critical value (Figure 8).

Because the Sklar and Dietrich (2004) analysis considers only a uniform-sized bedload supply, is limited to bedload abrasion as the only operative process, and is written only for a planar bed morphology, it is difficult to determine quantitatively what combinations of channel gradient, sediment supply, and flow rate might be sufficient to cross the threshold to decreasing erosion rates. However, since for a given flood discharge and sediment grain size, channel gradient maps directly into transport stage, we might expect channel reaches with extremely steep gradients to erode at a lower rate than more moderate gradients. In the limiting case of a nearly vertical channel bed, for example, a tributary mouth will become a waterfall and a process transition from relatively uniformly distributed bedrock abrasion and plucking to focused plunge pool erosion may occur. At this point, the rate of migration of an incisional pulse into the tributary basin will be more strongly influenced by the rock strength of the substrate than by the transport conditions in the channel. This decoupling of erosion rate from the transport conditions in the channel may explain the spatial pattern of oversteepened reaches in Taiwan: once the threshold transport stage is exceeded, the knickpoint migration rate is no longer a simple function of upstream drainage area (e.g., equation 3) allowing these oversteepened channel reaches to remain near the tributary mouths.

Using this conceptual model as a backdrop, we suggest that hanging valleys may form in response to a rapid increase in channel gradient at a tributary mouth, driven by an incisional pulse migrating headward in the mainstem. If the fluvial network generally responds to tectonic perturbation in a manner consistent with equations 4-6, an incisional pulse initiated near the basin mouth will propagate upstream at an initially rapid rate determined by the drainage area of the entire basin. As this incisional pulse works its way up the mainstem, it will steepen the mouth of each tributary basin it passes. Where the contrast between tributary and trunk stream

drainage areas is large, there will be a substantial mismatch between the rates of knickpoint migration in each basin (e.g., equation 3). This mismatch in knickpoint migration rates will drive a rapid steepening, and a rapid increase in transport stage, at the tributary mouth. If this increase in transport stage is large enough, erosion rates in the oversteepened tributary mouth will begin to decrease (e.g., Figure 8). Since sediment supply and all other transport conditions in the tributary basin remain at their unperturbed values, the tributary channel makes no internal adjustment to the new conditions. The oversteepened mouth of the tributary therefore remains at a new, lower erosion rate while further lowering in the mainstem increases the elevation of the hanging valley through time (Figure 9).

4. Discussion

4.1 Control of threshold conditions

We suggest that the formation of hanging valleys is controlled by two threshold conditions. First, as suggested by Sklar and Dietrich (2004), there must be a threshold transport stage beyond which erosion rates begin to decrease. And second, there must be a threshold mainstem lowering rate beyond which tributary mouths become oversteepened to exceed this critical transport stage. The first threshold should be controlled by the flow conditions in the tributary channel, including the dominant erosive process, sediment supply, and sediment transport capacity. Changes in channel gradient, driven by local baselevel lowering as incisional pulses sweep past the tributary junction in the mainstem, will alter these flow conditions as the system adjusts. The second threshold should be controlled by the size of the tributary basin, or by the ratio of drainage areas in the tributary and trunk streams, since we expect the relative rates of transient adjustment to scale with the contributing drainage areas in each basin (Crosby and

Whipple, in review; Niemann et al., 2001; Whipple and Tucker, 1999)(Equation 3). By examining the channel gradient and drainage area data we have compiled from our Taiwan case study, we can begin to place some constraints on the necessary conditions for hanging valley formation in natural systems.

Of the 182 tributaries we analyzed in the Hoping, Liwu and Mukua basins, fifteen were classified as hanging valleys. For these fifteen tributaries, the reach-averaged channel gradients below the knickpoints range from 0.28 to 0.85, with a mean of 0.46 (~25°). The highest gradients are generally associated with the lowest drainage areas, and the lowest gradients occur in tributaries with higher drainage areas (Figure 10). This drainage area dependence suggests that erosion rates at the tributary mouths are not completely decoupled from the transport conditions in the tributary channel: larger tributaries have lower gradients along their oversteepened reaches presumably because they have more erosive power. By fitting a regression line through all of the slope and drainage area data from the oversteepened reaches, we find the following relationship:

$$S = 12.2A^{-0.216} \quad (7)$$

For comparison with other published values, if we assume a reference concavity of 0.45, we find an average normalized steepness index along the oversteepened reaches of ~450 (Wobus et al., 2005). This value is near the upper limit of steepness indices observed in diverse environments worldwide (Whipple, 2004), and may place some bounds on the transport stages required to generate hanging valleys.

Our data also allow us to evaluate the drainage area requirements for hanging valley development. Based on our conceptual model, this area dependence may be related to either the absolute rate of knickpoint migration in the tributary channel, or to the relative rates of

knickpoint migration in the trunk and tributary channels. In the first case, we might expect hanging valleys to occur only in tributaries below a threshold drainage area, since the erosive power of a tributary depends on its water and sediment discharge, both of which can be related to contributing drainage area (Whipple, 2004). This would be analogous to the threshold area model discussed by Crosby and Whipple (2005), which suggests that knickpoints may form at small drainage areas during incisional pulses when erosive capacity can no longer keep pace with incision in the mainstem. In the case of a dependence on relative knickpoint migration rates, we would expect the ratio of drainage areas in the tributary and the trunk streams to be the controlling variable, since the knickpoint migration rate in each basin will depend on its upstream drainage area (Niemann et al., 2001; Whipple and Tucker, 1999).

Figure 11 summarizes all of the trunk and tributary drainage area data from the Hoping, Liwu and Mukua basins, along with the classification of each tributary as adjusted, linear, containing knickpoints with gradients commensurate with those in the trunk stream, or hanging. All of the channels classified as hanging valleys occur at a tributary drainage area less than 20 km^2, suggesting that this may be the threshold drainage area required to generate a hanging valley. However, nearly all of the hanging valleys (13 of 15) can also be found above a threshold ratio of trunk to tributary drainage area of 10:1, lending support to a model in which drainage area ratio is the relevant control on hanging valley development.

Either the threshold drainage area or the threshold drainage area ratio cases are characterized by abundant false positives, suggesting that absolute or relative drainage areas are at best necessary, but by no means sufficient, conditions to generate hanging valleys. Among the channels with a drainage area less than 20 km^2, for example, only 15 were classified as hanging, while 127 were placed in another category. Similarly, among channels with drainage area ratio

greater than 10:1, only 13 were categorized as hanging, while 83 were categorized as linear, adjusted or containing simple knickpoints. The relevant question, then, is why some tributaries with a small drainage area and a large trunk to tributary drainage area ratio become hanging valleys, while others do not.

One potential control on which tributaries form hanging valleys may be the position of the tributary junction within the drainage basin. This spatial control might be expected for two reasons: first, the trunk streams are simply larger in the lower reaches of the basin, and these junctions therefore have a greater likelihood of having a large trunk to tributary drainage area ratio. And second, since tectonic signals should originate downstream and propagate up the drainage network, the lower reaches of a basin are more likely to have seen an incisional pulse in the mainstem capable of steepening the tributary mouth. The data from Taiwan suggest that position in the basin is indeed an important control on which tributaries become hanging valleys: of the tributaries that were classified as hanging, none were found in the upper third of their drainage basins, and most were found in the lower third. In basins where prominent knickpoints could be identified in the trunk streams, hanging valleys are always found downstream of these knickpoints, supporting a model in which hanging valleys are initiated by headward propagating knickpoints in the trunk stream (Figure 12).

Another possible control on the initiation of hanging valleys is proximity to lithologic boundaries. Lithology has been shown to be an important control on the position of knickpoints in some settings (see Crosby and Whipple, 2005, and references therein) and may therefore be expected to play some role in the position of hanging valleys in Taiwan. Based on comparisons of the positions of hanging valleys with the positions of lithologic boundaries from available geologic maps, however, we do not find evidence for a strong lithologic control on hanging

valley development. In the three basins analyzed from northeastern Taiwan, for example, hanging valleys can be found within marbles, gneisses, migmatites and schists, which constitute all of the mapped lithologies in the region (Figure 13).

While lithology does not appear to be important in controlling where hanging valleys form in this setting, there does appear to be some lithologic control on how an individual basin responds to a baselevel lowering at its mouth. For example, most of the tributaries classified as linear are found within the foliated schists and meta-cherts which form the core of the Eastern Central Range (labeled "PM3" on the geologic map in Figure 13). The consistent, high gradients observed over a broad range of drainage areas suggest that these channels are eroding by debris flow incision, rather than by fluvial bedrock incision (Montgomery and Foufoula-Georgiou, 1993; Stock and Dietrich, 2003). We might expect well-foliated rocks to be susceptible to landsliding and debris-flow initiation, creating the observed correlation between lithology and linear profiles.

It is also notable that the tributaries with linear channel profiles are never found hanging above their junction with the trunk streams. Among the tributaries containing a trunk to tributary drainage area ratio greater than 10:1, for example, 39 have profiles classified as linear, suggesting erosion by debris flow processes. None of the profiles with linear morphologies contain substantial knickpoints between their headwaters and their junction with the trunk streams, and none of the channels containing knickpoints or hanging morphologies are linear upstream of the knickpoint. While we have only a small dataset to draw from, the observation that linear profiles do not hang above their mainstem channels suggests that debris flow incision is not susceptible to the same negative feedback as bedload abrasion, and hence may become the dominant erosion process on very steep slopes (Stock and Dietrich, 2003).

4.2 Implications for landscape response

The location of hanging valleys within the eastern Central Range of Taiwan may provide insights into how this orogen has evolved through time. Moreover, the existence of hanging valleys in fluvial channel networks has important implications for the timescales of landscape response in tectonically active settings in general.

Our initial work included a preliminary analysis of eight basins draining eastern Taiwan. Nearly all of the hanging valleys in Taiwan were found in the northernmost three basins discussed here. In addition, the majority of these hanging valleys (10 of 15) were found in a single basin – the Liwu – which lies approximately 100 km south of the northern tip of Taiwan. One possible reason for the clustering of hanging valleys within this basin is lithology. The lower reaches of the Liwu river basin comprise resistant marbles, gneisses and migmatites, which we would expect to transmit incisional pulses upstream in a relatively intact, "detachment-limited" manner (Crosby and Whipple, in review; Whipple and Tucker, 1999; Whipple and Tucker, 2002). As these coherent knickpoints pass tributary mouths, the tributary channels would therefore steepen quickly, favoring the creation of hanging valleys as described in our conceptual model. While field observations indicate that the lowermost reaches of the Liwu river are filled with alluvium which could potentially diffuse these coherent knickpoints, these alluviated reaches are likely to be quickly excavated during a baselevel fall, forcing detachment-limited erosive behavior (Whipple, 2004).

Another possible reason for the clustering of hanging valleys in northeastern Taiwan is purely tectonic. Due to the rough north-south space for time substitution along the eastern margin of Taiwan, the three basins discussed here lie within the most rapidly uplifting portion of

the Taiwan orogen between the ongoing arc-contintent collision in the south and its extensional collapse in the north (Dadson et al., 2003; Willett et al., 2003). Thermal models of Taiwan indicate that exhumational steady state may have been reached further to the south (Willett et al., 2003), but the clustering of hanging valleys in the north suggests that topographic adjustment to tectonic perturbation is still ongoing here. It is possible that northern Taiwan is simply ideally situated in space and time, which has enabled us to capture a number of knickpoints and hanging valleys within these basins during our single snapshot in time.

The presence of hanging valleys in the eastern Central Range challenges the notion that this landscape is in an approximate steady state balance between erosion and tectonic uplift (Suppe, 1981; Whipple, 2001; Willett and Brandon, 2002; Willett et al., 2003), or at least motivates the question of what spatial and temporal scales are relevant in assessing the steadiness of an orogenic system. Because incisional pulses are frequently stalled at tributary junctions, erosion rates along the eastern Central Range are likely to vary significantly on opposite sides of these junctions. This suggests a pattern of erosion rates that is highly variable in space, and uncorrelated with the positions of major tectonic structures. At the scale of individual drainage basins, then, a balance between rock uplift rate and erosion rate is unlikely to be achieved. In addition, while the distribution of cooling ages in Taiwan can be interpreted as evidence for an exhumational steady-state over million-year timescales (Willett et al., 2003), hanging valleys may be important in prolonging stochastic perturbations away from this steady form, such as those resulting from oscillatory changes in climate state (Whipple, 2001). Depending on our spatial and temporal scales of interest, then, models which invoke a steady-state hypothesis for Taiwan, or indeed for any orogen, should be interpreted with caution.

For a well-behaved system in which erosion rate scales predictably with parameters such as channel gradient and drainage area, theoretical considerations suggest that the minimum timescale for landscape response can be easily estimated (Whipple et al., 1999; Whipple, 2001; Whipple and Tucker, 2002). The possibility that hanging valleys may form in purely fluvial systems suggests that these theoretical estimates may not be sufficient to evaluate landscape response timescales in real systems, since much of the landscape lags behind in its response to tectonic perturbation. Incorporating into our models a non-monotonic relationship between channel gradient and erosion rate, and a description of other processes that become important at tributary junctions when thresholds are exceeded (e.g., plunge pool erosion, weathering, mass wasting, etc), may help us to make more reliable predictions about the timescales of landscape response.

5. Conclusions

Our analysis of the eastern Central Range of Taiwan indicates that many of the tributary channels in this landscape can be classified as hanging valleys, which are temporarily insulated from tectonic perturbations migrating up the trunk streams. While our conceptual model remains preliminary, we propose that hanging valleys can be explained by existing models of bedrock incision if we incorporate a non-monotonic relationship between transport stage and erosion rate into our bedrock erosion rules (Sklar and Dietrich, 2004). This simple modification to our existing erosion rules allows the rate of erosion to fall once a channel gradient exceeds a threshold value. Based on our observations from hanging valleys along the northeastern coast of Taiwan, it appears that a small contributing drainage area in the tributary and/or a large ratio between trunk and tributary drainage areas may be necessary, but not alone sufficient, conditions

for the formation of hanging valleys. Our conceptual model for hanging valley formation highlights the important first-order effects that thresholds in bedrock channel incision processes can have on landscape form. Recognition of process transitions at threshold conditions, and better physically-based rules describing those distinct processes, will greatly improve our ability to simulate landscape response to external forcing. In turn, incorporation of these more comprehensive erosion rules into landscape evolution models will help us to better predict landscape response timescales and the nature of the coupling between tectonics, climate and landscape form.

References

Bishop, P., Hoey, T.B., Jansen, J.D. and Artza, I.L., 2005. Knickpoint recession rate and catchment area: the case of uplifted rivers in Eastern Scotland. Earth Surface Processes and Landforms, 30: 767-778.

Blythe, A.E., Burbank, D.W., Farley, K.A. and Fielding, E.J., 2000. Structural and topographic evolution of the central Transverse Ranges, California, from apatite fission-track, (U-Th)/He and digital elevation model analyses. Basin Research, 12: 97-114.

Crosby, B.T. and Whipple, K.X., in review. Knickpoint initiation and distribution within fluvial networks: 236 waterfalls in the Waipaoa River, North Island, New Zealand. Geomorphology.

Dadson, S.J. et al., 2003. Links between erosion, runoff variability and seismicity in the Taiwan orogen. Nature, 426: 648-651.

Gasparini, N., 2003. Equilibrium and transient morphologies of river networks: discriminating among fluvial erosion models. PhD Thesis, Massachusetts Institute of Technology, Cambridge, MA.

Gasparini, N.M., Bras, R.L. and Whipple, K., in review. The role of a sediment-flux-dependent erosion equation in transient bedrock river networks. In: S. Willett, N. Hovius, D. Fisher and M. Brandon (Editors), Penrose Special Paper: Tectonics, climate and landscape evolution. Geological Society of America, Boulder, CO.

Hartshorn, K., Hovius, N., Dade, W.B. and Slingerland, R.L., 2002. Climate-driven bedrock incision in an active mountain belt. Science, 297: 2036-2038.

Hovius, N., Stark, C.P., Chu, H.-T. and Lin, J.-T., 2000. Supply and removal of sediment in a landslide-dominated mountain belt; Central Range, Taiwan. Journal of Geology, 108: 73-89.

Howard, A.D. and Kerby, G., 1983. Channel changes in badlands. Geological Society of America Bulletin, 94: 739-752.

Howard, A.D., Seidl, M.A. and Dietrich, W.E., 1994. Modeling fluvial erosion on regional to continental scales. Journal of Geophysical Research, 99: 13,971-13,986.

Kirby, E. and Whipple, K.X., 2001. Quantifying differential rock-uplift rates via stream profile analysis. Geology, 29(5): 415-418.

Lave, J. and Burbank, D., 2004. Denudation processes and rates in the Transverse Ranges, southern California: Erosional response of a transitional landscape to external and anthropogenic forcing. Journal of Geophysical Research, 109: doi: 10.1029/2003JF000023.

Montgomery, D.R. and Foufoula-Georgiou, E., 1993. Channel network representation using digital elevation models. Water Resources Research, 29: 1178-1191.

Niemann, J.D., Gasparini, N.M., Tucker, G.E. and Bras, R.L., 2001. A quantitative evaluation of Playfair's law and its use in testing long-term stream erosion models. Earth Surface Processes and Landforms, 26(12): 1317-1332.

Rosenbloom, N.A. and Anderson, R.S., 1994. Hillslope and channel evolution in a marine terraced landscape, Santa Cruz, California. Journal of Geophysical Research, B, Solid Earth and Planets, 99(B7): 14,013-14,029.

Schaller, M. et al., in press. Fluvial bedrock incision in the active mountain belt of Taiwan from *in situ*-produced cosmogenic nuclides. Earth Surface Processes and Landforms.

Sklar, L. and Dietrich, W.E., 1998. River longitudinal profiles and bedrock incision models: Stream power and the influence of sediment supply. In: K.J. Tinkler and E.E. Wohl (Editors), Rivers Over Rock: Fluvial Processes in Bedrock Channels. AGU, Washington, D. C., pp. 237-260.

Sklar, L. and Dietrich, W.E., 2004. A mechanistic model for river incision into bedrock by saltating bed load. Water Resources Research, 40: doi; 10.1029/2003WR02496.

Slingerland, R. and Willett, S.D., 1999. Systematic slope-area functions in the Central Range of Taiwan may imply topographic unsteadiness. Geological Society of America, Abstracts with Programs, 31: 296.

Snyder, N., Whipple, K., Tucker, G. and Merritts, D., 2000. Landscape response to tectonic forcing: DEM analysis of stream profiles in the Mendocino triple junction region, northern California. Geological Society of America, Bulletin, 112(8): 1250-1263.

Snyder, N.P., Whipple, K.X., Tucker, G.E. and Merrits, D.J., 2003. Channel response to tectonic forcing: field analysis of stream morphology and hydrology in the Mendocino triple junction region, northern California. Geomorphology, 53: 97-127.

Snyder, N.P., Whipple, K.X., Tucker, G.E. and Merritts, D.M., 2002. Interactions between onshore bedrock-channel incision and nearshore wave-base erosion forced by eustacy and tectonics. Basin Research, 14: 105-127.

Spotila, J.A., House, M.A., Blythe, A.E., Niemi, N. and Bank, G.C., 2002. Controls on the erosion and geomorphic evolution of the San Bernardino and San Gabriel Mountains, southern California. Geological Society of America Special Paper 365: 205-230.

Stock, J.D. and Dietrich, W.E., 2003. Valley incision by debris flows: evidence of a topographic signature. Water Resources Research, 39(4): doi: 10.1029/2001WR001057.

Suppe, J., 1981. Mechanics of mountain building and metamorphism in Taiwan. Geological Society of China Memoir, 4: 67-89.

Teng, L.S., 1990. Geotectonic evolution of late Cenozoic arc-continent collision in Taiwan. Tectonophysics, 183: 57-76.

Tucker, G.E., 2004. Drainage basin sensitivity to tectonic and climatic forcing: Implications of a stochastic model for the role of entrainment and erosion thresholds. Earth Surface Processes and Landforms, 29: 185-205.

Tucker, G.E. and Whipple, K.X., 2002. Topographic outcomes predicted by stream erosion models: sensitivity analysis and intermodel comparison. Journal of Geophysical Research, 107(B9): doi:10.1029/2001JB000162.

Whipple, K., 2004. Bedrock rivers and the geomorphology of active orogens. Annual Reviews of Earth and Planetary Science, 32: 151-185.

Whipple, K., Kirby, E. and Brocklehurst, S., 1999. Geomorphic limits to climatically induced increases in topographic relief. Nature, 401: 39-43.

Whipple, K.X., 2001. Fluvial landscape response time: how plausible is steady-state denudation? American Journal of Science, 301: 313-325.

Whipple, K.X. and Meade, B.J., 2004. Controls on the strength of coupling among climate, tectonics and deformation in two-sided, frictional orogenic wedges at steady state. Journal of Geophysical Research-Earth Surface, 109: doi: 10.1029/2003JF000019.

Whipple, K.X. and Tucker, G.E., 1999. Dynamics of the stream-power river incision model: Implications for height limits of mountain ranges, landscape response timescales, and research needs. Journal of Geophysical Research, 104: 17661-17674.

Whipple, K.X. and Tucker, G.E., 2002. Implications of sediment-flux-dependent river incision models for landscape evolution. JGR, 107(B2): doi:10.1029/2000JB000044.

Wiberg, P.L. and Smith, J.D., 1985. A theoretical model for saltating grains in water. Journal of Geophysical Research, 90(C4): 7341-7354.

Willett, S.D. and Brandon, M.T., 2002. On steady states in mountain belts. Geology, 30(2): 175-178.

Willett, S.D., Fisher, D., Fuller, C.W., Yeh, E.C. and Lu, C.Y., 2003. Erosion rates and orogenic wedge kinematics in Taiwan inferred from apatite fission track thermochronometry. Geology, 31: 945-948.

Willgoose, G.R., Bras, R.L. and Rodriguez-Iturbe, I., 1991. A physically based coupled network growth and hillslope evolution model, 1, Theory. Water Resources Research, 27: 1671-1684.

Wobus, C. et al., in press. Tectonics from topography: procedures, promise and pitfalls. GSA Special Penrose volume on tectonics, climate and landscape evolution.

Wobus, C.W., Heimsath, A.M., Whipple, K.X. and Hodges, K.V., 2005. Active out-of-sequence thrust faulting in the central Nepalese Himalaya. Nature, 434: 1008-1011.

Figure Captions

1. Longitudinal profiles (black lines; left and bottom axes) and slope-area data (grey crosses; right and top axes) for trunk stream (Mill Creek) and three tributaries to the Big Tujunga river in the San Gabriel Mountains of southern California. Note that knickpoints on tributaries (vertical arrows) all lie near 1000m elevation (blue line), consistent with a constant vertical migration rate as predicted by a basin-wide knickpoint retreat model (Equation 3). Large step on trunk stream between Fox and Clear Creeks is an engineered dam. Green line: projection of upper Mill Creek to mountain front using eqn 1. Shift in slope-area data at ~3e6 m^2 corresponds to knickpoint on Mill Creek.

2. Map view of normalized steepness indices ($\theta_{ref} = 0.45$) in the Big Tujunga basin. The boundary between high and low steepness values lies close to a constant elevation contour, and the highest steepness indices, with few exceptions, are generally clustered in the lowermost portions of the drainage basin, consistent with a model of basin-wide knickpoint retreat.

3. Map of study area in northeastern Taiwan. A: Tectonic setting. PSP = Philippine Sea Plate; MT = Manila Trench; RT = Ryukyu Trench. Arrows in northeast corner of map show zone of extension behind Ryukyu Trench. Red box outlines extent of Figure 3B. B: Physiography of eastern Taiwan with outlines of the three basins studied. Figure 3A modified from Schaller et al. (in press).

4. Examples of the four categories of longitudinal profiles identified in northeastern Taiwan. a) shows longitudinal profiles of all categories in one basin. b-e show slope-area data from the four profiles. b) Graded profile. Note smooth transition and consistent steepness indices between tributary and trunk streams. c) Linear profile. Concavity is near zero from the tributary channel head to its mouth. d) Knickpoint in longitudinal profile. The tributary channel has a significant convexity along its course, but the steepness index below this knickpoint is within the range of values found in the trunk stream. e) Hanging valley. The tributary channel has a significant convexity near its mouth, and the steepness index is much

higher than that found in the trunk stream. For plots b through e, trunk stream is shown in: grey, tributary in black

5. Map view of normalized steepness indices ($\theta_{ref} = 0.45$) for the Liwu basin in Taiwan. Note that the highest steepness indices are almost all found in short segments at tributary mouths. Boundary between "adjusted" and "unadjusted" landscape corresponds very closely to gorge along trunk stream (dashed black line, with star marking upper limit of high steepness values in trunk), rather than working its way up the tributary basins as in the example from the San Gabriel Mountains (Figure 2).

6. Long profile view of five hanging valleys in the Liwu basin, with slope-area data from the trunk stream (black crosses) and from tributary #2 (red crosses). Green lines show approximate steepness values below (k_s~250) and above (k_s~135) knickpoint on trunk stream (star). Note that the channel gradient at the mouth of tributary #2 is much higher than would be predicted based on the gradients in the mainstem.

7. Photographs of two tributary mouths classified as hanging valleys in the Liwu basin. A = Tributary #3 from Liwu basin; B = Sanchan River ("San" on Figure 5). Note the presence of waterfall plunge pool erosion in both channels. Upstream knickpoint migration rate should therefore be limited by the rock strength at the waterfall lip, and by the ability of these rivers to remove large boulders downstream of the plunge pool.

8. Schematic showing the expected relationship between transport stage and erosion rate based on the work of Sklar and Dietrich (2004). This relationship predicts that erosion rates will begin to fall as channel gradients increase to drive transport stage above a critical value.

9. Schematic showing the growth of hanging valleys through time, in extreme case with no response of tributary upstream of the knickpoint. An incisional pulse traveling up the mainstem oversteepens the tributary so that erosion rates fall at the tributary mouth. Once this threshold condition has been exceeded at the tributary mouth, further lowering in the mainstem increases the height of the hanging valley through time. Gradients along

oversteepened reaches are lower for larger tributaries than for smaller ones, and may relax with time.

10. Plot of channel gradient vs. upstream drainage area for oversteepened reaches at the mouths of tributary channels in the Liwu, Mukua and Hoping basins. Drainage area dependence of channel gradient for these oversteepened reaches suggests that the larger streams maintain a greater capacity to erode despite the process transition at the tributary mouth.

11. Plot of tributary vs trunk stream drainage area at each classified tributary junction for the Mukua, Liwu and Hoping basins. Symbols represent the style of tributary adjustment based on observations from long profile and slope-area data. Note that hanging valleys are clustered at small tributary drainage areas (< 2e7) or large trunk to tributary drainage area ratios (> 10:1), with numerous false positives in either case.

12. Longitudinal profile view of tributary junction classifications for A) Hoping, B) Liwu and C) Mukua basins. Symbols are the same as those in Figure 11. Note that many of the adjusted profiles with drainage area < 2e7 are found above knickpoints in the trunk streams.

13. Planview map of tributary junction classifications superimposed on geologic map of Taiwan. Hanging valley development does not appear to be strongly controlled by lithology. However, linear profiles (interpreted as reflecting dominant debris-flow erosion, Stock and Dietrich, 2003) appear to be most common in the foliated metasedimentary rocks, suggesting that the mechanism of erosion for a given tributary basin may be lithologically controlled.

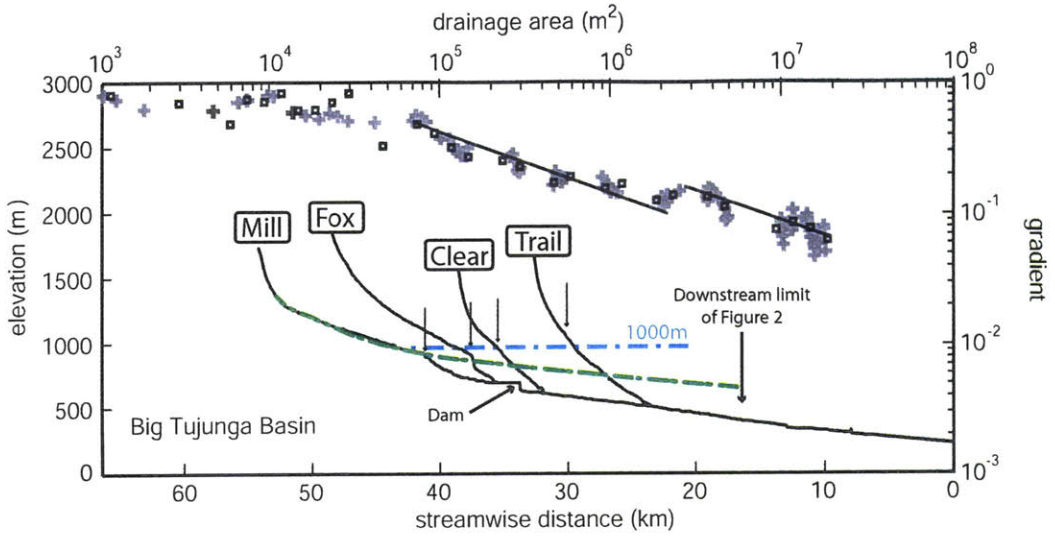

Wobus et al., Figure 1

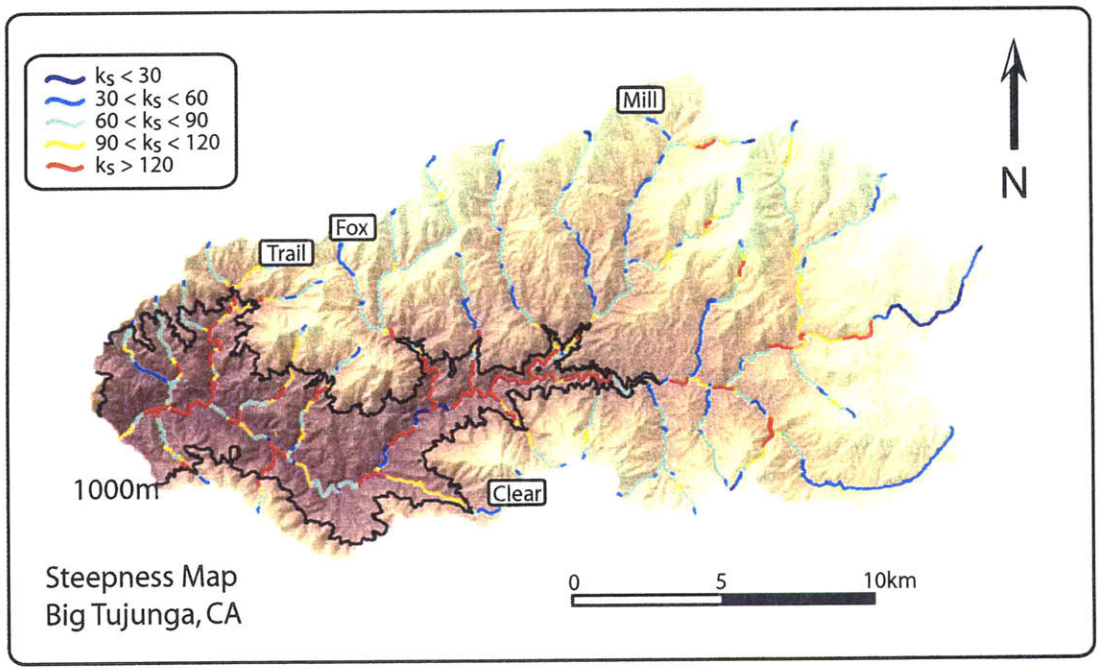

Wobus et al., Figure 2

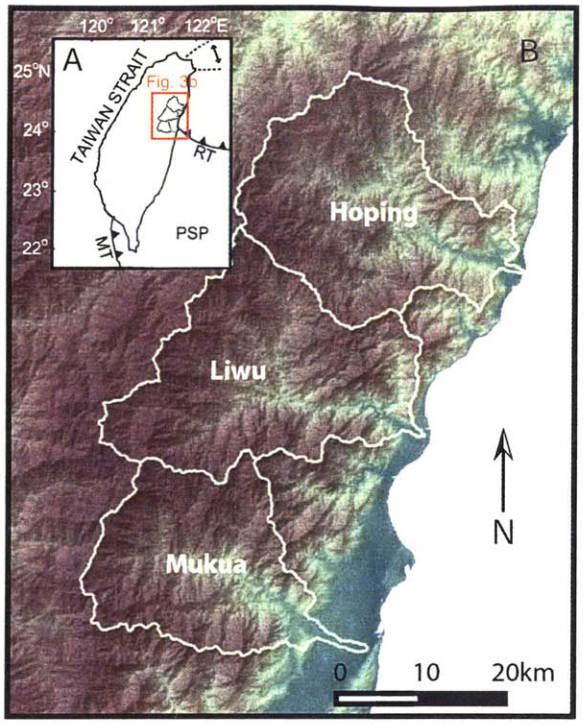

Wobus et al., Figure 3

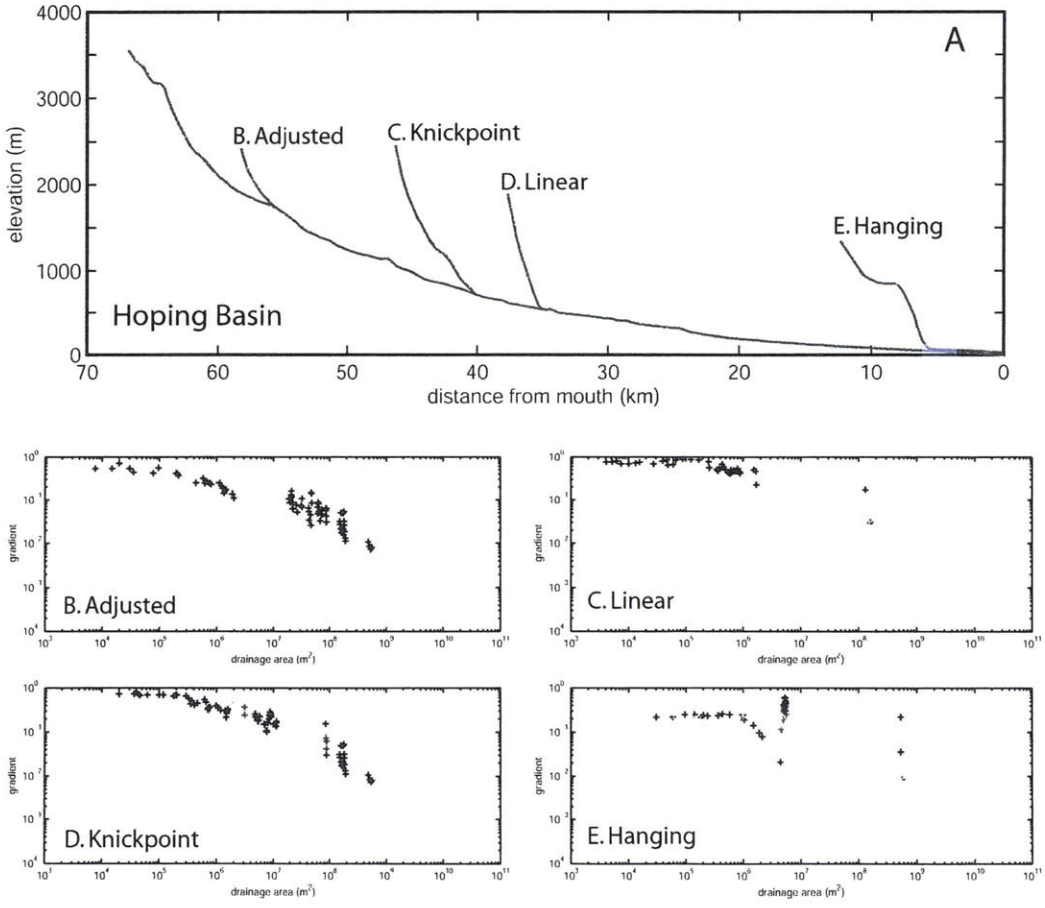

Wobus et al., Figure 4

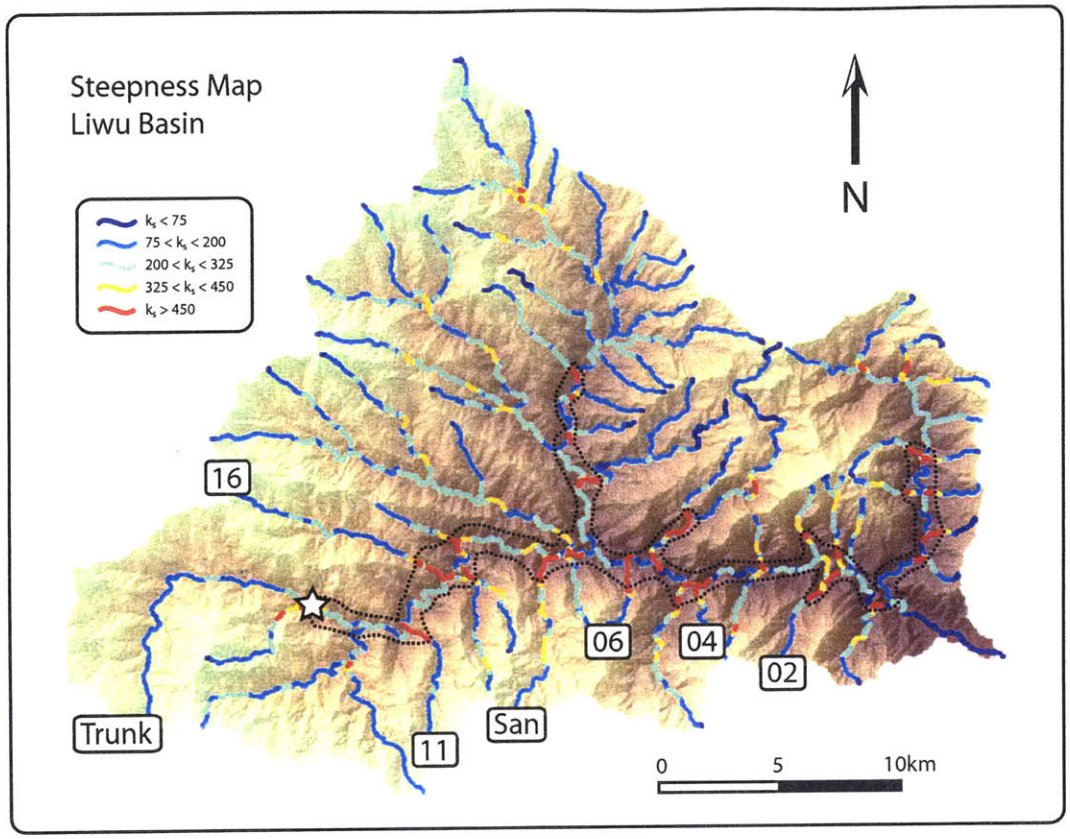

Wobus et al., Figure 5

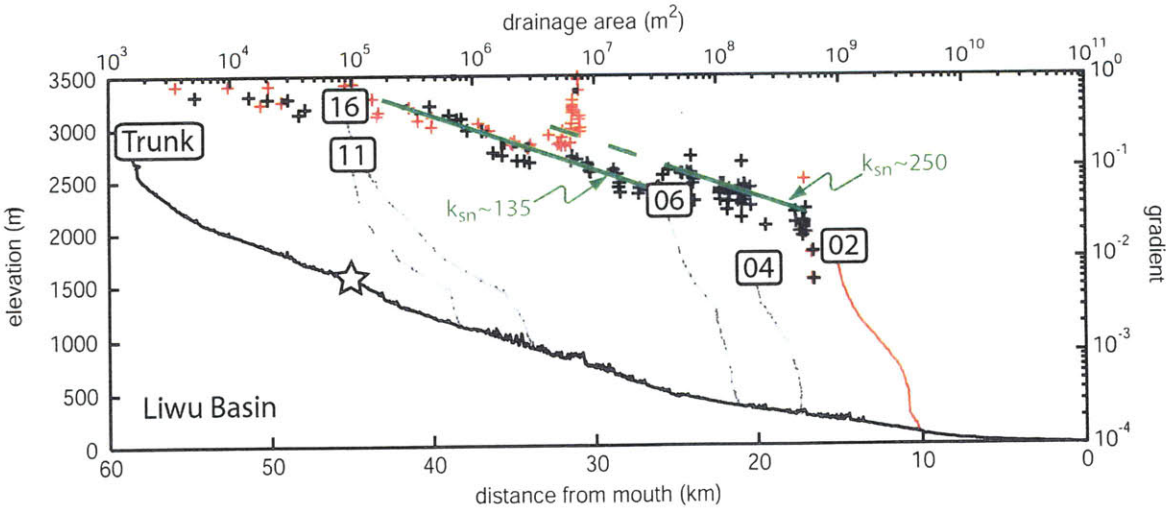

Wobus et al., Figure 6

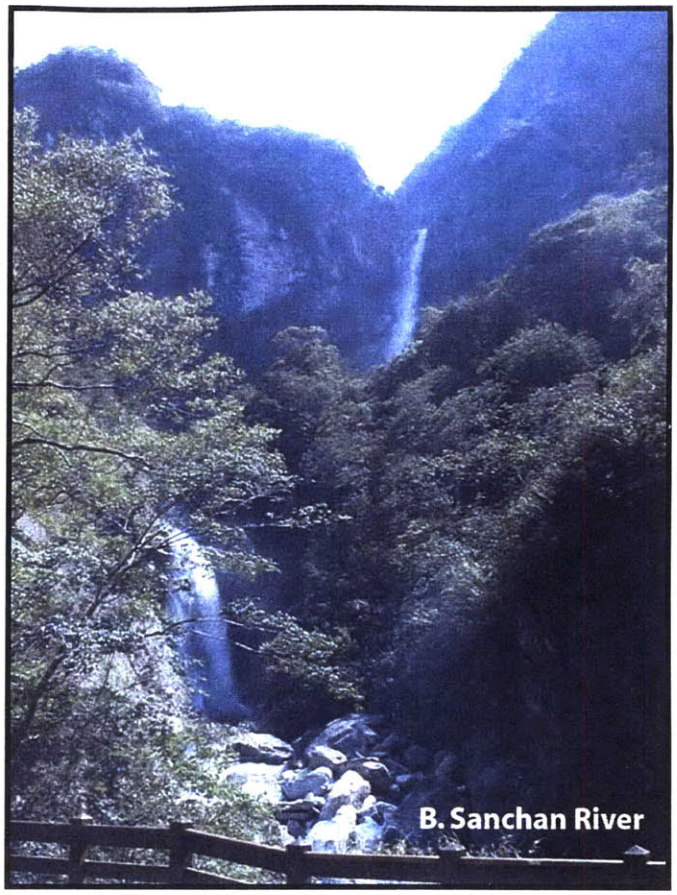

Wobus et al., Figure 7

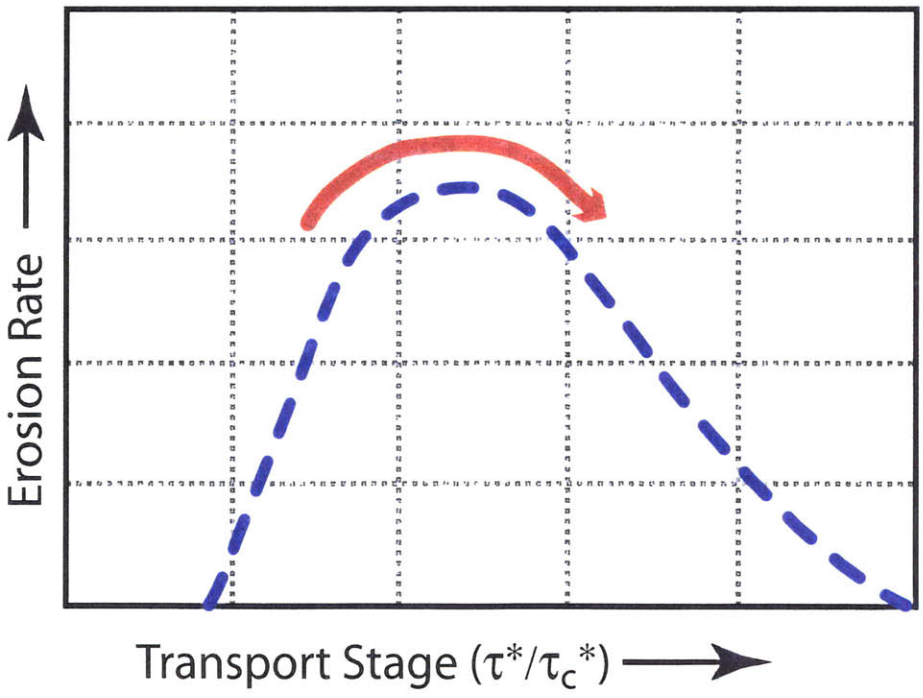

Wobus et al., Figure 8

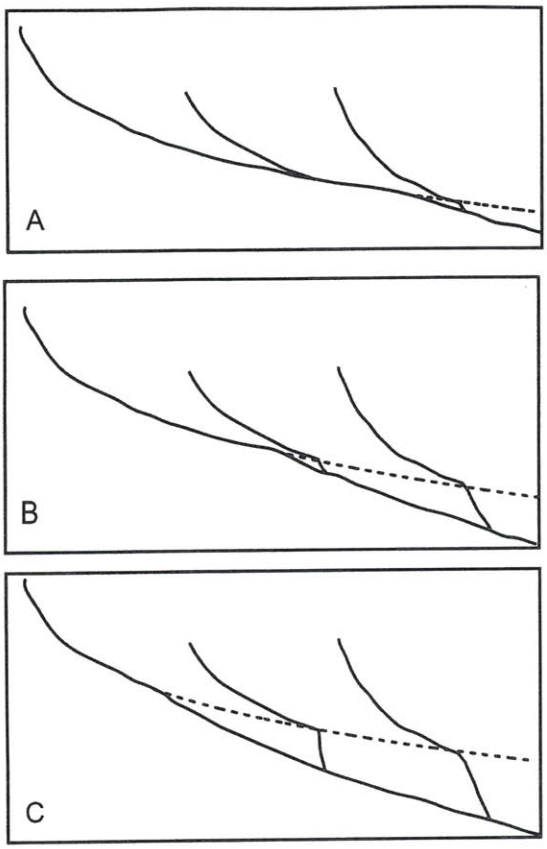

Wobus et al., Figure 9

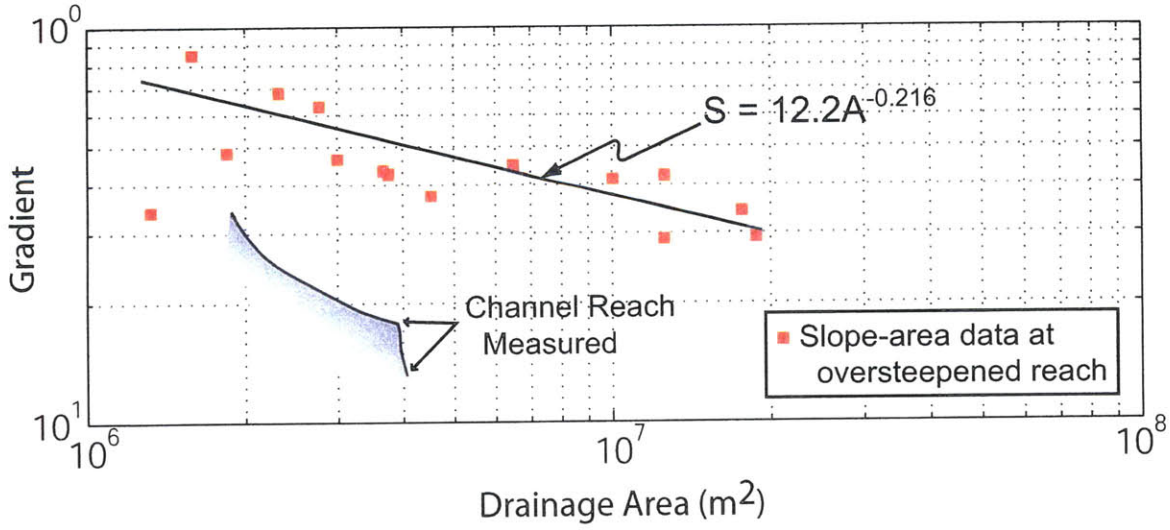

Wobus et al., Figure 10

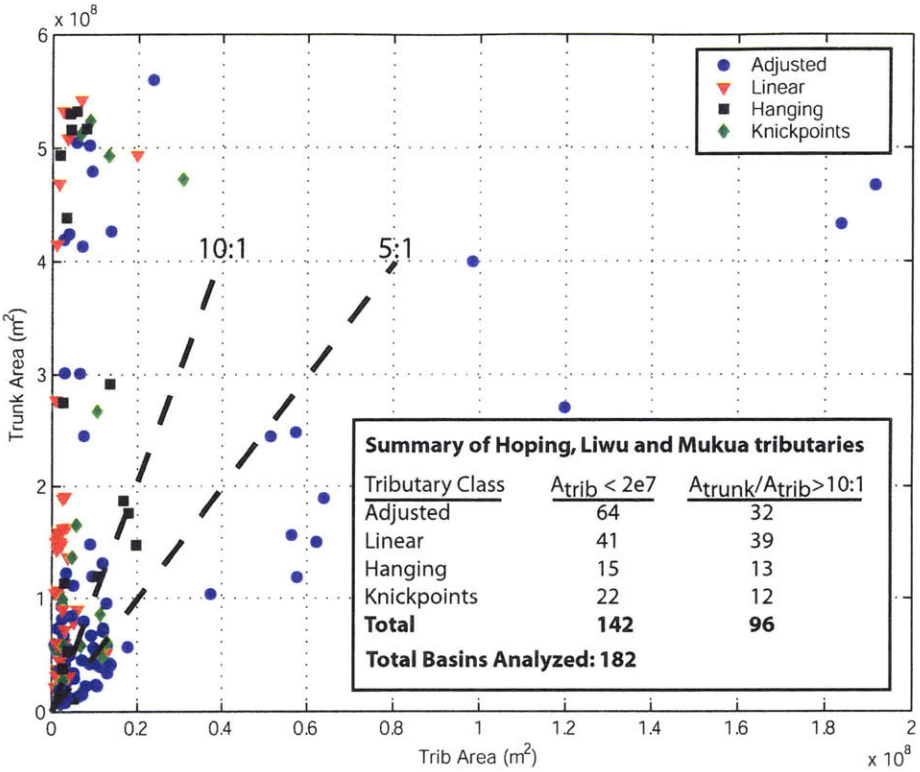

Wobus et al., Figure 11

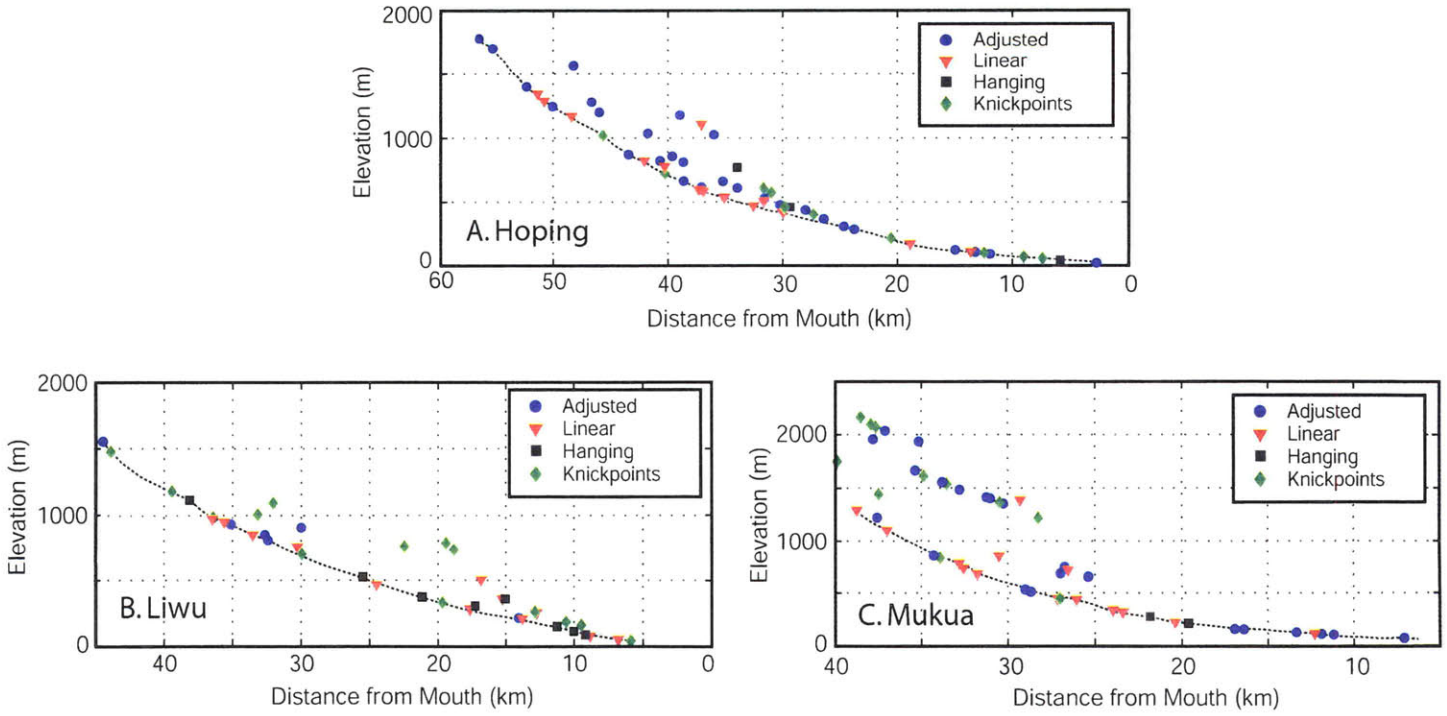

Wobus et al., Figure 12

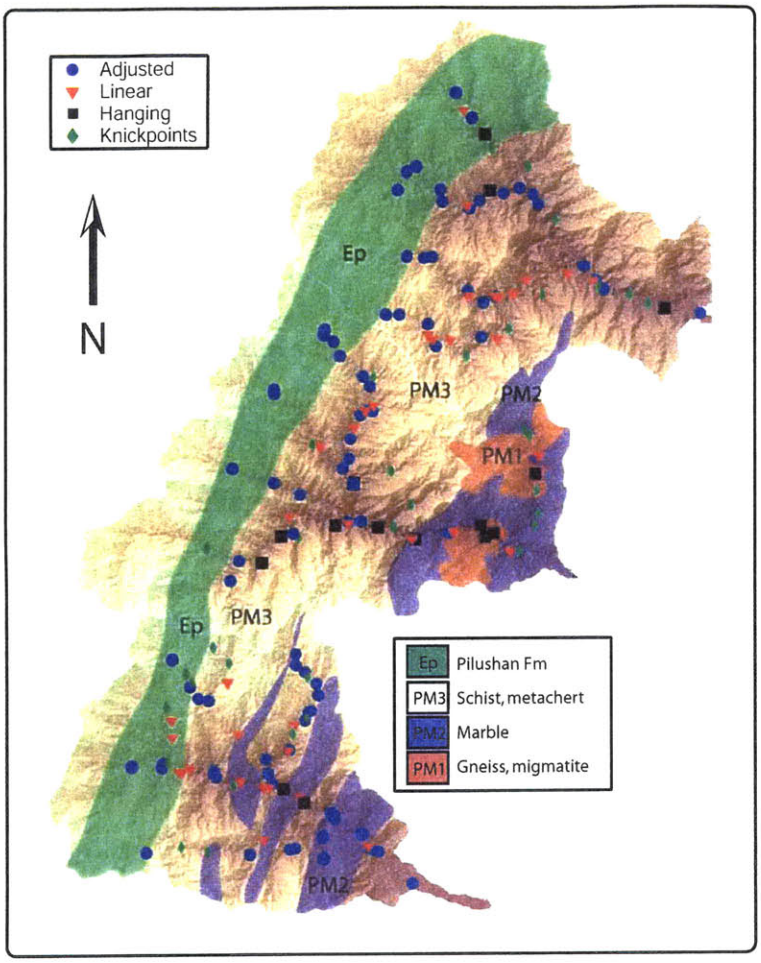

Wobus et al., Figure 13

Chapter 4: Has focused denudation sustained active thrusting at the Himalayan topographic front?

Cameron W. Wobus
Kip V. Hodges
Kelin X. Whipple

Department of Earth, Atmospheric and Planetary Sciences
Massachusetts Institute of Technology, Cambridge, Massachusetts 02139, USA

Published in October, 2003 issue of *Geology* (v. 31, p. 861-864).

Abstract

The geomorphic character of major river drainages in the Himalayan foothills of central Nepal suggests the existence of a discrete, west-northwest trending break in rock-uplift rates that does not correspond to previously mapped faults. $^{40}Ar/^{39}Ar$ thermochronologic data from detrital muscovites with provenance from both sides of the discontinuity indicate that this geomorphic break also corresponds to a major discontinuity in cooling ages: samples to the south are Proterozoic to Paleozoic, whereas those to the north are Miocene and younger. Combined, these observations virtually require recent (Pliocene–Holocene) motion on a thrust-sense shear zone in the central Nepal Himalaya, ~20–30 km south of the Main Central Thrust. Field observations are consistent with motion on a broad shear zone subparallel to the fabric of the Lesser Himalayan lithotectonic sequence. The results suggest that motion on thrusts in the toe of the Himalayan wedge may be synchronous with deeper exhumation on more hinterland structures in central Nepal. We speculate that this continued exhumation in the hinterland may be related to intense, sustained erosion driven by focused orographic precipitation at the foot of the High Himalaya.

1. Introduction

Recent geodynamic modeling of orogenic growth has led to the provocative hypothesis that erosion may exert first-order control on orogen-scale tectonics (e.g., Beaumont et al., 2001). However, direct field evidence of this feedback is not easily obtained. Here we present evidence for recent thrusting in the Himalayan hinterland at the position of the major topographic break between the physiographic lesser and higher Himalaya. Combined with evidence for Pliocene activity on the Main Central Thrust (e.g., Harrison et al., 1997; Catlos et al., 2001; Robinson et al., 2003), our data imply sustained out-of-sequence thrusting that is suggestive of a direct link between tectonics and the monsoon-driven erosion of the High Himalaya.

We utilize the geomorphology of the Burhi Gandaki and Trisuli watersheds in central Nepal—derived from a 90 m DEM (digital elevation model) and observations on the ground—to identify breaks in hillslope, valley, and channel morphologies that may reflect unmapped, active structures in this area. All of the geomorphic observations suggest a narrowly distributed decrease in rock uplift rates from north to south, centered ~20–30 km south of the Main Central Thrust zone. $^{40}Ar/^{39}Ar$ thermochronologic data from detrital muscovites also indicate a major break in cooling ages at this location, implying a significant change in exhumation rates across a 10-km-wide zone. The simplest explanation for all of the data is a tectonic model including Pliocene–Holocene thrusting on a surface-breaking shear zone near the base of the High Himalaya in central Nepal.

2. Geologic Setting

The Burhi Gandaki and Trisuli rivers carve through the High Himalaya ~80 km northwest of Kathmandu, Nepal (Fig. 1). Their upper reaches traverse primarily Neoproterozoic rocks of the Tibetan Sedimentary Sequence, which are bounded at their base by predominantly normal-sense structures of the South Tibetan fault system. Downstream (south) of the South Tibetan fault system, and for most of their courses, the rivers carve steep-walled gorges through the high-grade metamorphic core of the range, represented by the Greater Himalayan Sequence. The Greater Himalayan Sequence is bounded at its base by the Main Central Thrust zone, a crustal-scale feature that can be traced nearly the entire length of the Himalayan orogen (e.g., Hodges, 2000). In the footwall of the Main Central Thrust zone, the rivers traverse the Lesser Himalayan Sequence, which is dominated in central Nepal by phyllites, quartzites, psammites, and metacarbonates of the Kuncha Formation (e.g., Stöcklin, 1980). Recent studies suggest that there may be significant repetition of the Kuncha section along foliation-parallel thrusts (e.g., DeCelles et al., 2001).

The steep-walled gorges typical of the Greater Himalayan Sequence persist within the Lesser Himalayan Sequence for ~20–30 km south of the Main Central Thrust zone. Both rivers then cross a prominent physiographic transition, uncorrelated with any mapped structures or change in rock type, which is referred to as physiographic transition 2 (PT_2) by Hodges et al. (2001). PT_2 is characterized by a number of changes in landscape morphology, including (1) a change from narrow, steep-walled gorges in the north to wide, alluviated valleys in the south; (2) an abrupt decrease in hillslope gradient from north to south (Fig. 1); (3) an abrupt transition from fresh, landslide-covered hillslopes in the north to deeply weathered, red soils on hillslopes and channel banks; (4) an abrupt appearance from north to south of thick (up to 200 m) fluvial fill

terraces in both drainages; and (5) an abrupt decrease in channel gradient from north to south, discussed in more detail later in the paper. All of these observations suggest a profound and narrowly distributed decrease in the rates of denudation from north to south.

Noting the existence and position of this physiographic transition throughout the Himalaya, Seeber and Gornitz (1983) suggested that it may be indicative of recent movement on the Main Central Thrust system. However, this interpretation runs counter to the generally agreed upon developmental sequence for major thrust-fault systems in the Himalaya. For example, the Main Central Thrust system is thought to have been active at ca. 30–23 Ma, with shortening progressing southward to the Main Boundary Thrust system in late Miocene–Pliocene time and to the Main Frontal Thrust system in Pliocene–Holocene time (e.g., Hodges, 2000). Implicit in this model is the assumption that the Main Central Thrust became inactive as deformation stepped southward.

With this assumption, tectonic models of the Nepal Himalaya typically invoke a ramp-flat geometry on the basal décollement, or Himalayan Sole Thrust, to explain the prominent physiographic transition (e.g., Cattin and Avouac, 2000) (Fig. 2A). Alternatively, PT_2 may be an expression of recent motion on the Main Central Thrust through much of Nepal (e.g., Seeber and Gornitz, 1983), or on unmapped structures farther to the south in the Burhi Gandaki and Trisuli watersheds (Fig. 2B). Such "out-of-sequence" thrusting is relatively common in fold-and-thrust belts, and is predicted by many kinematic models as a way of preserving the critical taper of accretionary wedges with strong erosion gradients between the foreland and the hinterland (e.g., Dahlen and Suppe, 1988). Data from microseismicity and geodetics have been invoked as evidence for the ramp-flat model (e.g., Pandey et al., 1999; Bilham et al., 1997); however, these data are equally consistent with surface breaking structures at PT_2. Thermochronologic and

thermobarometric data suggest varied types of activity on the Main Central Thrust as recently as the early Pliocene, lending additional support to the hypothesis of "reactivated" hinterland structures (e.g., Macfarlane et al., 1992; Harrison et al., 1997; Catlos et al., 2001).

If PT_2 marks the locus of out-of-sequence thrusting rather than the position of a buried ramp in the Himalayan Sole Thrust, PT_2 would be expected to correspond with an abrupt change in rock uplift rates. In the following sections, a combination of stream-profile analysis and $^{40}Ar/^{39}Ar$ thermochronology is used to test this prediction.

3. Methods and Results

3.1 Stream Profiles

In a variety of natural settings, empirical data from river channels exhibit a scaling in which local channel slope can be expressed as a power-law function of contributing drainage area (e.g., Howard and Kerby, 1983). Previous work suggests that the pre-exponential factor in this function—referred to as the steepness coefficient (k_s)—is positively correlated with the rock uplift rate U (e.g., Snyder et al., 2000). The exponent on drainage area—referred to as the concavity index (θ)—typically falls in a narrow range between 0.3 and 0.6, but may approach much higher values in zones of distributed uplift (e.g., Snyder et al., 2000; Kirby and Whipple, 2001). We stress that our quantitative understanding of feedbacks related to changes in channel width, hydraulic roughness, the quantity and caliber of abrasive tools, and the relative importance of various erosive processes remains limited (e.g., Lavé and Avouac, 2001; Sklar and Dietrich, 1998; Whipple et al., 2000). Moreover, we note that k_s also depends on many factors including rock strength and climate, limiting our ability to derive quantitative estimates of uplift rates from slope vs. area data. However, where rock erodibility is nearly invariant and climatic

variability is smooth, abrupt changes in k_s may be confidently interpreted as reflecting a change in rock uplift rate.

Channel slope and drainage area data were extracted for 56 tributaries in the study area from a 90 m DEM of central Nepal. Using a reference concavity of 0.45 (e.g., Snyder et al., 2000), steepness coefficients derived from logarithmic plots of slope vs. area range from 84 to 560 $m^{0.9}$. Channels whose sources lie below PT_2 typically have uniformly low steepness values. Channels crossing PT_2 typically have low steepness values in the lowest reaches and approach the upper envelope of k_s values above PT_2. The trans-Himalayan trunk streams, including the Burhi Gandaki and Trisuli main stems, have high steepness values in their middle reaches, bounded above and below by sections having lower steepness (see Fig. DR-1[1]). In plan view, the boundary between high and low k_s values is nearly coincident with the break in hillslope gradients illustrated in Figure 1, suggesting that hillslopes and river channels may each be responding to a decrease in rock uplift rates from north to south (Fig. 3A). Although the Lesser Himalayan Sequence in the field area varies locally among phyllites, psammites, and metacarbonates, no systematic changes in rock character were observed at PT_2 in any of the drainages, suggesting that the transition from high to low steepness values is not a result of a change in rock erodibility (e.g., Snyder et al., 2000).

3.2 $^{40}Ar/^{39}Ar$ Thermochronology

Eight detrital samples were collected from small tributaries to the Burhi Gandaki for muscovite $^{40}Ar/^{39}Ar$ thermochronology (Fig. 3A). Selected tributary basins were oriented subparallel to PT_2 and the overall structural grain, ensuring that the sediment from each sample was derived from a similar tectonostratigraphic position. Basins were typically 20–25 km^2, with

maximum across-strike basin widths ranging from 2 to 5 km. The northernmost sample was collected from the Burhi Gandaki trunk stream, to provide a view of cooling histories upstream of the Main Central Thrust. Sampling locations span a distance of 47 km, as projected onto a line oriented at 19° east of north (approximately parallel to section A–A' in Fig. 1).

Muscovites were separated by standard mineral-separation techniques prior to irradiation at the McMaster University nuclear reactor in Ontario, Canada. For each sample, 20–80 aliquots of muscovite were analyzed by laser microprobe, each consisting of between 1 and 20 grains. Many of the smaller aliquots had low radiogenic yields and therefore high uncertainties. Analyses reported here are limited to those with >50% radiogenic yield, reducing the total number of reported analyses to between 18 and 68. Complete data are available in the Data Repository (see footnote 1).

Figure 3B shows the normalized probability-density functions (PDFs) of sample ages plotted against distance from PT_2. South of PT_2, dates range from Mesoproterozoic to Paleozoic, with an apparent trend toward older ages from north to south. This trend may reflect partial loss of radiogenic ^{40}Ar from samples near PT_2 due to footwall heating beneath a thin thrust sheet in the early stages of Main Central Thrust development (e.g., Arita et al., 1997). Argon release spectra from bedrock samples south of PT_2 and in the Kathmandu nappe are consistent with this hypothesis (e.g., Copeland et al., 1991; personal communication). North of PT_2, nearly all dates are Miocene or younger. The ~400 Ma break in cooling ages at PT_2 suggests a major discontinuity in rock uplift rates across the physiographic transition. Furthermore, the age distributions south of PT_2 require that none of the samples below PT_2 have experienced prolonged heating above ~350 °C during Himalayan orogenesis. This result seems inconsistent with tectonic models that require prolonged transport of the Main Central Thrust hanging wall

over a ramp on the Himalayan Sole Thrust, with a geometry as envisioned by Pandey et al. (1999) or Cattin and Avouac (2000).

3.3 Field Observations

Limited outcrop in the field area and a lack of marker beds in the Kuncha Formation phyllites limit our ability to constrain unequivocally the position of a thrust at PT_2. Any new thrusts in this setting are also likely to be parallel to—and thus difficult to deconvolve from—the more pervasive Himalayan fabric (nominally west-northwest- trending and dipping north at 30°–50°). Despite these limitations, however, a number of structural observations are consistent with the presence of a surface-breaking thrust at PT_2, including (1) numerous small-scale shear zones subparallel to and crosscutting the structural grain within the Kuncha Formation phyllites, (2) hydrothermal activity in tributary valleys along PT_2, and (3) large-scale changes in bedrock attitudes in available outcrop at the scale of tens to hundreds of meters.

4. Discussion and Conclusions

All of the data indicate a major change in rock uplift rates and thermal history in central Nepal, centered ~20–30 km south of the Main Central Thrust. The tectonic picture that emerges for central Nepal is therefore one in which activity at the frontal thrusts today (e.g., Main Boundary Thrust and Main Frontal Thrust) may be synchronous with motion on structures farther hinterland (e.g., Main Central Thrust and at PT_2). Previous work has suggested that modern activity on or near the Main Central Thrust may be favored by extreme topographic gradients between the Tibetan plateau and the Indian foreland (e.g., Hodges et al., 2001; Grujic et al., 2002). In central Nepal, the Main Central Thrust forms a major reentrant to the north, in

contrast to its more linear trend farther to the west (see Fig. 1). This geometric relationship may have favored the initiation of a new shear zone at PT_2, parallel to the regional trend of the Main Central Thrust and the pervasive structural grain.

Intense precipitation at the southern front of the High Himalaya is also likely to play a role in the kinematics of the Himalayan fold-and-thrust belt, and may have been important in maintaining a locus of active thrusting at PT_2 (e.g., Dahlen and Suppe, 1988). As the summer monsoons approach the Tibetan plateau, orographic focusing of precipitation results in strong north-south gradients in rainfall, which increases surface denudation rates on the windward side of the range. Coupled with extreme topographic gradients and continued convergence between India and Eurasia, this strong precipitation may have resulted in sustained focusing of exhumation along the metamorphic core of the Himalaya (e.g., Beaumont et al., 2001), rather than a complete transfer of shortening to the Main Boundary Thrust and Main Frontal Thrust. The combined geomorphic, thermochronologic, and field evidence for an active shear zone at the foot of the Himalaya may therefore provide evidence for erosionally driven rock uplift at the orogen scale.

ACKNOWLEDGMENTS

We thank F. Pazzaglia and P. DeCelles for constructive reviews of the original manuscript. Thanks also to B. Crosby, K. Ruhl, T. Schildgen, and N. Wobus for assistance in the field. Logistical support was provided by Himalayan Experience. Work was supported by NSF grant #EAR-008758.

References

Arita, K., Dallmeyer, R. D., and Takasu, A., 1997, Tectonothermal evolution of the Lesser Himalaya, Nepal: Constraints from $^{40}Ar/^{39}Ar$ ages from the Kathmandu Klippe: The island arc, v. 6, p. 372-384.

Beaumont, C., Jamieson, R.A., Nguyen, M.H., and Lee, B., 2001, Himalayan tectonics explained by extrusion of a low-viscosity crustal channel coupled to focused surface denudation: Nature, v. 414, p. 738–742.

Bilham, R., Larson, K., Freymuller, J., and Members, P.I., 1997, GPS measurements of present-day convergence across the Nepal Himalaya: Nature, v. 386, p. 61–64.

Catlos, E. J., Harrison, T. M., Kohn, M. J., Grove, M., Ryerson, F. J., Manning, C. E., and Upreti, B. N., 2001, Geochronologic and thermobarometric constraints on the evolution of the Main Central Thrust, central Nepal Himalaya: Journal of Geophysical Research, v. 106, no. B8, p. 16177-16204.

Cattin, R., and Avouac, J.P., 2000, Modeling mountain building and the seismic cycle in the Himalaya of Nepal: Journal of Geophysical Research, v. 105, p. 13,389–13,407.

Colchen, M., Le Fort, P., and Pêcher, A., 1986, Recherches géologiques dans l'Himalaya du Népal, Annapurna–Manaslu–Ganesh Himal: Paris, Centre National de la Recherche Scientifique, 136 p.

Copeland, P., Harrison, T.M., Hodges, K.V., Maruejol, P., Le Fort, P., and Pecher, A., 1991, An early Pliocene thermal disturbance of the Main Central Thrust, central Nepal: Implications for Himalayan tectonics: Journal of Geophysical Research, v. 96, p. 8475–8500.

Dahlen, F.A., and Suppe, J., 1988, Mechanics, growth, and erosion of mountain belts, in Clark, S.P.J., et al., eds., Processes in continental lithospheric deformation: Geological Society of America Special Paper 218, p. 161–178.

DeCelles, P. G., Robinson, D. M., Quade, J., Ojha, T. P., Garzione, C. N., Copeland, P., and Upreti, B. N., 2001, Stratigraphy, structure, and tectonic evolution of the Himalayan fold-thrust belt in western Nepal: Tectonics, v. 20, p. 487-509.

Grujic, D., Hollister, L.S., and Parrish, R.R., 2002, Himalayan metamorphic sequence as an orogenic channel: Insight from Bhutan: Earth and Planetary Science Letters, v. 198, p. 177–191.

Harrison, T.M., Ryerson, F.J., Le Fort, P., Yin, A., Lovera, O., and Catlos, E.J., 1997, A late Miocene–Pliocene origin for the central Himalayan inverted metamorphism: Earth and Planetary Science Letters, v. 146, p. E1–E7.

Hodges, K.V., 2000, Tectonics of the Himalaya and southern Tibet from two perspectives: Geological Society of America Bulletin, v. 112, p. 324–350.

Hodges, K.V., Hurtado, J.M., and Whipple, K.X., 2001, Southward extrusion of Tibetan crust and its effect on Himalayan tectonics: Tectonics, v. 20, p. 799–809.

Howard, A.D., and Kerby, G., 1983, Channel changes in badlands: Geological Society of America Bulletin, v. 94, p. 739–752.

Kirby, E., and Whipple, K.X., 2001, Quantifying differential rock-uplift rates via stream profile analysis: Geology, v. 29, p. 415–418.

Lavé, J., and Avouac, J.P., 2001, Fluvial incision and tectonic uplift across the Himalayas of central Nepal: Journal of Geophysical Research, v. 106, p. 26,561–26,591.

Macfarlane, A., Hodges, K.V., and Lux, D., 1992, A structural analysis of the Main Central thrust zone, Langtang National Park, central Nepal Himalaya: Geological Society of America Bulletin, v. 104, p. 1389–1402.

Pandey, M.R., Tandukar, R.P., Avouac, J.P., Vergne, J., Heritier, T., Le Fort, P., and Upreti, B.N., 1999, Seismotectonics of the Nepal Himalaya from a local seismic network: Journal of Asian Earth Sciences, v. 17, p. 703–712.

Robinson, D. M., DeCelles, P. G., Garzione, C. N., Pearson, O. N., Harrison, T. M., and Catlos, E. J., 2003, Kinematic model for the Main Central Thrust in Nepal: Geology, v. 31, p. 359-362.

Searle, M.P., Parrish, R.R., Hodges, K.V., Hurford, A., Ayres, M.W., and Whitehouse, M.J., 1997, Shisha Pangma leucogranite, South Tibetan Himalaya: Field relations, geochemistry, age, origin, and emplacement: Journal of Geology, v. 105, p. 295–317.

Seeber, L., and Gornitz, V., 1983, River profiles along the Himalayan arc as indicators of active tectonics: Tectonophysics, v. 92, p. 335–367.

Sklar, L., and Dietrich, W.E., 1998, River longitudinal profiles and bedrock incision models: Stream power and the influence of sediment supply, in Tinkler, K.J., and Wohl, E.E., eds., Rivers over rock: Fluvial processes in bedrock channels: American Geophysical Union Geophysical Monograph 107, p. 237–260.

Snyder, N., Whipple, K., Tucker, G., and Merritts, D., 2000, Landscape response to tectonic forcing: DEM analysis of stream profiles in the Mendocino triple junction region, northern California: Geological Society of America Bulletin, v. 112, p. 1250–1263.

Stöcklin, J., 1980, Geology of Nepal and its regional frame: Geological Society [London] Journal, v. 137, p. 1–34.

Whipple, K.X., Hancock, G.S., and Anderson, R.S., 2000, River incision into bedrock: Mechanics and relative efficacy of plucking, abrasion, and cavitation: Geological Society of America Bulletin, v. 112, p. 490–503.

Figure Captions

Figure 1. Site location map (inset) and slope map for study area. PT_2 is prominent break in hillslope gradient between yellow arrows. Structural and lithotectonic units: TSS—Tibetan Sedimentary Sequence; GHS—Greater Himalayan Sequence; LHS—Lesser Himalayan Sequence; STF—South Tibetan fault system; MCT—Main Central Thrust; MBT—Main Boundary Thrust. Rivers: BG—Burhi Gandaki; TR—Trisuli; BK—Bhote Kosi. Section A–A' is shown in Figure 2. Fault locations approximated from Colchen et al. (1986), Searle et al. (1997), Macfarlane et al. (1992), and Hodges (2000).

Figure 2. Two interpretations of Holocene tectonics of central Nepal. MFT—Main Frontal Thrust; HST—Himalayan Sole Thrust; MT—Mahabarat Thrust; KTM—Kathmandu. Other locations and structural units explained in Figure 1 caption. A: Passive transport over ramp in Himalayan Sole Thrust explains uplift gradients beneath PT_2; modern shortening is accommodated at toe of range (southwest end of cross section). B: Thrusting at Main Central Thrust continues today, stepping forward to PT_2 in study area. Deep exhumation is confined to zone between South Tibetan fault system and PT_2, and décollement beneath Kathmandu is entirely thin-skinned.

Figure 3. A: Distribution of k_s values for channel segments in study area (see text). Black arrows show position of PT_2, as in Figure 1. Rivers: BG—Burhi Gandaki; TR—Trisuli; TH—Thopal Khola; BA—Balephi Khola. Long profiles are available (see footnote 1 in text). White dots along Burhi Gandaki trunk stream show sediment sampling locations. B: Distribution of muscovite $^{40}Ar/^{39}Ar$ cooling ages for sediment samples. Apparent ages (y-axis) are plotted on log scale for ease of presentation; peak of distribution for sample 01WBS7 is ~400 m.y. younger than peak for 01WBS8. Note tail on 01WBS7 distribution, indicating an input of older material and possibly presence of both hanging-wall and footwall rocks from a surface-breaking thrust within this catchment. Normalized probabilities (z-axis) illustrate relative abundances of ages from each sample.

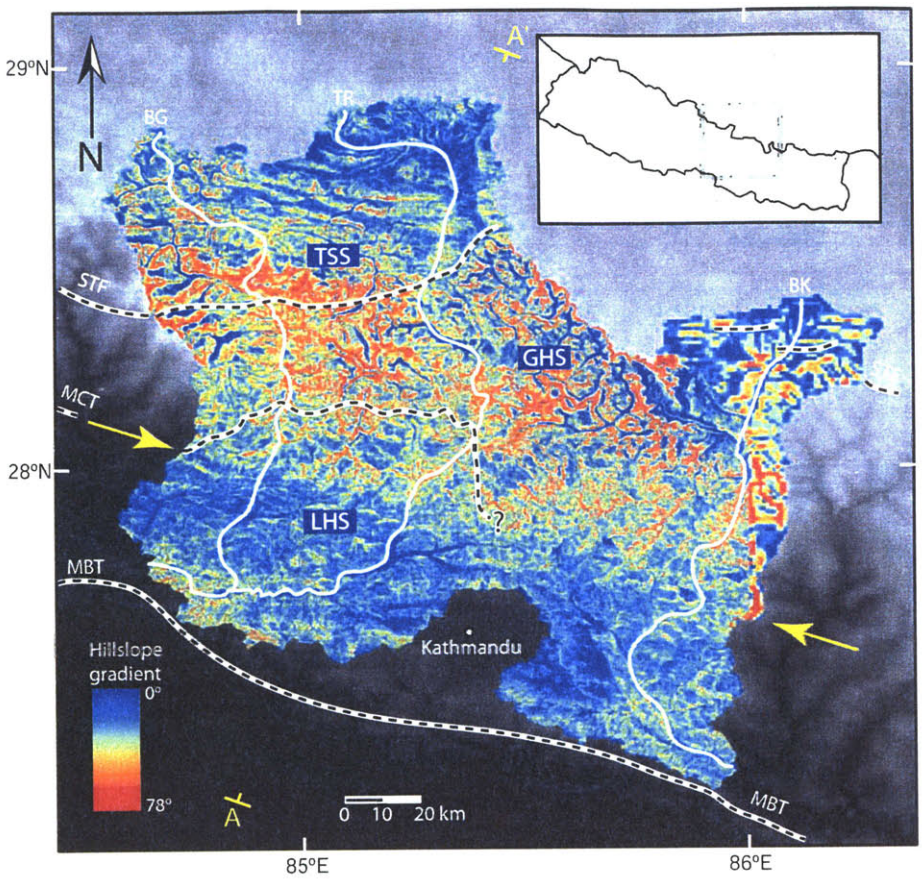

Wobus et al., Figure 1

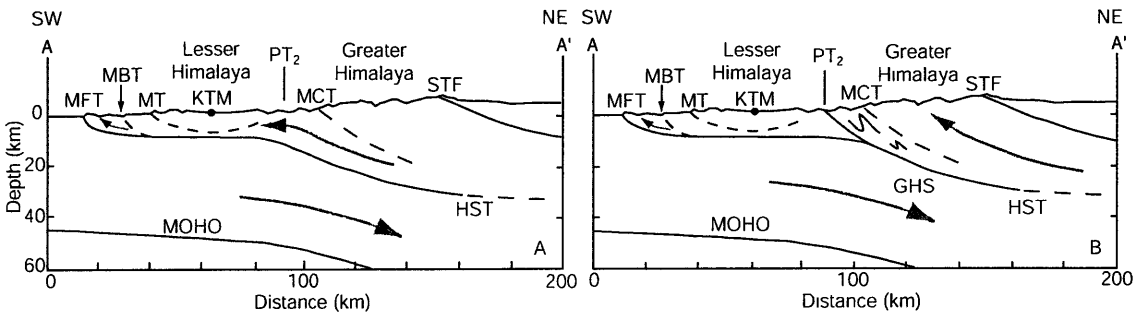

Wobus et al., Figure 2

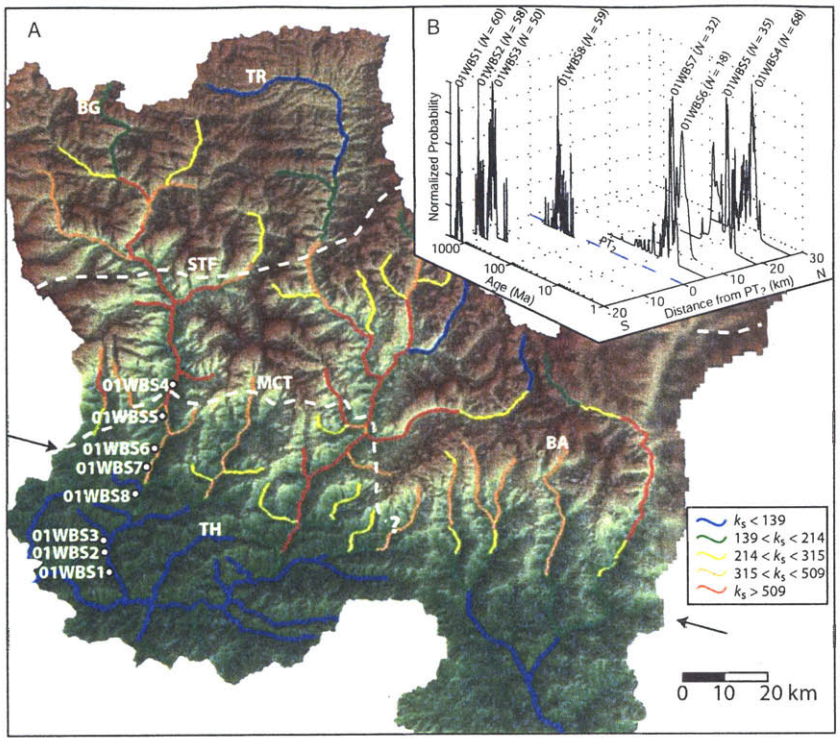

Wobus et al., Figure 3

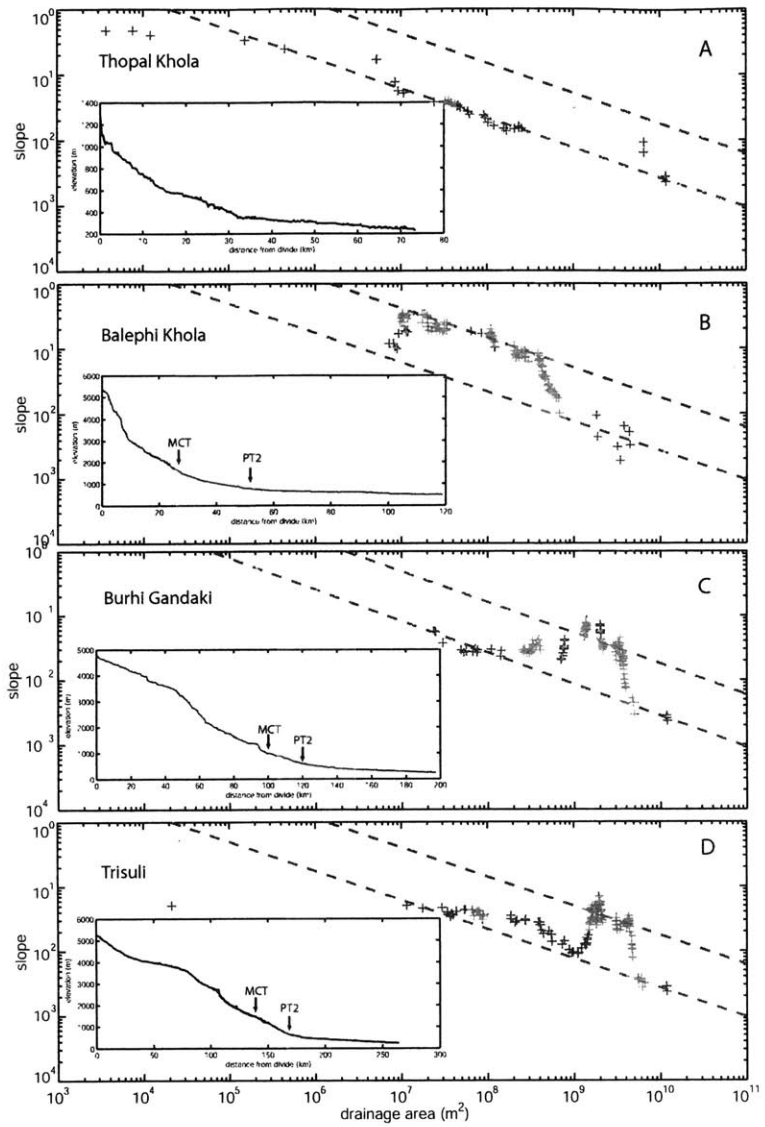

Figure DR-1: Stream profiles from four representative tributaries in central Nepal. A: Thopal Khola, sourced below PT2; B: Balephi Khola, sourced above PT2; C: Burhi Gandaki trunk stream, sourced above STF. D: Trisuli trunk stream, sourced above STF Dashed lines show upper and lower bounds of steepness values for a reference concavity of 0.45, determined from superposition of all data from the 56 tributaries analyzed (see text). Grey bands in Balephi, Burhi Gandaki and Trisuli rivers show zones of locally high concavity, interpreted as the distance over which rock uplift rates are increasing across PT2. Location of channel heads for stream profiles are shown in Figure 3.

Wobus et al., Figure DR-1

Table DR-1
40Ar/39Ar Data for Detrital Muscovites
Burhi Gandaki River - Sample 01WBS1

Analysis Number	$^{36}Ar/^{40}Ar$ $(x10^{-5})^{++}$	$^{39}Ar/^{40}Ar$ $(x10^{-3})^{++}$	$^{39}Ar_K$ $(x10^{-16}$ mol$)^{**}$	$^{40}Ar^*$ $(\%)^{\#}$	Age $(Ma)^{\$}$
1	2.53 (1.41)	1.45 (0.008)	5.065	99.3	1456.17 ± 8.88 (5.31)
2	0.02 (2.47)	1 43 (0.001)	3.643	100.0	1478.16 ± 7.21 (0.61)
3	0.55 (1.91)	1.39 (0.002)	4.820	99.8	1509.76 ± 7.51 (1.82)
4	13.81 (2.11)	1.48 (0.000)	5.999	95.9	1403.26 ± 6.95 (0.14)
5	22.16 (3.20)	1.58 (0.005)	3.988	93.5	1316.55 ± 7.49 (3.44)
6	12.33 (3.08)	1.61 (0.009)	7.292	96.4	1328.79 ± 8.49 (5.22)
7	15.79 (2.99)	1.72 (0.006)	6.092	95.3	1258.47 ± 7.31 (3.44)
8	18.47 (1.60)	1.56 (0.010)	4.741	94.5	1338.43 ± 9.10 (6.12)
9	26.70 (5.23)	1.73 (0.015)	3.620	92.1	1221.21 ± 10.58 (8.48)
10	19.73 (1.74)	1.36 (0.004)	3.853	94.2	1468.69 ± 7.68 (2.79)
11	2.94 (5 43)	1.34 (0.004)	3.810	99.1	1537 21 ± 8.07 (3 29)
12	1.94 (2.62)	1.59 (0.009)	4.964	99.4	1368.79 ± 8.59 (5.20)
13	2.41 (1 32)	1.64 (0.007)	5.727	99 3	1335.67 ± 7.83 (4 02)
14	3.64 (3.04)	1.29 (0.009)	3.545	98.9	1571.75 ± 10.72 (7.68)
15	4.34 (4.12)	1.25 (0.007)	3.679	98.7	1604.37 ± 9.43 (5.62)
16	3.70 (2.13)	1.24 (0.010)	2.392	98.9	1616.35 ± 11.49 (8.62)
17	4.64 (3.31)	1.30 (0.006)	4.029	98.6	1565 26 ± 8.97 (4.98)
18	5.95 (5.40)	1.40 (0.005)	2.850	98.2	1483.80 ± 8.25 (4.03)
19	3.24 (3.00)	1.48 (0.005)	4.068	99.0	1433.53 ± 7.91 (3.59)
20	4.39 (3.47)	1 56 (0.013)	4.726	98.7	1377.53 ± 10.40 (7.82)
21	5.69 (2.04)	1.46 (0.023)	7.312	98.3	1439.18 ± 17.31 (15.80)
22	0.04 (2.16)	1.46 (0.004)	7.159	100.0	1455.94 ± 7.65 (2.80)
23	0.37 (0.91)	1.57 (0 016)	6.656	99.9	1384.63 ± 12.09 (9.93)
24	0.22 (1.29)	1.59 (0.033)	5.816	99.9	1371.95 ± 20.84 (19.68)
25	0.34 (3.00)	1.55 (0.016)	5.999	99.9	1400.33 ± 12.24 (10.08)
26	7.20 (1.78)	1.52 (0.024)	5.906	97.9	1398.05 ± 16.89 (15.40)
27	0.18 (2.25)	1.56 (0.021)	6.291	99.9	1395.05 ± 14.96 (13.26)
28	6.81 (2.74)	1.68 (0.039)	6.962	98.0	1305.65 ± 22.83 (21.84)
29	0.26 (2.06)	1.47 (0.018)	5.648	100.0	1451.87 ± 14.33 (12.44)
30	1.87 (2.71)	1.62 (0.040)	4.982	99.4	1351.03 ± 24.36 (23.40)
31	2.32 (1.60)	1 44 (0.021)	4.853	99.3	1464.00 ± 16.38 (14.74)
32	3.25 (2.67)	1.54 (0.047)	4.026	99.0	1393.27 ± 30.72 (29.93)
33	1.75 (1.83)	1.44 (0.025)	4.719	99.5	1463.49 ± 18.59 (17.17)
34	4.66 (0.76)	1.41 (0.005)	3.753	98.6	1479.65 ± 8.22 (3.99)
35	2 63 (3.53)	1.49 (0.026)	5.754	99.2	1429.37 ± 18 58 (17.20)
36	4.74 (0.68)	1.53 (0.018)	5.743	98.6	1401.00 ± 13.51 (11.59)
37	1.85 (3.04)	1.40 (0.017)	6.676	99.5	1491.90 ± 14 51 (12.58)
38	2.15 (3.24)	1.49 (0.029)	3.830	99.4	1433.82 ± 20.47 (19.21)
39	3 03 (3 26)	1.42 (0.014)	4.877	99.1	1477.40 ± 12.29 (9.97)
40	3.02 (5.15)	1.35 (0.002)	3.019	99.1	1529.79 ± 7.60 (1.95)
41	13.14 (2.77)	1.46 (0.018)	4.437	96 1	1418.76 ± 14 56 (12.76)
42	13.44 (2.90)	1.44 (0.028)	4.296	96.0	1431.52 ± 21.13 (19.92)
43	15.65 (5.42)	1.39 (0.021)	3.558	95.4	1459.53 ± 17 39 (15.86)
44	10.18 (1.92)	1.40 (0.016)	5.543	97.0	1472.71 ± 13.89 (11.90)
45	15.07 (1.80)	1.35 (0.008)	3.587	95.5	1494.86 ± 9.54 (6.22)
46	9.02 (1.34)	1 35 (0.003)	6.032	97.3	1513.85 ± 7.60 (2.13)
47	15.63 (4.58)	1.43 (0.017)	3.639	95.4	1431.53 ± 14.16 (12.29)
48	19 30 (3 12)	1.58 (0.004)	3.238	94.3	1326.00 ± 7.33 (2.99)
49	11 32 (2 51)	1.46 (0.011)	5.126	96.7	1427.07 ± 10.45 (7.73)
50	16.05 (2.49)	1.48 (0 009)	3.683	95.3	1393.63 ± 9.09 (5.90)
51	12.56 (4.55)	1 48 (0.013)	4.613	96.3	1405.88 ± 11.46 (9.11)
52	15.76 (5.14)	1.49 (0.002)	3.690	95.3	1389.99 ± 7.10 (1.64)
53	18.40 (3.84)	1.23 (0.002)	2.642	94.6	1574.48 ± 7.80 (2.21)
54	0 20 (2.88)	1 26 (0.007)	4.680	100.0	1614.93 ± 9.64 (5.93)
55	11.65 (4.01)	1.54 (0.011)	5.248	96.6	1371.17 ± 9.72 (6.91)
56	15.08 (3.16)	1.38 (0.012)	3.585	95.5	1465.76 ± 11.86 (9.46)
57	13.05 (2.93)	1.46 (0.014)	4.361	96.1	1422.05 ± 12 38 (10.20)
58	10.51 (1.10)	1.41 (0.006)	5.235	96.9	1458.26 ± 8.56 (4.75)
59	18 62 (4.00)	1.06 (0.010)	2.231	94.5	1736.08 ± 13.45 (10.85)
60	16.25 (5.33)	1.15 (0.006)	2.776	95.2	1652.34 ± 9.48 (5.52)

Table DR-1
40Ar/39Ar Data for Detrital Muscovites
Burhi Gandaki River - Sample 01WBS2

Analysis Number	$^{36}Ar/^{40}Ar$ $(x10^{-5})^{++}$	$^{39}Ar/^{40}Ar$ $(x10^{-3})^{++}$	$^{39}Ar_K$ $(x10^{-16}\ mol)^{**}$	$^{40}Ar^*$ (%)#	Age (Ma)$
1	3.86 (3.44)	1.71 (0.011)	4.924	98.9	1292.90 ± 8.78 (5.81)
2	23.60 (12.85)	2.82 (0.022)	1.714	93 0	845 87 ± 7.47 (5 72)
3	3.06 (2.51)	1.70 (0.008)	5 175	99.1	1300.42 ± 7.89 (4.33)
4	2.65 (1.84)	1.47 (0.006)	6.288	99.2	1440.70 ± 8.16 (4.07)
5	2.55 (1.19)	1.78 (0 008)	7 802	99.2	1260.67 ± 7 65 (4 09)
6	2.65 (3 13)	2.33 (0.018)	9 452	99.2	1034.70 ± 8.39 (6 23)
7	3.04 (2.71)	1.71 (0.014)	5.312	99 1	1297.72 ± 10.08 (7.63)
8	4.24 (1 81)	2.02 (0 007)	7.681	98.7	1147.66 ± 6 80 (3 10)
9	2 85 (3 87)	1.63 (0.005)	8.386	99.2	1341.57 ± 7.44 (3.14)
10	3.20 (0.77)	2.43 (0 007)	12 496	99 1	999 17 ± 5.85 (2.08)
11	20.82 (3.45)	1.96 (0.007)	5.194	93.8	1128.85 ± 6.86 (3.37)
12	14.72 (2.57)	1.87 (0.008)	6 994	95 6	1185 31 ± 7.30 (3.86)
13	1.42 (1.36)	1.97 (0 015)	7.540	99.6	1174.83 ± 9.16 (6.79)
14	2.34 (2.30)	1 98 (0.013)	6.065	99.3	1167.95 ± 8.47 (5.85)
15	16.30 (2.53)	1.87 (0 024)	6.344	95.2	1180 95 ± 13.40 (11.89)
16	11.11 (2.51)	2.11 (0 007)	10.500	96.7	1092 59 ± 6 41 (2 64)
17	0.63 (0.93)	2.16 (0.014)	6.961	99.8	1099.60 ± 7.83 (5.19)
18	16 07 (2.55)	2.36 (0.020)	8.105	95.3	991.51 ± 8.77 (6.88)
19	19.15 (2.48)	2.12 (0 010)	6 127	94.3	1067 92 ± 6 95 (3.92)
20	14.67 (4.81)	2.25 (0.017)	8.483	95.7	1031 69 ± 8 46 (6.34)
21	6 83 (1 01)	1.85 (0.000)	9.548	98.0	1215.25 ± 6.30 (0.10)
22	9 31 (3 66)	1.66 (0.026)	6.238	97 2	1307.07 ± 16.59 (15.21)
23	8.47 (1.93)	1.99 (0.030)	8.311	97.5	1148.33 ± 14.29 (12.95)
24	6.84 (1 33)	1 89 (0.000)	9.764	98.0	1195.52 ± 6.23 (0.14)
25	8.82 (2.08)	1.79 (0.018)	7.156	97 4	1239.23 ± 11.24 (9.26)
26	0.37 (0.90)	1.52 (0 039)	7.772	99.9	1418.96 ± 26 17 (25.22)
27	10.83 (3 76)	1 71 (0.014)	5.555	96.8	1277 78 ± 10.31 (7.98)
28	0 06 (1.57)	1.57 (0 010)	6 596	100 0	1388.64 ± 9.32 (6 26)
29	10.00 (2.53)	1.54 (0.016)	5.388	97.0	1376.81 ± 12 40 (10 33)
30	9.94 (2 07)	1 63 (0.035)	5.730	97.1	1323.07 ± 21 76 (20 71)
31	13.43 (4.24)	1 36 (0.008)	3.162	96.0	1489.57 ± 9.47 (6.13)
32	6 02 (1.48)	1.83 (0.000)	9 422	98.2	1228.89 ± 6.35 (0.13)
33	0.77 (0.59)	1.68 (0 000)	8 636	99 8	1322 94 ± 6.68 (0.17)
34	8.95 (1.49)	1 62 (0 012)	5.567	97 4	1330 35 ± 9.69 (7.00)
35	10 44 (1 61)	1.68 (0 033)	4.963	96.9	1291.05 ± 19 78 (18.66)
36	9 62 (2.23)	1.59 (0.010)	5 087	97.2	1348.23 ± 8 98 (5 90)
37	10 82 (3.30)	1.58 (0 061)	4.516	96 8	1350 35 ± 38.44 (37.84)
38	7.34 (3.01)	1 65 (0.015)	6.921	97.8	1320.82 ± 10.79 (8.48)
39	7.72 (0.81)	1.50 (0.015)	5.989	97.7	1405.88 ± 11.90 (9.66)
40	9.39 (2 03)	1.71 (0 016)	7.412	97.2	1279 01 ± 10 76 (8 55)
41	17.19 (1 78)	1 43 (0.006)	3.373	94.9	1424.44 ± 8.13 (4.10)
42	11.33 (3.91)	1.67 (0 027)	5 996	96 7	1294.86 ± 16.70 (15 35)
43	10.29 (1.36)	1.68 (0.031)	6.633	97.0	1292 35 ± 18.52 (17 31)
44	12 69 (2.05)	1 36 (0.017)	4.330	96.2	1491.37 ± 14.71 (12.81)
45	8 52 (1.46)	1.75 (0.019)	8 321	97.5	1261 59 ± 11.88 (9 97)
46	9 00 (1.59)	1.75 (0 014)	7.900	97.3	1257.36 ± 10.00 (7.64)
47	9.24 (2.76)	1.63 (0 003)	7.145	97.3	1322.57 ± 6.98 (2.04)
48	13.62 (3.23)	1 59 (0.011)	4 702	96 0	1337.33 ± 9.67 (6.95)
49	11.96 (1 67)	1.71 (0 072)	5 046	96 5	1274 95 ± 40.36 (39.83)
50	8.46 (2.54)	1.65 (0.014)	6.884	97 5	1316.36 ± 10.65 (8 32)
51	12.69 (2.10)	1.67 (0.009)	4.663	96.2	1293.23 ± 8.24 (4.96)
52	12 29 (3.80)	1.81 (0 036)	5.202	96 4	1221.03 ± 19.42 (18.36)
53	1.26 (1.05)	1.61 (0 028)	6.582	99.6	1360.47 ± 17 95 (16 61)
54	10 04 (3.20)	1 57 (0.043)	5.527	97.0	1356.57 ± 27 71 (26.87)
55	7 63 (2 23)	1.64 (0.036)	7.594	97.7	1323.08 ± 21.94 (20 90)
56	10 03 (1.31)	1.60 (0.031)	5.692	97.0	1339.35 ± 20 22 (19 07)
57	13.52 (3 17)	1 52 (0.019)	3.994	96.0	1376.81 ± 14 50 (12.78)
58	8.84 (1 34)	1.80 (0.047)	7 194	97 4	1235 67 ± 25.05 (24.22)

Table DR-1
40Ar/39Ar Data for Detrital Muscovites
Burhi Gandaki River - Sample 01WBS3

Analysis Number	$^{36}Ar/^{40}Ar$ $(x10^{-5})^{++}$	$^{39}Ar/^{40}Ar$ $(x10^{-3})^{++}$	$^{39}Ar_K$ $(x10^{-16}\ mol)^{**}$	$^{40}Ar^*$ $(\%)^{\#}$	Age $(Ma)^{\$}$
1	12.00 (2.74)	2.41 (0.009)	8.837	96.5	972.55 ± 14.29 (2.98)
2	8.46 (1.60)	2.39 (0.039)	12.455	97.5	986.35 ± 18.91 (12.59)
3	11.93 (1.89)	4.74 (0.004)	17.482	96.5	559.30 ± 8 95 (0.46)
4	0.48 (1.34)	2.57 (0.004)	10.811	99.9	950.70 ± 13.77 (1.02)
5	1.11 (1.78)	5.63 (0 014)	18.444	99.7	495.97 ± 8.13 (1.09)
6	14.56 (3.70)	2.36 (0.019)	7.108	95.7	983.03 ± 15.53 (6.54)
7	1.23 (4.82)	2.91 (0.012)	9 652	99 6	860 61 ± 13.04 (2.88)
8	0.16 (1.54)	2.91 (0.006)	8.250	100.0	862.32 ± 12.81 (1.35)
9	0.62 (1.56)	1.86 (0.009)	9.268	99.8	1214.79 ± 16.99 (4.33)
10	2.77 (1.80)	2.61 (0.016)	11.446	99.2	933.51 ± 14.29 (4.55)
11	0.15 (2.95)	1.95 (0.005)	6.411	100.0	1175.46 ± 16.18 (2.05)
12	18.99 (4.32)	1.82 (0.009)	4.808	94.4	1183.62 ± 16.78 (4.64)
13	16.37 (4.10)	2.00 (0.007)	6.092	95.2	1111.07 ± 15.76 (3.27)
14	0.43 (2.45)	1.80 (0.007)	6.984	99.9	1241.60 ± 17.05 (3.51)
15	0.20 (3.81)	2.52 (0.030)	6.915	100.0	967.85 ± 16.48 (8.82)
16	18.68 (2.90)	2.38 (0.013)	6.442	94.5	966.00 ± 14.51 (4.17)
17	12.47 (0.94)	2.59 (0.000)	13.307	96.3	919.99 ± 13.39 (0.15)
18	1.57 (3.35)	1.92 (0.001)	7.791	99.5	1183.86 ± 16.14 (0.35)
19	2.02 (3.33)	2.17 (0.017)	6.989	99.4	1079.51 ± 16.34 (6.24)
20	0.58 (2.97)	3.01 (0.011)	7.660	99.8	839.81 ± 12.71 (2.42)
21	1.91 (0.91)	2.90 (0.000)	14.978	99.4	860.84 ± 12.72 (0.10)
22	0.02 (3.96)	2.11 (0.033)	6.203	100.0	1104.72 ± 20.07 (12.92)
23	3.95 (2.21)	2.10 (0.008)	5.536	98.8	1099.90 ± 15.61 (3.06)
24	11.23 (2.27)	2.24 (0.009)	6.141	96.7	1031.97 ± 14.93 (3.10)
25	2.54 (2.65)	2.05 (0.011)	6.215	99.2	1123.95 ± 16.22 (4.63)
26	2.68 (1.50)	2.37 (0.018)	8.580	99.2	1007.88 ± 15.46 (5.75)
27	12.74 (2.91)	2.66 (0.026)	6.465	96.2	898.28 ± 14.95 (7.12)
28	1.58 (3.62)	2.37 (0.026)	7.503	99.5	1009.85 ± 16.68 (8.46)
29	2.07 (3.39)	2.61 (0.007)	11.246	99 4	935.10 ± 13.70 (1.96)
30	0.92 (2.62)	1.79 (0.018)	8.634	99.7	1246.85 ± 19.07 (9.16)
31	0.08 (1.97)	2.39 (0.017)	7.576	100.0	1008.24 ± 15 33 (5.40)
32	10 91 (2 64)	1.88 (0.021)	6.875	96.8	1178.41 ± 18.86 (9.85)
33	10.02 (2.07)	2.23 (0.008)	8.970	97.0	1037.88 ± 14.95 (2.90)
34	14.82 (3 05)	2.28 (0.014)	6.165	95.6	1007.79 ± 15.21 (5 04)
35	12.32 (2.77)	1.93 (0.014)	6.278	96.4	1148.50 ± 16.95 (6.16)
36	15.55 (4.21)	1.97 (0.008)	5 081	95.4	1124.40 ± 15.98 (3.68)
37	9.38 (1.51)	2.22 (0.014)	9.515	97.2	1044.43 ± 15.58 (5.07)
38	11.96 (3.43)	2.40 (0.009)	8.001	96.5	976.87 ± 14 32 (2.94)
39	13.54 (2.89)	2.07 (0.015)	6.159	96.0	1088.63 ± 16 36 (6.08)
40	12.41 (3.82)	2.05 (0.010)	6.593	96.3	1099.62 ± 15.81 (3.99)
41	0.91 (4.42)	3.10 (0.054)	9.294	99.7	819.46 ± 16.78 (11.47)
42	0.27 (2.24)	2.03 (0.001)	6.556	99.9	1137.79 ± 15.69 (0.44)
43	1.32 (0.64)	2.18 (0.013)	11.432	99.6	1075.62 ± 15.82 (4.85)
44	0.47 (1.48)	2.28 (0.000)	11.743	99.9	1043.50 ± 14.73 (0.10)
45	0.02 (1.13)	3.01 (0.025)	11.516	100.0	841.24 ± 13.72 (5.66)
46	1.93 (2.66)	2 64 (0.024)	10.549	99.4	928.19 ± 15.01 (6.59)
47	1.50 (1.45)	2.77 (0.006)	9.721	99.6	895.05 ± 13.20 (1.52)
48	2.54 (1.12)	2.85 (0.019)	8.948	99.2	873.80 ± 13.66 (4.57)
49	1.41 (1.90)	2.53 (0.015)	12.267	99.6	961.70 ± 14.53 (4.37)
50	2.07 (4.71)	2 35 (0.006)	8.360	99.4	1016.79 ± 14.59 (2.03)

Table DR-1
40Ar/39Ar Data for Detrital Muscovites
Burhi Gandaki River - Sample 01WBS4

Analysis Number	$^{36}Ar/^{40}Ar$ $(x10^{-4})^{++}$	$^{39}Ar/^{40}Ar$ $(x10^{-1})^{++}$	$^{39}Ar_K$ $(x10^{-15}$ mol$)^{**}$	$^{40}Ar^*$ $(\%)^{\#}$	Age $(Ma)^{\$}$
1	2.96 (2.01)	5.31 (0.096)	29.732	91.0	5.53 ± 0.39 (.38)
2	6.31 (1.47)	4.02 (0.081)	45.192	81.2	6.51 ± 0 40 (38)
3	9.64 (2.48)	3.83 (0 052)	29.038	71 4	6.01 ± 0.63 (.62)
4	10.13 (2.95)	3.88 (0.029)	25.871	69.9	5 81 ± 0 73 (.72)
5	11 73 (2.39)	3.57 (0.024)	21.843	65 2	5.90 ± 0 65 (.64)
6	7.71 (0.75)	3.66 (0.022)	48.025	77.1	6.78 ± 0.24 (.2)
7	11 27 (3.14)	3 65 (0.061)	38.780	66.6	5 88 ± 0.84 (83)
8	12 60 (1.98)	3.15 (0.059)	37.903	62 7	6.41 ± 0.63 (.62)
9	16.10 (1.41)	2.92 (0 081)	27 779	52.4	5 78 ± 0.54 (53)
10	6.67 (10.14)	4 61 (0.262)	17.137	80.1	5 60 ± 2.13 (2.12)
11	0.12 (7.17)	3.97 (0 215)	20.022	99 4	8.06 ± 1.77 (1.76)
12	14 77 (9.24)	2.99 (0.118)	13.471	56 3	6.07 ± 2.96 (2 96)
13	3.47 (7.40)	4.61 (0 202)	19 543	89.5	6.27 ± 1.56 (1 55)
14	0.66 (6.22)	3.11 (0.027)	11.322	97.9	10.13 ± 1.90 (1.89)
15	5.81 (4.65)	4.82 (0.223)	46.171	82 6	5 53 ± 0.97 (96)
16	5.74 (5.34)	3.91 (0.119)	26.461	82 9	6 83 ± 1 32 (1 32)
17	0.56 (13 20)	3.34 (0.128)	7.467	98.2	9.46 ± 3.76 (3 76)
18	8 73 (4 56)	4.01 (0 192)	20.162	74.1	5 95 ± 1.15 (1.14)
19	1 02 (4 71)	4 27 (0.291)	16.692	96 8	7.31 ± 1 17 (1 17)
20	1.80 (1.64)	1.83 (0 010)	19.215	94 6	16 58 ± 0.32 (.09)
21	4 15 (2 02)	1.87 (0 012)	5.741	87.6	15.02 ± 0.30 (.11)
22	1.63 (0.56)	1.94 (0.014)	33.398	95 1	15 76 ± 0 32 (.12)
23	2.90 (0.79)	2.02 (0.015)	15.431	91.3	14 52 ± 0.29 (.12)
24	2.13 (1.54)	1 44 (0 011)	8.030	93.6	20.79 ± 0 42 (16)
25	5 25 (3.12)	3.27 (0.025)	14.683	84.3	8.31 ± 0 17 (.08)
26	5.47 (2.05)	3.50 (0.010)	13 477	83.7	7.70 ± 0.15 (.03)
27	3.70 (1 09)	3.32 (0 037)	31.760	88.9	8.64 ± 0 19 (11)
28	1.86 (0.52)	1 95 (0.022)	38.705	94 4	15 59 ± 0.35 (.19)
29	8.96 (1.26)	1.51 (0.014)	9 155	73.5	15.62 ± 0.35 (2)
30	1 50 (0 67)	2.73 (0.025)	28.225	95.4	11.26 ± 0 24 (.11)
31	2 24 (2.47)	4 52 (0.063)	17.679	93 2	6 64 ± 0.16 (.1)
32	1.48 (0.69)	2.67 (0.017)	23.476	95 5	11.51 ± 0.23 (.07)
33	6.44 (0 65)	3.68 (0.019)	31.024	80.8	7.08 ± 0 14 (04)
34	0.71 (1.17)	2 63 (0.019)	28.170	97.8	11.97 ± 0 24 (09)
35	0.73 (1 04)	2.03 (0.016)	21.916	97.7	15.50 ± 0.31 (12)
36	2.83 (1.95)	4.35 (0.071)	27.250	91.4	6 78 ± 0.17 (12)
37	5 47 (0 91)	2.39 (0.035)	18.175	83 7	11.27 ± 0 28 (.19)
38	4.07 (2.12)	2 65 (0.019)	11 045	87 9	10 68 ± 0.22 (.09)
39	14.20 (1 58)	3.13 (0.032)	14.838	57.9	5.97 ± 0 15 (.1)
40	6 38 (1.25)	2 57 (0 013)	27.128	81.0	10 15 ± 0 20 (.06)
41	9.26 (1 28)	2.59 (0.016)	18.850	72.5	9.00 ± 0.18 (08)
42	9 84 (1 40)	3.26 (0 039)	22 324	70.8	6 99 ± 0 18 (12)
43	11.26 (2 00)	3.37 (0.027)	20.129	66.6	6.37 ± 0 14 (08)
44	8.80 (0.99)	2.45 (0 028)	18.764	73.9	9.69 ± 0.23 (.15)
45	2 58 (0.35)	0 85 (0 003)	22.221	92.3	34.49 ± 0 65 (15)
46	0.02 (0.91)	2.55 (0.029)	17.462	99.8	12 59 ± 0.27 (.14)
47	8.47 (1.55)	2.72 (0 011)	21 649	74 9	8.85 ± 0 17 (.05)
48	1.01 (1.56)	2 96 (0.020)	17.634	96 9	10.54 ± 0.21 (.07)
49	6.07 (1.06)	3 58 (0.016)	14.894	81 9	7 00 ± 0.27 (.04)
50	2.42 (0 71)	2.80 (0.017)	25.178	92.7	10.13 ± 0.40 (07)
51	5.81 (3.65)	2.89 (0 058)	8.046	82.7	8.74 ± 0 40 (.21)
52	2 24 (1.23)	1.80 (0.030)	12 793	93.3	15.79 ± 0 67 (.28)
53	6.24 (1.54)	3 11 (0.038)	7.709	81 4	8.01 ± 0.33 (.12)
54	3.24 (1.27)	3.47 (0 024)	22 295	90 3	7 96 ± 0.31 (.06)
55	7.15 (1.67)	2.43 (0.007)	13.136	78.8	9.93 ± 0.39 (.04)
56	7.34 (1.23)	2.32 (0 046)	6.188	78.2	10.28 ± 0 47 (.26)
57	9 70 (4.65)	4.77 (0.054)	9.399	71 2	4.57 ± 0.19 (.07)
58	2.03 (1.09)	2.99 (0.008)	22 164	93.9	9.60 ± 0.37 (.03)
59	0.66 (0.16)	2.46 (0.026)	42.239	97.9	12.15 ± 0 49 (.13)
60	2 62 (1.00)	2.00 (0.035)	20 739	92.2	14 05 ± 0.60 (.26)
61	5 20 (1.43)	2.35 (0 055)	15.079	84.5	10.98 ± 0.52 (.3)
62	0 52 (2.51)	3.88 (0 055)	17.647	98.3	7.76 ± 0.32 (.11)
63	6.94 (2.06)	3 66 (0.051)	17.594	79.4	6.63 ± 0.28 (.12)
64	0.51 (0.37)	1.83 (0.026)	29 693	98.4	16 41 ± 0.68 (23)
65	0.37 (1.86)	4.76 (0 084)	20.042	98.7	6.35 ± 0.27 (.11)
66	0.36 (0 09)	0.98 (0.006)	17.261	98.9	30.72 ± 1.20 (.19)
67	2.20 (0.90)	2.06 (0.035)	6 641	93.4	13.82 ± 0.59 (.25)
68	0.50 (0.54)	1.38 (0.014)	26.406	98.5	21.66 ± 0 87 (.23)

Table DR-1
40Ar/39Ar Data for Detrital Muscovites
Burhi Gandaki River - Sample 01WBS5

Analysis Number	$^{36}Ar/^{40}Ar$ $(x10^{-4})^{++}$	$^{39}Ar/^{40}Ar$ $(x10^{-1})^{++}$	$^{39}Ar_K$ $(x10^{-15}$ mol$)^{**}$	$^{40}Ar^*$ $(\%)^{\#}$	Age $(Ma)^{\$}$
1	10.28 (5.62)	5.04 (0.037)	4.808	69.5	4.23 ± 0 17 (.05)
2	12.28 (8.06)	4.92 (0.011)	6.304	63.6	3.96 ± 0.15 (.01)
3	13.43 (7.74)	6.20 (0.039)	5.558	60.1	2.98 ± 0.12 (.03)
4	10.76 (18 36)	4.80 (0.051)	1.924	68.0	4.34 ± 0.18 (.07)
5	10.34 (8.25)	5.34 (0.019)	4.788	69.3	3.98 ± 0.16 (.02)
6	9.04 (2.54)	4.06 (0.020)	6.217	73.1	5.52 ± 0.22 (.04)
7	3.12 (3.49)	3.41 (0.021)	4.943	90.6	8.12 ± 0.32 (.05)
8	3.47 (3.31)	3.19 (0.048)	6.386	89.6	8.58 ± 0.36 (.14)
9	3.44 (4.10)	1.89 (0 013)	4.291	89.7	14.46 ± 0.57 (.11)
10	9.53 (9.08)	5.20 (0 043)	3.909	71.7	4.22 ± 0.17 (.05)
11	14.93 (8.70)	4.48 (0.030)	4.939	55.8	3.82 ± 0.15 (.05)
12	14.52 (18.43)	5.45 (0.040)	3.878	56.9	3.20 ± 0.13 (.04)
13	16.53 (15.12)	3.34 (0.085)	6.463	51.1	4.69 ± 4.10 (4.09)
14	14.89 (4 15)	3.83 (0.035)	17.047	55.9	4.47 ± 1.00 (.98)
15	14.96 (4.80)	2.63 (0.013)	13.808	55.7	6.49 ± 1.67 (1.65)
16	10.29 (8.87)	3.39 (0.055)	11.250	69.5	6.27 ± 2.38 (2.36)
17	8.85 (9.02)	2 68 (0.029)	4.077	73.7	8.42 ± 3.05 (3.03)
18	15.29 (7.52)	2.44 (0.049)	5.925	54.8	6.85 ± 2.79 (2.78)
19	3.14 (2.46)	3.96 (0.032)	21.858	90.5	7.00 ± 0.62 (.56)
20	9.74 (4.59)	2.75 (0 034)	9.768	71.1	7.92 ± 1.54 (1.51)
21	11.17 (3.65)	2.47 (0.035)	8.886	66.9	8.28 ± 1.38 (1.34)
22	8.74 (2 61)	3 79 (0.024)	18.049	74.0	5.98 ± 0.66 (.62)
23	9.36 (3.82)	2.42 (0.018)	13.438	72.3	9.12 ± 1.47 (1.42)
24	11 38 (4.98)	1.63 (0.052)	7.093	66.3	12.40 ± 2.84 (2.8)
25	0.09 (6.86)	3.84 (0.050)	12.290	99.5	7.94 ± 1.64 (1.61)
26	5.14 (11.56)	3.50 (0.113)	7.248	84.7	7.39 ± 3.00 (2.98)
27	6.64 (4 43)	3.87 (0.033)	25.047	80.2	6.34 ± 1.06 (1.03)
28	7.88 (5.08)	3.05 (0.033)	13.747	76.6	7.68 ± 1.53 (1 5)
29	7.45 (2.85)	2.85 (0.017)	29.345	77.9	8.35 ± 0.96 (.9)
30	14.42 (3.73)	1.88 (0.005)	9.891	57.3	9.30 ± 1.82 (1.78)
31	9.74 (2.15)	2.53 (0.045)	20.600	71.1	8.59 ± 0.86 (.79)
32	13.60 (5.07)	1.41 (0.035)	6.611	59.8	12.94 ± 3.30 (3.26)
33	13.88 (8.41)	2.56 (0.072)	10.283	58.9	7.04 ± 2.99 (2.98)
34	13.33 (4.93)	2.53 (0.032)	11.773	60.5	7.32 ± 1.78 (1.76)
35	2.29 (17.79)	2.86 (0.074)	3.923	93.1	9.97 ± 5.62 (5.61)

Table DR-1
40Ar/39Ar Data for Detrital Muscovites
Burhi Gandaki River - Sample 01WBS6

Analysis Number	$^{36}Ar/^{40}Ar$ $(x10^{-4})^{++}$	$^{39}Ar/^{40}Ar$ $(x10^{-1})^{++}$	$^{39}Ar_K$ $(x10^{-15}$ mol)**	$^{40}Ar^*$ (%)#	Age (Ma)$
1	0.61 (3.18)	1.51 (0.040)	13.310	98.1	19.78 ± 2.10 (1 96)
2	1.30 (3 03)	1.56 (0.014)	9.740	96.1	18.76 ± 1.89 (1.75)
3	2 14 (4 02)	2 09 (0.023)	12.217	93 6	13.66 ± 1.81 (1.73)
4	9.52 (5.33)	2 64 (0 046)	13.525	71.8	8 30 ± 1.85 (1 83)
5	9.48 (4 36)	1.95 (0.022)	9.454	71.9	11.23 ± 2 06 (2.01)
6	5 61 (4.34)	1.95 (0.019)	8 198	83.3	13 03 ± 2.06 (2.)
7	10.81 (3.42)	2.59 (0 074)	12.280	68 0	8 04 ± 1.27 (1 23)
8	7.09 (1.45)	1.83 (0.017)	12.336	79.0	13.18 ± 0.89 (.72)
9	12.37 (2 86)	1 42 (0 007)	5.996	63.4	13.58 ± 1 88 (1 8)
10	2.31 (8.09)	3.65 (0.112)	8.054	93.0	7.79 ± 2.03 (2 01)
11	5.64 (4 16)	2.74 (0 107)	14.708	83.2	9.27 ± 1 47 (1.43)
12	15.15 (2.81)	1.99 (0.053)	15 856	55.2	8 46 ± 1.36 (1 32)
13	5.47 (1.76)	2.35 (0.022)	44.003	83.7	10.88 ± 0.80 (.68)
14	6 88 (1.99)	1.56 (0 053)	22.813	79.6	15.53 ± 1.44 (1.31)
15	5 64 (1 83)	1.85 (0.030)	42.324	83.2	13.74 ± 1 07 (93)
16	8.38 (1.23)	1 54 (0.031)	29.191	75 2	14.85 ± 0.99 (.81)
17	10.56 (2.60)	1.33 (0.014)	23.203	68.7	15.73 ± 1.87 (1.77)
18	14 69 (3 33)	2.72 (0.037)	30.904	56.5	6.37 ± 1.14 (1.11)

Table DR-1
40Ar/39Ar Data for Detrital Muscovites
Burhi Gandaki River - Sample 01WBS7

Analysis Number	$^{36}Ar/^{40}Ar$ $(x10^{-4})^{++}$	$^{39}Ar/^{40}Ar$ $(x10^{-1})^{++}$	$^{39}Ar_K$ $(x10^{-15}\ mol)^{**}$	$^{40}Ar^*$ $(\%)^{\#}$	Age $(Ma)^{\$}$
1	7.32 (1.76)	0.91 (0.009)	7.737	78.3	26.09 ± 1.06 (34)
2	1 63 (7.17)	2.13 (0.035)	3.863	95.1	13.62 ± 0.58 (.23)
3	0.40 (2.91)	1.06 (0.010)	4.182	98.8	28.39 ± 1.12 (.26)
4	4.82 (2.77)	1.20 (0.006)	2.609	85.7	21.81 ± 0.85 (.13)
5	1.08 (3.14)	2.12 (0.030)	3.135	96.7	13 95 ± 0.58 (.21)
6	0.12 (0.38)	0.26 (0.002)	7.141	99.6	113 81 ± 4.34 (.74)
7	16.73 (3.45)	2.08 (0.030)	8.015	50.5	7.42 ± 0.35 (21)
8	0.25 (1.31)	0.94 (0.008)	9.296	99.2	31.95 ± 1.26 (27)
9	6.68 (11.74)	3.32 (0.069)	2.700	80.1	7.39 ± 0.34 (.19)
10	0.54 (8.03)	1.69 (0.025)	3.128	98.3	17.74 ± 0.73 (.26)
11	0.77 (4.43)	4.31 (0.049)	16.586	97.5	6.93 ± 0.28 (.08)
12	3.03 (4.15)	5.09 (0.101)	15.111	90.8	5.47 ± 0.24 (.12)
13	9.52 (7.11)	4.84 (0.092)	9.407	71.7	4.53 ± 0.21 (.12)
14	10.14 (3.52)	5.03 (0.129)	10.324	69.9	4.26 ± 0.23 (.16)
15	0 88 (10.31)	5.22 (0.025)	7.119	97.1	5.70 ± 0.22 (.03)
16	1.65 (2.00)	2.03 (0.007)	9.153	95.0	14.31 ± 0.56 (.05)
17	3.12 (3.49)	3.24 (0.018)	6.880	90.6	8.56 ± 0.34 (.05)
18	0.45 (4.31)	3.06 (0.008)	8.722	98.5	9.84 ± 0.38 (.03)
19	2.17 (3.54)	3.59 (0.042)	8.803	93.4	7.96 ± 0.32 (.1)
20	5.44 (5.27)	4.45 (0.047)	6.900	83.8	5.77 ± 0.23 (.07)
21	0.85 (6.32)	4.90 (0.023)	6.547	97.2	6.08 ± 0.24 (03)
22	2.91 (9.03)	4.50 (0.051)	8.013	91 2	6.20 ± 0.25 (.08)
23	1.82 (2.51)	3.93 (0.066)	9.093	94.4	7.35 ± 0.31 (.13)
24	3.53 (9.19)	4.63 (0.028)	4.426	89.3	5.91 ± 0.23 (.04)
25	0.28 (0.60)	0.45 (0.005)	6.238	99.1	66.91 ± 2.65 (.73)
26	0.34 (0.93)	0.89 (0.011)	7.176	99.0	33.80 ± 1.37 (.43)
27	4.67 (4.28)	4.43 (0.012)	7.914	86.0	5.95 ± 0.23 (.02)
28	0.17 (12.96)	4.96 (0.025)	7.190	99.3	6.13 ± 0.24 (.03)
29	3.84 (5.73)	5.35 (0.061)	7.799	88.4	5.06 ± 0 21 (.07)
30	2.13 (9.61)	3.24 (0.012)	4.355	93.6	8.84 ± 0.34 (.03)
31	0.70 (4.39)	4.80 (0.089)	11.820	97.7	6.24 ± 0.27 (.12)
32	5.26 (25.13)	5.48 (0.117)	1.915	84.2	4.71 ± 0.22 (.12)

Table DR-1
40Ar/39Ar Data for Detrital Muscovites
Burhi Gandaki River - Sample 01WBS8

Analysis Number	$^{36}Ar/^{40}Ar$ $(x10^{-5})^{++}$	$^{39}Ar/^{40}Ar$ $(x10^{-3})^{++}$	$^{39}Ar_K$ $(x10^{-16}$ mol)**	$^{40}Ar^*$ (%)#	Age (Ma)$
1	34.49 (3.17)	8.48 (0.115)	21.282	89.8	317.45 ± 4.85 (4 39)
2	33.19 (5.12)	6 23 (0.053)	16.234	90.2	421 09 ± 4.45 (3.55)
3	32.71 (4.42)	2.93 (0.046)	7.754	90.3	801.83 ± 12.12 (11.21)
4	26.38 (2.23)	5 85 (0.060)	19.216	92.2	454 03 ± 5.27 (4.43)
5	38 95 (5.08)	4.52 (0.073)	10.044	88.5	548.65 ± 9 28 (8 65)
6	34 07 (6.37)	7.61 (0.017)	19.354	89.9	350.67 ± 2.40 (0.79)
7	27.27 (2.84)	7 03 (0.084)	22.328	91.9	384 41 ± 5 15 (4.52)
8	26.91 (1 14)	4.33 (0.081)	13.929	92 0	589.25 ± 10.81 (10.20)
9	27.42 (1.99)	9.51 (0.062)	30.019	91.9	291 88 ± 2.70 (1 90)
10	30.43 (5.68)	12.49 (0.230)	35.529	91.0	224.33 ± 4 52 (4.26)
11	26.11 (1.43)	10 31 (0.094)	28.873	92 3	271.75 ± 3.07 (2.48)
12	31.01 (7.04)	6.41 (0.220)	15 113	90.8	412.99 ± 14 20 (13.96)
13	21.30 (4 87)	3.06 (0 009)	10.453	93.7	797.02 ± 5 03 (2.07)
14	18.40 (2.53)	3 65 (0.050)	14.456	94.6	696.50 ± 9.35 (8.40)
15	25.47 (5.12)	5.88 (0.016)	16.834	92 5	453.22 ± 3.08 (1.15)
16	22.07 (1 32)	7.67 (0.100)	25.382	93 5	360.87 ± 5.12 (4.56)
17	31.37 (3.88)	6.66 (0.084)	15.515	90 7	398 88 ± 5.58 (4.96)
18	22.97 (1.08)	5 59 (0.060)	17.764	93.2	477.19 ± 5 65 (4.80)
19	30.16 (3.48)	3.53 (0.038)	8.510	91.1	693 35 ± 7.91 (6.77)
20	23.84 (3.48)	12.75 (0 047)	39.069	93.0	224 41 ± 1.72 (0 84)
21	0 47 (1.77)	6.12 (0.015)	21.644	99.9	468.02 ± 3 10 (1.00)
22	0 89 (0 75)	6.60 (0.044)	21.789	99.7	437.48 ± 3.79 (2.60)
23	1.06 (3.77)	11.70 (0 082)	28 267	99 7	259 62 ± 2.42 (1.70)
24	0 74 (2.88)	6.70 (0.067)	20.039	99.8	432.05 ± 4.73 (3.85)
25	1 26 (1.62)	7.07 (0 047)	21.905	99.6	410.97 ± 3 60 (2 47)
26	1.86 (2 38)	5.95 (0.042)	18.012	99.4	478.46 ± 4.21 (2 96)
27	1.21 (1.91)	6 09 (0.030)	18.363	99.6	469 64 ± 3.60 (2.07)
28	1.26 (1.17)	7 17 (0.077)	34 598	99 6	406.08 ± 4 69 (3.91)
29	1 66 (2.19)	6.86 (0 113)	24 879	99.5	421.93 ± 6.78 (6 23)
30	1.61 (2.00)	7.69 (0.076)	27.277	99.5	380.92 ± 4.21 (3 42)
31	9.81 (3.72)	6.63 (0.036)	20.303	97.1	425.58 ± 3.43 (2.11)
32	7.17 (1 70)	5 39 (0.051)	22.584	97.9	514.27 ± 5 37 (4.32)
33	9.62 (3.94)	6 68 (0.065)	20.877	97.2	422.65 ± 4 65 (3 79)
34	9 26 (2 35)	8.17 (0.107)	26 490	97.3	353 01 ± 4.89 (4.32)
35	7 12 (1.04)	7.33 (0.003)	30 887	97.9	391 82 ± 2.51 (0.17)
36	13.42 (3 74)	8 99 (0.007)	20.169	96.0	320.03 ± 2 10 (0 25)
37	10 26 (4.02)	6 16 (0.060)	17.934	97.0	453.54 ± 4 93 (4 02)
38	3 25 (0.48)	8.56 (0 020)	28.201	99.0	344.21 ± 2.36 (0.75)
39	0 15 (3.50)	7.33 (0.062)	18.656	100.0	399.40 ± 3 96 (3.03)
40	0.50 (2 21)	6.90 (0.059)	31.323	99.8	421.04 ± 4.18 (3 21)
41	10 81 (2 53)	9 65 (0.078)	26 532	96 8	302 02 ± 3.06 (2 34)
42	0.26 (2.60)	5.79 (0.036)	19.472	99 9	491 58 ± 4.05 (2.64)
43	2 96 (1.71)	8 85 (0.104)	27.792	99.1	334.04 ± 4 21 (3.60)
44	0.82 (2 73)	7.64 (0.089)	24 452	99.8	384.04 ± 4 73 (4 04)
45	0.14 (1.74)	6.62 (0.050)	16 696	100.0	437.14 ± 4.04 (2 94)
46	0.40 (0.96)	5.16 (0.037)	22 302	99 9	543 37 ± 4.74 (3 36)
47	0.85 (3.50)	7.07 (0.047)	16.891	99.7	411.76 ± 3.60 (2.46)
48	1 61 (2 16)	10.53 (0.021)	34.564	99.5	285 75 ± 1.95 (0.52)
49	0.58 (2.30)	7 69 (0.033)	28.240	99.8	382.13 ± 2.86 (1 47)
50	1 27 (3.48)	6.88 (0 030)	20 673	99.6	421 13 ± 3.15 (1 66)
51	6.43 (0.65)	6.48 (0.001)	33.422	98 1	438 08 ± 2.77 (0.05)
52	0.18 (0 53)	6.64 (0.002)	24.177	99.9	436.14 ± 2 76 (0 13)
53	7 73 (1.26)	6.70 (0 047)	28 723	97 7	423.97 ± 3.83 (2.73)
54	0.12 (2.09)	7.98 (0.033)	30.138	100.0	369.75 ± 2.76 (1.40)
55	9.42 (1.71)	7 20 (0.059)	25.345	97.2	395.81 ± 3.93 (3.00)
56	10 07 (1.80)	6.72 (0.046)	22.183	97 0	420.23 ± 3 78 (2.67)
57	0.92 (1 66)	7.08 (0 032)	31.305	99.7	411 09 ± 3 10 (1 65)
58	2 55 (1.01)	15.05 (0.177)	39.463	99.2	204.15 ± 2 67 (2 29)
59	0 28 (3.87)	8 71 (0.059)	28.545	99.9	341.47 ± 3.06 (2.12)

Notes:

++. Numbers in parenthesis indicate 2 σ error on individual measurements

**: Number of moles of K-derived ^{39}Ar ($^{39}Ar_K$)released for each analysis

#: Percentage of radiogenic ^{40}Ar ($^{40}Ar^*$) in the total ^{40}Ar for each analysis

$: Uncertainties include propagated error in the irradiation parameter, J. Uncertainties in parenthesis represent the contribution of analytical error to the total uncertainty.

Taylor creek sanidine (28 34 ± 0.16 Ma) was used as a neutron flux monitor for all analyses (see Renne et al , 1998; *Chemical Geology* v 145, p 117-152)

Chapter 5: Active out-of-sequence thrust faulting in the central Nepalese Himalaya

Cameron Wobus[1]
Arjun Heimsath[2]
Kelin Whipple[1]
Kip Hodges[1]

[1]Department of Earth, Atmospheric and Planetary Sciences
Massachusetts Institute of Technology, Cambridge, MA 02139

[2]Department of Earth Sciences
Dartmouth College, Hanover, NH 03755

Published in the April 21, 2005 issue of *Nature*

Abstract

Modern convergence between India and Eurasia is commonly assumed to be accommodated largely along a single fault—the Main Himalayan Thrust (MHT)—which reaches the surface in the Siwalik Hills of southern Nepal[1-3]. While this model is consistent with geodetic [4, 5], geomorphic [6], and microseismic data [7], a different model incorporating slip on more northerly surface faults is equally consistent with these data[8-10]. Here we report a fourfold increase in millennial timescale erosion rates from in-situ cosmogenic ^{10}Be over a distance of less than two kilometers in central Nepal, delineating for the first time an active thrust fault nearly 100 km north of the surface expression of the MHT. These data challenge the view that rock uplift gradients in central Nepal reflect only passive transport over a ramp in the MHT. Instead, when combined with previously reported ^{40}Ar/^{39}Ar data[9], our results indicate persistent exhumation above deep-seated, surface-breaking structures at the foot of the high Himalaya. These results suggest that a strong dynamic coupling among climate, erosion and tectonics has maintained a locus of active deformation well to the north of the Himalayan deformation front.

The central Nepalese Himalaya are a textbook example of continent-continent collision, where underthrusting of India has been concentrated on several roughly east-west trending fault zones within an approximately 100 km wide belt. The northernmost of these fault zones is the Main Central Thrust (MCT), which marks a transition from the high-grade metamorphic Greater Himalayan Sequence in the north to the lower grade Lesser Himalayan Sequence in the south. Geochronologic data suggest that the MCT is also the oldest structure, with evidence for initial activity on this thrust fault by 23-20 Myr ago [11]. More southerly structures—the Main Boundary Thrust (MBT), and the Main Frontal Thrust (MFT)—developed progressively in a north-to-south sequence, consistent with observations in foreland fold and thrust belts worldwide[12] (Fig. 1a). Most researchers working in the Nepal orogen assume that recent surface faulting has been concentrated at the trace of the MFT, which defines the southern limit of deformation in the Himalayan system. In this model, the MFT absorbs virtually all slip on the MHT. However, this interpretation does not provide a direct explanation for the striking contrast between high modern surface uplift rates in the high Himalayan ranges and the much lower rates in the Himalayan foothills[4], which occurs nearly 100 km north of the MFT across a distinctive physiographic transition. It has been suggested that these changes in physiography and surface uplift rate are best explained by a gradual ramp in the MHT in the middle crust [1, 4-6] (Fig. 1b).

While the ramp hypothesis is consistent with most geological and geophysical data from the Nepalese Himalaya, both the sharpness of the physiographic transition in central Nepal and the relatively abrupt change in surface uplift rate across it are difficult to reconcile with the broader transitions that might be expected as manifestations of a midcrustal ramp[1]. In the Burhi Gandaki valley, for example, mean elevation and relief (as measured along a 20 km-wide swath profile) each increase by more than a factor of two over a distance of less than eight kilometers (Fig. 2). The lower boundary of this physiographic transition can be precisely delineated based

on changes in valley morphology, hillslope gradients, channel gradients, and the extent of thick alluvial fill deposits[9]. Importantly, this lower boundary occurs between 20 and 30 km south of the surface trace of the MCT, suggesting that an unmapped thrust fault may be accommodating gradients in rock uplift in this valley. Farther west in the Marsyandi valley, changes in landscape morphology occur more gradually, consistent with a more broadly distributed strain field. In the Marsyandi drainage, the upper boundary of the physiographic transition is nearly coincident with the mapped trace of the MCT, suggesting that strands of the Main Central Thrust itself may play an important role in accommodating modern rock uplift gradients in this valley [10]. These along-strike differences suggest spatial variations in how recent deformation is accommodated along the Himalayan front. Nonetheless, the physiographic data from central Nepal are all broadly consistent with independent evidence for recent deformation in the region including young, brittle shear zones near the MCT in the Marsyandi valley[10] and sharp discontinuities in the patterns of Late Miocene-Quaternary $^{40}Ar/^{39}Ar$ and fission-track mineral cooling ages throughout central Nepal[9, 13, 14].

Unfortunately, while the physiographic transition is sharp and well-defined in the Burhi Gandaki river, the poor quality of bedrock exposure makes it difficult to construct detailed structural maps to determine unequivocally whether young, surface-breaking faults are present. Here we report the results of a different approach to the problem based on deducing differences in erosional patterns from cosmogenic radionuclide data in detrital sediments. We measured concentrations of in situ produced ^{10}Be in modern sediment from eight small tributaries to the Burhi Gandaki as a proxy for millennial timescale erosion rates in each catchment. The concentration of ^{10}Be in quartz, interpreted with nuclide production rates scaled for altitude, latitude, and local topography, enables erosion rates to be quantified at the outcrop scale [15]. At the basin scale, ^{10}Be concentrations in sediment have been shown to represent reliable basin-

average erosion rates in a variety of climatic and tectonic settings [15-19]. We utilize the spatial pattern of erosion rates from the Burhi Gandaki tributaries to delineate discontinuities in rock uplift rates across the rangefront. Field observations suggest that hillslope angles approach threshold values near the physiographic transition, so that landscape response should be rapid: as bedrock rivers adjust their incision rates in response to spatial variations in rock uplift, we expect the hillslopes to match this incision rate by landsliding to maintain their critical condition[20, 21].

The calculation of a basin-average erosion rate from ^{10}Be concentrations in sediment from steep, landslide-dominated catchments requires an assumption that the sediment collected at the basin outlet is well-mixed, so that pulses of cosmogenically "underexposed" landslide-derived material are integrated into the bulk sediment sample. Larger basins will more effectively integrate these stochastic sediment pulses downstream, suggesting that basin scale may be an important factor in controlling the fidelity of the cosmogenic signal[22-24]. Basins sampled for this study have drainage areas ranging from ~3 to ~22 km^2 (Table 1), a range where preliminary numerical modeling suggests a high probability that basin-average erosion rates will be closely predicted – or only slightly underestimated – from detrital cosmogenic radionuclide concentrations[24]. Furthermore, the drainage pattern in the Burhi Gandaki is trellised, with tributaries draining narrow (~2-5 km wide) catchments subparallel to the structural grain of the orogen (Fig. 2a). Sediment from each tributary therefore records an estimate of the basin-average erosion rate from a narrowly constrained tectonostratigraphic position.

The ^{10}Be data reveal a sharp discontinuity in erosion rates centered approximately 23 kilometers south of the MCT, within the zone of the physiographic transition as defined by independent methods[9]. To the south of this discontinuity, erosion rates are uniform at ~0.2 mm/yr. To the north, erosion rates abruptly jump to ~0.8 mm/yr and then fall gradually back to

~0.2 mm/yr over a distance of 10 km (Fig. 3a). ^{10}Be concentrations (Table 1) indicate minimum exposure ages ranging from approximately one to three thousand years, suggesting sharp spatial gradients in basin-average erosion rates over late Holocene timescales. This break in erosion rates is not correlated with any mappable break in lithology: rocks to the north and south of this transition each comprise phyllites and schists of the Lesser Himalayan sequence. Furthermore, there is no correlation between the cosmogenically determined erosion rates and basin size, and the fourfold increase in erosion rates is larger than any bias that might be predicted by preliminary modeling accounting for undersampling of landslide-derived material in small catchments[24]. The spatial trend is therefore unlikely to reflect a sampling bias controlled by the stochasticity of landsliding. Instead, the ^{10}Be data corroborate our interpretations of tectonics based solely on landscape morphology, and allow us to more narrowly constrain the locus of active thrust faulting in the Burhi Gandaki valley.

The discontinuity in short-term erosion rates is also co-located with a prominent break in long-term cooling rates from thermochronology (Fig. 3b): to the north of the physiographic transition, muscovite ^{40}Ar/^{39}Ar cooling ages are young (Cenozoic), while they are substantially older to the south (Paleozoic-Proterozoic)[9]. Calculation of long-term exhumation rates from these data would require a detailed thermal model accounting for lateral advection of rock and temporal variations in the subsurface thermal structure. While this calculation is beyond the scope of this study, the abrupt discontinuity in cooling ages is a robust finding which corroborates our interpretation of a surface-breaking thrust fault at the physiographic transition. Furthermore, the thermochronologic data provide the additional constraint that active thrust faulting has persisted at least long enough to create a substantial discontinuity in the total depth of exhumation from north to south.

The presence of a tectonically significant, thrust-sense fault zone at the physiographic transition, as implied by the spatial coincidence of breaks in short-term (cosmogenic) and long-term ($^{40}Ar/^{39}Ar$) erosion rates, is consistent with field observations of brittle deformational fabrics parallel to the northward-dipping foliations in the Lesser Himalayan Sequence[9]. Physiographic data from along strike suggest that this fault zone extends eastward to the Trisuli valley, maintaining its position substantially south of the Main Central Thrust. To the west of the Burhi Gandaki valley, the orientation of the physiographic transition and the more diffuse gradients in landscape morphology suggest that this fault zone becomes more broadly distributed in the Marsyandi valley, and may correspond with recent activity within the Main Central Thrust zone[10, 14].

We speculate that the origin of this fault zone may be intimately tied to the presence of strong precipitation gradients across the central Nepalese Himalaya. Focused monsoonal precipitation is well documented on the southern flank of the Nepalese Himalaya[14, 25] and has been posited to drive localized tectonic uplift by removing mass from the top of an extruding ductile channel[26, 27]. While the energy driver for this channel extrusion is gravitational potential energy from the Tibetan plateau, erosion must play an important role in determining where the energy is dissipated. Our data suggest that there is a dynamic feedback between climate and tectonics in the Himalayan orogen, so much so that the locus of deep exhumation has been maintained nearly 100 km northward of the Himalayan thrust front. This focused exhumation sustains the dramatic topographic front of the high Himalaya, and increases the efficiency of energy dissipation from the Himalayan system.

References

1. Cattin, R. & Avouac, J. P. Modeling mountain building and the seismic cycle in the Himalaya of Nepal. Journal of Geophysical Research 105, 13389-13407 (2000).
2. Lave, J. & Avouac, J. P. Fluvial incision and tectonic uplift across the Himalayas of central Nepal. Journal of Geophysical Research 106, 26561-26591 (2001).
3. Pandey, M. R., Tandukar, R. P., Avouac, J. P., Lave, J. & Massot, J. P. Interseismic strain accumulation on the Himalayan crustal ramp (Nepal). Geophysical Research Letters 22, 751-754 (1995).
4. Jackson, M. & Bilham, R. Constraints on Himalayan deformation inferred from vertical velocity fields in Nepal and Tibet. Journal of Geophysical Research 99, 13897-13912 (1994).
5. Bilham, R., Larson, K., Freymuller, J. & Members, P. I. GPS measurements of present-day convergence across the Nepal Himalaya. Nature 386, 61-64 (1997).
6. Lave, J. & Avouac, J. P. Active folding of fluvial terraces across the Siwaliks Hills, Himalayas of central Nepal. Journal of Geophysical Research 105, 5735-5770 (2000).
7. Pandey, M. R. et al. Seismotectonics of the Nepal Himalaya from a local seismic network. Journal of Asian Earth Sciences 17, 703-712 (1999).
8. Catlos, E. J. et al. Geochronologic and thermobarometric constraints on the evolution of the Main Central Thrust, central Nepal Himalaya. Journal of Geophysical Research 106, 16177-16204 (2001).
9. Wobus, C. W., Hodges, K. V. & Whipple, K. X. Has focused denudation sustained active thrusting at the Himalayan topographic front? Geology 31, 861-864 (2003).
10. Hodges, K., Wobus, C., Ruhl, K., Schildgen, T. & Whipple, K. Quaternary deformation, river steepening and heavy precipitation at the front of the Higher Himalayan ranges. Earth and Planetary Science Letters 220, 379-389 (2004).
11. Hodges, K. V. Tectonics of the Himalaya and southern Tibet from two perspectives. GSA Bulletin 112, 324-350 (2000).
12. DeCelles, P. G. et al. Stratigraphy, structure, and tectonic evolution of the Himalayan fold-thrust belt in western Nepal. Tectonics 20, 487-509 (2001).
13. Copeland, P. et al. An early Pliocene thermal disturbance of the Main Central Thrust, central Nepal; implications for Himalayan tectonics. Journal of Geophysical Research, B, Solid Earth and Planets 96, 8475-8500 (1991).
14. Burbank, D. W. et al. Decoupling of erosion and climate in the Himalaya. Nature 426, 652-655 (2003).
15. Bierman, P. R. & Nichols, K. K. Rock to sediment-slope to sea with ^{10}Be-rates of landscape change. Annual Reviews of Earth and Planetary Sciences 32, 215-255 (2004).
16. Brown, E. T., Stallard, R. F., Larsen, M. C., Raisbeck, G. M. & Yiou, F. Denudation rates determined from the accumulation of in-situ produced ^{10}Be in the Luquillo Experimental Forest, Puerto Rico. Earth and Planetary Science Letters 129, 193-202 (1995).
17. Riebe, C. S., Kirchner, J. W., Granger, D. E. & Finkel, R. C. Erosional equilibrium and disequilibrium in the Sierra Nevada, inferred from cosmogenic ^{26}Al and ^{10}Be in alluvial sediment. Geology 28, 803-806 (2000).
18. Schaller, M., von Blanckenburg, F., Hovius, N. & Kubik, P. W. Large-scale erosion rates from in-situ produced cosmogenic nuclides in European river sediments. Earth and Planetary Science Letters 188, 441-458 (2001).
19. Vance, D., Bickle, M., Ivy-Ochs, S. & Kubik, P. W. Erosion and exhumation in the Himalaya from cosmogenic isotope inventories in river sediments. Earth and Planetary Science Letters 206, 273-288 (2003).
20. Burbank, D. W. et al. Bedrock incision, rock uplift and threshold hillslopes in the northwestern Himalayas. Nature (London) 379, 505-510 (1996).
21. Roering, J. J., Kirchner, J. W. & Dietrich, W. E. Hillslope evolution by nonlinear, slope-dependent transport: steady state morphology and equilibrium adjustment timescales. Journal of Geophysical Research 106, 16499-16513 (2001).
22. Bierman, P. & Steig, E. Estimating rates of denudation using cosmogenic isotope abundances in sediment. Earth Surface Processes and Landforms 21, 125-139 (1996).
23. Granger, D. E., Kirchner, J. W. & Finkel, R. Spatially averaged long-term erosion rates measured from in situ-produced cosmogenic nuclides in alluvial sediment. Journal of Geology 104, 249-257 (1996).
24. Niemi, N. A., Oskin, M. E. & Burbank, D. A numerical simulation of the effects of mass-wasting on cosmogenically determined erosion rates. EOS: Transactions of the American Geophysical Union 85, Fall Meet. Suppl., Abstract H51C-1157 (2004).
25. Putkonen, J. Continuous snow and rain data at 500 to 4400 m altitude near Annapurna, Nepal, 1999-2001. Arctic, Antarctic and Alpine Research 36, 244-248 (2004).

26. Beaumont, C., Jamieson, R. A., Nguyen, M. H. & Lee, B. Himalayan tectonics explained by extrusion of a low-viscosity crustal channel coupled to focused surface denudation. Nature 414, 738-742 (2001).
27. Hodges, K. V., Hurtado, J. M. & Whipple, K. X. Southward Extrusion of Tibetan Crust and its Effect on Himalayan Tectonics. Tectonics 20, 799-809 (2001).

Acknowledgements We thank D. Burbank and P. Bierman for constructive reviews, which greatly improved the quality of the original manuscript. Field assistance was provided by B. Crosby, K. Ruhl, T. Schildgen, N. Wobus and Himalayan Experience. Work was funded by NSF and NSF Continental Dynamics.

Figure Captions

Figure 1 Geologic setting. **a,** Regional geologic map showing major tectonic structures and river systems. Dash-dot lines: MAR = Marsyandi river, BG = Burhi Gandaki river, TR = Trisuli river. STF = South Tibetan fault. All other abbreviations in text. A-A' indicates location of schematic cross section in **b**. Dashed grey line shows lower boundary of physiographic transition where it is well-defined (see text for explanation). Grey box indicates location of Fig. 2a. **b,** Schematic cross section across central Nepal, showing ramp in Main Himalayan Thrust (MHT), and inferred projection of physiographic transition (PT) to surface.

Figure 2 Sampling locations and study area physiography. **a,** Sample collection points (white dots) and drainage basins (black outlines). Dashed gray line shows approximate trace of physiographic transition. Yellow rectangle delineates boundaries of swath profile shown in Fig. 2b. **b,** Mean (black line), minimum and maximum elevations (dashed grey lines) along 20-km wide swath profile oriented orthogonal to the strike of the range. Vertical gray line marks the base of the physiographic transition (see text). Black bars show extent of alluvial fill terraces (T), knickpoints on Burhi Gandaki tributaries (K), and zone of increasing steepness on Burhi Gandaki trunk stream (S).

Figure 3 Erosion rate and cooling-age data. **a,** ^{10}Be erosion rate (dots) versus distance from MCT, projected onto N18°E line. X error bars represent projected distance to basin limits. Y error bars represent 1σ uncertainty in analytical results. **b,** ^{40}Ar/^{39}Ar cooling ages (log scale) versus distance from MCT. Horizontal lines, boxes and whiskers represent median, interquartile range, and limits of analysis results, respectively. Black dots represent outliers (more than 1.5 times the interquartile range beyond box limits). Widths of boxes represent widths of individual basins. Complete data can be found in (Ref. 9). Vertical shading and dashed lines show physiographic transition.

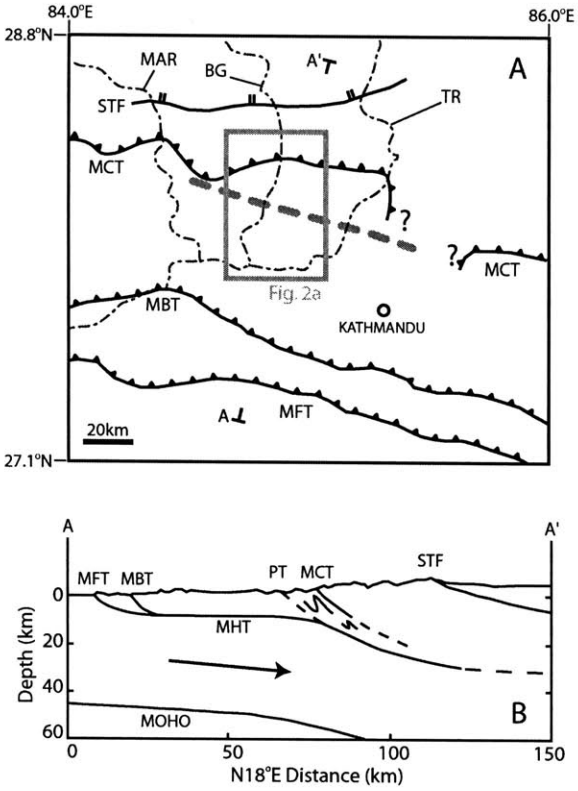

Wobus et al., Figure 1
MS #2004-10-25330

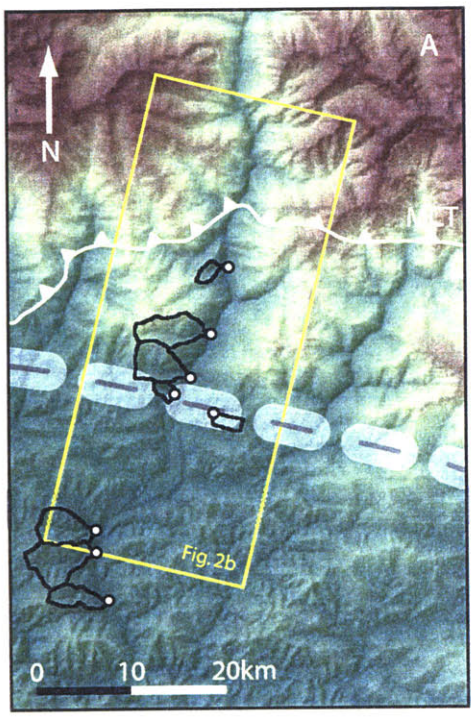

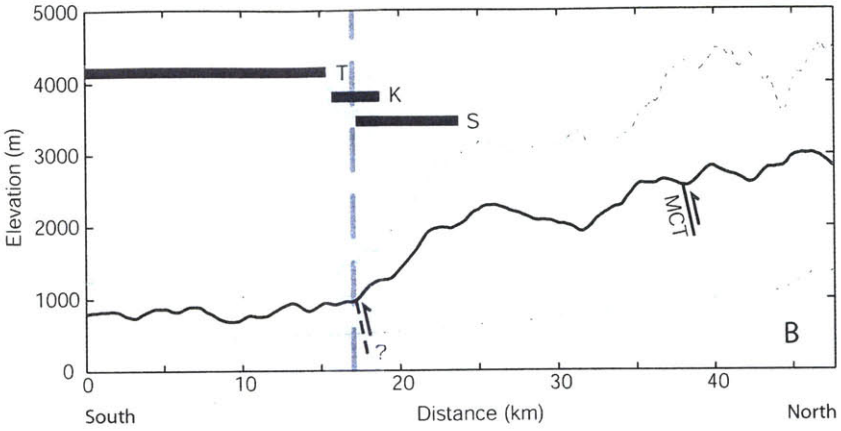

Wobus et al., Figure 2
MS #2004-10-25330

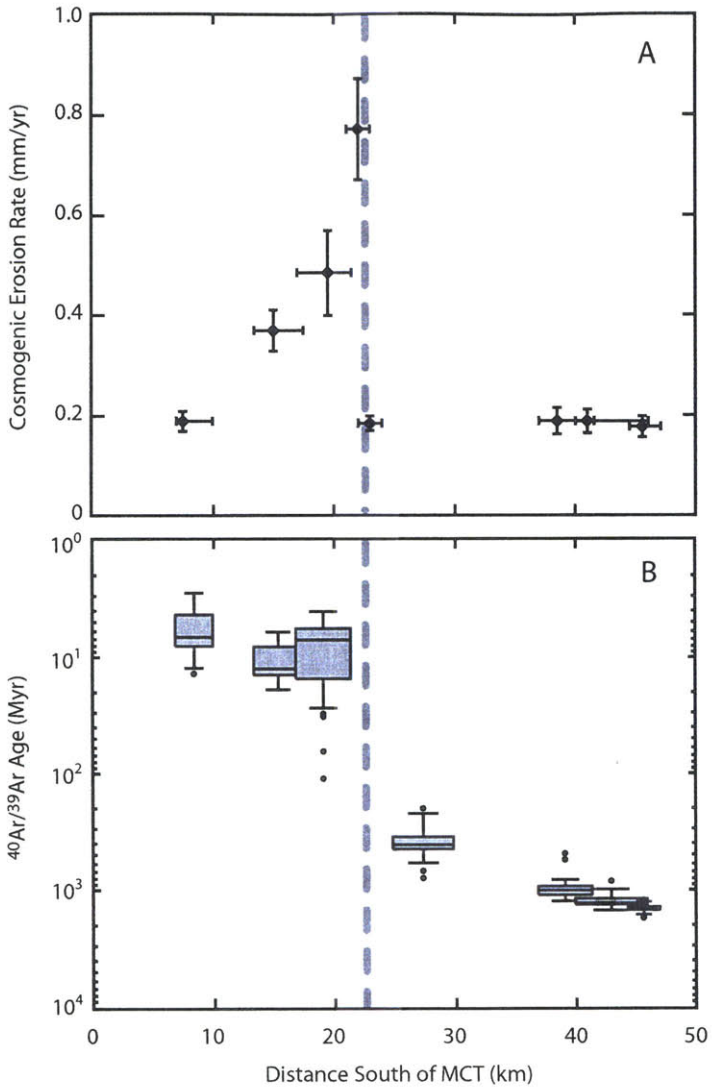

Wobus et al., Figure 3
MS #2004-10-25330

Table 1 **Basin characteristics and cosmogenic erosion rate data**

Sample	Dist from MCT (km) [a]	Drainage area (km^2)	Mean Slope (deg) [b]	Elevation range (m) [c]	Mass quartz (gm)	[^{10}Be] (10^3 atoms/gm)	Erosion rate (mm/yr)
01WBS5	7.0 - 10.0 (7.5)	3.4	21.4	797 - 2372	58.64	42.1 ± 2.3	0.19 ± 0.02
01WBS6	13.5 - 17.5 (15)	18.4	21.9	604 - 3158	79.32	27.8 ± 1.6	0.37 ± 0.04
01WBS7	17.0 - 21.5 (19.5)	17.5	22.0	533 - 2455	69.25	13.9 ± 1.7	0.48 ± 0.08
03WBS1	21.0 - 23.0 (22.0)	3.2	17.6	643 - 1325	150.90	6.0 ± 0.5	0.77 ± 0.10
03WBS2	22.0 - 24.0 (23.0)	3.9	21.4	723 - 1475	150.24	27.9 ± 0.9	0.19 ± 0.01
01WBS3	37.0 - 41.5 (38.5)	16.7	24.6	413 - 1412	67.14	21.9 ± 1.9	0.19 ± 0.03
01WBS2	40.0 - 46.0 (41.0)	22.4	30.8	370 - 1574	70.03	23.4 ± 1.8	0.19 ± 0.02
01WBS1	44.5 - 47.0 (45.5)	10.5	28.4	348 - 1670	84.88	25.4 ± 1.7	0.18 ± 0.02

[a]Distance to northern and southern edges of basin, rounded to nearest half-kilometer and projected onto line oriented N18 °E. Numbers in parenthesis represent distance to basin outlet.

[b]Slopes calculated from 3x3 moving window over 90m pixel DEM.

[c]Production rates calculated pixel by pixel using 90 meter DEM.

Chapter 6: Tectonic architecture of the central Nepalese Himalaya constrained by geomorphology, detrital $^{40}Ar/^{39}Ar$ thermochronology and thermal modeling

Cameron W. Wobus
Kelin X. Whipple
Kip V. Hodges

Department of Earth, Atmospheric and Planetary Sciences
Massachusetts Institute of Technology
Cambridge, Massachusetts 02139

For submittal to *Tectonics*

Abstract

Much of the central Nepalese Himalaya are characterized by a sharp transition in landscape morphology that is suggestive of narrowly distributed transitions in surface uplift and exhumation rates. An integrated study of geomorphology and $^{40}Ar/^{39}Ar$ thermochronology from central Nepal, combined with a simple thermal and kinematic model of particle trajectories through the Himalayan wedge, provides a means of evaluating the range of tectonic geometries that might be consistent with the observed trends in physiography and cooling history. Our $^{40}Ar/^{39}Ar$ data require a significant northward increase in the total depth of exhumation along three trans-Himalayan transects, which can be replicated by a tectonic model including either surface thrusting at the base of the high Himalaya, or accretion at depth across the décollement separating India from Eurasia. While our $^{40}Ar/^{39}Ar$ data suggest similarities in the thermal histories preserved in all three transects, along-strike changes in physiography might be indicative of along-strike changes in the degree to which surface thrusting has developed. Additional structural and thermochronologic data are needed to test the hypothesis that along-strike changes in physiography reflect differences in structural style along the rangefront.

1. Introduction

1.1 Motivation

As a textbook example of continent-continent collision, the Himalaya may provide our best natural laboratory to study the tectonic architecture of an evolving orogenic system. Over the past decade, a wealth of new data have been published allowing us to refine our estimates of exhumation rates, rock uplift rates, and pressure-temperature paths along local transects across the range [*Bollinger, et al.*, 2004; *Brewer, et al.*, 2003; *Burbank, et al.*, 2003; *Catlos, et al.*, 2001; *Copeland, et al.*, 1991; *Harrison, et al.*, 1997; *Kohn, et al.*, 2001; *Ruhl and Hodges*, in press; *Vannay, et al.*, 2004; *Vannay and Hodges*, 1996; *Viskupic, et al.*, 2005; *Wobus, et al.*, 2005]. However, while each new dataset narrows the range of appropriate tectonic models [*Beaumont, et al.*, 2004; *Jamieson, et al.*, 2004], extrapolating our observations at the surface to the architecture of the subsurface leaves ample room for interpretation.

In the central Nepalese Himalaya, at least three classes of tectonic models have been proposed to explain the observed breaks in surface uplift rates across a dramatic physiographic transition between the high Himalayan ranges and their foothills [*Cattin and Avouac*, 2000; *DeCelles, et al.*, 2001; *Wobus, et al.*, 2005]. Each of these models implies a different degree of exhumation at the foot of the high range, and therefore each suggests a different degree of importance for surface processes in driving this exhumation. As a result, the differences in the details of these models may lead to varying interpretations of how closely climate and tectonics may be coupled in the Himalaya [*Beaumont, et al.*, 2001; *Burbank, et al.*, 2003; *Hodges, et al.*, 2004; *Molnar*, 2003; *Wobus, et al.*, 2005].

1.2 Approach and Scope

Our approach to understanding the tectonics of the central Nepalese Himalaya involves three major avenues of inquiry. We begin with an analysis of landscape morphology in central Nepal, with the assumption that changes in physiography can be used at some level to characterize the distribution of rock uplift rates, and therefore the locus of active deformation, across the rangefront [*Snyder, et al.*, 2000; *Wobus, et al.*, in press]. This analysis builds on previous work which has identified and characterized a prominent morphologic break in central Nepal – hereafter referred to as physiographic transition 2, or PT_2, following the terminology of Hodges et al. (2001) [*Hodges, et al.*, 2004; *Hodges, et al.*, 2001; *Seeber and Gornitz*, 1983; *Wobus, et al.*, 2005; *Wobus, et al.*, 2003]. Our goal is to characterize the position of this physiographic transition and its relation to mapped structures, as a proxy for along-strike variability in the tectonic architecture of central Nepal.

We supplement our analysis from landscape morphology with detrital $^{40}Ar/^{39}Ar$ cooling-age data from two transects. These $^{40}Ar/^{39}Ar$ cooling ages provide a means of characterizing the exhumation history of rocks between middle-crustal positions (~350°C) and the surface. Samples are derived from small tributaries to the Trisuli and Bhote Kosi rivers, and each set of samples represents a strike-normal transect of approximately 50 km across PT_2. In conjunction with additional detrital $^{40}Ar/^{39}Ar$ data from the Burhi Gandaki river [*Wobus, et al.*, 2003], these data characterize cooling ages across the physiographic transition for nearly 100 km along strike. We use the cooling-age data to identify discontinuities in exhumation history across PT_2, and the along-strike variability in this signal.

Finally, we explore a simple thermal and kinematic model for the tectonic evolution of central Nepal, in order to evaluate the range of structural geometries that can produce the observed pattern of $^{40}Ar/^{39}Ar$ ages from our detrital samples. The goal of our modeling is not to determine exhumation rates directly from the observed distributions of cooling ages at the catchment scale [*Brewer*, 2000; *Brewer, et al.*, 2003; *Ruhl and Hodges*, in press]. Rather, we use the first-order patterns of cooling ages across PT_2 to constrain the structural geometry of the Himalaya if a model of continuous frontal accretion is invoked for the neotectonics of central Nepal, rather than a model of surface thrusting [*Bollinger, et al.*, 2004; *Wobus, et al.*, 2005]. We find that our thermal and kinematic model allows us to place narrow constraints on the rate of accretion if we assume reasonable values for the footwall underthrusting rate, the hanging wall overthrusting rate, and the geometry of the system.

2. Background

As early as 1975, Le Fort [1975] recognized that the structural geometry of the Himalaya is characterized by three major south-vergent thrust systems. From north to south, they are the Main Central Thrust (MCT), the Main Boundary Thrust (MBT), and the Main Frontal Thrust (MFT) systems (Figure 1). The MCT places high-grade schists, gneisses and migmatites of the Greater Himalayan Sequence (GHS) atop amphibolite-greenschist facies phyllites and psammites of the Lesser Himalayan Sequence (LHS). The LHS is thrust over unmetamorphosed foreland strata along the MBT, and these "Subhimalayan" units are, in turn, thrust over the undeformed Indian subcontinent on the Main Frontal Thrust [*Hodges*, 2000]. Structural mapping from central Nepal suggests that all three of these structures root at depth into a basal décollement

typically referred to as the Main Himalayan Thrust (MHT) [*Hauck, et al.*, 1998; *Schelling and Arita*, 1991].

The simplified tectonic stratigraphy of the Himalaya is complicated somewhat in central Nepal by the presence of the Kathmandu allochthon, an ~100 km wide exposure of amphibolite-facies metamorphic rocks and granitic intrusions that is preserved in the core of a broad synform overlying less metamorphosed LHS units. On the southern flank of the synform, the allochthon is separated from underlying rocks by the north-dipping Mahabarat Thrust (MT). Some workers [*Stöcklin*, 1980] regard the MT as a southward extension of the Main Central Thrust, making the Kathmandu allochthon a klippe or half-klippe of Greater Himalayan sequence rocks. Unfortunately, exposures of the northern flank of the synform are very poor, and a variety of structural relationships between the allochthon and the GHS have been proposed. Although basal units of the Kathmandu allochthon are, in some places, similar to GHS units, the precise relationship between the Mahabarat and Main Central Thrusts remains unclear [*Gehrels, et al.*, 2003; *Hodges*, 2000].

Seismic reflection profiles in southern Tibet [*Zhao, et al.*, 1993] have identified the MHT at a deeper level than would be expected from simple down-dip projections of the shallow dip of the MHT beneath the Himalayan foreland [*Schelling and Arita*, 1991]. This observation supports the interpretation of Lyon-Caen and Molnar [*Lyon-Caen and Molnar*, 1983], of the existence of a large ramp in the MHT positioned just below PT_2. Subsequent workers [*Avouac*, 2004; *Cattin and Avouac*, 2000; *Pandey, et al.*, 1995] have sought to refine models of the geometry and position of this ramp using a variety of geophysical datasets. The inferred ramp-flat geometry has been used to explain changes in surface uplift rates between the foothills and the high Himalayas [*Bilham, et al.*, 1997; *Jackson and Bilham*, 1994], as well as the existence of

PT_2 [*Lave and Avouac*, 2001] (Figure 2a). However, a persistent ramp geometry is inconsistent with unreset $^{40}Ar/^{39}Ar$ cooling ages in the hanging wall of the MHT as observed by [*Copeland, et al.*, 1991] and [*Wobus, et al.*, 2003], since the kinematics implied by such a model require exhumation of all hanging wall rocks from below the closure isotherm.

The folding of the Kathmandu allochthon and further structural mapping from western and central Nepal suggest at least some degree of duplexing along this ramp at depth. Most cross-sections through western and central Nepal, for example, include a crustal-scale structure commonly referred to as the "Lesser Himalayan Duplex", which is proposed to date to the Middle Miocene [*DeCelles, et al.*, 2001; *Robinson, et al.*, 2003]. More recent work has suggested that accretion at depth may actually be a quasi-steady state process, continuing throughout much of the past 20 Myr [*Bollinger, et al.*, 2004] (Figure 2b). This "steady-state" accretion model suggests that the ramp in the MHT propagates southward with time, abandoning a succession of blind thrust faults in the hanging wall. An important kinematic requirement of the Bollinger et al. model is that the hanging wall continues to deform during ramp propagation by incremental slip along a penetrative set of foliation-parallel shear zones. This penetrative deformation suggests that hanging wall rocks should record smooth gradients in the total depth of exhumation from south to north. Under the right set of geometric constraints, an accretion model should also be capable of producing a break from reset to unreset $^{40}Ar/^{39}Ar$ cooling ages within the Lesser Himalayan Sequence, since the kinematics require at least some of the footwall rocks accreted to the hanging wall to be re-exhumed before reaching the depth of the closure isotherm for $^{40}Ar/^{39}Ar$. One of the goals of our thermal modeling is to evaluate the range of structural geometries that might create such a break in cooling ages.

A final class of models suggests that new thrust faults break to the surface near the up-dip projection of the inferred MHT ramp. This geometry is supported by thermochronologic data from central Nepal, which suggest rapid exhumation of rocks in the footwall of the Main Central Thrust [*Catlos, et al.*, 2001; *Harrison, et al.*, 1997; *Kohn, et al.*, 2001]. In addition, reports of unreset $^{40}Ar/^{39}Ar$ ages to the south of the physiographic transition [*Copeland, et al.*, 1991; *Wobus, et al.*, 2003], a sharp discontinuity in surface erosion rates constrained by cosmogenic isotopes [*Wobus, et al.*, 2005], and the presence of young brittle deformation in the vicinity of the MCT [*Hodges, et al.*, 2004] are most easily explained by a model of sustained or punctuated exhumation along surface-breaking thrusts near PT_2 (Figure 2c).

The differences in structural configuration between duplexing at depth and thrusting at the surface may appear to be minor, but the details of these two models suggest fundamental differences in the way the Himalayan range has evolved. In particular, the degree to which surface thrusting has been sustained during the growth of the Himalaya may have implications for how strongly climate can influence structural style [*Simon*, 2005], and how closely climate and tectonics are coupled at the orogen scale [*Beaumont, et al.*, 2001; *Koons*, 1995; *Whipple and Meade*, 2004; *Willett*, 1999]. In the remainder of this paper we examine the geomorphology and thermal history across approximately 100 km of central Nepal, to evaluate the variability in surface thrusting and structural style along the strike of the High Himalaya.

3. Geomorphology

If tectonically driven rock uplift is ultimately the engine driving relief production in active orogens, then the geomorphology of the Himalaya should provide some constraints on the distribution of rock uplift rates through central Nepal. With this in mind, one of the more

enigmatic characteristics of the central Nepalese Himalaya is the position of PT_2 nearly 100 km north of the active Himalayan thrust front [*Seeber and Gornitz*, 1983]. Previous work has described the distribution of potential energy, hillslope gradients and channel steepness indices through central Nepal, all of which suggest that PT_2 may be a morphologic signature of surface thrust faulting at the base of the high range [*Hodges, et al.*, 2004; *Hodges, et al.*, 2001; *Wobus, et al.*, in press; *Wobus, et al.*, 2003]. Our goal here is to narrowly constrain the position of PT_2 where it is well-defined in central Nepal, and to examine the along-strike variations in physiography that might reflect along-strike variations in tectonics.

Our physiographic data include maps of local relief, calculated over a 2.5-km radius circular window (Figure 3a), hillslope gradients calculated over an ~250 meter square and smoothed with a 1 km radius window (Figure 3b), and major knickpoints and normalized steepness indices for the trans-Himalayan rivers and their tributaries in central Nepal (Figure 3c). In the latter dataset, knickpoints were marked at the downstream limit of high concavity zones, where channel gradients drop abruptly from north to south and may mark the southern limit of a downstream decrease in rock uplift rates [*Kirby and Whipple*, 2001]. Steepness indices (k_s) are a measure of the local channel gradient normalized to the contributing drainage area, and have been shown to be correlated with the rate of rock uplift in settings where the tectonics have been independently constrained [*Kirby and Whipple*, 2001; *Snyder, et al.*, 2000; *Wobus, et al.*, in press]. We calculated steepness indices over a 1-km moving window along each channel, and color-coded channel reaches by their k_s values throughout central Nepal.

All of the data from regional maps of hillslope gradients, local relief, channel gradients and knickpoints are presented in cross-sectional view in Figure 4. Each cross section presents data from a 17-20 km wide swath profile (see Figure 1), plotting minimum, maximum and mean

values of topography, relief or hillslope gradient within the swath. We present five swath profiles, following the courses of the Marsyandi, Burhi Gandaki, Trisuli, Indrawati and Bhote Kosi rivers[1].

At the scale of the entire orogen, PT_2 corresponds very closely to the position of the Main Central Thrust [*Seeber and Gornitz*, 1983]. As an example, maps of hillslope gradients, mean relief and steepness index all indicate a physiographic transition straddling the MCT in the Marsyandi valley (Figures 3a-c). This near-coincidence of the physiographic transition with the MCT is highlighted by swath profiles from the Marsyandi (Figure 4a), in which the minimum and maximum topography diverge gradually beginning approximately 10 km south of the MCT. The proximity of the physiographic transition to the Main Central Thrust, and the presence of Quaternary deformation along more than 10 km of river distance in this area [*Hodges, et al.*, 2004], suggest that the physiographic transition along the Marsyandi transect may reflect distributed strain extending from south to north across the MCT zone.

While PT_2 broadly corresponds to the MCT at the scale of the entire range, it diverges significantly from the MCT along a line trending east-southeast across the lower Burhi Gandaki and Trisuli Rivers in central Nepal [*Hodges, et al.*, 2001; *Wobus, et al.*, 2003]. Maps of local relief and hillslope gradients highlight this abrupt transition in physiography (Figures 3a-b), while swath profiles indicate an approximate doubling of relief across only 8-10 km in both the Burhi Gandaki and Trisuli valleys (Figures 4b-c). The observed increase in relief is correlated with a south-north disappearance of thick alluvial terraces and valley fills, a clustering of knickpoints along trunk and tributary channels, and the base of a zone of increasing steepness index along each of the trunk stream profiles (Figures 3c, 4). Notably, the abrupt transition in

[1] The width of the Bhote Kosi profile was limited by the extent of our 90-meter resolution topographic data. Swath profiles using ~1 kilometer GTOPO30 data corroborate the results from our higher-resolution dataset, but show

physiography highlighted by all of these data is most prominent where the MCT forms a major reentrant to the north, suggesting that recent tectonic displacements have activated a new fault truncating the bend in the MCT. This hypothesis is corroborated by cosmogenic isotope data already published from the Burhi Gandaki valley, which indicate a fourfold increase in erosion rates over an across-strike distance of ~2 km [*Wobus, et al.*, 2005].

To the east in the Indrawati and Bhote Kosi valleys, changes in physiography occur more gradually than in the valleys to the west, as shown both in map view and cross sectional views of topography, relief and hillslope gradient. The mean topography in these transects of course increases across the profiles, but relief changes far less in these transects than in the rivers to the west (Figures 4d-e). These increases in mean topography without associated changes in relief may reflect a system in which tectonic uplift outpaces the rate of river incision, thereby passively uplifting the Indrawati and Bhote Kosi river valleys without substantially altering the relief across the range. Because these two rivers have considerably smaller drainage areas than the rivers to the west, these along-strike changes in physiography may simply reflect differences in the relative strength of the fluvial systems. In this case, it may be difficult to deconvolve the differences in geomorphic character between the western (Figures 4a-c) and eastern (Figures 4d-e) swath profiles from the changes in tectonics that we hope to characterize. In addition, our data are sparse for the extent of alluvial fill, knickpoints and channel gradients, reflecting both a lack of field observations and a limit to our digital topographic dataset. Nonetheless, the inflections in minimum, maximum and mean topography in the Indrawati and Bhote Kosi rivers are all suggestive of a broadly distributed increase in rock uplift rates from south to north. In the sections that follow, we supplement our inferences from geomorphology with the results of

---

considerably less detail. We therefore focus our discussion on the highest resolution data we have available.

$^{40}Ar/^{39}Ar$ thermochronology and thermal modeling, to better constrain the tectonic architecture of the central Nepalese Himalaya.

4. Detrital $^{40}Ar/^{39}Ar$ Thermochronology

4.1 Previous work

With a nominal closure temperature of ~350°C, the muscovite $^{40}Ar/^{39}Ar$ thermochronometer is a useful tool for understanding the mid-crustal tectonic architecture of evolving orogenic systems [*Hodges*, 2003]. In contrast to lower temperature chronometers such as apatite (U-Th)/He and fission track, the nominal closure isotherm for $^{40}Ar/^{39}Ar$ is relatively unaffected by topography such as that found in the Himalayas [*Mancktelow and Grasemann*, 1997; *Stüwe, et al.*, 1994], while remaining useful for characterizing changes in exhumation rates through the middle crust.

Due in part to the difficulties in accessing much of the steep topography of the Himalaya, most available bedrock $^{40}Ar/^{39}Ar$ dates from central Nepal are confined to widely spaced river valleys and roadways [*Bollinger, et al.*, 2004; *Copeland, et al.*, 1991; *Edwards*, 1995; *Macfarlane, et al.*, 1992]. In addition, the low metamorphic grade of rocks from the Lesser Himalayan Sequence makes micas difficult to extract from these lithologies, leading to a sampling bias toward the higher grade Greater Himalayan Sequence. Bedrock cooling ages from available samples in central Nepal typically range from middle Miocene to early Pliocene, with an apparent northward younging from ~20 Ma to ~3 Ma within the Kathmandu allochthon [*Bollinger, et al.*, 2004]. Notably, some exceptionally old ages have been reported from the Lesser Himalayan Sequence rocks structurally beneath the Kathmandu allochthon [*Copeland, et*

al., 1991], directly indicating a lack of Himalayan-aged thermal resetting in at least part of that sequence.

Many of the problems related to poor access and lithology can be eliminated by using detrital thermochronology to characterize the integrated cooling history of complete drainage basins [*Hodges, et al.*, in press]. Recent detrital $^{40}Ar/^{39}Ar$ thermochronologic investigations of modern sediments from central Nepal have begun to provide a more complete picture of cooling ages in the high Himalayas [*Brewer, et al.*, 2003; *Ruhl and Hodges*, in press], with a distribution of ages that is broadly consistent with the Middle Miocene to Early Pliocene ages reported for bedrock samples from the same region. Farther to the south, detrital samples from small basins within the Lesser Himalayan Sequence corroborate reports of exceptionally old bedrock cooling ages in the Lower Himalaya [*Wobus, et al.*, 2003]. One of the goals of this contribution is to evaluate the persistence of this cooling age discontinuity along strike.

4.2 Methods

The sampling strategy for this study was designed to mimic that of Wobus et al. (2003) in the Burhi Gandaki river. Modern river sediments were collected from six tributaries to the Trisuli river and six tributaries to the Bhote Kosi river, with drainage areas ranging from ~9 to 52 km^2. Because the basins sampled feed large trans-Himalayan trunk streams, they are generally oriented parallel to the structural grain of the orogen and therefore sample small strike-parallel swaths of the landscape (Figure 1b). Together, the tributary basins for each river system constitute a strike-normal transect that can be compared with transects for other river systems. Samples were collected from small bars within the active channel, focusing on the medium to coarse sand size fraction. As in the Burhi Gandaki river, thick fill terraces within the Trisuli and

Bhote Kosi trunk stream valleys suggest a period of extensive basin infilling across much of the physiographic Lower Himalayas. In order to avoid contamination of tributary sediments with inputs from these trunk stream terraces, basins with clear evidence of recent infilling were sampled up to 2 km upstream from the tributary mouths. Sample volumes ranged from ~2-4 liters.

Samples were washed, dried and sieved to remove any organic material and to isolate size fractions for mineral separations. Muscovites were separated using standard mineral separation techniques, focusing on the 500-1000 μm size fraction where possible. In some cases, finer-grained lithologies from the tributary basins required muscovites to be picked instead from the 250-500 μm fraction. In all cases, final mineral separates were picked by hand to ensure sample purity. Following mineral separation, muscovite separates were packaged in aluminum foil and sent to the McMaster University nuclear reactor for irradiation, using Taylor Creek sanidine as a neutron flux monitor (28.34 $\pm$ 0.16 Ma; [*Renne, et al.*, 1998]).

Irradiated muscovite grains were loaded into stainless steel planchets and before loading into the vacuum system. Gas was liberated from each sample by total fusion using an argon ion laser, gettered between 5 and 10 minutes, and analyzed on an MAP 215-50 mass spectrometer with an electron multiplier detector. For each sample, between 50 and 100 single muscovite grains were analyzed. This analytical procedure differs from that of Wobus et al. (2003), in which high spectrometer blanks and small grain sizes required multiple-grain aliquots to be fused for each analysis. The analytical procedure used here ensures that each analysis represents a single grain with a unique cooling history, rather than a mixture of gas from multiple grains that may have diverse cooling histories and thus may mask some discrete modes in the distribution of ages. Data were reduced using ArArCalc [*Koppers*, 2002], with all blanks air corrected. In rare

cases, high spectrometer blanks or poorly fused samples yielded very low radiogenic ^{40}Ar yields. Analyses reported here are limited to those with radiogenic yields greater than 50%, representing 77% of the samples analyzed in the Trisuli and 96% of the samples analyzed in the Bhote Kosi.

4.3 Results

Both the Trisuli and the Bhote Kosi transects are characterized by a sharp break in $^{40}Ar/^{39}Ar$ ages from north to south (Figure 5). Cooling ages from basins in the north are middle Miocene and younger, while apparent ages from basins in the south are early Proterozoic through Paleozoic (Table 1; Appendix 1). The sharp break in cooling ages from north to south is consistent with thermochronologic data from the Burhi Gandaki valley, which indicate a northward increase in the total depth of exhumation across the physiographic transition [*Wobus, et al.*, 2003]. The general continuity of this cooling age signal along strike suggests that this northward increase in the total depth of exhumation across the range may be regionally extensive.

Using the break in physiography as a proxy for a break in rock uplift rates, we would predict that discontinuities in cooling ages through central Nepal should coincide exactly with the position of PT_2, which lies along a line oriented slightly south of east between the Burhi Gandaki and Bhote Kosi rivers (Figures 3-4) [*Wobus, et al.*, in press; *Wobus, et al.*, 2003]. In the Bhote Kosi valley, the break from Miocene to Proterozoic cooling ages lies directly along the eastward projection of PT_2 (Figure 5b), supporting a model in which sharp across-strike changes in exhumation history may continue from the Burhi Gandaki eastward. In the Trisuli valley, however, the break in cooling ages lies nearly 15 kilometers north of PT_2 as defined geomorphically, suggesting a somewhat more complicated tectonic architecture (Figure 5c).

The bedrock geology in the Trisuli valley changes near PT_2 from Kuncha Formation phyllites, schists and psammites to the much more resistant Ulleri augen gneiss. Both of the samples yielding Proterozoic ages from the north side of PT_2 are derived from this augen gneiss, and many of the apparent $^{40}Ar/^{39}Ar$ ages approach the U-Pb ages of ~1.85 Ga reported for the Ulleri augen gneiss in western and central Nepal [*DeCelles, et al.*, 2000]. These extremely old ages suggest that this body of the Ulleri augen gneiss has experienced very little burial and re-exhumation during Himalayan orogenesis. The much younger (Miocene) ages immediately to the north indicate a sharp discontinuity in exhumation history along the northern limit of the Ulleri augen gneiss. Notably, the Miocene samples to the north are derived almost entirely from the hanging wall of a Main Central Thrust sidewall ramp [*Macfarlane, et al.*, 1992] (Figure 1b), suggesting that the MCT has been responsible for the differential exhumation juxtaposing the old and young cooling ages in the Trisuli valley [*Macfarlane*, 1993].

The southern limit of the Ulleri augen gneiss in the Trisuli valley lies at PT_2. If the profound change in physiography in the lower Trisuli valley is the surface manifestation of an active thrust, rather than simply reflecting differences in rock strength between the Ulleri augen gneiss and underlying Kuncha Formation phyllites, then the relative continuity in cooling ages between the Ulleri augen gneiss and the underlying Kuncha Formation requires that active thrusting has been relatively short-lived here. More protracted thrusting would juxtapose rocks with diverse muscovite cooling ages, but a complete lack of surface thrusting would be difficult to reconcile with the sharpness of PT_2. Although the contacts between the Ulleri and the underlying phyllites were not observed in the field, the thermochronologic data from the north and the geomorphic data from the south suggest that the Ulleri augen gneiss may be fault bounded on both its northern and its southern sides in the Trisuli valley, an interpretation similar

to that of Pearson and DeCelles (in press). We speculate that the more complicated structural configuration in the Trisuli valley may be related to strong rheologic contrasts between the Ulleri augen gneiss and the surrounding phyllites, and/or to the geometric configuration of the MCT sidewall ramp along the east side of the Trisuli valley (Figure 1b). Additional data from low temperature thermochronometers such as (U-Th)/He apatite would provide important additional constraints on the cooling histories across PT_2, which might help to resolve the tectonic configuration in the lower Trisuli valley.

The transition from young (Miocene) to very old (Paleozoic-Proterozoic) ages in all three transects appears to be a robust and tectonically significant result. However, we note that the old apparent ages from samples to the south of PT_2 are characterized by extremely wide age variability within individual samples and poor precision on individual analyses. This poor data quality is most likely a result of an analytical design that was optimized for Miocene samples: as a consequence, these older grains were substantially under-irradiated. Since the magnitude of the radiogenic ^{40}Ar peak dictates the amount of gas that can be analyzed with the electron multiplier detector without saturating this detector, ^{39}Ar peaks became very small, and the associated measurement error propagated into large age errors. Thus, the absolute ages from the south side of the physiographic transition should be viewed with caution. What we can say with confidence, however, is that none of the samples to the south of PT_2 (and samples 03WTS4 and 01WTS1 on the north side of the transition in the Trisuli drainage) has experienced any significant loss of radiogenic argon during Himalayan orogenesis. This finding places important constraints on the range of thermal histories, and therefore tectonic histories, that these samples may have experienced during the growth of the orogen. In the sections that follow, we employ a

simple thermal model to evaluate the range of tectonic geometries that could be consistent with the patterns of ages observed in these three transects.

5. Thermal Modeling

5.1 Model setup

Our thermal model was designed to explore the range of tectonic geometries that can produce a change from reset to unreset cooling ages at PT_2. A model of steady thrusting over a ramp in the MHT [*Cattin and Avouac*, 2000], if sustained for a timescale necessary to exhume rocks in the hanging wall from a depth corresponding to the muscovite closure isotherm, will predict reset cooling ages throughout the LHS, and is therefore inconsistent with our observed data. A model of surface thrusting, if sustained long enough, will always create a break in cooling ages coincident with the physiographic transition [*Wobus, et al.*, 2003], and is therefore consistent with our observations given the proper range of hanging wall exhumation rates [*Brewer*, 2000]. We therefore focus our modeling efforts on the continuous accretion model of Bollinger et al. (2004). In particular, we seek a range of model parameters that can produce a break in cooling ages co-located with PT_2 for a prescribed structural geometry

To simplify the problem, we focused our model domain on the ramp in the MHT, which we assume to dip northward at approximately 18 degrees [*Avouac*, 2004; *Lave and Avouac*, 2001]. Our model grid was 100 km wide by 60 km deep, with a horizontal resolution of 1000 meters and a vertical resolution of 325 meters. Under our simplified geometry, the upper boundary of the model represents the elevation at the MHT flat (Figure 6). This upper boundary was assigned a constant temperature boundary condition in both the hanging wall and the footwall: in the footwall of the MHT, we assign this upper boundary condition a temperature of

100°C; this relatively low temperature was chosen to approximately match the temperatures at this depth from existing thermal models, and might be expected due to the presence of a cold Indian slab underthrusting along the MHT [*Brewer and Burbank*, in review; *Henry, et al.*, 1997; *Huerta, et al.*, 1996]. In the hanging wall, we assign a higher temperature of 150°C at this upper boundary, to reflect the additional ~1.5 kilometers of topography in the hanging wall of the MHT. Note that these boundary conditions, while clearly over-simplified, should not significantly influence the geometry of the 350°C isotherm in our region of interest near the MHT ramp.

The boundary conditions along the sides were assumed to be constant temperature, steady-state geotherms. Heat production was assumed to be layered, with 15 km thick heat producing layers with radioactivity of 2e-6 and 1.5e-6 Wm^{-3} for the hanging wall and footwall of the MHT, respectively. The lower layer was assumed to have heat production of 1e-6 Wm^{-3} in both units. Our upper crustal heat production values are comparable to those reported elsewhere for the GHS and LHS [*Macfarlane*, 1992] and used in other thermal models for the Himalaya [*Bollinger, et al.*, 2004; *Henry, et al.*, 1997; *Huerta, et al.*, 1996]. Our lower crustal heat production value is slightly higher than that used by Henry al. (1997) and Bollinger et al. (2004). We chose this higher heat production value in the lower crust to reproduce reasonable 1-D geotherms for the LHS and the GHS at depth.

The model was run using a 2-D finite differencing algorithm, assuming a thermal diffusivity of 1e-6 m^2s^{-1} and a thermal conductivity of 2.5 $Wm^{-1}K^{-1}$. For consistency with previous modeling efforts, fault-parallel convergence rates of 5 mm/yr and 15 mm/yr were used for the hanging wall overthrusting and footwall underthrusting rates, respectively [*Brewer and Burbank*, in review; *Bollinger, et al.*, 2004]. The model was initially run to create a steady-state

thermal structure, assuming that all motion occurs along the MHT with no accretion. This scenario may provide a reasonable simulation for the early evolution of the Himalaya, prior to the development of the Lesser Himalayan duplex and structures farther south. The model was found to be thermally equilibrated to the prescribed convergence velocities after ≤10 Myr, with a geometry of the closure isotherm similar to that observed in other thermal models for the Himalaya [*Henry, et al.*, 1997; *Huerta, et al.*, 1996] This thermal structure was then exported to a model in which accretion was allowed to occur along the ramp in the MHT.

In the accretion model, material was allowed to continue advecting parallel to the fault, and an additional component of advection was added across the fault to simulate accretion (underplating) of material to the hanging wall. We consider only the horizontal component of the accretion vector across the MHT ramp. The resulting velocities in the hanging wall and footwall are simple vector sums of the fault-parallel convergence velocity and the underplating velocity. The co-evolving kinematic and thermal states could then be used to evaluate the expected distribution of cooling ages at the surface.

5.2 Model results

As the accretion velocity approaches zero, the model simulates a tectonic scenario where thrusting is sustained along a discrete fault corresponding to the MHT. This scenario can be assumed to replicate either of two endmember cases for the tectonics of central Nepal: if the ramp on the MHT is presumed to remain buried and merge with the approximately flat décollement in the physiographic Lower Himalayas (Figure 2a), we would predict a break in rock uplift rates at the surface without a sharp break from reset to unreset ages. This structural geometry would instead produce a smooth increase in cooling ages from north to south, as the

transport time from the closure isotherm increases toward the foreland [*Brewer and Burbank*, in review]. The presence of unreset $^{40}Ar/^{39}Ar$ cooling ages in the LHS, as reported here for three different transects from trans-Himalayan river systems, would appear to preclude such a structural configuration persisting over long timescales.

If the MHT ramp is instead presumed to merge into a surface breaking thrust (Figure 2c), all rocks to the north of this surface faulting should be reset, while all those to the south should remain unreset. This first-order result is insensitive to the overthrusting and underthrusting rates across the MHT: given sufficient time for rocks in the hanging wall to reach the surface, this geometry will always create a break from reset to unreset cooling ages co-located with the break in rock uplift rates. In this case, a surface-breaking thrust provides a simple explanation for the change in rock uplift rates and the change in cooling ages, consistent with the interpretations proposed in [*Wobus, et al.*, 2005] and [*Wobus, et al.*, 2003].

We explored a range of models with varying rates of accretion across the MHT ramp [*Bollinger, et al.*, 2004]. Because accretion adds cold material from the footwall to the hanging wall, the geometry of the 350°C isotherm gradually relaxes through these model runs. Despite this gradual thermal relaxation due to accretion, however, the position of the break in cooling ages at the surface is dictated to first order by kinematics, and only secondarily by the thermal structure. Determining the position of the break in cooling ages therefore becomes largely a geometric problem, as discussed below.

In a model of continuous accretion, the particle paths in the hanging wall are a vector sum of the rate of accretion and the rate of hanging wall overthrusting. If we assume that the rate of accretion approaches a steady value, the position of the cooling age break can therefore be determined by projecting a line from the intersection of the closure isotherm and the MHT to the

surface along one of these particle paths (Figure 6). Because the inflection in the particle trajectories occurs at the base of the accretion zone (i.e., the MHT), the most important contribution from the thermal model is determining where the closure isotherm intersects the MHT ramp. Even with substantial thermal relaxation due to accretion of cold material from the footwall to the hanging wall, this position (marked "C" on Figure 6) does not vary significantly as the rate of duplexing is changed. For a given set of thermal parameters (e.g., heat production, thickness of heat producing layers, diffusivity, thermal conductivity) and structural geometries (e.g., dip of MHT ramp, depth of decollement at the position of the physiographic transition) we can therefore predict the position of the cooling age break at the surface within a relatively narrow range of uncertainties introduced by the thermal state in the upper crust. For brevity, we discuss here only the results of the kinematic/thermal model using thermal and structural parameters similar to those used by Bollinger et al., (2004).

As dictated by our simple kinematic framework, the position of the break in cooling ages at the surface migrates northward as the rate of accretion increases (Figure 7). Using the particle trajectories determined by the kinematic model, and assuming decollement depths between 5-10 km at the position of the physiographic transition, we find that the position of the cooling age break coincides with the position of the uplift rate break for an accretion velocity between ~1.8 – 2.5 mm/yr. This rate of accretion is considerably smaller than the upper limit of ~15 mm/yr calculated by Bollinger et al. (2004) assuming an undeforming footwall that is passively incorporated into the hanging wall by frontal accretion across the MHT ramp.

6. Discussion

The prominent discontinuity in cooling ages first observed in the Burhi Gandaki river [*Wobus, et al.*, 2003] appears to be regionally extensive in the central Nepalese Himalaya, continuing along strike nearly 100 km eastward to the Bhote Kosi river. Such a pattern of cooling ages requires a northward increase in the total depth of exhumation along each of the three trans-Himalayan transects analyzed here. To first order, either a tectonic model with surface thrusting at the physiographic transition or a model including accretion along a buried ramp in the MHT is capable of reproducing this observed distribution of $^{40}Ar/^{39}Ar$ cooling ages. Active surface thrusting will produce a sharp break in cooling ages coincident with a sharp change in surface uplift rates and physiography, regardless of the details of overthrusting rate, underthrusting rate, and tectonic geometry. An accretion model might imply more diffuse topographic gradients, and requires a narrow range of geometric and kinematic constraints in order to produce the observed pattern of cooling ages across the physiographic transition. We speculate that the along-strike changes in physiography observed in central Nepal may be related to along-strike variations in tectonics, both in terms of the degree to which recent structures are developed and in terms of the proximity of neotectonic displacements to longer-lived structures such as the Main Central Thrust.

In the Marsyandi valley, relatively diffuse changes in physiography overlap with the observed surface trace of the MCT. Penetrative brittle deformation extending at least 10 km south from the MCT and postdating Pliocene muscovite growth suggests Quaternary displacements along these brittle structures [*Hodges, et al.*, 2004]. Neotectonic displacements in the Marsyandi valley therefore appear to correspond to a wide zone of recent strain broadly coincident with the Main Central Thrust. To the east in the Burhi Gandaki valley, more abrupt

changes in physiography are co-located with a break in cooling ages and erosion rates approximately 20 km south of the MCT [*Wobus, et al.*, 2005; *Wobus, et al.*, 2003]. These observations strongly favor a model including surface displacements on a newly developed thrust at PT_2. Strong lithologic contrasts in the Trisuli valley, superimposed on the physiographic transition without a sharp break from reset to unreset $^{40}Ar/^{39}Ar$ ages, complicate the tectonic picture somewhat, but remain consistent with a model of surface thrusting assuming shallow to moderate depths of exhumation in the hanging wall. Finally, in the Bhote Kosi transect furthest to the east, relatively gradual changes in physiography coupled with a sharp break in $^{40}Ar/^{39}Ar$ cooling ages might imply more distributed gradients in rock uplift rates, possibly favoring a model of more penetrative foliation-parallel displacements in the hanging wall of the MHT.

If our inferences are correct, the along-strike differences in tectonic architecture may reflect varying stages of structural development in an evolving tectonic system (Figure 8). The first stage is characterized by accretion along the basal ramp. During this stage, shear zones develop parallel to the metamorphic foliations above the basal ramp, broadly deforming the hanging wall above [*Bollinger, et al.*, 2004]. Eventually, focused erosion above the zone of accretion exposes one or more of these foliation-parallel shear zones at the surface. This surface-breaking thrust then becomes the primary locus of deformation, along which hanging wall overthrusting can be accommodated as a steady-state structural configuration.

The variations in physiography, cooling history, and structural geometry across the central Nepalese Himalaya suggest that we may be witnessing multiple stages of this structural evolution during our snapshot in time. On one extreme, sharp changes in physiography, cooling history and surface uplift rates in the Trisuli and Burhi Gandaki valleys indicate a fully developed, surface-breaking thrust. On the other extreme, most maps show that the Mahabarat

Thrust is not offset by major deformational features associated with PT_2, and the presence of Tertiary $^{40}Ar/^{39}Ar$ ages throughout the Kathmandu allochthon without a sharp discontinuity in ages from south to north suggest a system that has not yet been breached. These along-strike contrasts suggest that surface-breaking structures in the Trisuli and Burhi Gandaki drainages may be in the process of propagating eastward. To the west in the Marsyandi river, the near-coincidence of the physiographic transition with the surface trace of the MCT suggests that recent displacements may be reactivating older structures associated with the Main Central Thrust. Continued structural development may eventually lead to a system in which a single surface-breaking shear zone is fully developed throughout central Nepal.

Because our data include limited structural measurements, broadly based geomorphic observations, and thermochronometers sensitive only to middle-crustal temperatures, our inferences about along-strike variability in tectonics remain somewhat equivocal. However, with the proper combination of additional structural measurements and thermochronologic data, the viability of either tectonic model can be tested more completely. For example, the kinematic geometries implied by each of the models should create distinct structural relationships in the hanging wall of the MHT, and the patterns of cooling ages at the surface should also be distinct for the two models if both high and low temperature thermochronometers are combined. Below, we summarize a range of additional geologic data that we have, and discuss additional data needed in order to better evaluate how the tectonic architecture might vary along strike.

Field observations in all of the drainages studied document consistently northward dipping foliations and a northward plunging stretching lineation along the physiographic transition. Although we commonly found evidence of tectonic slip parallel to the dominant foliation in these drainages (e.g., slickenlines, sheared phyllites interspersed with more resistant

psammites), we did not observe any major structures crosscutting the metamorphic fabric. The lack of a "master" fault oblique to the metamorphic foliation at PT_2 requires that the tectonic displacements in the hanging wall are accommodated along foliation-parallel shear zones, which may be consistent with either an accretion or a surface thrusting model.

If we had more extensive structural measurements upstream and downstream from PT_2, we might be able to more narrowly constrain the tectonic architecture in each transect. For example, an accretion model predicts that uplift in the hanging wall of the MHT is largely passive, such that foliations should be rotated hinterland with each successive thrust sheet accreted from the footwall to the hanging wall (Figure 8). This hypothesis could be tested by detailed structural mapping of long transects extending across the physiographic transition: if foliations systematically steepen northward and consistently exhibit penetrative foliation-parallel shear, this observation might support a model of continous accretion across the physiographic transition. Note, however, that the structural relationships preserved in central Nepal are complicated by a poorly understood tectonic stratigraphy, such that even these additional data might remain equivocal.

All three transects sampled lie within the "inverted metamorphic sequence" of central Nepal, but it is notable that the abrupt changes in physiography and cooling history in the Burhi Gandaki and Bhote Kosi rivers are superimposed on far more gradual changes in lithology and metamorphic grade. A change in uplift and exhumation history without a sharp change in metamorphic grade requires that surface thrusting, if present, has been relatively short-lived. The gradual changes in metamorphic grade are also consistent with an accretion model, since exhumation in this model is accommodated along foliation-parallel shear zones without juxtaposing heterogeneous lithologies or facies. The presence of the Ulleri augen gneiss in the

Trisuli drainage marks a sharp change in lithology at the physiographic transition, making changes in metamorphic grade more difficult to assess.

In our simplified geometric solution to the accretion problem, we have assumed that the closure of the muscovite system to diffusive loss of argon occurs at a discrete temperature. In fact, the closure of muscovite depends in a nonlinear way on both temperature and cooling rate, both of which will evolve for a given particle as it is transported through the upper crust [*Dodson*, 1973]. Because many of the particle paths for the accretion model include prolonged transport of material subparallel to the closure isotherm in the footwall, the break in cooling ages at the surface may not be as abrupt as our simplified kinematic modeling would predict. An accretion geometry might instead create a zone of partial argon loss at the surface between the fully reset ages to the north of the physiographic transition and the fully unreset ages to the south.

Although the precision is poor for our older apparent age samples, the $^{40}Ar/^{39}Ar$ results from the Burhi Gandaki and Bhote Kosi transects appear to follow a northward-younging trend approaching the physiographic transition from the south (Figure 5). If we assume that the oldest apparent age in each transect is the original closure age, the data outline a zone of partial loss approximately 25 km wide in the Burhi Gandaki transect, and 20 km wide in the Bhote Kosi (Figure 9). These data are consistent with our predictions if particle paths are oriented subparallel to the closure isotherm prior to being accreted to the hanging wall of the MHT (e.g., Figure 5).

We note, however, that a similar northward-younging of cooling ages approaching PT_2 may also be a result of the irregular structural geometry of central Nepal. Between the Bhote Kosi and the Burhi Gandaki rivers, the Kathmandu allochthon accounts for many of the surface

exposures in the physiographic Lower Himalaya, such that the Lesser Himalayan units in the lower Burhi Gandaki, Trisuli and Bhote Kosi drainages lie structurally beneath the allochthon (Figure 1). The origin of this thrust sheet and its relation to the MCT remain unclear [*Gehrels, et al.*, 2003; *Hodges*, 2000], but the geometry of this allochthon indicates that the lower Burhi Gandaki, Trisuli and Bhote Kosi drainages are tectonic windows through a formerly more extensive thrust sheet. Assuming high heat production in the Kathmandu allochthon and rapid erosion, it is possible that the emplacement of a thin crystalline thrust sheet over the LHS in central Nepal may have been a sufficient thermal perturbation to create the partial argon loss signal now observed in the Burhi Gandaki and Bhote Kosi transects [*Royden*, 1993]. Deformation may then have stepped back closer to the present position of the MCT, where more focused exhumation persisted for longer timescales prior to the development of recent surface thrusting at the physiographic transition.

The addition of data from low-temperature thermochronometry such as (U-Th)/He apatite would provide a useful test of whether the patterns of cooling ages approaching the physiographic transition are related to the geometry of particle paths in the footwall of the MHT. For example, the particle trajectories implied by an accretion model should create a zone of reset (U-Th)/He apatite ages at the surface in which the $^{40}Ar/^{39}Ar$ ages are not reset. This spatial offset between the reset zones for different temperature thermochronometers would be less likely in a surface thrusting architecture, since this geometry at steady state provides no mechanism of passing through the lower temperature closure isotherm without first passing through the higher one. This distinction might be complicated somewhat by the possibility of footwall heating from a rapidly exhuming hanging wall, but would provide additional evidence to support or reject alternative structural geometries.

7. Conclusions

Physiographic transition PT_2 between the Lower and the Higher Himalaya in central Nepal results from spatial gradients in rock uplift rates over relatively short length scales. As evidenced by detrital $^{40}Ar/^{39}Ar$ data from the Burhi Gandaki, Trisuli and Bhote Kosi valleys, these gradients in rock uplift have persisted at least long enough to juxtapose rocks with very different cooling histories across the physiographic transition. Simple thermal and kinematic modeling suggests that this break in cooling ages may be consistent with structural geometries ranging from active thrusting at the surface to accretion at depth. Along-strike changes in the position and nature of the physiographic transition through central Nepal may reflect variability in this structural style across length scales of less than 100 km along strike, possibly reflecting varying stages of development in an evolving tectonic system.

One of the variables that might control the relative maturity of this evolving system is surface erosion. In a system with only weak or moderate erosion, accretion at depth may be the favored tectonic mode, passively uplifting the surface above it while allowing the orogen to widen foreland. The sharp physiographic transition observed in the Burhi Gandaki and Trisuli valleys suggests that much of the tectonic displacement in central Nepal has been upward, rather than outward, in recent time. This upward growth requires a mechanism for removing material at the surface as it is replenished at depth. The breaching of a passively uplifted MHT hanging wall by surface erosion may have provided such a mechanism, allowing exhumation to become concentrated along discrete structures through much of central Nepal.

References

Avouac, J. P. (2004), Mountain building, erosion and the seismic cycle in the Nepal Himalaya, *Advances in Geophysics*, *48*.

Beaumont, C., et al. (2001), Himalayan tectonics explained by extrusion of a low-viscosity crustal channel coupled to focused surface denudation, *Nature*, *414*, 738-742.

Beaumont, C., et al. (2004), Crustal channel flows: 1. Numerical models with implications to the tectonics of the Himalayan-Tibetan orogen, *Journal of Geophysical Research*, *109*, doi: 10.1029/2003JB002811.

Bilham, R., et al. (1997), GPS measurements of present-day convergence across the Nepal Himalaya, *Nature*, *386*, 61-64.

Bollinger, L., et al. (2004), Thermal structure and exhumation history of the Lesser Himalaya in central Nepal, *Tectonics*, *23*.

Brewer, I. D. (2000), Detrital-mineral thermochronology: investigations of orogenic denudation in the Himalaya of Central Nepal, PhD thesis, Pennsylvania State University, University Park, PA.

Brewer, I. D., and D. Burbank (in review), Thermal and kinematic modeling of bedrock and detrital cooling ages in the Central Himalaya, *Journal of Geophysical Research*.

Brewer, I. D., et al. (2003), Modeling detrital cooling-age populations: insights from two Himalayan catchments, *Basin Research*, *15*, 305-320.

Burbank, D. W., et al. (2003), Decoupling of erosion and climate in the Himalaya, *Nature*, *426*, 652-655.

Catlos, E. J., et al. (2001), Geochronologic and thermobarometric constraints on the evolution of the Main Central Thrust, central Nepal Himalaya, *Journal of Geophysical Research*, *106*, 16177-16204.

Cattin, R., and J. P. Avouac (2000), Modeling mountain building and the seismic cycle in the Himalaya of Nepal, *Journal of Geophysical Research*, *105*, 13389-13407.

Copeland, P., et al. (1991), An early Pliocene thermal disturbance of the Main Central Thrust, central Nepal; implications for Himalayan tectonics, *Journal of Geophysical Research, B, Solid Earth and Planets*, *96*, 8475-8500.

DeCelles, P. G., et al. (2000), Tectonic implications of U-Pb zircon ages of the Himalayan orogenic belt in Nepal, *Science*, *288*, 497-499.

DeCelles, P. G., et al. (2001), Stratigraphy, structure, and tectonic evolution of the Himalayan fold-thrust belt in western Nepal, *Tectonics*, *20*, 487-509.

Dodson, M. H. (1973), Closure temperature in cooling geochronological and petrological systems, *Contributions to Mineralogy and Petrology*, *40*, 259-274.

Edwards, R. M. (1995), 40Ar/39Ar geochronology of the Main Central thrust (MCT) region: Evidence for Late Miocene to Pliocene disturbances along the MCT, Marsyangdi River valley, west-central Nepal Himalaya, *Journal of the Nepal Geological Society*, *10*, 41-46.

Gehrels, G. E., et al. (2003), Initiation of the Himalayan orogen as an early Paleozoic thin-skinned thrust belt, *GSA Today*.

Harrison, T. M., et al. (1997), A Late Miocene-Pliocene origin for the central Himalayan inverted metamorphism, *Earth and Planetary Science Letters*, *146*, E1-E7.

Hauck, M. L., et al. (1998), Crustal structure of the Himalayan Orogen at approximately 90³ east longitude from Project INDEPTH deep reflection profiles, *Tectonics*, *17*, 481-500.

Henry, P., et al. (1997), Kinematic, thermal and petrological model of the Himalayas: Constraints related to metamorphism within the underthrust Indian crust and topographic elevation, *Tectonophysics*, *273*, 31-56.

Hodges, K. (2003), Thermochronology of orogenic systems, in *Treatise on Geochemistry: The Crust, Vol. 3*, edited by R. L. Rudnick, Elsevier Science, Amsterdam.

Hodges, K., et al. (2004), Quaternary deformation, river steepening and heavy precipitation at the front of the Higher Himalayan ranges, *Earth and Planetary Science Letters*, *220*, 379-389.

Hodges, K. V. (2000), Tectonics of the Himalaya and southern Tibet from two perspectives, *GSA Bulletin*, *112*, 324-350.

Hodges, K. V., et al. (2001), Southward Extrusion of Tibetan Crust and its Effect on Himalayan Tectonics, *Tectonics*, *20*, 799-809.

Hodges, K. V., et al. (in press), 40Ar/39Ar geochronology of detrital minerals, in *Thermochronology*, edited by P. W. Reiners and T. A. Ehlers, Mineralogical Society of America, Washington, D.C.

Huerta, A. D., et al. (1996), The interdependence of deformational and thermal processes in mountain belts, *Science*, *273*, 637-639.

Jackson, M., and R. Bilham (1994), Constraints on Himalayan deformation inferred from vertical velocity fields in Nepal and Tibet, *Journal of Geophysical Research, 99*, 13897-13912.

Jamieson, R. A., et al. (2004), Crustal channel flows: 2. Numerical models with implications for metamorphism in the Himalayan-Tibetan orogen, *Journal of Geophysical Research, 109*, doi:10.1029/2003JB002811.

Kirby, E., and K. X. Whipple (2001), Quantifying differential rock-uplift rates via stream profile analysis, *Geology, 29*, 415-418.

Kohn, M. J., et al. (2001), Pressure-temperature-time path discontinuity in the Main Central thrust zone, central nepal, *Geology, 29*, 571-574.

Koons, P. O. (1995), Modeling the topographic evolution of collisional belts, *Annual Review of Earth and Planetary Sciences, 23*, 375-408.

Koppers, A. P. (2002), ArArCALC software for 40Ar/39Ar age calculations, *Computers & Geosciences, 28*, 605-619.

Lave, J., and J. P. Avouac (2001), Fluvial incision and tectonic uplift across the Himalayas of central Nepal, *Journal of Geophysical Research, 106*, 26561-26591.

Lyon-Caen, H., and P. Molnar (1983), Constraints on the structure of the Himalaya from an analysis of gravity anomalies and a flexural model of the lithosphere, *Journal of Geophysical Research, 88*, 8171-8191.

Macfarlane, A., et al. (1992), A structural analysis of the Main Central thrust zone, Langtang National Park, central Nepal Himalaya, *Geological Society of America Bulletin, 104*, 1389-1402.

Macfarlane, A. M. (1992), The Tectonic Evolution of the Core of the Himalaya, Langtang National Park, Central Nepal, Ph.D. thesis, Massachusetts Institute of Technology.

Macfarlane, A. M. (1993), The chronology of tectonic events in the crystalline core of the Himalayas, Langtang National Park, central Nepal, *Tectonics, 12*, 1004-1025.

Mancktelow, N. S., and B. Grasemann (1997), Time-dependent effects of heat advection and topography on cooling histories during erosion, *Tectonophysics, 270*, 167-195.

Molnar, P. (2003), Nature, nurture, and landscape, *Nature, 426*, 612-614.

Pandey, M. R., et al. (1995), Interseismic strain accumulation on the Himalayan crustal ramp (Nepal), *Geophysical Research Letters, 22*, 751-754.

Renne, P. R., et al. (1998), Intercalibration of standards, absolute ages and uncertainties in 40Ar/39Ar dating, *Chemical Geology (Isotope Geoscience section), 145*, 117-152.

Robinson, D. M., et al. (2003), Kinematic model for the Main Central Thrust in Nepal, *Geology, 31*, 359-362.

Royden, L. H. (1993), The steady state thermal structure of eroding orogenic belts and accretionary prisms, *Journal of Geophysical Research, 98*, 4487-4507.

Ruhl, K., and K. Hodges (in press), The use of detrital mineral cooling ages to evaluate steady-state assumptions in active orogens: An example from the central Nepalese Himalaya, *Tectonics*.

Schelling, D., and K. Arita (1991), Thrust tectonics, crustal shortening, and the structure of the far-eastern Nepal Himalaya, *Tectonics, 10*, 851-862.

Seeber, L., and V. Gornitz (1983), River profiles along the Himalayan arc as indicators of active tectonics, *Tectonophysics, 92*, 335-367.

Simon, J. (2005), Erosion-controlled geometry of buckle fold interference, *Geology, 33*, 561-564.

Snyder, N., et al. (2000), Landscape response to tectonic forcing: DEM analysis of stream profiles in the Mendocino triple junction region, northern California, *Geological Society of America, Bulletin, 112*, 1250-1263.

Stöcklin, J. (1980), Geology of Nepal and its regional frame, *Journal of the Geological Society of London, 137*, 1-34.

Stüwe, K., et al. (1994), The influence of eroding topography on steady-state isotherms. Application to fission track analysis, *Earth and Planetary Science Letters, 124*, 63-74.

Vannay, J.-C., et al. (2004), Miocene to Holocene exhumation of metamorphic crustal wedges in the NW Himalaya: Evidence for tectonic extrusion coupled to fluvial erosion, *Tectonics, 23*, doi: 10.1029/2002TC001429.

Vannay, J.-C., and K. V. Hodges (1996), Tectonometamorphic evolution of the Himalayan metamorphic core between Annapurna and Dhaulagiri, central Nepal, *Journal of Metamorphic Geology, 14*, 635-656.

Viskupic, K. M., et al. (2005), Timescales of melt generation and the thermal evolution of the Himalyan metamorphic core, Everest region, eastern Nepal, *Contributions to Mineralogy and Petrology, 149*, 1-21.

Whipple, K. X., and B. J. Meade (2004), Controls on the strength of coupling among climate, tectonics and deformation in two-sided, frictional orogenic wedges at steady state, *Journal of Geophysical Research-Earth Surface, 109*, doi: 10.1029/2003JF000019.

Willett, S. D. (1999), Orogeny and orography: the effects of erosion on the structure of mountain belts, *Journal of Geophysical Research, 104*, 28957-28981.

Wobus, C., et al. (in press), Tectonics from topography: procedures, promise and pitfalls, *GSA Special Penrose volume on tectonics, climate and landscape evolution.*

Wobus, C. W., et al. (2005), Active out-of-sequence thrust faulting in the central Nepalese Himalaya, *Nature*, *434*, 1008-1011.

Wobus, C. W., et al. (2003), Has focused denudation sustained active thrusting at the Himalayan topographic front? *Geology*, *31*, 861-864.

Zhao, W., et al. (1993), Deep seismic reflection evidence for continental underthrusting beneath southern Tibet, *Nature*, *366*, 557-559.

Figure Captions

1. Site location and sampling maps. a) Regional geologic map showing major tectonic structures and river systems. Dash-dot lines: MAR = Marsyandi river, BG = Burhi Gandaki river, TR = Trisuli river, BK = Bhote Kosi river. STF = South Tibetan fault. All other abbreviations in text. A-A' indicates location of schematic cross sections in figure 2. Grey box indicates location of Fig. 1b. b) Location of sediment samples (dots with basins outlined in white) and swath profiles (grey rectangles). White dots depict samples with Miocene and younger cooling ages; grey dots depict samples with Paleozoic and older apparent ages. Dashed basin outlines show previously reported data from [*Wobus, et al.*, 2003].

2. Simplified schematic diagrams showing three viable models for neotectonics in central Nepal. a) Thrusting is concentrated along the ramp in the MHT. Break in surface uplift rates and the position of the physiographic transition result from passive transport of hanging wall material over this ramp [*Cattin and Avouac*, 2000; *Lave and Avouac*, 2001]. b) Hanging wall beneath the physiographic transition is passively uplifted by accretion of material from the footwall to the hanging wall. Motion is accommodated along foliation-parallel slip planes in the hanging wall [*Bollinger, et al.*, 2004]. c) Active thrusting occurs at the physiographic transition. The break in surface uplift rates and the position of the physiographic transition result from differential motion along this fault [*Wobus, et al.*, 2005].

3. Three maps of physiographic data from central Nepal. a) Local relief calculated over a circular, 2.5-km radius window. b) Hillslope gradients, calculated over a 3x3 pixel (~260 meter) square window and smoothed with a 500m radius moving average. c) Map of knickpoints and steepness indices for major river systems of central Nepal and their tributaries (see text for description). Black arrows in a) and b) show PT_2 in the vicinity of the Burhi Gandaki and Trisuli valleys. In all three maps, white barbed line represents the surface trace of the MCT where it is well-constrained.

4. Swath profiles along five transects across the rangefront in central Nepal, arranged from west to east (see Figure 1 for locations) a) Marsyandi River b) Burhi Gandaki River; c) Trisuli River; d) Indrawati River; e) Bhote Kosi River. Swaths of topography, slope and relief are

shown for all transects. In all plots, dashed grey lines show minimum and maximum values within the swath, and black lines show mean values. Horizontal bars show the approximate extent of alluvial fills and terraces (T), knickpoints (K) and zone of increasing steepness index along trunk streams (S) projected onto swaths where these parameters are well defined. Vertical grey shading on plots of topography show the limits of the physiographic transition based on all available data, where the transition is well-defined in the Marsyandi, Burhi Gandaki and Trisuli rivers.

5. Distribution of $^{40}Ar/^{39}Ar$ cooling ages in transects along a) Burhi Gandaki, b) Trisuli, and c) Bhote Kosi rivers, projected onto lines oriented approximately N18°E. In each case, horizontal lines within grey boxes correspond to median ages, upper and lower limits of boxes correspond to 25th and 75th percentiles, and whiskers extend to the limits of the data or 1.5 times the interquartile range, whichever is greater. Small dots represent outliers beyond 1.5 times the IQR. Widths of boxes correspond to widths of basins projected onto section line. Dashed grey lines show the location of the physiographic transition in each transect (lines in Bhote Kosi show the eastward projection of the physiographic transition from the Trisuli valley, where it is well defined). Datum is taken as the position of the MCT along each transect. Note that this position is complicated by the geometry of the MCT in the Trisuli valley (see Figure 1); the northernmost position of the MCT is used as the datum in the Trisuli drainage.

6. Schematic of model setup and particle paths for a continuous model of accretion. Break in cooling ages at the surface will coincide with the physiographic transition only if the physiographic transition (point A) lies directly along a particle path from the intersection of the closure isotherm and the main décollement (point C). Our simplified model predicts this position at the top of our model domain (point B) using the following geometric constraints (see inset): α: dip of the MHT ramp; θ: angle between particle trajectory and the vertical; β: orientation of kink in particle trajectories above ramp tip (assumed to bisect the supplement to angle α); D_d: depth of décollement beneath physiographic transition.

7. Position of cooling age break at the surface for varying underplating velocities. Grey shaded zone along MHT ramp shows range of intersection points between 350°C isotherm and basal thrust through all model runs. 150°C, 350°C and 500°C isotherms are shown for initial steady-state condition with overthrusting and underthrusting rates of 5 mm/yr and 15 mm/yr, respectively, and no accretion (e.g., Bollinger et al., 2004; see text for description). Diagonal arrows show particle trajectories bounding reset and unreset ages for underplating velocities ranging from 1 to 4 mm/yr. Break in ages coincides with the physiographic transition for an underplating rate of ~1.8 mm/yr assuming a decollement depth of 5 km (dashed black line), or ~2.5 mm/yr assuming a decollement depth of 10 km (dashed grey line).

8. Schematic model for duplex evolution, following Bollinger et al. (2004). a-b) Duplex grows by addition of successive slivers of material from footwall to hanging wall (dashed lines), and upper plate deforms by foliation-parallel shear. Once surface erosion breaches the duplex (c), one of these roof thrusts may become a master fault localizing exhumation from the hanging wall directly to the surface.

9. Plots of apparent fractional $^{40}Ar^*$ loss vs. distance from MCT, using median age for each sample and assuming "true" age in each transect is represented by the oldest median age in each transect. Results are shown for a) Burhi Gandaki and b) Bhote Kosi rivers. Shaded region in each transect shows zone of apparent fractional argon loss, possibly due to heating from subhorizontal particle paths near the closure isotherm in the footwall, or heating from above by a thin crystalline thrust sheet (see text).

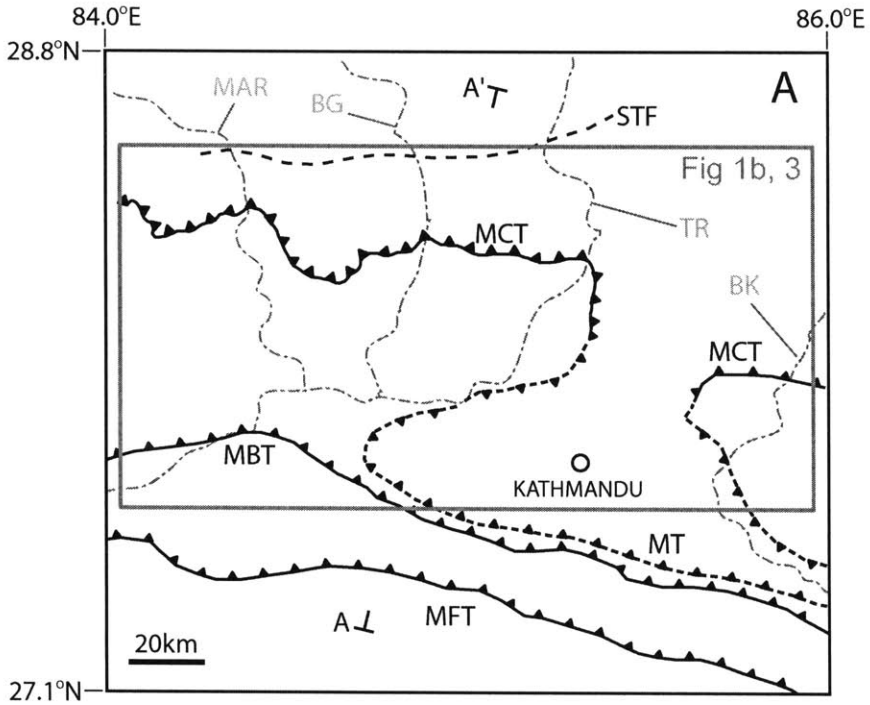

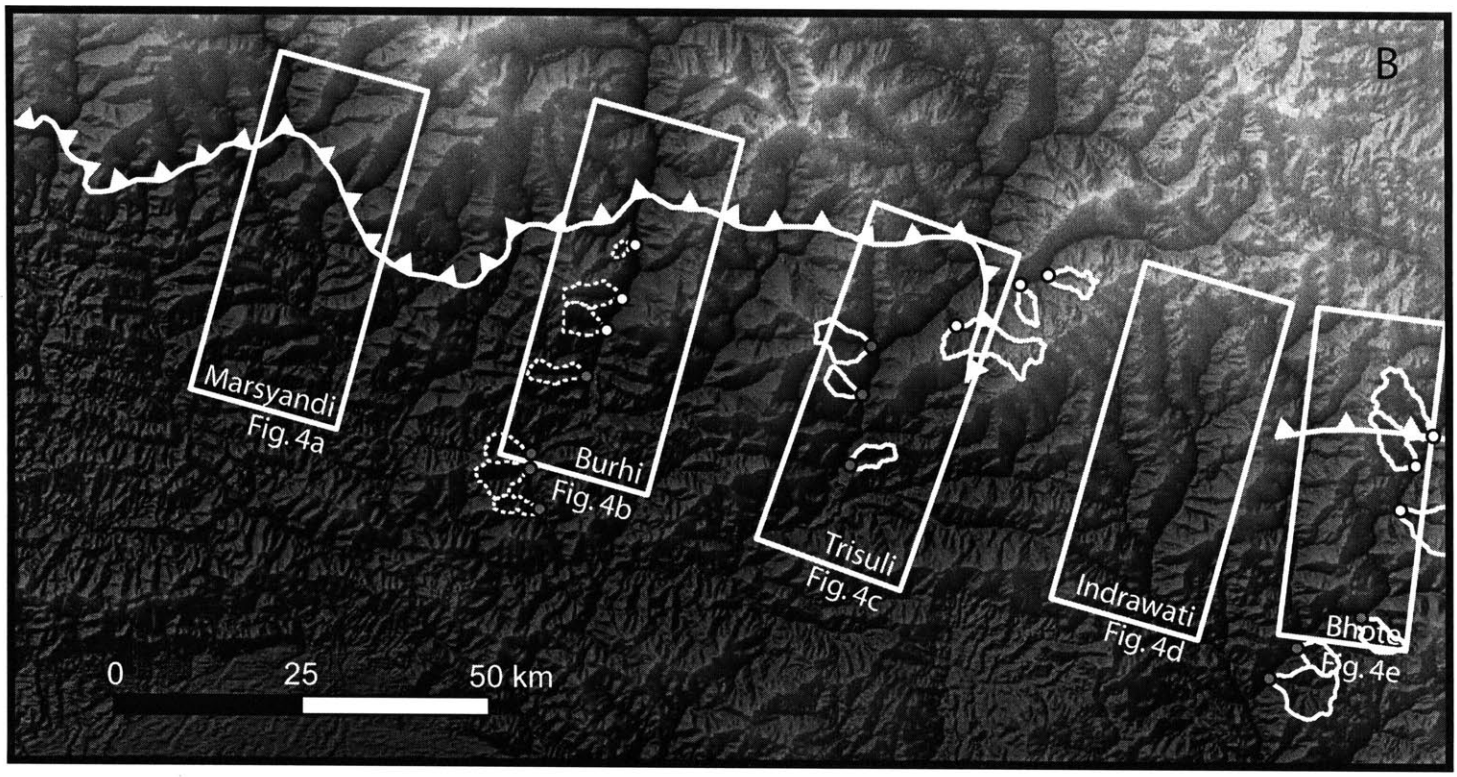

Wobus et al., Figure 1

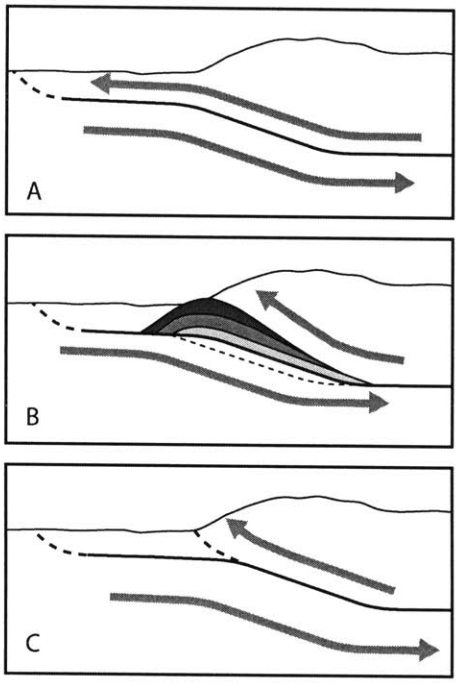

Wobus et al., Figure 2

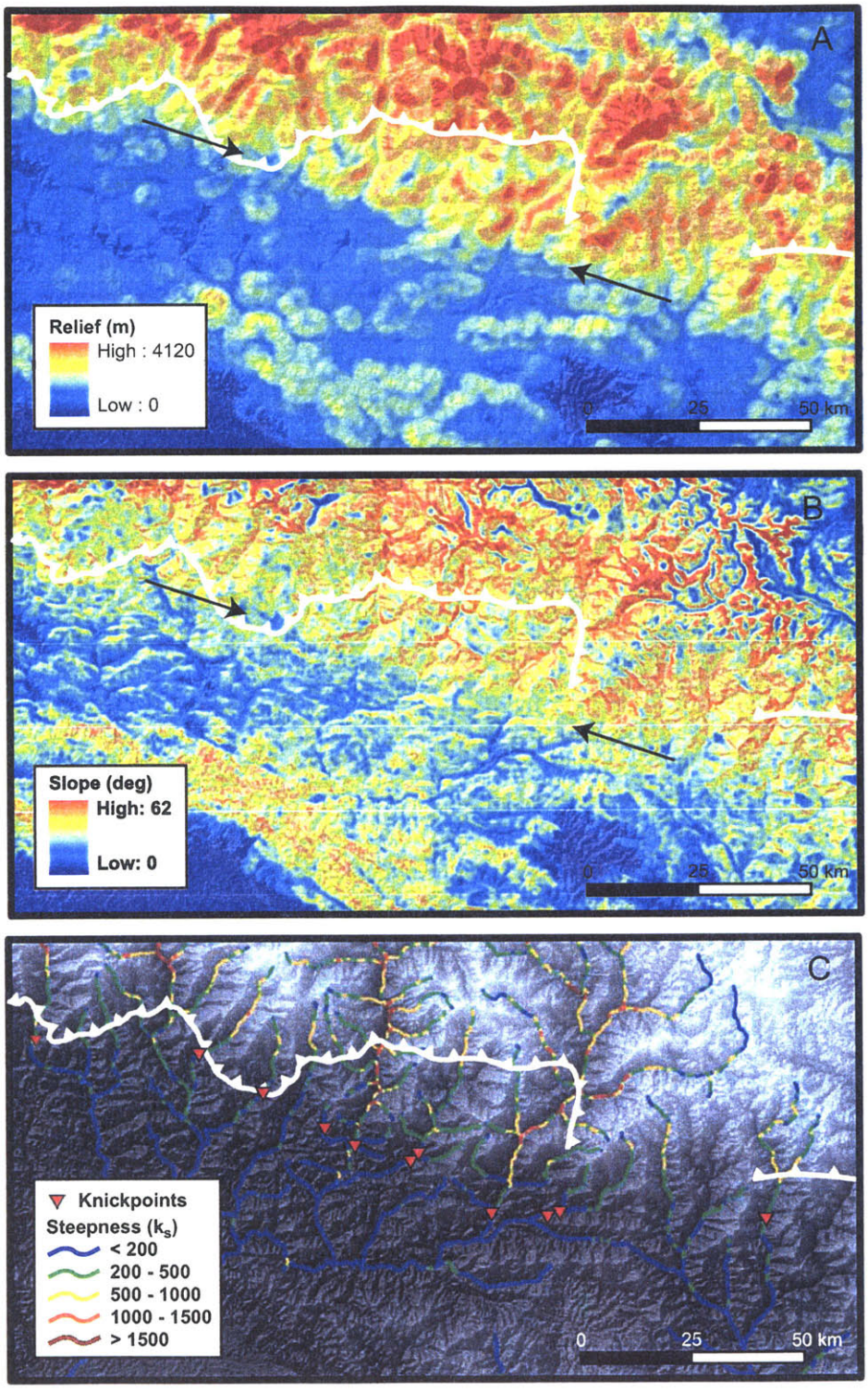

Wobus et al., Figure 3

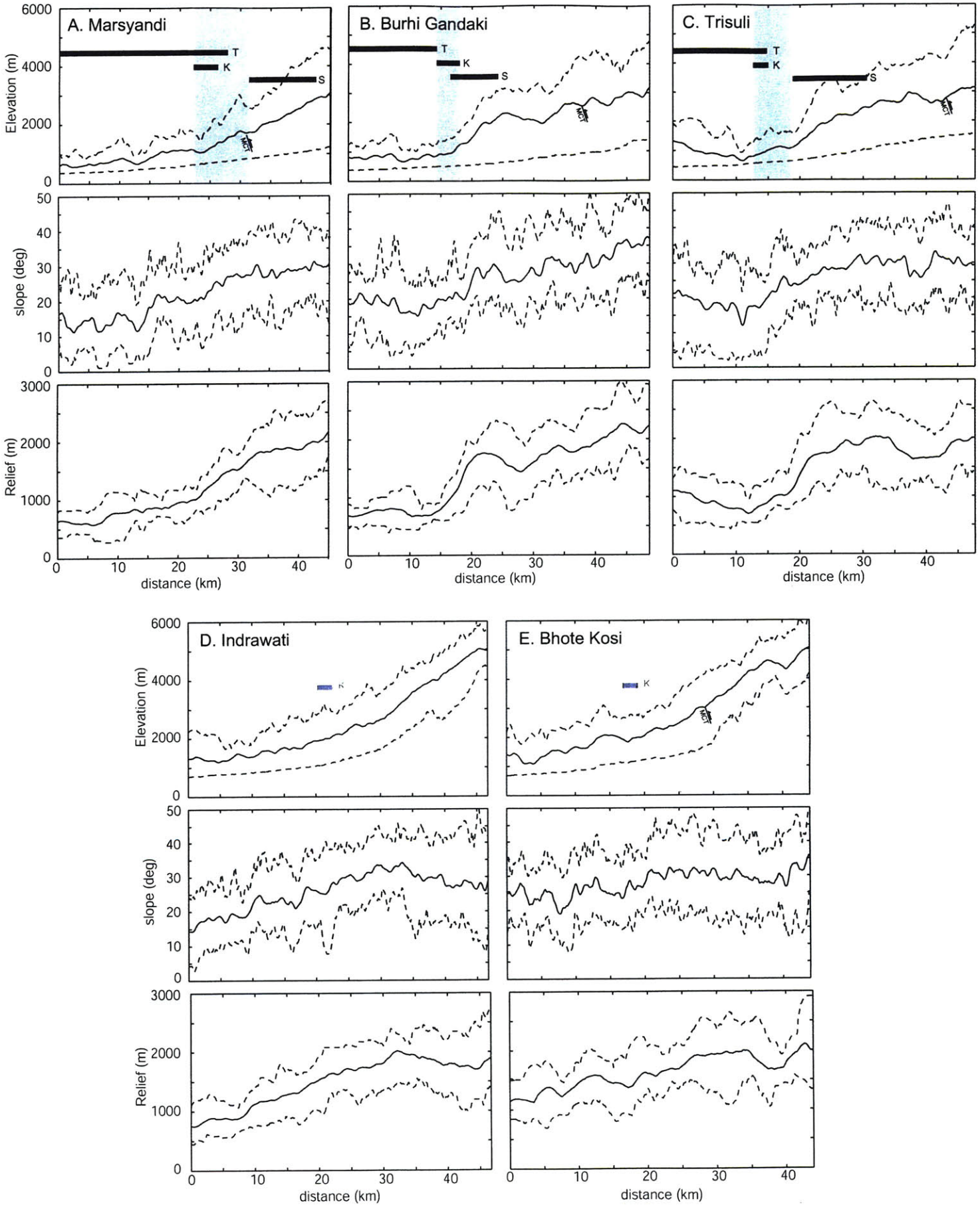

Wobus et al., Figure 4

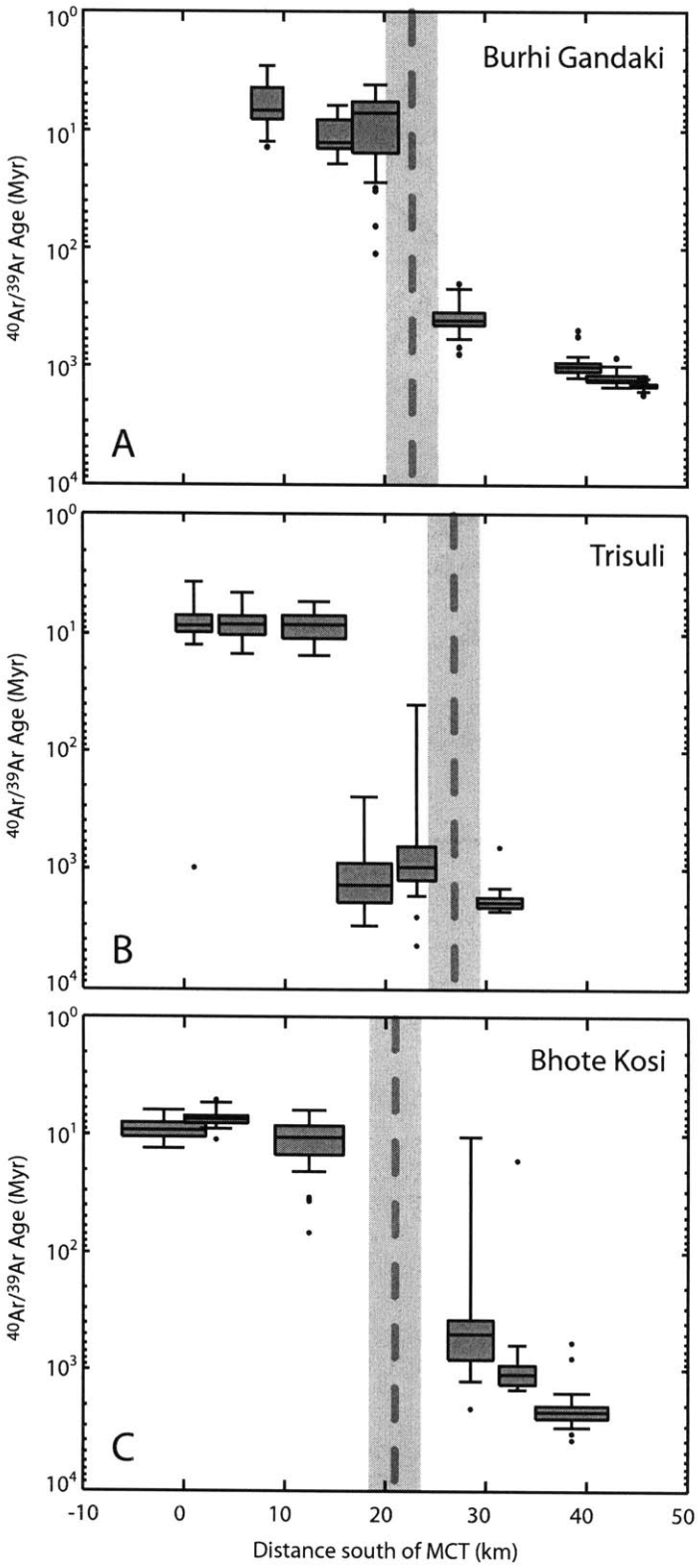

Wobus et al., Figure 5

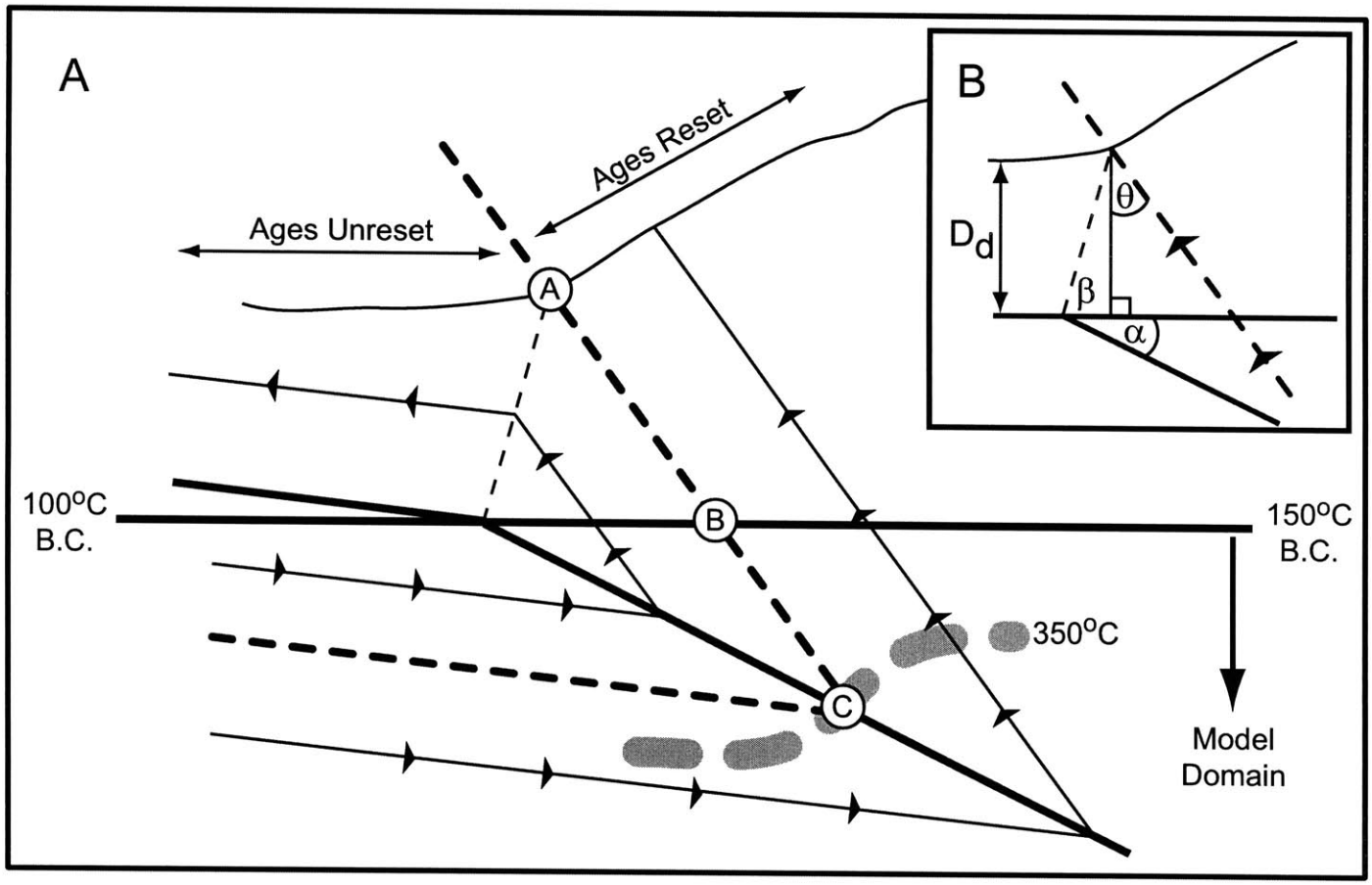

Wobus et al., Figure 6

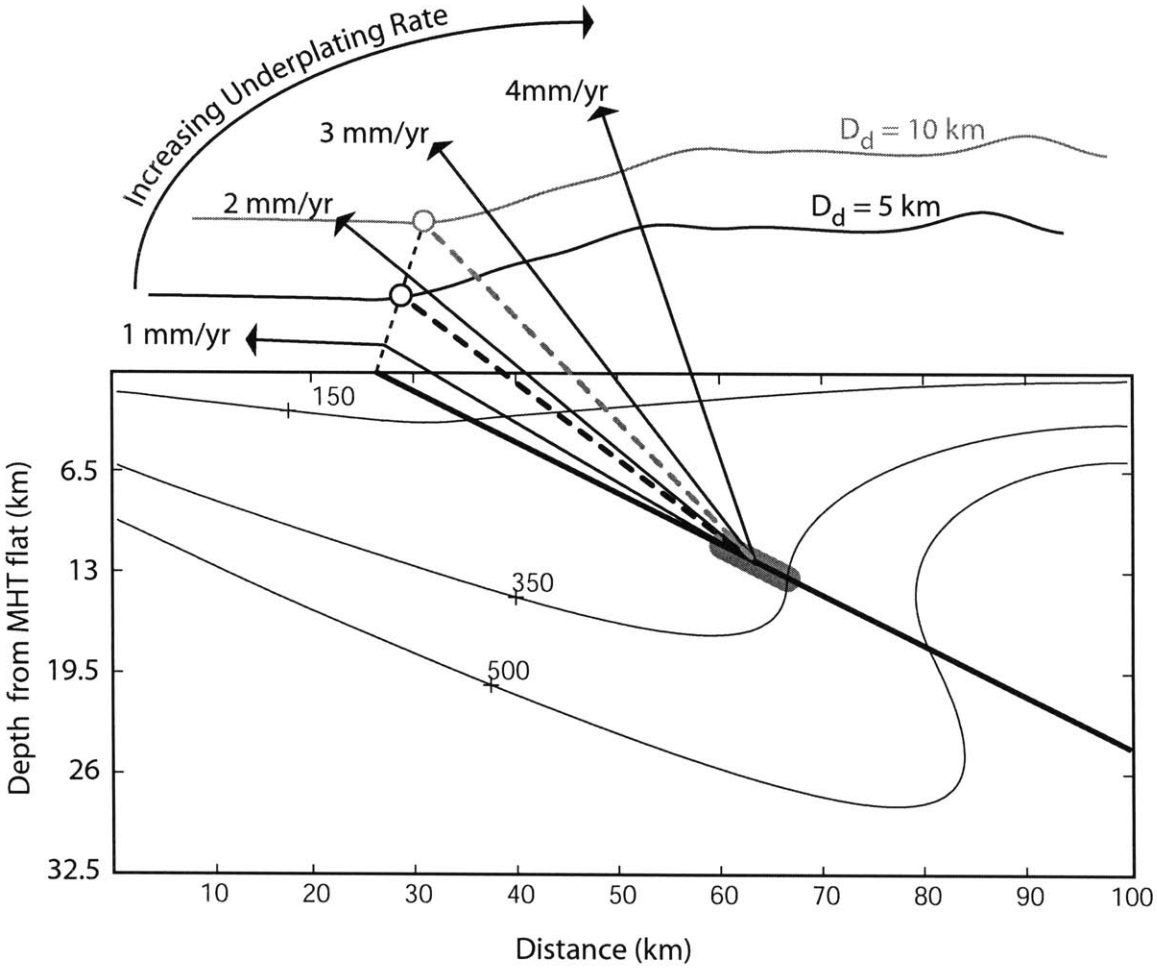

Wobus et al., Figure 7

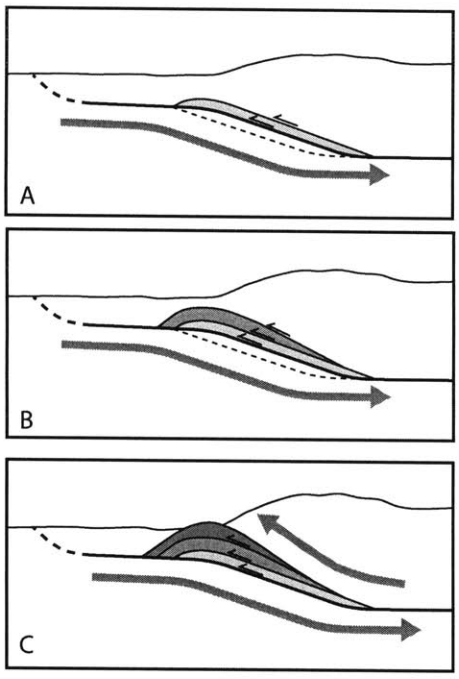

Wobus et al., Figure 8

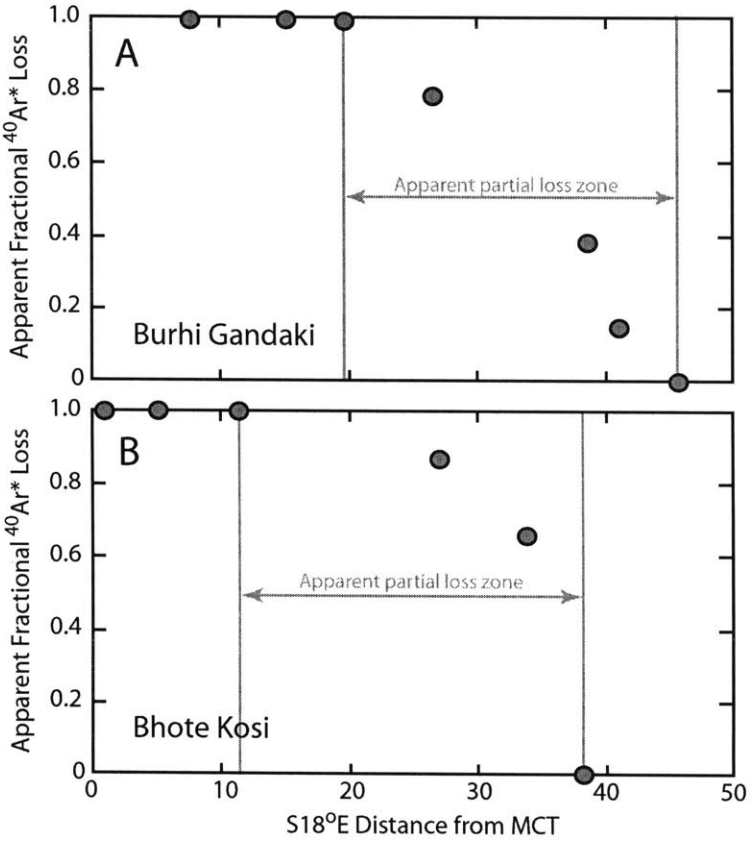

Wobus et al., Figure 9

Table 1 - Summary of $^{40}Ar/^{39}Ar$ results

Sample	Distance to MCT (km)	Drainage Area (km^2)	Elevation Range (m)	Analyses Reported	$^{40}Ar/^{39}Ar$ Apparent Ages		
					1st quartile	Median	3rd quartile
Trisuli River							
02WTS1	1.1	13.5	3072 - 5810	60	7.3	8.7	9.9
02WTS2	3.5	8.8	2075 - 4752	68	7.3	8.5	10.4
02WTS4	10.9	51.8	1821 - 4951	64	7.2	8.6	11.2
03WTS4	17.1	26	1154 - 3978	46	879.3	1337.7	1854.4
01WTS1	24	10.1	739 - 3468	86	637.0	948.7	1204.5
03WTS1	33.6	13.4	626 - 1656	45	1690.3	1872.3	2043.4
Bhote Kosi River							
03WKS1	0.9	40.3	1729 - 5422	46	7.9	9.1	10.4
03WKS2	5.1	24	1440 - 4416	48	6.9	7.4	8.0
03WKS3	11.4	34	1202 - 3645	49	8.5	10.5	14.6
03WKS5	27	17.4	780 - 2447	49	362.0	474.9	770.2
03WKS6	33.8	15.5	675 - 2225 ++	45	878.5	1037.0	1262.1
03WKS7	38.2	40.8	650 - 2100 ++	43	1906.0	2137.4	2426.1
Burhi Gandaki River *							
01WBS5	7.5	3.4	797 - 2372	35	4.6	7.0	8.4
01WBS6	15.0	18.4	604 - 3158	18	8.7	13.1	14.6
01WBS7	19.5	17.5	533 - 2455	32	5.9	7.4	15.2
01WBS8	26.4	15.6	508 - 1262	59	356.9	413.0	453.4
01WBS3	38.5	16.7	413 - 1412	50	929.5	1008.1	1103.5
01WBS2	41.0	22.4	370 - 1574	58	1163.0	1285.0	1333.2
01WBS1	45.5	10.5	348 - 1670	60	1392.5	1433.7	1480.7

++ Estimated upper limit (basin extends beyond the range of high-resolution topographic data)

* Previously reported analyses [*Wobus et al.*, 2003]

Appendix 1

Summary of $^{40}Ar/^{39}Ar$ Analytical Results

Summary of Analytical Results
Sample 02WTS1

Analysis Number	39(k)/40(a+r) ± 2σ	36(a)/40(a+r) ± 2σ	39Ar(k) (x1e-14 mol)	40Ar(r) (%)	Age ± 2σ (Ma)
1	0 834859 ± 0.012935	0.001515 ± 0.000917	0.76121	55.19	3.99 ± 1.96
2	0.687463 ± 0.019771	0.000000 ± 0.000846	0.51819	99.93	8 77 ± 2 20
3	0.452372 ± 0.007649	0.001609 ± 0.000498	0.79170	52.43	6.99 ± 1.96
4	0.645241 ± 0.024759	0.000698 ± 0.000984	0.47210	79.32	7.42 ± 2.73
5	0 478785 ± 0.020112	0.001088 ± 0.001434	0.22741	67.81	8 54 ± 5 34
6	0.586910 ± 0.020787	0.000000 ± 0.000000	0.19625	99.95	10.27 ± 0 36
7	0.711127 ± 0.018263	0.000717 ± 0.001240	0.79683	78.75	6.68 ± 3.11
8	0.879769 ± 0 026815	0.001526 ± 0.000681	1.22542	54 85	3.77 ± 1.39
9	0 505534 ± 0.017262	0.000609 ± 0.000848	0.41436	81.96	9.78 ± 3 00
10	0.617730 ± 0.015537	0.001608 ± 0.000611	0.68384	52.45	5.13 ± 1.77
11	0.124104 ± 0.177926	0.000000 ± 0.000000	0.00154	99.99	48.05 ± 67.98
12	0.611537 ± 0.024269	0.001448 ± 0.001377	0.34569	57.18	5.64 ± 4.02
13	0.545772 ± 0.017139	0.001287 ± 0.000843	0.47139	61.93	6.85 ± 2.76
14	0.466832 ± 0.015122	0.001322 ± 0.001660	0.19326	60.90	7.87 ± 6.33
15	0.652008 ± 0.018568	0.000611 ± 0.001738	0.27780	81.90	7.58 ± 4.75
16	0.529326 ± 0.014172	0.000460 ± 0.000692	0.51012	86.36	9.84 ± 2.34
17	0.553831 ± 0.015069	0.000073 ± 0.000715	0.60742	97.81	10.65 ± 2.31
18	0.513110 ± 0 017985	0.000000 ± 0.000000	0 38628	99.96	11.74 ± 0.41
19	0.541738 ± 0.014364	0.000577 ± 0.001049	0.28767	82.91	9.23 ± 3.45
20	0.489240 ± 0.019384	0.000365 ± 0.001737	0.20147	89.18	10.99 ± 6.32
21	0.688507 ± 0.029386	0.000454 ± 0.001295	0.29948	86.52	7.58 ± 3.36
22	0.606000 ± 0.010916	0.000231 ± 0.000532	0 91996	93.13	9.27 ± 1.57
23	0.517836 ± 0.016902	0.000019 ± 0.000700	0 49488	99.40	11.57 ± 2.43
24	0.657362 ± 0.021142	0.000362 ± 0.000696	0.72036	89.24	8.19 ± 1.90
25	0 621291 ± 0.028031	0 000000 ± 0.000000	0.17856	99.95	9.70 ± 0.44
26	0.681288 ± 0.032168	0.000000 ± 0.000000	0 20381	99 94	8.85 ± 0.42
27	0 809180 ± 0.039165	0.000113 ± 0.003557	0 24154	96.60	7.21 ± 7.83
28	0.555351 ± 0.021827	0.000000 ± 0.000000	0.34992	99.95	10.85 ± 0.43
29	0.760558 ± 0.027229	0.000041 ± 0.000983	0.54927	98.72	7.83 ± 2.32
30	0.665207 ± 0.027459	0.000000 ± 0.000000	0.30279	99.94	9.06 ± 0 37
31	0 530990 ± 0.019622	0 000046 ± 0.000630	0.47323	98.60	11.19 ± 2.15
32	0.058935 ± 0.209128	0.000000 ± 0.000000	0.00065	99 99	99.74 ± 344.32
33	0 612758 ± 0.016399	0 000569 ± 0.000780	0.54182	83.13	8.19 ± 2.27
34	0.666897 ± 0.021170	0.000454 ± 0.000715	0.66149	86.53	7.83 ± 1.92
35	0.581244 ± 0.025629	0.000000 ± 0.000000	0.12922	99.95	10.37 ± 0.46
36	0.005377 ± 0.000199	0.000567 ± 0.000116	0.69207	83.25	753.85 ± 34.77
37	0.492271 ± 0.012132	0 000647 ± 0.001107	0.30647	80 86	9.90 ± 4.01
38	0.661607 ± 0.019492	0 000825 ± 0.000640	0.74523	75.57	6.89 ± 1.73
39	0 598374 ± 0.021079	0.000706 ± 0.000987	0.42456	79.11	7.98 ± 2.95
40	0 827798 ± 0 022476	0.000711 ± 0.001049	0 70280	78.93	5 76 ± 2 26
41	0.546790 ± 0.017631	0.000667 ± 0.001298	0.29047	80.25	8.85 ± 4.23
42	0.627290 ± 0.030755	0.000000 ± 0.000000	0.13184	99 95	9.61 ± 0.47
43	0.528065 ± 0.020218	0.000169 ± 0.000767	0.49386	94 96	10.84 ± 2.61
44	0.863138 ± 0.031552	0.000376 ± 0 000989	0.48692	88 83	6.21 ± 2.05
45	0 508332 ± 0.016189	0.000694 ± 0 000695	0 59364	79.46	9 43 ± 2 45
46	0.407350 ± 0.014978	0.000484 ± 0.000483	0.46271	85.66	12.67 ± 2.16
47	0.597843 ± 0.020139	0.000034 ± 0.000673	0.52688	98.94	9.98 ± 2.03
48	0.464671 ± 0.018443	0.001072 ± 0.001365	0.23199	68.31	8.87 ± 5.24
49	0.669070 ± 0.018150	0 000957 ± 0.001764	0.28095	71 67	6.47 ± 4.70
50	0.566733 ± 0.019964	0.001051 ± 0.000611	0.53431	68.90	7.34 ± 1 94
51	0 613377 ± 0.032642	0.000000 ± 0.000000	0.12217	99.95	9 83 ± 0.52
52	0.657714 ± 0.024419	0.000000 ± 0.000000	0.19235	99.94	9.17 ± 0.34
53	0.531413 ± 0.014438	0.000256 ± 0.001554	0.22478	92.40	10.48 ± 5.20
54	0.589194 ± 0.019578	0.001070 ± 0.001710	0.25347	68.33	7.00 ± 5.17
55	0.739514 ± 0.021348	0.001369 ± 0.000385	1.30636	59.52	4.86 ± 0.95
56	0.775284 ± 0.043380	0.000560 ± 0.004622	0.12687	83.39	6.49 ± 10.62
57	0.754974 ± 0.026040	0.000182 ± 0.002814	0.19568	94 56	7.56 ± 6.63
58	0.744311 ± 0.020205	0 001056 ± 0.001027	0.44813	68.74	5.58 ± 2.46
59	0.548427 ± 0.016787	0 000718 ± 0 002272	0.15916	78.75	8.66 ± 7.37
60	0.727943 ± 0.026003	0.000741 ± 0.001940	0.21011	78.06	6.47 ± 4 75
61	0 711550 ± 0.021528	0 001550 ± 0.002847	0 20468	54.16	4.60 ± 7.13
62	0.646132 ± 0 016378	0.000518 ± 0.001137	0.48029	84.66	7.91 ± 3.14
63	0.576917 ± 0 026870	0.000795 ± 0.004321	0.11063	76.48	8.00 ± 13.32
64	0.437082 ± 0.012051	0.000727 ± 0.000440	0.54186	78.49	10.82 ± 1.82
65	0.411476 ± 0.008191	0.001647 ± 0 000792	0.32936	51.31	7.52 ± 3.43

Summary of Analytical Results
Sample 02WTS2

Analysis Number	39(k)/40(a+r) ± 2σ	36(a)/40(a+r) ± 2σ	39Ar(k) (x1e-14 mol)	40Ar(r) (%)	Age ± 2σ (Ma)
1	0 624022 ± 0.010547	0 001099 ± 0.000994	0 59716	67.49	6 53 ± 2 84
2	0.524108 ± 0 009429	0.001330 ± 0.000519	0.98492	60 67	6.99 ± 1.77
3	0 006499 ± 0 002315	0 000683 ± 0.001976	0 00346	79 81	621 61 ± 428.00
4	0 578063 ± 0.013397	0.001601 ± 0.000839	0 61596	52 65	5.50 ± 2.59
5	0 479182 ± 0 007847	0 001216 ± 0 000853	0 52767	64 05	8 06 ± 3.17
6	0 482214 ± 0.011667	0 001456 ± 0.001033	0 57601	56 95	7 13 ± 3 81
7	0.568600 ± 0 011770	0.000826 ± 0.001361	0 39229	75 57	8 02 ± 4 26
8	0.490266 ± 0 009777	0 000533 ± 0.001066	0 41510	84 21	10 36 ± 3 87
9	0 614978 ± 0 016466	0 000770 ± 0.000916	0 66695	77 21	7 58 ± 2 66
10	0.530051 ± 0 018157	0 001654 ± 0 001519	0.39701	51.11	5 82 ± 5 11
11	0 491185 ± 0 012658	0.001422 ± 0 000939	0 48212	57.96	7.12 ± 3 41
12	0 489011 ± 0 014082	0 001014 ± 0.000853	0.52934	70 01	8 63 ± 3 11
13	0 518248 ± 0 013966	0.001347 ± 0.001987	0 23953	60.18	7.01 ± 6 83
14	0.421334 ± 0 010011	0.000019 ± 0.001152	0 32671	99.39	14.21 ± 4 86
15	0 517187 ± 0.016671	0 001040 ± 0.001554	0.31489	69 22	8 07 ± 5 35
16	0 517390 ± 0.016867	0 000906 ± 0.001975	0 27951	73.18	8.53 ± 6.79
17	0 518271 ± 0.013551	0 000606 ± 0.000766	0 63157	82 05	9.55 ± 2.64
18	0 485117 ± 0 010415	0 001341 ± 0.001331	0.34153	60 33	7.50 ± 4 88
19	0 593406 ± 0 017739	0.001067 ± 0 000988	0.62614	68.42	6.96 ± 2 97
20	0 415633 ± 0 012857	0 001318 ± 0 001648	0 30898	61.04	8 86 ± 7 05
21	0.499215 ± 0.011830	0.000577 ± 0.000355	1.49810	82.91	10 01 ± 1 29
22	0.517973 ± 0 013972	0.000868 ± 0.002891	0 17367	74.32	8 66 ± 9.93
23	0.617895 ± 0 014135	0.000590 ± 0 001227	0 51443	82.54	8.06 ± 3.54
25	0 450229 ± 0 006093	0.000000 ± 0.000000	0.76412	99.96	13.37 ± 0 18
26	0 624411 ± 0 017987	0.000000 ± 0.000000	0 32328	99 95	9.65 ± 0.28
27	0 540283 ± 0 019032	0.000000 ± 0.000000	0 28889	99 95	11.15 ± 0.39
28	0.599435 ± 0.018177	0 000000 ± 0.000000	0.26447	99 95	10 05 ± 0.30
29	0.527698 ± 0 013146	0 000000 ± 0.000000	0 22969	99 95	11.42 ± 0 28
30	0.532108 ± 0.013941	0 000000 ± 0.000000	0.17515	99 95	11.32 ± 0 30
31	0.622239 ± 0.011509	0.000482 ± 0.000988	0 73168	85.71	8 31 ± 2.83
32	0.570553 ± 0.014733	0.000000 ± 0.000000	0.27376	99.95	10 56 ± 0.27
33	0 532823 ± 0.011785	0.001033 ± 0.001413	0 38420	69.43	7 86 ± 4 72
34	0.610275 ± 0 012114	0 000000 ± 0.000000	0 29775	99 95	9.88 ± 0.20
35	0.442086 ± 0 009252	0.000000 ± 0 000000	0.20873	99 96	13 62 ± 0.28
36	0 666175 ± 0 011771	0 000000 ± 0 000000	0 40247	99 94	9.05 ± 0 16
37	0 515930 ± 0 012580	0.000323 ± 0.001020	0 47763	90.43	10.57 ± 3 52
38	0.476411 ± 0 010349	0.000419 ± 0.001368	0 36879	87.58	11 08 ± 5 10
39	0.659841 ± 0.018335	0 000208 ± 0.002432	0 27314	93.79	8 57 ± 6.56
40	0.555432 ± 0.008143	0 000641 ± 0 001511	0 43003	81.01	8 80 ± 4 84
41	0.477982 ± 0 009566	0 000513 ± 0.002292	0 24775	84.80	10 69 ± 8 52
42	0.536757 ± 0 010104	0 000221 ± 0 001106	0 42740	93.42	10 49 ± 3 66
43	0.497137 ± 0 009587	0.000019 ± 0.001427	0 32822	99.39	12 05 ± 5.10
44	0 619442 ± 0 016248	0.000576 ± 0.001844	0.31438	82 93	8 08 ± 5 30
45	0 534570 ± 0 021449	0.000000 ± 0 000000	0 13902	99 95	11.27 ± 0 45
46	0 491691 ± 0 015612	0 000000 ± 0 000000	0.13572	99 96	12.25 ± 0 39
47	0 550695 ± 0 012557	0 000859 ± 0.002350	0.30357	74 58	8.17 ± 7 59
48	0 645962 ± 0.018004	0.001044 ± 0 002742	0.28830	69 10	6.46 ± 7.56
49	0.607245 ± 0 008427	0.000882 ± 0.000856	0.59703	73.91	7.34 ± 2.51
50	0 579838 ± 0 011127	0 000606 ± 0.001210	0.52943	82.06	8.54 ± 3.71
51	0.592707 ± 0 013972	0.001123 ± 0.002566	0.26751	66.78	6.80 ± 7.71
52	0 540589 ± 0 008261	0 000438 ± 0 001137	0.40962	87 01	9.71 ± 3 74
53	0 504026 ± 0 014426	0 000758 ± 0 001335	0 37444	77 56	9 28 ± 4 72
54	0.538980 ± 0 012092	0 000649 ± 0 000751	0.83017	80.79	9.04 ± 2 49
55	0.494690 ± 0.007451	0 000272 ± 0.001275	0.37549	91.92	11 20 ± 4 58
56	0.562899 ± 0.013268	0 001035 ± 0 001446	0 41845	69 38	7 44 ± 4 57
57	0.518707 ± 0.011420	0 000932 ± 0.001449	0 32887	72.43	8.42 ± 4.97
58	0 417762 ± 0.047779	0 001543 ± 0.009789	0 04150	54.37	7 85 ± 41 69
59	0 504685 ± 0 009697	0 001564 ± 0.001541	0 28236	53.77	6.43 ± 5.44
60	0 599122 ± 0.022418	0.001578 ± 0 002116	0 24358	53 35	5.38 ± 6 30
61	0.623428 ± 0.013035	0 001310 ± 0 001923	0 31768	61.25	5.93 ± 5.49
62	0 711715 ± 0.012579	0 001539 ± 0 001617	0.47102	54 49	4.62 ± 4.05
63	0 634772 ± 0.009373	0.001066 ± 0.000715	1.07398	68 46	6 51 ± 2 01
64	0 548996 ± 0 011273	0.001525 ± 0 001598	0.32599	54.91	6 04 ± 5 18
65	0 501730 ± 0.008399	0.000463 ± 0.000657	0.71339	86 28	10.37 ± 2.33
66	0.465621 ± 0.008045	0 001654 ± 0 000955	0.46469	51.10	6.62 ± 3 65
67	0.578705 ± 0.011794	0 000850 ± 0 000721	0.71467	74.86	7.80 ± 2.22
68	0.718250 ± 0.013615	0.001126 ± 0.001159	0.60683	66 70	5.61 ± 2.88
69	0.627422 ± 0.012031	0.000752 ± 0.001131	0 59984	77 74	7.48 ± 3.21
70	0.527212 ± 0 009697	0.000950 ± 0.001500	0.33053	71 89	8.23 ± 5.06
71	0 550151 ± 0 013670	0 001445 ± 0.001414	0.36909	57 28	6 28 ± 4 58
72	0.561252 ± 0 016232	0 000576 ± 0 001470	0.35063	82 94	8 91 ± 4 66
73	0 543422 ± 0 014473	0.001295 ± 0.001923	0 29478	61 71	6.85 ± 6.30
74	0.548927 ± 0 020633	0.000662 ± 0.004812	0.12179	80 40	8 83 ± 15 58
75	0 451812 ± 0 015884	0.000206 ± 0.004270	0 12458	93.89	12.52 ± 16.77
76	0 388835 ± 0 007876	0 000073 ± 0.000677	0 57754	97 82	15 15 ± 3 10
77	0 445551 ± 0 028220	0 000106 ± 0 007895	0.06702	96 84	13.09 ± 31.43
78	0.458122 ± 0 010739	0 000396 ± 0.000785	0 54349	88 26	11.61 ± 3 06

Summary of Analytical Results
Sample 02WTS4

Analysis Number	39(k)/40(a+r) ± 2σ	36(a)/40(a+r) ± 2σ	39Ar(k) (x1e-14 mol)	40Ar(r) (%)	Age ± 2σ (Ma)
1	0.432754 ± 0 005520	0.000343 ± 0 000275	0.78522	89.83	12.51 ± 1.14
2	0.547518 ± 0.007234	0.000601 ± 0.000727	0.56420	82 20	9.05 ± 2.36
3	0.378767 ± 0.008922	0.001331 ± 0.001345	0 19721	60.64	9.65 ± 6 32
4	0.484832 ± 0.006965	0.001047 ± 0.001054	0.53941	69.03	8.59 ± 3.87
5	0.486154 ± 0.008812	0.001040 ± 0.000863	0.40221	69.24	8.59 ± 3.16
6	0.500696 ± 0.007211	0.001203 ± 0.000510	0.46428	64.43	7.76 ± 1.82
7	0 545545 ± 0.008564	0.001532 ± 0.000932	0.38581	54.69	6.05 ± 3.04
8	0.552671 ± 0.008242	0.000746 ± 0.000326	1.26564	77.93	8.51 ± 1.06
9	0.607829 ± 0.009195	0.001068 ± 0.001260	0.50473	68.40	6.79 ± 3.69
10	0.606484 ± 0.008340	0.000914 ± 0.000522	1.17837	72.94	7.26 ± 1.54
11	0.459276 ± 0.006132	0.001373 ± 0.000819	0.34480	59 39	7.80 ± 3.17
12	0.529941 ± 0.006368	0.000514 ± 0.000342	1.02743	84.77	9.65 ± 1.15
13	0.576258 ± 0.010536	0.001424 ± 0.000684	0 51941	57.90	6 07 ± 2.12
14	0.618234 ± 0.010106	0.000721 ± 0.000480	0.82482	78.66	7.68 ± 1.39
15	0.482452 ± 0.008653	0.000882 ± 0.000264	0.94919	73.90	9.24 ± 0.99
16	0.547714 ± 0.007662	0.001255 ± 0.000525	0.54607	62.87	6.93 ± 1.71
17	0.471730 ± 0.006494	0.001496 ± 0.000592	0.45739	55.77	7.13 ± 2.24
18	0.580359 ± 0.007171	0 000677 ± 0.000253	1 22774	79.96	8.31 ± 0.78
19	0.526548 ± 0.011344	0.001676 ± 0.001842	0.20364	50.44	5.78 ± 6.23
20	0.554872 ± 0.008384	0.000848 ± 0.000550	0.68565	74.91	8.14 ± 1.77
21	0.447422 ± 0.006865	0.001621 ± 0.001016	0.36612	52.07	7.02 ± 4.04
22	0.348238 ± 0.004935	0 000903 ± 0.000457	0.61779	73.30	12.68 ± 2.34
23	0.471311 ± 0.007235	0.001266 ± 0 000706	0.47654	62.56	8.01 ± 2.67
24	0.492985 ± 0.007978	0.000635 ± 0.000289	1.45801	81.21	9.93 ± 1.06
25	0.428134 ± 0.005098	0.000274 ± 0.000299	1.54062	91.86	12.93 ± 1.25
26	0.477951 ± 0.007733	0.001656 ± 0.000977	0.36405	51.05	6.45 ± 3.64
27	0.445646 ± 0.006614	0.000571 ± 0.000340	1.02012	83.10	11.24 ± 1.36
28	0.299933 ± 0.003593	0.000754 ± 0.000379	0.43946	77.69	15.59 ± 2.25
29	0.514769 ± 0.007164	0.001446 ± 0.000597	0.53301	57 26	6.71 ± 2.07
30	0.342534 ± 0.005835	0.000512 ± 0.000278	0.84065	84.85	14.91 ± 1.46
31	0.444962 ± 0.006054	0.000670 ± 0 000221	0.96783	80.18	10.86 ± 0 90
32	0.602365 ± 0.009006	0.001060 ± 0.000603	0.99078	68.64	6.88 ± 1.79
33	0.649462 ± 0.011478	0.001392 ± 0.000595	0.94186	58 84	5.47 ± 1.63
34	0.500905 ± 0.006616	0.001284 ± 0.000762	0.64300	62.05	7.47 ± 2 71
35	0.514522 ± 0.012135	0.001685 ± 0.000930	0.39335	50.18	5 89 ± 3 22
36	0.717123 ± 0.010705	0.001142 ± 0.001165	0 48353	66.22	5.58 ± 2.89
37	0.511583 ± 0.010006	0.001159 ± 0.000819	0.44880	65.71	7 75 ± 2.85
38	0.552231 ± 0.009232	0.001115 ± 0.000381	0.62150	67.02	7.32 ± 1.23
39	0.611066 ± 0.008898	0.000928 ± 0.000473	1.25423	72.55	7.16 ± 1.38
40	0.542069 ± 0.009796	0 001515 ± 0.000630	0.57494	55.21	6.15 ± 2.08
41	0.670811 ± 0.009079	0.000751 ± 0.000642	0.54465	77.76	7.00 ± 1.71
42	0 424503 ± 0 009631	0.000744 ± 0.000249	1.11499	77.99	11 07 ± 1.08
43	0.595751 ± 0.013908	0.001531 ± 0.001093	0.51542	54.74	5.55 ± 3.27
44	0.463592 ± 0.012913	0.000000 ± 0.000000	0.15058	99 96	12.99 ± 0.36
45	0.442780 ± 0.007142	0.000000 ± 0.000000	0 25005	99.96	13.60 ± 0 22
46	0.474904 ± 0.006626	0.000566 ± 0 000698	0.41499	83.24	10.57 ± 2.61
47	0 362990 ± 0.005453	0.000729 ± 0.000355	0.69920	78.45	13.02 ± 1.75
48	0 449648 ± 0 012291	0.000546 ± 0.001083	0.20934	83 84	11.24 ± 4.29
49	0.504518 ± 0.006243	0.000555 ± 0.000458	0 59390	83.56	9.99 ± 1 62
50	0.569812 ± 0.018275	0.000000 ± 0.000000	0.12470	99.95	10.58 ± 0.34
51	0.539135 ± 0.007745	0.000189 ± 0.000669	0.52297	94.38	10.55 ± 2.21
52	0.542046 ± 0.007110	0.000642 ± 0.000318	0.77246	80.99	9.01 ± 1 05
53	0.565379 ± 0.006852	0.000658 ± 0.000610	0.74917	80.51	8.59 ± 1.92
54	0.538558 ± 0.006427	0.000802 ± 0.000605	0.67220	76.26	8.54 ± 2 00
55	0.678757 ± 0.012053	0.000504 ± 0.001139	0.31104	85.06	7.56 ± 2.99
56	0.794819 ± 0.011498	0.000371 ± 0.000364	1.01254	88.98	6.76 ± 0.82
57	0.423040 ± 0.005092	0.000757 ± 0.000472	0.56026	77.61	11.06 ± 1.98
58	0.436864 ± 0.006524	0.000484 ± 0.000187	1.40439	85.67	11.82 ± 0.78
59	0.455901 ± 0.011502	0.000208 ± 0.002232	0.11486	93 82	12.40 ± 8.69
60	0.472022 ± 0.007940	0.000002 ± 0.000955	0.27975	99.89	12.75 ± 3.59
61	0.634274 ± 0.015103	0.001628 ± 0.002209	0.16890	51.85	4.94 ± 6.21
62	0.379148 ± 0.014494	0.000283 ± 0.003733	0.07133	91.61	14 55 ± 17.45
63	0.554651 ± 0.008391	0.000448 ± 0.000885	0.39366	86.71	9.43 ± 2.84
64	0 379098 ± 0.006880	0.000332 ± 0.000323	0.60821	90.17	14.32 ± 1.53
65	0.457733 ± 0.012256	0.000250 ± 0 001164	0.20057	92.58	12.19 ± 4.52
66	0.353496 ± 0.010983	0.000334 ± 0.000771	0.29955	90.10	15.34 ± 3.89
67	0.470850 ± 0.006014	0.000172 ± 0.000257	1.11542	94 89	12.14 ± 0 98

Summary of Analytical Results
Sample 03WTS4

Analysis Number	39(k)/40(a+r) ± 2σ	36(a)/40(a+r) ± 2σ	39Ar(k) (x1e-14 mol)	40Ar(r) (%)	Age ± 2σ (Ma)
1	0.002809 ± 0.000123	0.000005 ± 0.000044	0.01505	99.85	1414.82 ± 44.72
2	0.002104 ± 0.000073	0.000005 ± 0.000027	0.01942	99.85	1716.93 ± 39.41
3	0.004838 ± 0.000113	0.000011 ± 0.000038	0.03052	99.68	946.98 ± 19.07
4	0.002607 ± 0.000073	0.000002 ± 0.000026	0.02409	99.93	1490.33 ± 29.46
5	0.002279 ± 0.000093	0.000004 ± 0.000033	0.01645	99.88	1630.05 ± 44.98
6	0.003819 ± 0.000080	0.000004 ± 0.000025	0.03656	99.89	1135.18 ± 18.70
7	0.003364 ± 0.010346	0.000000 ± 0.000000	0.01605	100.00	1246.79 ± 2768.65
8	0.001762 ± 0.000101	0.000007 ± 0.000037	0.01166	99.81	1919.58 ± 68.73
9	0.006971 ± 0.000145	0.000009 ± 0.000029	0.05858	99.74	706.48 ± 13.13
10	0.004157 ± 0.000086	0.000011 ± 0.000028	0.03579	99.68	1063.81 ± 18.03
11	0.001827 ± 0.000091	0.000019 ± 0.000033	0.01373	99.45	1872.84 ± 59.30
12	0.003693 ± 0.000094	0.000014 ± 0.000029	0.03127	99.60	1161.20 ± 22.89
13	0.005496 ± 0.000098	0.000017 ± 0.000031	0.04247	99.49	855.15 ± 13.72
14	0.006689 ± 0.000134	0.000007 ± 0.000044	0.03686	99.78	731.16 ± 14.33
15	0.000817 ± 0.000080	0.000021 ± 0.000032	0.00644	99.38	2929.51 ± 142.02
16	0.001754 ± 0.000078	0.000012 ± 0.000030	0.01504	99.65	1922.69 ± 53.92
17	0.004430 ± 0.000084	0.000008 ± 0.000027	0.04094	99.78	1014.26 ± 15.91
18	0.014850 ± 0.000175	0.000019 ± 0.000034	0.10889	99.45	365.15 ± 5.15
19	0.002225 ± 0.000082	0.000008 ± 0.000028	0.01908	99.77	1654.40 ± 41.10
20	0.005351 ± 0.000102	0.000000 ± 0.000000	0.04551	100.00	877.07 ± 13.24
21	0.009094 ± 0.000132	0.000000 ± 0.000000	0.07949	100.00	565.79 ± 7.06
22	0.005065 ± 0.000103	0.000000 ± 0.000000	0.05003	100.00	915.93 ± 14.58
23	0.001525 ± 0.000070	0.000000 ± 0.000000	0.01417	100.00	2096.86 ± 57.10
24	0.003107 ± 0.000073	0.000000 ± 0.000000	0.02957	100.00	1319.62 ± 22.01
25	0.005283 ± 0.000083	0.000000 ± 0.000000	0.05283	100.00	886.00 ± 11.02
26	0.002731 ± 0.000076	0.000000 ± 0.000000	0.02597	100.00	1444.28 ± 27.70
27	0.001578 ± 0.000068	0.000000 ± 0.000000	0.01533	100.00	2054.80 ± 52.62
28	0.023045 ± 0.000246	0.000009 ± 0.000029	0.18710	99.74	244.28 ± 3.13
29	0.005246 ± 0.000081	0.000000 ± 0.000000	0.05268	100.00	890.92 ± 10.88
30	0.001491 ± 0.000066	0.000000 ± 0.000000	0.01457	100.00	2124.26 ± 54.96
31	0.017373 ± 0.000260	0.000003 ± 0.000071	0.05898	99.92	317.88 ± 7.53
32	0.004060 ± 0.000086	0.000000 ± 0.000000	0.03976	100.00	1085.39 ± 17.32
33	0.001600 ± 0.000067	0.000000 ± 0.000000	0.01587	100.00	2037.67 ± 51.37
34	0.001646 ± 0.000076	0.000000 ± 0.000000	0.01468	100.00	2002.88 ± 55.74
35	0.002990 ± 0.000078	0.000000 ± 0.000000	0.02856	100.00	1355.84 ± 24.94
36	0.001413 ± 0.000074	0.000000 ± 0.000000	0.01288	100.00	2192.66 ± 66.10
37	0.002154 ± 0.000071	0.000000 ± 0.000000	0.02077	100.00	1692.62 ± 36.12
38	0.005554 ± 0.000089	0.000000 ± 0.000000	0.05485	100.00	851.51 ± 10.82
39	0.002164 ± 0.000070	0.000000 ± 0.000000	0.02085	100.00	1687.42 ± 35.64
40	0.001545 ± 0.000072	0.000000 ± 0.000000	0.01375	100.00	2080.19 ± 57.54
41	0.002595 ± 0.000085	0.000000 ± 0.000000	0.02295	100.00	1495.42 ± 33.23
42	0.011358 ± 0.000153	0.000000 ± 0.000000	0.10771	100.00	466.29 ± 5.54
43	0.006035 ± 0.000096	0.000000 ± 0.000000	0.05807	100.00	796.57 ± 10.26
44	0.001958 ± 0.000104	0.000000 ± 0.000000	0.01205	100.00	1799.19 ± 60.48
45	0.001704 ± 0.000091	0.000000 ± 0.000000	0.01237	100.00	1961.67 ± 63.75
46	0.006814 ± 0.000105	0.000000 ± 0.000000	0.06527	100.00	721.43 ± 9.20
47	0.004323 ± 0.000114	0.000000 ± 0.000000	0.03923	100.00	1035.05 ± 20.75

Summary of Analytical Results
Sample 01WTS1

Analysis Number	39(k)/40(a+r) ± 2σ	36(a)/40(a+r) ± 2σ	39Ar(k) (x1e-14 mol)	40Ar(r) (%)	Age ± 2σ (Ma)
1	0 004120 ± 0.000821	0 000564 ± 0 000352	0 01447	83 33	933 37 ± 172 07
2	0 004434 ± 0 000712	0 000576 ± 0 000360	0 01771	82 98	878 01 ± 143 44
3	0 008018 ± 0 000861	0 000854 ± 0 000378	0 02710	74 77	490.42 ± 79 92
4	0 006261 ± 0.000627	0 000351 ± 0 000289	0 03011	89 64	706 74 ± 81.21
5	0 006840 ± 0 001259	0 000546 ± 0.000508	0 01652	83 85	620 72 ± 135 77
6	0 009578 ± 0 000906	0 000477 ± 0 000374	0 03239	85 91	474 03 ± 66.98
7	0.004305 ± 0 001045	0 000388 ± 0 000442	0 01304	88 54	945 53 ± 209 61
8	0 007757 ± 0 001216	0 000674 ± 0 000515	0.01949	80 09	535 91 ± 115 22
9	0 006983 ± 0 000680	0 000380 ± 0 000274	0 03546	88 78	640 13 ± 72 22
10	0 005419 ± 0 001183	0 000845 ± 0 000496	0.01405	75 03	687 43 ± 168 72
11	0.006069 ± 0.000988	0 000447 ± 0 000388	0 01898	86 79	706 17 ± 123 17
12	0 004902 ± 0 000736	0 000446 ± 0 000299	0 02230	86 82	840.34 ± 122 24
13	0 011803 ± 0 001229	0 000695 ± 0 000500	0 03279	79 46	366 87 ± 71 46
14	0 003977 ± 0 000819	0 000309 ± 0 000334	0 01496	90.88	1025 43 ± 182 47
15	0 023444 ± 0 001257	0 000475 ± 0 000289	0 10510	85.95	208 99 ± 22 49
16	0 010668 ± 0 000954	0 000423 ± 0 000332	0 04097	87 51	438 03 ± 56 09
17	0 007109 ± 0 000715	0 000349 ± 0 000324	0 02827	89 69	635 95 ± 78 99
18	0.003717 ± 0.000672	0 000239 ± 0 000293	0 01685	92 92	1097 66 ± 167 44
19	0 003956 ± 0 001110	0.000607 ± 0 000487	0.00984	82 05	951 88 ± 245 79
20	0 010554 ± 0 000921	0 000337 ± 0 000271	0 04730	90 03	453 46 ± 50 21
21	0 003582 ± 0 000728	0.000324 ± 0.000346	0 01356	90 42	1105 51 ± 192 56
22	0 012486 ± 0 000857	0 000227 ± 0 000316	0 04920	93 29	403 01 ± 44 08
23	0 012751 ± 0 000849	0 000417 ± 0 000288	0 05466	87 68	374 00 ± 40 03
24	0 005613 ± 0 000870	0 000315 ± 0 000349	0 02097	90 70	780 53 ± 122 13
25	0 003471 ± 0 000778	0 000354 ± 0 000347	0 01241	89 54	1123 67 ± 210.79
26	0 003693 ± 0 000784	0 000000 ± 0 000000	0 01357	100 00	1164 71 ± 182 11
27	0 003033 ± 0 000568	0.000000 ± 0 000000	0 01509	100 00	1342 53 ± 177 30
28	0 005702 ± 0.000998	0 000042 ± 0 000362	0 01899	98 76	825 54 ± 136.34
29	0 002842 ± 0 000858	0 000056 ± 0 000355	0 00972	98 34	1388 64 ± 310 15
30	0 002904 ± 0 000624	0 000065 ± 0 000269	0 01378	98 08	1365 24 ± 219 90
31	0 003632 ± 0 000645	0 000132 ± 0 000280	0 01749	96 09	1144.86 ± 167 28
32	0 003222 ± 0 001322	0 000141 ± 0 000451	0 00875	95 84	1247.23 ± 390 09
33	0 004027 ± 0 000612	0 000058 ± 0 000265	0 01862	98 30	1078 17 ± 139 37
34	0 002216 ± 0 000666	0 000058 ± 0 000311	0 00938	98 28	1642 77 ± 339 28
35	0 007385 ± 0 000849	0 000249 ± 0 000311	0 03195	92 65	632 95 ± 81 28
36	0 003016 ± 0 000743	0 000026 ± 0 000319	0 01237	99 24	1340 65 ± 249 81
37	0 002711 ± 0 000703	0 000081 ± 0 000258	0 01319	97 62	1427 49 ± 267 17
38	0 005187 ± 0 000827	0 000139 ± 0 000276	0 02317	95.89	869 62 ± 124 87
39	0 001121 ± 0 000628	0 000060 ± 0 000249	0 00544	98 24	2471.20 ± 760 24
40	0 003559 ± 0 000662	0 000169 ± 0 000242	0 01848	95 02	1152.53 ± 171 00
41	0 002465 ± 0 000524	0 000054 ± 0 000223	0 01359	98 41	1531 75 ± 229 97
42	0 011090 ± 0 001106	0 000230 ± 0 000357	0 03805	93 20	447 50 ± 59 97
43	0 004420 ± 0 000759	0 000178 ± 0 000304	0 01879	94 75	976 35 ± 148 00
44	0 004287 ± 0 000647	0 000057 ± 0 000245	0 02151	98 30	1028 27 ± 131 67
45	0 012263 ± 0 001355	0 000284 ± 0 000494	0.03110	91 61	402 93 ± 70 36
46	0 004732 ± 0 000626	0 000440 ± 0 000280	0 02181	87 01	865 86 ± 112 55
47	0 002565 ± 0 001301	0.000345 ± 0.000425	0 00787	89 82	1400 08 ± 512 71
48	0 097667 ± 0 004767	0 001167 ± 0 000757	0 24516	65 50	40 09 ± 13 80
49	0 004683 ± 0 000526	0 000421 ± 0 000235	0 02659	87 55	877 35 ± 95 89
50	0 004329 ± 0 001057	0 000442 ± 0 000456	0 01303	86 95	928 21 ± 210 32
51	0 003679 ± 0 001170	0 000000 ± 0 000000	0 01170	100 00	1168 01 ± 273 35
52	0 007840 ± 0 001284	0 000000 ± 0 000000	0 02049	100 00	641 83 ± 88 43
53	0 003304 ± 0.000949	0 000165 ± 0 000401	0 01120	95 11	1218.17 ± 277 57
54	0 003335 ± 0 000791	0 000141 ± 0.000264	0 01636	95 85	1216 61 ± 222 04
55	0 002334 ± 0.001331	0 000351 ± 0.000334	0 00881	89 63	1492 12 ± 589 81
56	0 004650 ± 0 000850	0 000522 ± 0 000296	0 02111	84 57	858 37 ± 143 80
57	0 002190 ± 0 001007	0 000103 ± 0 000323	0 00826	96 97	1640 77 ± 506 54
58	0 009759 ± 0 001332	0 001055 ± 0 000527	0 02675	68 83	382 64 ± 92 19
59	0 007195 ± 0 000853	0 000397 ± 0 000317	0 03599	88 27	621 14 ± 83 96
60	0 003689 ± 0 000979	0 000372 ± 0 000327	0 01534	89 02	1068 74 ± 231 52
61	0 000316 ± 0 001234	0 000265 ± 0 000395	0 00101	92 17	4289 68 ± 6400 92
62	0 005233 ± 0 001504	0 000483 ± 0 000398	0 01858	85 71	789 09 ± 204 03
63	0 000000 ± 0 000000	0 000458 ± 0 000447	0 00000	86 48	1049 31 ± 0 00
64	0 009914 ± 0 000996	0 000313 ± 0 000469	0 03496	90 75	482 54 ± 77 67
65	0 002523 ± 0 001010	0.000372 ± 0 000341	0 01180	89 01	1407 29 ± 406 71
66	0 004649 ± 0 000764	0 000554 ± 0 000413	0 01739	83 62	850 76 ± 149 65
67	0 001967 ± 0 001218	0 001002 ± 0 000452	0 00628	70 40	1421 76 ± 638 26
68	0 008087 ± 0 000588	0 000854 ± 0 000278	0 04109	74.76	486 73 ± 56.94
69	0 002776 ± 0 001142	0 000990 ± 0 000432	0 00888	70 74	1113 41 ± 374 16
70	0 002164 ± 0.000859	0 000850 ± 0 000456	0 00794	74 88	1388 74 ± 422 74
71	0 008633 ± 0 001031	0 000562 ± 0 000261	0 04434	83 41	505 88 ± 66 92
72	0 001871 ± 0 001023	0 000845 ± 0 000392	0 00681	75 02	1536 02 ± 587 75
73	0 004263 ± 0 000845	0.000657 ± 0 000354	0 01672	80 58	885 07 ± 166 32
74	0 004463 ± 0 000874	0 000943 ± 0 000360	0 01573	72 14	780 76 ± 156 42
75	0 003564 ± 0.001362	0 001330 ± 0 000425	0 01141	60 70	814 52 ± 286 10
76	0 002191 ± 0 000851	0 000973 ± 0 000369	0 00885	71 25	1329 39 ± 393 56
77	0 006911 ± 0 000910	0 000828 ± 0 000372	0 02659	75 53	562 84 ± 95 58
78	0 002839 ± 0 001023	0 000944 ± 0 000324	0 01126	72 12	1110 70 ± 319 06
79	0 003026 ± 0 000984	0 000939 ± 0 000347	0 01172	72 25	1060 36 ± 285 35
80	0 003698 ± 0 000984	0 000656 ± 0 000305	0.01913	80 63	989 24 ± 220 16
81	0 003402 ± 0 001107	0 000469 ± 0.000372	0 01239	86 13	1108 12 ± 289 81
82	0 002168 ± 0 000900	0 000980 ± 0 000363	0 00775	71 05	1336 60 ± 418 08
83	0 000437 ± 0 001610	0 000824 ± 0 000422	0.00140	75 64	3457 69 ± 5672 54
84	0 002631 ± 0 001394	0 001068 ± 0 000396	0 00885	68 45	1130.84 ± 468 71
85	0 002771 ± 0 000981	0 001433 ± 0 000372	0 01015	57 65	954 01 ± 299 24
86	0 002153 ± 0 001342	0 001276 ± 0 000331	0 00987	62 29	1222 60 ± 571 46
87	0 006097 ± 0 000854	0 001527 ± 0 000263	0 03575	54 89	475 50 ± 83 90

Summary of Analytical Results
Sample 03WTS1

Analysis Number	39(k)/40(a+r) ± 2σ	36(a)/40(a+r) ± 2σ	39Ar(k) (x1e-14 mol)	40Ar(r) (%)	Age ± 2σ (Ma)
1	0.001921 ± 0.000037	0.000000 ± 0.000000	0.01859	100.00	1820.76 ± 22.31
2	0.007715 ± 0.000084	0.000000 ± 0.000000	0.06642	100.00	650.61 ± 5.98
3	0.001564 ± 0.000042	0.000000 ± 0.000000	0.01389	100.00	2065.75 ± 32.65
4	0.001573 ± 0.000041	0.000000 ± 0.000000	0.01152	100.00	2058.61 ± 32.01
5	0.197048 ± 0.002687	0.000926 ± 0.000278	0.07932	72.61	22.14 ± 2.51
6	0.001541 ± 0.000053	0.000001 ± 0.000013	0.00843	99.98	2083.38 ± 42.92
7	0.002720 ± 0.000054	0.000009 ± 0.000013	0.01564	99.72	1445.54 ± 20.21
8	0.194060 ± 0.002422	0.000937 ± 0.000177	0.09593	72.30	22.38 ± 1.63
9	0.001537 ± 0.000045	0.000006 ± 0.000014	0.00927	99.83	2084.73 ± 36.26
10	0.002158 ± 0.000043	0.000000 ± 0.000000	0.01847	100.00	1690.30 ± 21.62
11	0.001539 ± 0.000036	0.000001 ± 0.000010	0.01257	99.97	2084.93 ± 28.91
12	0.002159 ± 0.000051	0.000009 ± 0.000018	0.01362	99.75	1687.01 ± 26.38
13	0.001572 ± 0.000050	0.000003 ± 0.000014	0.00880	99.90	2058.02 ± 39.01
14	0.216304 ± 0.002564	0.000801 ± 0.000155	0.12746	76.33	21.20 ± 1.29
15	0.001605 ± 0.000042	0.000000 ± 0.000000	0.01482	100.00	2033.70 ± 31.60
16	0.001926 ± 0.000038	0.000000 ± 0.000000	0.01894	100.00	1818.22 ± 22.64
17	0.001810 ± 0.000068	0.000008 ± 0.000016	0.01017	99.76	1886.85 ± 44.15
18	0.241919 ± 0.002693	0.000875 ± 0.000117	0.16825	74.12	18.43 ± 0.88
19	0.001606 ± 0.000044	0.000003 ± 0.000015	0.00961	99.91	2031.56 ± 33.58
20	0.001534 ± 0.000047	0.000004 ± 0.000010	0.01176	99.87	2087.93 ± 38.27
21	0.001516 ± 0.000036	0.000006 ± 0.000012	0.01154	99.83	2101.95 ± 30.12
22	0.001729 ± 0.000052	0.000014 ± 0.000014	0.00957	99.58	1938.71 ± 36.04
23	0.001830 ± 0.000050	0.000013 ± 0.000018	0.01030	99.61	1872.31 ± 32.20
24	0.002731 ± 0.000050	0.000005 ± 0.000011	0.02230	99.84	1442.59 ± 18.58
25	0.002161 ± 0.000047	0.000003 ± 0.000011	0.01515	99.90	1687.95 ± 23.99
26	0.001397 ± 0.000041	0.000004 ± 0.000011	0.01045	99.87	2205.12 ± 37.25
27	0.001844 ± 0.000039	0.000000 ± 0.000010	0.01473	100.00	1868.17 ± 24.56
28	0.001813 ± 0.000052	0.000007 ± 0.000019	0.01340	99.79	1885.65 ± 34.14
29	0.002327 ± 0.000058	0.000013 ± 0.000013	0.01786	99.61	1604.84 ± 26.72
30	0.001908 ± 0.000048	0.000014 ± 0.000015	0.01066	99.59	1823.74 ± 29.11
31	0.001638 ± 0.000054	0.000007 ± 0.000015	0.01091	99.79	2006.28 ± 40.44
32	0.001589 ± 0.000054	0.000007 ± 0.000015	0.01104	99.80	2043.38 ± 42.01
33	0.001501 ± 0.000043	0.000002 ± 0.000013	0.01019	99.96	2115.40 ± 36.15
34	0.001976 ± 0.000047	0.000000 ± 0.000000	0.01661	100.00	1789.07 ± 27.14
35	0.001677 ± 0.000047	0.000008 ± 0.000010	0.01466	99.77	1978.09 ± 33.57
36	0.001539 ± 0.000047	0.000014 ± 0.000015	0.00934	99.59	2080.46 ± 37.74
37	0.001988 ± 0.000052	0.000014 ± 0.000016	0.01083	99.60	1777.45 ± 29.78
38	0.002831 ± 0.000040	0.000010 ± 0.000009	0.02613	99.69	1405.82 ± 13.90
39	0.002256 ± 0.000045	0.000004 ± 0.000011	0.01689	99.88	1640.79 ± 21.98
40	0.001677 ± 0.000031	0.000000 ± 0.000000	0.01538	100.00	1980.62 ± 22.12
41	0.001976 ± 0.000049	0.000007 ± 0.000018	0.01084	99.79	1786.31 ± 28.62
42	0.001633 ± 0.000043	0.000000 ± 0.000000	0.01580	100.00	2012.43 ± 31.80
43	0.002224 ± 0.000046	0.000012 ± 0.000017	0.01267	99.64	1653.77 ± 23.09
44	0.001816 ± 0.000046	0.000000 ± 0.000000	0.01562	100.00	1886.31 ± 29.87
45	0.002043 ± 0.000044	0.000005 ± 0.000012	0.01319	99.84	1749.36 ± 24.59
46	0.002762 ± 0.000048	0.000011 ± 0.000012	0.01686	99.68	1429.83 ± 17.36
47	0.002519 ± 0.000048	0.000000 ± 0.000000	0.02212	100.00	1525.77 ± 19.59
48	0.001839 ± 0.000053	0.000013 ± 0.000014	0.01024	99.62	1866.89 ± 33.61
49	0.002067 ± 0.000055	0.000001 ± 0.000010	0.01821	99.97	1737.63 ± 29.62

Summary of Analytical Results
Sample 03WKS1

Analysis Number	$^{39}(k)/^{40}(a+r) \pm 2\sigma$	$^{36}(a)/^{40}(a+r) \pm 2\sigma$	$^{39}Ar(k)$ (x1e-14 mol)	$^{40}Ar(r)$ (%)	Age $\pm 2\sigma$ (Ma)
1	0.384719 ± 0.005179	0.000000 ± 0.000000	0.10417	99.97	10.10 ± 0.14
2	0.370590 ± 0.004327	0.000000 ± 0.000000	0.09214	99.97	10.48 ± 0.12
3	0.464105 ± 0.005124	0.000000 ± 0.000000	0.07825	99.96	8.38 ± 0.09
4	0.377353 ± 0.004234	0.000000 ± 0.000000	0.13054	99.97	10.30 ± 0.12
5	0.301010 ± 0.003083	0.000000 ± 0.000000	0.29595	99.97	12.90 ± 0.13
6	0.316708 ± 0.003379	0.000089 ± 0.000165	0.27308	97.35	11.94 ± 0.61
7	0.497586 ± 0.006553	0.000000 ± 0.000000	0.08140	99.96	7.81 ± 0.10
8	0.444203 ± 0.004856	0.000000 ± 0.000000	0.11306	99.96	8.75 ± 0.10
9	0.416406 ± 0.004553	0.000000 ± 0.000000	0.17955	99.96	9.33 ± 0.10
10	0.368681 ± 0.004262	0.000000 ± 0.000000	0.08173	99.97	10.54 ± 0.12
11	0.526868 ± 0.005881	0.000000 ± 0.000000	0.13822	99.95	7.38 ± 0.08
12	0.369548 ± 0.004717	0.000000 ± 0.000000	0.06880	99.97	10.51 ± 0.13
13	0.437797 ± 0.004815	0.000000 ± 0.000000	0.12037	99.96	8.88 ± 0.10
14	0.628538 ± 0.009053	0.000000 ± 0.000000	0.04801	99.95	6.19 ± 0.09
15	0.370220 ± 0.004513	0.000000 ± 0.000000	0.08682	99.97	10.50 ± 0.13
16	0.325763 ± 0.004997	0.000000 ± 0.000000	0.04172	99.97	11.92 ± 0.18
17	0.436686 ± 0.008531	0.000000 ± 0.000000	0.02193	99.96	8.90 ± 0.17
18	0.355005 ± 0.004594	0.000000 ± 0.000000	0.04626	99.97	10.94 ± 0.14
19	0.418897 ± 0.007479	0.000000 ± 0.000000	0.02303	99.96	9.28 ± 0.17
20	0.476276 ± 0.009301	0.000000 ± 0.000000	0.03901	99.96	8.16 ± 0.16
21	0.315044 ± 0.004582	0.000000 ± 0.000000	0.03654	99.97	12.33 ± 0.18
22	0.593211 ± 0.007476	0.000000 ± 0.000000	0.06415	99.95	6.56 ± 0.08
23	0.389558 ± 0.004529	0.000000 ± 0.000000	0.11086	99.97	9.98 ± 0.12
24	0.402109 ± 0.004496	0.000000 ± 0.000000	0.12806	99.97	9.66 ± 0.11
25	0.467819 ± 0.005873	0.000301 ± 0.001195	0.05688	91.08	7.57 ± 2.93
26	0.492722 ± 0.007005	0.000000 ± 0.000000	0.03239	99.96	7.89 ± 0.11
27	0.461879 ± 0.007671	0.000000 ± 0.000000	0.04699	99.96	8.42 ± 0.14
28	0.496932 ± 0.006699	0.000000 ± 0.000000	0.06979	99.96	7.82 ± 0.11
29	0.576976 ± 0.009304	0.000000 ± 0.000000	0.04138	99.95	6.74 ± 0.11
30	0.382346 ± 0.004913	0.000000 ± 0.000000	0.08476	99.97	10.16 ± 0.13
31	0.490130 ± 0.009459	0.000000 ± 0.000000	0.02312	99.96	7.93 ± 0.15
32	0.496162 ± 0.005382	0.000000 ± 0.000000	0.22835	99.96	7.84 ± 0.08
33	0.341129 ± 0.003938	0.000000 ± 0.000000	0.07259	99.97	11.39 ± 0.13
34	0.495508 ± 0.005723	0.000000 ± 0.000000	0.06054	99.96	7.85 ± 0.09
35	0.405319 ± 0.005498	0.000000 ± 0.000000	0.05745	99.97	9.59 ± 0.13
36	0.462632 ± 0.006512	0.000000 ± 0.000000	0.04645	99.96	8.40 ± 0.12
37	0.444211 ± 0.006331	0.000000 ± 0.000000	0.04634	99.96	8.75 ± 0.12
38	0.378587 ± 0.005138	0.000000 ± 0.000000	0.04489	99.97	10.26 ± 0.14
39	0.384360 ± 0.005963	0.000000 ± 0.000000	0.02847	99.97	10.11 ± 0.16
40	0.374503 ± 0.004099	0.000000 ± 0.000000	0.09573	99.97	10.38 ± 0.11
41	0.470891 ± 0.006131	0.000000 ± 0.000000	0.12321	99.96	8.26 ± 0.11
42	0.391185 ± 0.004670	0.000000 ± 0.000000	0.06856	99.97	9.93 ± 0.12
43	0.526423 ± 0.006567	0.000000 ± 0.000000	0.07182	99.95	7.39 ± 0.09
44	0.355618 ± 0.005589	0.000000 ± 0.000000	0.03902	99.97	10.92 ± 0.17
45	0.595048 ± 0.012308	0.000000 ± 0.000000	0.01835	99.95	6.54 ± 0.13
46	0.476108 ± 0.006589	0.000000 ± 0.000000	0.04941	99.96	8.17 ± 0.11

Summary of Analytical Results
Sample 03WKS2

Analysis Number	$^{39}(k)/^{40}(a+r) \pm 2\sigma$	$^{36}(a)/^{40}(a+r) \pm 2\sigma$	$^{39}Ar(k)$ (x1e-14 mol)	$^{40}Ar(r)$ (%)	Age $\pm 2\sigma$ (Ma)
1	0.311581 ± 0.003457	0.001278 ± 0.000574	0.08636	62.23	7.77 ± 2.11
2	0.395559 ± 0.004457	0.000359 ± 0.000245	0.20712	89.36	8.78 ± 0.72
3	0.466220 ± 0.007049	0.000409 ± 0.000891	0.07183	87.87	7.33 ± 2.20
4	0.631193 ± 0.012963	0.000030 ± 0.001625	0.05545	99.06	6.11 ± 2.96
5	0.516696 ± 0.005920	0.000000 ± 0.000000	0.07713	99.96	7.53 ± 0.09
6	0.504597 ± 0.006724	0.000000 ± 0.000000	0.12134	99.96	7.71 ± 0.10
7	0.571545 ± 0.007182	0.000000 ± 0.000000	0.13447	99.95	6.81 ± 0.09
8	0.561913 ± 0.011404	0.000000 ± 0.000000	0.04972	99.95	6.92 ± 0.14
9	0.513124 ± 0.006152	0.000000 ± 0.000000	0.21646	99.96	7.58 ± 0.09
10	0.487305 ± 0.006299	0.000000 ± 0.000000	0.14361	99.96	7.98 ± 0.10
11	0.491031 ± 0.009540	0.000000 ± 0.000000	0.06060	99.96	7.92 ± 0.15
12	0.438086 ± 0.006450	0.000000 ± 0.000000	0.04445	99.96	8.87 ± 0.13
13	0.485520 ± 0.007505	0.000000 ± 0.000000	0.05366	99.96	8.01 ± 0.12
14	0.545731 ± 0.009942	0.000000 ± 0.000000	0.06123	99.95	7.13 ± 0.13
15	0.465016 ± 0.006211	0.000000 ± 0.000000	0.10166	99.96	8.36 ± 0.11
16	0.489570 ± 0.005521	0.000000 ± 0.000000	0.17160	99.96	7.94 ± 0.09
17	0.355684 ± 0.004011	0.000000 ± 0.000000	0.18145	99.97	10.92 ± 0.12
18	0.527284 ± 0.007349	0.000000 ± 0.000000	0.03762	99.95	7.38 ± 0.10
19	0.457346 ± 0.005150	0.000000 ± 0.000000	0.11744	99.96	8.50 ± 0.10
20	0.471506 ± 0.007368	0.000000 ± 0.000000	0.04471	99.96	8.25 ± 0.13
21	0.438174 ± 0.004657	0.000000 ± 0.000000	0.11639	99.96	8.87 ± 0.09
22	0.520294 ± 0.005432	0.000000 ± 0.000000	0.08803	99.96	7.47 ± 0.08
23	0.541905 ± 0.007310	0.000000 ± 0.000000	0.09344	99.95	7.18 ± 0.10
24	0.518514 ± 0.006129	0.000000 ± 0.000000	0.10640	99.96	7.50 ± 0.09
25	0.767150 ± 0.024790	0.000000 ± 0.000000	0.01743	99.93	5.07 ± 0.16
26	0.564034 ± 0.009238	0.000000 ± 0.000000	0.04250	99.95	6.90 ± 0.11
27	0.667326 ± 0.009499	0.000000 ± 0.000000	0.03965	99.94	5.83 ± 0.08
28	0.502753 ± 0.010327	0.000000 ± 0.000000	0.01391	99.96	7.73 ± 0.16
29	0.540673 ± 0.006880	0.000000 ± 0.000000	0.07034	99.95	7.19 ± 0.09
30	0.460769 ± 0.005080	0.000000 ± 0.000000	0.09916	99.96	8.44 ± 0.09
31	0.547757 ± 0.006774	0.000000 ± 0.000000	0.09009	99.95	7.10 ± 0.09
32	0.726521 ± 0.011962	0.000000 ± 0.000000	0.03245	99.94	5.36 ± 0.09
33	0.565034 ± 0.010420	0.000000 ± 0.000000	0.05034	99.95	6.88 ± 0.13
34	0.632390 ± 0.007951	0.000000 ± 0.000000	0.07848	99.95	6.15 ± 0.08
35	0.495788 ± 0.006318	0.000000 ± 0.000000	0.08432	99.96	7.84 ± 0.10
36	0.536791 ± 0.008113	0.000000 ± 0.000000	0.05280	99.95	7.24 ± 0.11
37	0.548520 ± 0.009328	0.000000 ± 0.000000	0.03410	99.95	7.09 ± 0.12
38	0.529371 ± 0.007555	0.000000 ± 0.000000	0.04110	99.95	7.35 ± 0.10
39	0.468953 ± 0.006371	0.000000 ± 0.000000	0.08980	99.96	8.29 ± 0.11
40	0.548363 ± 0.008575	0.000000 ± 0.000000	0.05728	99.95	7.09 ± 0.11
41	0.529237 ± 0.010969	0.000000 ± 0.000000	0.03492	99.95	7.35 ± 0.15
42	0.573926 ± 0.009515	0.000000 ± 0.000000	0.04137	99.95	6.78 ± 0.11
43	0.445858 ± 0.006428	0.000000 ± 0.000000	0.06116	99.96	8.72 ± 0.13
44	0.579921 ± 0.012164	0.000000 ± 0.000000	0.02543	99.95	6.71 ± 0.14
45	0.563071 ± 0.014115	0.000000 ± 0.000000	0.01987	99.95	6.91 ± 0.17
46	0.635396 ± 0.010103	0.000000 ± 0.000000	0.05273	99.95	6.12 ± 0.10
47	0.469780 ± 0.005837	0.000000 ± 0.000000	0.10742	99.96	8.28 ± 0.10
48	0.691862 ± 0.008829	0.000000 ± 0.000000	0.06373	99.94	5.62 ± 0.07

Summary of Analytical Results
Sample 03WKS3

Analysis Number	39(k)/40(a+r) ± 2σ	36(a)/40(a+r) ± 2σ	39Ar(k) (x1e-14 mol)	40Ar(r) (%)	Age ± 2σ (Ma)
1	0.403169 ± 0.004729	0.000636 ± 0.000183	0.24433	81.18	7.83 ± 0.53
2	0.413505 ± 0.005704	0.000635 ± 0.000208	0.21850	81.21	7.64 ± 0.59
3	0.378067 ± 0.004194	0.000848 ± 0.000378	0.10343	74.93	7.71 ± 1.15
4	0.393763 ± 0.005014	0.000462 ± 0.000286	0.14603	86.34	8.53 ± 0.84
5	0.318413 ± 0.003359	0.000487 ± 0.000070	0.49811	85.60	10.45 ± 0.27
6	0.452370 ± 0.005078	0.000431 ± 0.000261	0.17705	87.24	7.50 ± 0.67
7	0.433858 ± 0.005005	0.000449 ± 0.000149	0.30287	86.73	7.77 ± 0.40
8	0.224418 ± 0.002982	0.000202 ± 0.000029	0.89741	94.02	16.25 ± 0.26
9	0.241903 ± 0.003542	0.000295 ± 0.000153	0.16151	91.29	14.65 ± 0.75
10	0.232764 ± 0.002415	0.000192 ± 0.000088	0.26987	94.31	15.72 ± 0.46
11	0.284154 ± 0.003128	0.000238 ± 0.000120	0.23990	92.96	12.71 ± 0.50
12	0.358827 ± 0.003705	0.000331 ± 0.000128	0.30497	90.20	9.77 ± 0.42
13	0.295721 ± 0.003006	0.000211 ± 0.000044	0.71344	93.74	12.31 ± 0.21
14	0.300813 ± 0.003118	0.000127 ± 0.000185	0.17732	96.24	12.43 ± 0.71
15	0.290866 ± 0.003041	0.000203 ± 0.000158	0.19195	94.00	12.55 ± 0.64
16	0.482231 ± 0.005038	0.000288 ± 0.000159	0.31032	91.47	7.38 ± 0.39
17	0.478687 ± 0.005042	0.000211 ± 0.000165	0.29070	93.75	7.62 ± 0.40
18	0.267495 ± 0.002911	0.000201 ± 0.000055	0.51458	94.05	13.65 ± 0.28
19	0.107026 ± 0.001110	0.000109 ± 0.000058	0.20636	96.77	34.90 ± 0.71
20	0.378054 ± 0.004417	0.001191 ± 0.000404	0.10159	64.78	6.67 ± 1.23
21	0.360538 ± 0.004244	0.000181 ± 0.000181	0.20496	94.62	10.20 ± 0.59
22	0.192531 ± 0.002011	0.000119 ± 0.000042	0.48871	96.47	19.42 ± 0.32
23	0.387476 ± 0.004133	0.000472 ± 0.000177	0.22781	86.04	8.63 ± 0.53
24	0.243507 ± 0.002668	0.000209 ± 0.000092	0.26992	93.80	14.95 ± 0.46
25	0.450971 ± 0.004621	0.000211 ± 0.000156	0.31771	93.75	8.08 ± 0.40
26	0.376553 ± 0.003869	0.000300 ± 0.000118	0.33173	91.13	9.41 ± 0.37
27	0.431440 ± 0.004882	0.000618 ± 0.000293	0.16332	81.71	7.37 ± 0.78
28	0.210082 ± 0.002369	0.000279 ± 0.000112	0.19819	91.76	16.94 ± 0.64
29	0.376254 ± 0.003999	0.000217 ± 0.000198	0.19999	93.56	9.67 ± 0.61
30	0.056460 ± 0.000738	0.000095 ± 0.000049	0.11783	97.19	65.86 ± 1.28
31	0.186059 ± 0.002301	0.000099 ± 0.000268	0.07499	97.07	20.22 ± 1.66
32	0.345238 ± 0.004205	0.000075 ± 0.000386	0.09023	97.77	11.00 ± 1.29
33	0.279254 ± 0.002904	0.000092 ± 0.000101	0.29200	97.28	13.53 ± 0.44
34	0.335588 ± 0.004473	0.000203 ± 0.000159	0.21588	93.98	10.88 ± 0.56
35	0.114151 ± 0.001253	0.000054 ± 0.000150	0.08634	98.41	33.29 ± 1.53
36	0.104592 ± 0.001195	0.000094 ± 0.000044	0.24565	97.21	35.86 ± 0.63
37	0.303531 ± 0.003540	0.001070 ± 0.000240	0.13946	68.38	8.76 ± 0.91
38	0.520750 ± 0.006067	0.000441 ± 0.000217	0.26607	86.95	6.50 ± 0.48
39	0.192889 ± 0.002920	0.000141 ± 0.000148	0.14032	95.83	19.26 ± 0.92
41	0.381205 ± 0.003991	0.000279 ± 0.000159	0.26115	91.75	9.36 ± 0.49
42	0.351434 ± 0.003653	0.000178 ± 0.000059	0.64605	94.74	10.48 ± 0.22
43	0.373675 ± 0.004015	0.000629 ± 0.000168	0.25170	81.39	8.47 ± 0.52
44	0.338220 ± 0.003622	0.000620 ± 0.000192	0.20266	81.68	9.39 ± 0.66
45	0.285976 ± 0.003469	0.000141 ± 0.000343	0.09395	95.83	13.01 ± 1.38
46	0.559366 ± 0.006829	0.000363 ± 0.000453	0.13121	89.26	6.21 ± 0.93
47	0.448380 ± 0.007352	0.000000 ± 0.000000	0.07873	99.98	8.67 ± 0.14
48	0.259402 ± 0.003024	0.000080 ± 0.000266	0.10480	97.62	14.61 ± 1.19
49	0.354172 ± 0.004224	0.000109 ± 0.000179	0.20583	96.77	10.62 ± 0.59
50	0.378080 ± 0.004329	0.000448 ± 0.000143	0.28909	86.74	8.92 ± 0.44

Summary of Analytical Results
Sample 03WKS5

Analysis Number	39(k)/40(a+r) ± 2σ	36(a)/40(a+r) ± 2σ	39Ar(k) (x1e-14 mol)	40Ar(r) (%)	Age ± 2σ (Ma)
1	0.009345 ± 0.000191	0.000026 ± 0.000016	0.05976	99.23	372.52 ± 7.07
2	0.007922 ± 0.000120	0.000014 ± 0.000011	0.05031	99.58	433.34 ± 5.98
3	0.002372 ± 0.000062	0.000013 ± 0.000007	0.01924	99.60	1164.75 ± 22.36
4	0.010088 ± 0.000110	0.000018 ± 0.000007	0.09590	99.47	348.31 ± 3.52
5	0.006173 ± 0.000087	0.000002 ± 0.000007	0.05461	99.95	541.04 ± 6.69
6	0.007782 ± 0.000114	0.000114 ± 0.000012	0.04141	96.64	428.69 ± 5.76
7	0.008104 ± 0.000112	0.000112 ± 0.000011	0.04498	96.68	413.61 ± 5.30
8	0.009714 ± 0.000118	0.000002 ± 0.000007	0.06641	99.93	361.99 ± 4.03
9	0.004696 ± 0.000074	0.000095 ± 0.000012	0.03116	97.21	666.78 ± 8.98
10	0.005818 ± 0.000084	0.000009 ± 0.000008	0.04862	99.72	568.27 ± 7.14
11	0.308460 ± 0.005034	0.000000 ± 0.000000	0.10168	99.98	12.59 ± 0.20
12	0.204338 ± 0.003135	0.000000 ± 0.000000	0.19663	99.99	18.97 ± 0.29
13	0.006792 ± 0.000102	0.000114 ± 0.000013	0.03586	96.63	483.44 ± 6.60
14	0.003470 ± 0.000049	0.000020 ± 0.000006	0.02799	99.41	868.93 ± 9.90
15	0.003022 ± 0.000063	0.000002 ± 0.000012	0.01620	99.95	972.49 ± 15.97
16	0.005363 ± 0.000074	0.000016 ± 0.000007	0.04437	99.54	608.17 ± 7.17
17	0.004037 ± 0.000064	0.000016 ± 0.000013	0.02921	99.53	770.15 ± 10.17
18	0.376833 ± 0.005537	0.000000 ± 0.000000	0.14896	99.98	10.31 ± 0.15
19	0.007245 ± 0.000107	0.000014 ± 0.000007	0.05236	99.57	468.99 ± 6.19
20	0.004489 ± 0.000069	0.000017 ± 0.000009	0.03393	99.50	705.80 ± 9.08
21	0.003827 ± 0.000093	0.000018 ± 0.000010	0.03208	99.46	803.77 ± 15.90
22	0.006435 ± 0.000076	0.000020 ± 0.000007	0.05545	99.42	519.56 ± 5.43
23	0.005032 ± 0.000080	0.000012 ± 0.000010	0.03573	99.65	642.45 ± 8.75
24	0.003565 ± 0.000059	0.000009 ± 0.000009	0.02466	99.73	852.62 ± 11.45
25	0.004469 ± 0.000059	0.000016 ± 0.000007	0.04200	99.54	708.66 ± 7.76
26	0.007779 ± 0.000095	0.000014 ± 0.000010	0.05403	99.58	440.45 ± 4.90
27	0.040694 ± 0.000652	0.000102 ± 0.000021	0.11888	97.00	90.57 ± 1.53
28	0.007108 ± 0.000080	0.000030 ± 0.000005	0.05337	99.10	474.94 ± 4.72
29	0.002864 ± 0.000055	0.000013 ± 0.000008	0.01804	99.62	1010.95 ± 15.07
30	0.007308 ± 0.000084	0.000038 ± 0.000007	0.04598	98.89	462.55 ± 4.77
31	0.325463 ± 0.004529	0.000214 ± 0.000088	0.15409	93.66	11.18 ± 0.35
32	0.003413 ± 0.000062	0.000038 ± 0.000010	0.01844	98.87	876.81 ± 12.83
33	0.004427 ± 0.000052	0.000021 ± 0.000005	0.03915	99.38	713.23 ± 7.02
34	0.002333 ± 0.000049	0.000018 ± 0.000006	0.01599	99.46	1177.80 ± 18.21
35	0.008272 ± 0.000183	0.000015 ± 0.000007	0.04548	99.55	416.86 ± 8.27
36	0.007909 ± 0.000087	0.000022 ± 0.000006	0.05137	99.36	433.15 ± 4.31
37	0.031977 ± 0.000520	0.000037 ± 0.000013	0.10788	98.92	116.69 ± 1.89
38	0.019912 ± 0.000228	0.000021 ± 0.000006	0.14931	99.39	184.72 ± 2.03
39	0.013945 ± 0.000209	0.000026 ± 0.000006	0.10001	99.24	257.97 ± 3.63
40	0.002324 ± 0.000043	0.000014 ± 0.000007	0.01667	99.59	1181.97 ± 16.04
41	0.018172 ± 0.000226	0.000020 ± 0.000006	0.14540	99.42	201.52 ± 2.40
42	0.007442 ± 0.000089	0.000015 ± 0.000009	0.05690	99.55	457.92 ± 4.95
43	0.001018 ± 0.000110	0.000118 ± 0.000022	0.00244	96.52	2011.16 ± 131.26
44	0.003851 ± 0.000061	0.000023 ± 0.000007	0.02644	99.33	798.99 ± 10.24
45	0.006092 ± 0.000089	0.000018 ± 0.000009	0.04234	99.46	544.97 ± 7.02
46	0.003461 ± 0.000058	0.000017 ± 0.000007	0.02342	99.49	871.36 ± 11.72
47	0.010093 ± 0.000110	0.000023 ± 0.000005	0.09074	99.33	347.73 ± 3.48
48	0.007257 ± 0.000118	0.000020 ± 0.000009	0.04769	99.42	467.69 ± 6.81
49	0.013057 ± 0.000158	0.000031 ± 0.000005	0.11214	99.08	273.84 ± 3.10

Summary of Analytical Results
Sample 03WKS6

Analysis Number	39(k)/40(a+r) ± 2σ	36(a)/40(a+r) ± 2σ	39Ar(k) (x1e-14 mol)	40Ar(r) (%)	Age ± 2σ (Ma)
1	0.003198 ± 0.000108	0.000012 ± 0.000009	0.03314	99.65	941.75 ± 24.96
2	0.004587 ± 0.000105	0.000021 ± 0.000016	0.02583	99.37	703.11 ± 13.59
3	0.002091 ± 0.000067	0.000022 ± 0.000014	0.01660	99.34	1290.63 ± 29.82
4	0.001885 ± 0.000075	0.000018 ± 0.000014	0.01309	99.47	1390.35 ± 38.95
5	0.003942 ± 0.000085	0.000026 ± 0.000013	0.02936	99.24	795.17 ± 14.13
6	0.001920 ± 0.000068	0.000033 ± 0.000012	0.01653	99.01	1367.83 ± 34.20
7	0.002946 ± 0.000082	0.000028 ± 0.000013	0.02099	99.19	1000.03 ± 21.70
8	0.002016 ± 0.000070	0.000021 ± 0.000011	0.01606	99.38	1325.05 ± 32.52
9	0.003448 ± 0.000080	0.000019 ± 0.000012	0.02563	99.43	886.38 ± 16.38
10	0.004780 ± 0.000107	0.000018 ± 0.000017	0.03397	99.47	679.97 ± 13.04
11	0.002000 ± 0.000072	0.000014 ± 0.000011	0.01708	99.57	1334.64 ± 34.21
12	0.003922 ± 0.000078	0.000010 ± 0.000011	0.03326	99.69	801.32 ± 13.00
13	0.002584 ± 0.000073	0.000000 ± 0.000000	0.01989	100.00	1111.18 ± 23.33
14	0.002307 ± 0.000082	0.000021 ± 0.000013	0.01625	99.38	1202.72 ± 31.49
15	0.005694 ± 0.000109	0.000016 ± 0.000017	0.03122	99.52	587.00 ± 9.91
16	0.001949 ± 0.000078	0.000011 ± 0.000013	0.01418	99.67	1359.70 ± 38.62
17	0.002284 ± 0.000091	0.000016 ± 0.000015	0.01413	99.53	1212.97 ± 35.30
18	0.002056 ± 0.000107	0.000009 ± 0.000017	0.01078	99.75	1310.11 ± 48.68
19	0.002382 ± 0.000061	0.000018 ± 0.000010	0.02105	99.46	1175.36 ± 22.20
20	0.001921 ± 0.000080	0.000026 ± 0.000014	0.01384	99.22	1369.58 ± 40.16
21	0.002154 ± 0.000076	0.000023 ± 0.000013	0.01606	99.32	1263.54 ± 32.44
22	0.002978 ± 0.000099	0.000049 ± 0.000020	0.01668	98.55	986.79 ± 25.75
23	0.003472 ± 0.000072	0.000033 ± 0.000015	0.02799	99.01	878.50 ± 14.77
24	0.003337 ± 0.000084	0.000028 ± 0.000013	0.02379	99.17	907.72 ± 18.06
25	0.003191 ± 0.000072	0.000025 ± 0.000012	0.02763	99.27	940.63 ± 16.65
26	0.215093 ± 0.003369	0.000385 ± 0.000158	0.12238	88.62	16.28 ± 0.89
27	0.002807 ± 0.000069	0.000030 ± 0.000012	0.02388	99.11	1036.96 ± 19.56
28	0.003054 ± 0.000081	0.000028 ± 0.000010	0.03051	99.17	972.35 ± 20.03
29	0.003459 ± 0.000078	0.000037 ± 0.000013	0.02517	98.92	880.41 ± 16.04
30	0.003701 ± 0.000109	0.000040 ± 0.000013	0.02740	98.80	833.53 ± 19.85
31	0.002581 ± 0.000113	0.000050 ± 0.000020	0.01340	98.53	1100.00 ± 36.52
32	0.002163 ± 0.000093	0.000015 ± 0.000016	0.01202	99.57	1262.07 ± 39.44
33	0.002967 ± 0.000089	0.000021 ± 0.000014	0.01940	99.39	996.15 ± 23.23
34	0.002138 ± 0.000070	0.000021 ± 0.000011	0.01801	99.39	1270.67 ± 29.87
35	0.005618 ± 0.000103	0.000032 ± 0.000013	0.04089	99.05	591.34 ± 9.49
36	0.002048 ± 0.000056	0.000022 ± 0.000009	0.02048	99.36	1310.32 ± 25.50
37	0.002725 ± 0.000087	0.000025 ± 0.000014	0.01737	99.26	1061.69 ± 25.76
38	0.003855 ± 0.000074	0.000026 ± 0.000012	0.03076	99.24	809.57 ± 12.80
39	0.005345 ± 0.000113	0.000028 ± 0.000015	0.03277	99.17	617.52 ± 11.28
40	0.002448 ± 0.000086	0.000030 ± 0.000013	0.01684	99.12	1149.25 ± 29.97
41	0.004639 ± 0.000082	0.000029 ± 0.000011	0.04067	99.13	695.15 ± 10.33
42	0.002319 ± 0.000087	0.000024 ± 0.000015	0.01531	99.29	1197.27 ± 32.96
43	0.002994 ± 0.000060	0.000027 ± 0.000010	0.02954	99.21	987.75 ± 15.39
44	0.002639 ± 0.000075	0.000029 ± 0.000011	0.02152	99.14	1086.79 ± 23.43
45	0.002681 ± 0.000104	0.000033 ± 0.000016	0.01593	99.01	1073.02 ± 31.53

Summary of Analytical Results
Sample 03WKS7

Analysis Number	39(k)/40(a+r) ± 2σ	36(a)/40(a+r) ± 2σ	39Ar(k) (x1e-14 mol)	40Ar(r) (%)	Age ± 2σ (Ma)
1	0.004125 ± 0.000146	0.000060 ± 0.000096	0.03233	98.24	760.09 ± 28.30
2	0.000565 ± 0.000148	0.000018 ± 0.000295	0.00395	99.46	2858.09 ± 397.38
3	0.001244 ± 0.000133	0.000025 ± 0.000139	0.00991	99.27	1828.95 ± 131.76
4	0.001426 ± 0.000169	0.000231 ± 0.000151	0.01147	93.18	1607.54 ± 136.18
5	0.001361 ± 0.000191	0.000203 ± 0.000488	0.00817	94.00	1667.14 ± 226.24
6	0.000968 ± 0.000129	0.000060 ± 0.000174	0.00863	98.23	2117.04 ± 178.96
7	0.000968 ± 0.000188	0.000073 ± 0.000100	0.00771	97.85	2111.87 ± 244.45
8	0.001123 ± 0.000143	0.000086 ± 0.000144	0.01177	97.46	1926.20 ± 158.87
9	0.001012 ± 0.000344	0.000070 ± 0.000128	0.00903	97.92	2057.72 ± 419.37
10	0.000962 ± 0.000130	0.000137 ± 0.000186	0.00774	95.94	2094.80 ± 181.47
11	0.280961 ± 0.007146	0.000944 ± 0.005828	0.08150	72.08	10.16 ± 24.19
12	0.000675 ± 0.000228	0.000059 ± 0.000155	0.00401	98.25	2589.63 ± 469.57
13	0.000920 ± 0.000141	0.000036 ± 0.000077	0.00925	98.93	2189.47 ± 196.11
14	0.001107 ± 0.000368	0.000064 ± 0.000280	0.01019	98.12	1952.13 ± 408.89
15	0.001175 ± 0.000115	0.000051 ± 0.000095	0.01093	98.49	1885.72 ± 119.57
16	0.000865 ± 0.000140	0.000029 ± 0.000142	0.00774	99.14	2270.95 ± 216.70
17	0.001442 ± 0.000255	0.000076 ± 0.000238	0.01112	97.76	1646.99 ± 205.90
18	0.000756 ± 0.000125	0.000102 ± 0.000126	0.00663	96.98	2418.23 ± 225.22
19	0.000843 ± 0.000192	0.000140 ± 0.000130	0.00711	95.85	2260.85 ± 298.10
20	0.001048 ± 0.000182	0.000133 ± 0.000510	0.00878	96.07	1991.62 ± 282.56
21	0.001692 ± 0.000202	0.000064 ± 0.000092	0.01029	98.12	1483.44 ± 124.03
22	0.000946 ± 0.000159	0.000081 ± 0.000057	0.00649	97.62	2137.42 ± 212.11
23	0.000944 ± 0.000122	0.000042 ± 0.000108	0.00985	98.76	2155.05 ± 167.94
24	0.000833 ± 0.000179	0.000049 ± 0.000083	0.00525	98.54	2311.72 ± 281.24
25	0.397824 ± 0.007105	0.000325 ± 0.003104	0.14246	90.38	9.00 ± 9.11
26	0.000430 ± 0.000210	0.000016 ± 0.000192	0.00287	99.52	3259.29 ± 740.35
27	0.001230 ± 0.000159	0.000062 ± 0.000103	0.00907	98.17	1828.96 ± 152.66
28	0.001359 ± 0.000284	0.000244 ± 0.000228	0.01166	92.78	1654.55 ± 239.78
29	0.433753 ± 0.016646	0.001481 ± 0.022352	0.04137	56.22	5.14 ± 60.27
30	0.000790 ± 0.000152	0.000004 ± 0.000156	0.00800	99.89	2400.58 ± 262.44
31	0.154833 ± 0.004478	0.000462 ± 0.002156	0.08299	86.35	22.00 ± 16.15
32	0.000756 ± 0.000176	0.000027 ± 0.000178	0.00452	99.19	2448.21 ± 319.14
33	0.000325 ± 0.000190	0.000006 ± 0.000142	0.00247	99.82	3697.40 ± 922.56
34	0.000993 ± 0.000219	0.000215 ± 0.000191	0.00959	93.65	2026.81 ± 278.71
35	0.000800 ± 0.000166	0.000005 ± 0.000163	0.00606	99.86	2382.09 ± 280.86
36	0.000981 ± 0.000207	0.000070 ± 0.000185	0.00727	97.93	2096.74 ± 270.99
37	0.000810 ± 0.000149	0.000013 ± 0.000114	0.00660	99.62	2363.02 ± 247.02
38	0.000589 ± 0.000277	0.000083 ± 0.000355	0.00445	97.54	2770.87 ± 683.94
39	0.000757 ± 0.000253	0.000061 ± 0.000253	0.00567	98.20	2433.93 ± 458.12
40	0.000844 ± 0.000104	0.000004 ± 0.000148	0.00843	99.87	2312.33 ± 170.69
41	0.001011 ± 0.000178	0.000006 ± 0.000144	0.00596	99.84	2082.56 ± 223.43
42	0.000644 ± 0.000176	0.000068 ± 0.000106	0.00422	97.98	2652.03 ± 382.86
43	0.000736 ± 0.000139	0.000049 ± 0.000095	0.00630	98.56	2476.01 ± 257.24
44	0.000557 ± 0.000190	0.000017 ± 0.000118	0.00393	99.50	2878.49 ± 492.13
45	0.000749 ± 0.000101	0.000031 ± 0.000121	0.00819	99.09	2460.96 ± 188.15
46	0.005970 ± 0.000272	0.000038 ± 0.000130	0.04132	98.87	560.50 ± 28.86
47	0.001244 ± 0.000286	0.000028 ± 0.000190	0.00781	99.18	1827.43 ± 271.76

Chapter 7: Summary

A demonstrable correlation between the physiography and tectonics of central Nepal illustrates the expected behavior of a landscape subject to tectonic forcing: the landscape is systematically steeper, higher, and has higher relief where exhumation and erosion rates are the greatest (Kirby et al., 2003; Snyder et al., 2000). This correlation between landscape morphology and tectonic forcing highlights one of the primary messages of this thesis: a detailed analysis of landscape form can be a valuable tool for unraveling the distribution of uplift and erosion rates in active tectonic settings. Clearly, geomorphology will never be a substitute for detailed structural mapping, GPS measurements, or seismic moment data in settings where these data can be easily obtained. However, as the resolution of digital topographic data improves for sites around the world, landscape morphology can at least be a valuable reconnaissance tool, and can perhaps be the foundation for detailed tectonic analyses in field settings where other tools are more difficult to implement.

While a correlation between tectonics and landscape morphology has been demonstrated in this thesis, the nature of a complete feedback in which erosion actually plays a role in localizing tectonic displacements remains an open question. Numerical and analytical simulations demonstrate that such a feedback should exist at some level (Beaumont et al., 2001; Koons, 1995; Whipple and Meade, 2004; Willett, 1999); and studies demonstrating a correlation between precipitation and long-term exhumation rates are suggestive of a feedback in other field settings (Dadson et al., 2003; Reiners et al., 2003). What is lacking, however, is a complete understanding of the role that discrete tectonic structures play in accommodating changes in

exhumation rates driven by focused erosional unloading. Indeed, two interpretations of similar datasets from the Marsyandi river in Nepal suggest a first order role, and no role, respectively, of precipitation in localizing deformation along discrete structures near the MCT (Burbank et al., 2003; Hodges et al., 2004). Other field studies from wet, tectonically active settings are needed to evaluate how closely tectonic deformation mimics precipitation, and how strain may be localized by erosion in active environments. As we build this database for tectonically active settings around the world, we can then begin to evaluate the degree to which climate and tectonics might actually co-evolve as a coupled earth system.

The capacity for surface processes to localize tectonic displacements must be modulated by the degree to which erosion can influence the energetics of an orogenic system by removing mass from its upper boundary (Beaumont et al., 2004; Hodges et al., 2001; Zeitler et al., 2001). Central to our ability to demonstrate a causal link between erosion and tectonics, then, is a better understanding of how erosional signals are transmitted through landscapes to drive this mass removal (Burbank et al., 1996; Crosby and Whipple, in review; Roering et al., 2001). Chapter 3 illustrates one example of how our simplified rules for bedrock channel response might fall short of fully describing the transient behavior of natural systems, and we have only begun to delve into an understanding of how whole landscapes respond to tectonic perturbation (Dietrich et al., 2003). Integrated studies of hillslope and channel response, including quantification of erosion rates at sub-catchment scales in actively adjusting landscapes, will help us to understand the mechanisms and timescales over which mass is removed from landscapes through focused erosion.

Integration of data from a variety of temporal scales will also continue to be important, so that we can begin to bridge the gap between decadal climatic observations and million-year

thermochronologic data. Chapter 5 begins to do this for one field setting by utilizing both cosmogenic and thermochronologic data, but additional field sites in which climatic, stratigraphic, cosmogenic, and thermochronologic data can be combined will allow us to more definitively illustrate the persistence of exhumation and erosion signals through time. Such a demonstration of persistence is still one step removed from causality, but building additional databases to compare observations from multiple timescales can only bring us closer to an understanding of climate-tectonic interactions at the scale of entire orogens (Hodges et al., 2004).

Added to the remaining questions of how climate and tectonics interact in general are specific questions about the tectonics of central Nepal. Most importantly, if the physiographic transition in central Nepal reflects surface-breaking fault displacements rather than strain accumulation along a ramp in the MHT, what are the implications for seismic hazard along the rangefront? Most studies suggest that the locked MHT flat between the rangefront and the MFT represents the most substantial seismic hazard in Nepal (Bilham et al., 2001), but if major thrust earthquakes are also a possibility further hinterland, it is possible that the distribution of seismic hazard zones in central Nepal needs to be reconsidered.

The physiographic data summarized in Chapter 6 suggest that the tectonic architecture of the Himalaya, and the associated seismic hazards, may vary substantially along strike. Further studies are warranted to evaluate the degree to which the tectonics of the range actually change along strike. One key piece of additional data that would greatly improve our understanding is low-temperature thermochronologic data from transects across the Himalayan front. Combination of $^{40}Ar/^{39}Ar$ and (U-Th)/He data, for example, might allow models of accretion and pure overthrusting to be distinguished on the basis of the different patterns of cooling ages implied by the two models.

If, with new data, along-strike changes in the tectonics of the Himalaya are confirmed, the question of why the tectonic architecture of the Himalayan system might vary at 100 km spatial scales remains. In addition, the question remains of how the across-strike architecture of the Himalaya has evolved such that activity on the MFT and structures along the foot of the High Himalaya have apparently overlapped in time. Are along-strike and across strike variations in tectonics related to spatial variations in precipitation and erosion? Or would these variations in tectonic style exist in the absence of strong climatic forcing? Some of these questions may ultimately remain unanswerable; but additional interdisciplinary studies of the Himalaya and other active ranges might bring us closer to understanding the relationships among climate, erosion and tectonics in active orogens.

References

Beaumont, C., Jamieson, R. A., Nguyen, M. H., and Lee, B., 2001, Himalayan tectonics explained by extrusion of a low-viscosity crustal channel coupled to focused surface denudation: Nature, v. 414, p. 738-742.

Beaumont, C., Jamieson, R. A., Nguyen, M. H., and Medvedev, S., 2004, Crustal channel flows: 1. Numerical models with implications to the tectonics of the Himalayan-Tibetan orogen: Journal of Geophysical Research, v. 109, p. doi: 10.1029/2003JB002811.

Bilham, R., Gaur, V. K., and Molnar, P., 2001, Himalayan Seismic Hazard: Science, v. 293, p. 1442-1444.

Burbank, D. W., Blythe, A. E., Putkonen, J., Pratt-Sitaula, B. A., Gabet, E. J., Oskin, M. E., Barros, A. P., and Ojha, T., 2003, Decoupling of erosion and climate in the Himalaya: Nature, v. 426, p. 652-655.

Burbank, D. W., Leland, J., Fielding, E., Anderson, R. S., Brozovic, N., Reid, M. R., and Duncan, C., 1996, Bedrock incision, rock uplift and threshold hillslopes in the northwestern Himalayas: Nature (London), v. 379, no. 6565, p. 505-510.

Crosby, B. T., and Whipple, K. X., in review, Knickpoint initiation and distribution within fluvial networks: 236 waterfalls in the Waipaoa River, North Island, New Zealand: Geomorphology.

Dadson, S. J., Hovius, N., Chen, H., Dade, W. B., Hsieh, M.-L., Willett, S., Hu, J.-C., Horng, M.-J., Chen, M.-C., Stark, C. P., Lague, D., and Lin, J.-C., 2003, Links between erosion, runoff variability and seismicity in the Taiwan orogen: Nature, v. 426, p. 648-651.

Dietrich, W. E., Bellugi, D., Heimsath, A. M., Roering, J. J., Sklar, L., and Stock, J. D., 2003, Geomorphic transport laws for predicting landscape form and dynamics, *in* Wilcock, P., and Iverson, R., eds., Prediction in geomorphology: Washington, D.C., American Geophysical Union, p. 103-132.

Hodges, K., Wobus, C., Ruhl, K., Schildgen, T., and Whipple, K., 2004, Quaternary deformation, river steepening and heavy precipitation at the front of the Higher Himalayan ranges: Earth and Planetary Science Letters, v. 220, no. 3-4, p. 379-389.

Hodges, K. V., Hurtado, J. M., and Whipple, K. X., 2001, Southward Extrusion of Tibetan Crust and its Effect on Himalayan Tectonics: Tectonics, v. 20, no. 6, p. 799-809.

Kirby, E., Whipple, K., Tang, W., and Chen, Z., 2003, Distribution of active rock uplift along the eastern margin of the Tibetan Plateau: inferences from bedrock channel longitudinal profiles: Journal of Geophysical Research, v. 108, no. B4, p. doi: 10.1029/2001JB000861.

Koons, P. O., 1995, Modeling the topographic evolution of collisional belts: Annual Review of Earth and Planetary Sciences, v. 23, p. 375-408.

Reiners, P. W., Ehlers, T. A., Mitchell, S. G., and Montgomery, D. R., 2003, Coupled spatial variations in precipitation and long-term erosion rates across the Washington Cascades: Nature, v. 426, p. 645-647.

Roering, J. J., Kirchner, J. W., and Dietrich, W. E., 2001, Hillslope evolution by nonlinear, slope-dependent transport: steady state morphology and equilibrium adjustment timescales: Journal of Geophysical Research, v. 106, no. B8, p. 16499-16513.

Snyder, N., Whipple, K., Tucker, G., and Merritts, D., 2000, Landscape response to tectonic forcing: DEM analysis of stream profiles in the Mendocino triple junction region, northern California: Geological Society of America, Bulletin, v. 112, no. 8, p. 1250-1263.

Whipple, K. X., and Meade, B. J., 2004, Controls on the strength of coupling among climate, tectonics and deformation in two-sided, frictional orogenic wedges at steady state: Journal of Geophysical Research-Earth Surface, v. 109, p. doi: 10.1029/2003JF000019.

Willett, S. D., 1999, Orogeny and orography: the effects of erosion on the structure of mountain belts: Journal of Geophysical Research, v. 104, p. 28957-28981.

Zeitler, P. K., Meltzer, A. S., Koons, P. O., Craw, D., Hallet, B., Chamberlain, C. P., Kidd, W. S. F., Park, S. K., Seeber, L., Bishop, M., and Shroder, J., 2001, Erosion, Himalayan geodynamics, and the geomorphology of metamorphism: GSA Today, v. 11, p. 4-9.